A Study on Quenching and Galaxy Growth in $z \sim 1$ Clusters using HST WFC3 Grism Observations

A thesis submitted
by
Jasleen Kaur Matharu
to
The University of Cambridge
&
Churchill College

in fulfillment of the requirements
for the degree of
Doctor of Philosophy
in the subject of
Astronomy

Under the supervision of
Dr. Adam Muzzin
Prof. Paul C. Hewett
&
Dr. Matthew W. Auger

May 2019

Declaration

This thesis is the result of my own work and includes nothing which is the outcome of work done in collaboration except as declared on this page and specified in the text where reference is made to the work of others.

It is not substantially the same as any that I have submitted, or, is being concurrently submitted for a degree or diploma or other qualification at the University of Cambridge or any other University or similar institution except as declared on this page and specified in the text. I further state that no substantial part of my thesis has already been submitted, or, is being concurrently submitted for any such degree, diploma or other qualification at the University of Cambridge or any other University or similar institution except as declared on this page and specified in the text.

It does not exceed the prescribed word limit of 60,000 words as set by the Physics and Chemistry Degree Committee.

- Chapter 2 is based on work published in Matharu et al. (2019).
- Chapter 3 is based on a paper currently in the referee process with the journal *Monthly Notices of the Royal Astronomical Society* entitled:

  "HST/WFC3 grism observations of $z \sim 1$ clusters: poststarburst galaxies and evidence for evolution in the mass–size relation of quiescent galaxies from recently quenched galaxies"

  by **Jasleen Matharu**, Adam Muzzin, Gabriel B. Brammer, Remco F.J. van der Burg, Matthew W. Auger, Paul C. Hewett, Jeffrey C.C Chan, Ricardo Demarco, Pieter van Dokkum, Danilo Marchesini, Erica. J. Nelson, Allison G. Noble and Gillian Wilson.
- Chapter 4 is based on work currently being prepared for publication.

The *Hubble Space Telescope* (HST) data for the ten galaxy clusters this thesis is based on were reduced by Gabriel Brammer. Grism redshifts were also derived by Gabriel Brammer. Photometric redshifts and stellar masses were calculated by Remco van der Burg, details of which can be found in van der Burg et al. (2013).

Jasleen Matharu
28th May 2019

A Study on Quenching and Galaxy Growth in $z \sim 1$ Clusters using HST WFC3 Grism Observations

Summary

The work in this thesis uses 38 orbits worth of *Hubble Space Telescope* (HST), *Wide Field Camera 3* (WFC3) infrared F140W imaging and G141 grism data on 10 galaxy clusters at $z \sim 1$ to study how the quenching of star formation in galaxies and galaxy size growth operates in different environments at this redshift. The unique capabilities of space-based slitless spectroscopy with the G141 grism allows for the construction of spatially resolved Hα maps, providing the possibility to directly observe environmental quenching at $z \sim 1$ for the first time. This allows us to understand the detailed physics behind environmental quenching mechanisms and how they operate on galaxies at this high redshift.

The quenching of star formation leads to the build-up of quenched (or "quiescent") galaxies in the Universe. Observations have also shown that quiescent galaxies grow disproportionately more in size than stellar mass from high to low redshifts. Many studies have argued that minor mergers are responsible for this size growth. To test this hypothesis, it is possible to use the cluster environment as a laboratory. Cluster galaxies have high peculiar velocities, making mergers between them rare. Since minor mergers are expected to increase galaxy size more than they do stellar mass, the most direct way to test this is to measure the stellar mass–size relations in both the cluster and field environments at fixed redshift and compare them to see if there is a significant offset in size. If the predictions of minor mergers driving galaxy size growth are true, cluster galaxies should find themselves inhibited from size growth and will therefore be significantly smaller than field galaxies at fixed stellar mass. In Chapter 2 of this thesis, we do this experiment at $z \sim 1$, finding that quiescent cluster galaxies are smaller than quiescent field galaxies at fixed stellar mass. This supports the case for minor mergers driving size growth in quiescent field galaxies.

Nevertheless, the process whereby large star-forming galaxies quench and join the quiescent population at the large size end has also been suggested as an explanation for the size growth of quiescent galaxies. Using ancillary spectroscopy of our 10 clusters from the Gemini Cluster Astrophysics Spectroscopic Survey (GCLASS), we pick out 23 spectroscopically confirmed recently quenched galaxies in the clusters and study their position on the stellar mass–size relation in Chapter 3. We find that they follow a mass–size relation lying midway between the star-forming and quiescent relations. This result provides direct evidence showing galaxies which quench later are on average larger than the bulk of the quiescent galaxy population at fixed stellar mass and redshift. This work showed that at least in the cluster environment, recently quenched galaxies will induce a rise in the average size of quiescent galaxies with decreasing redshift.

Finally, this thesis attempts to tackle one of the biggest unanswered questions in galaxy evolution: how does quenching operate in the high-redshift Universe? Surveys such as GASP and VESTIGE have already allowed us to build a comprehensive understanding of environmental quenching in the local Universe. Obtained using the WFC3 G141 grism, we use spatially resolved Hα maps of cluster and field galaxies at $z \sim 1$ to directly observe where star formation is occurring in these galaxies and where it is not. In Chapter 4, we measure the stellar mass–size relations of $z \sim 1$ star-forming cluster and field galaxies in F140W and Hα. The lack of a clear environmental quenching signature in this work hints at the rapidity of environmental quenching in the high-redshift Universe, and/or a complete change in the physics of environmental quenching.

To my parents Manjit Kaur & Manjeet Singh Matharu,

who let their only child become something other than a Doctor or an Engineer.

Acknowledgments

First and foremost, I would like to thank my primary supervisor Adam Muzzin. You were the first Astronomer I met that could laugh with me at my mistakes, rather than at them. I especially thank you for your courage in giving me the freedom to conduct my PhD my way, and encouraging originality in my work. Considering that my knowledge of galaxy formation and evolution rested on a single Galactic Dynamics course during my Masters year at UCL, you should be proud of what you've helped me to accomplish.

Secondly, I would like to express my gratitude to my supervisors Paul Hewett and Matt Auger. I am truly grateful you both agreed to become additional supervisors of mine after Adam's departure from Cambridge. The wealth of knowledge and experience you both have in all things science has helped steer my PhD and career towards success. In particular, I would like to give my sincere gratitude to Matt Auger for putting in the time and effort to ensure my postdoctoral job applications were of top quality.

Thirdly, I would like to acknowledge my office mates Nick Henden and Sophie Koudmani, for being constant sources of humour. Completing a PhD is particularly taxing on the mind. Bursting out in laughter now and again has only made this marathon easier.

Along the same lines, I would like to thank all the frequent attenders of the weekly board games sessions here at the Institute of Astronomy – Douglas Boubert, Douglas Buisson, Sid Gandhi and Lukas Hergt – as well as Pooneh Nazari, Laura Rogers and Amy Rankine for being some of the most supportive colleagues and friends I have had during my time at the IoA. I will cherish memories from the weekly board games sessions: they have always been a great stress release and generated immense amounts of laughter.

I would also like to thank my housemate Matteo Sbroscia, with whom I have lived in Cambridge from the very beginning of my PhD, and have enjoyed all the trials and tribulations of student living.

Thank you to Priyanka Singh, whom I asked when we were both aged about 12, sitting in the front row of a History class, "why do you work so hard?". Her response single-handedly gave me reason to achieve in life.

Thank you to my parents, who have supported me unconditionally, completely unfazed even when it was difficult to understand the problems I was going through.

To my grandma, who began this journey with me when she held my hand to take me to school, till the day I came home and cried in her arms at how bad my Physics exam went at the age of 18. Today, in exasperation, she asks me: "When are you going to stop studying and get married?"

Finally, I would like to thank Krishna Naidoo. During my PhD, you refused to let me put myself down for even a single instance. The completion of my PhD is just as much your achievement as it is mine.

There are two kinds of important men. There are those who, when the boulder of time rolls toward them, stand up in front of it and hold out their hands. All their lives, they've been told how great they are. They assume the world itself will bend to their whims as their nurse did when fetching them a fresh cup of milk.

Those men end up squished.

Other men stand to the side when the boulder of time passes, but are quick to say, 'See what I did! I made the boulder roll there. Don't make me do it again!'

These men end up getting everyone else squished.

"Is there not a third type of person?" There is, but they are oh so rare. These know they can't stop the boulder. So they walk beside it, study it, and bide their time. Then they shove it – ever so slightly – to create a deviation in its path.

These are the men... well, these are the men who actually change the world.

– Brandon Sanderson, The Stormlight Archive Book Three: Oathbringer
Chapter 68: Aim for the Sun

Contents

I declare that no accomplishment has substance nearly as great as the road used to achieve it.

Brandon Sanderson, The Way of Kings

1

Introduction

Early observations of galaxies led Edwin Hubble to define what is today known as The Hubble sequence. Introduced in his book *The Realm of the Nebulae* (Hubble, 1936), Hubble classified the morphologies of galaxies into a 'tuning fork' diagram, shown in Figure 1.1. Hubble suggested that galaxies evolved from having elliptical morphologies to spiral morphologies, which has led to the convention of calling elliptical galaxies "early-type" and spiral galaxies "late-type". However, we know today that this is not the case (Binney & Merrifield, 1998).

Subsequent to Hubble's suggested classification, multi-wavelength observations allowed us to observe the *colours* of galaxies for the first time. The advantage of measuring colours rather than morphology is that it is less subjective than measuring morphology. The colours of galaxies provide information on their stellar populations and therefore their physical properties.

The advent of large redshift surveys in the 1980s allowed for multi-wavelength observations to be conducted over large areas of the sky (e.g. Geller & Huchra 1983; Folkes et al. 1999). One of the most impactful of these is the Sloan Digital Sky Survey (SDSS) which began in 2000 (York et al., 2000). Figure 1.2 shows what the Hubble sequence looks like in SDSS when composite colour images are created from combining imaging in optical and infrared bands. Immediately recognisable is the blue colour of spiral arms and the more redder colours of elliptical galaxies.

Upon closer inspection, it can be shown that most galaxies are either red in colour with high

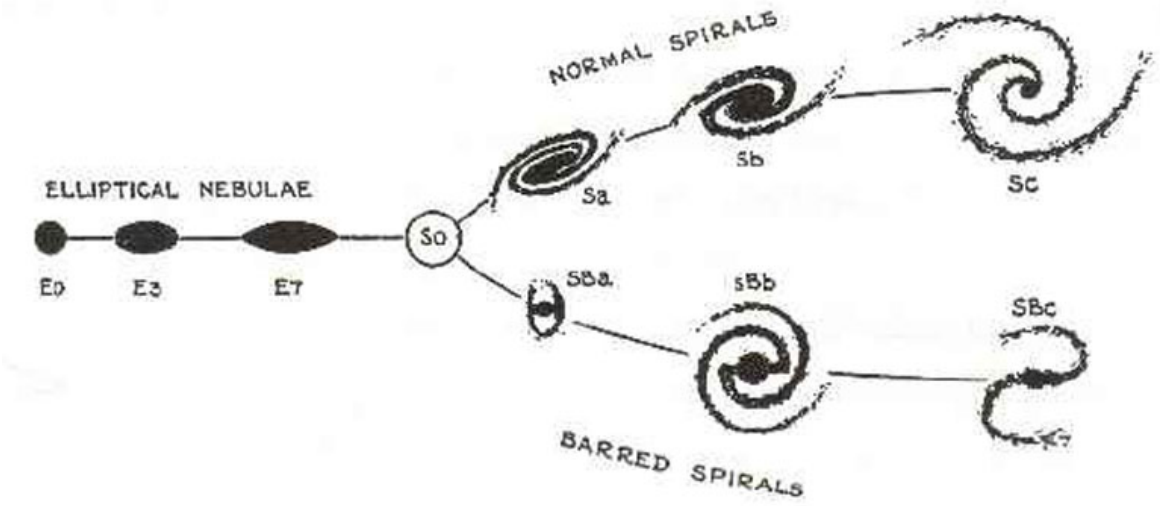

Figure 1.1: The Hubble sequence as defined by Edwin Hubble in Hubble (1936).

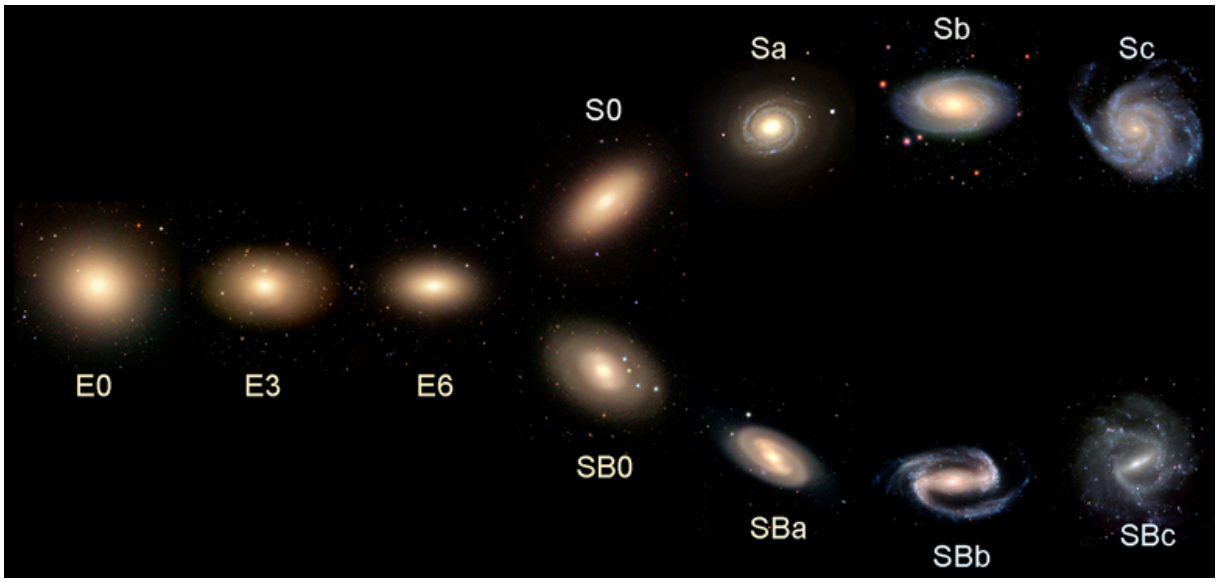

Figure 1.2: The Hubble sequence as observed in the Sloan Digital Sky Survey. Credit: Galaxy Zoo (https://blog.galaxyzoo.org/2010/05/12/types-of-galaxies/).

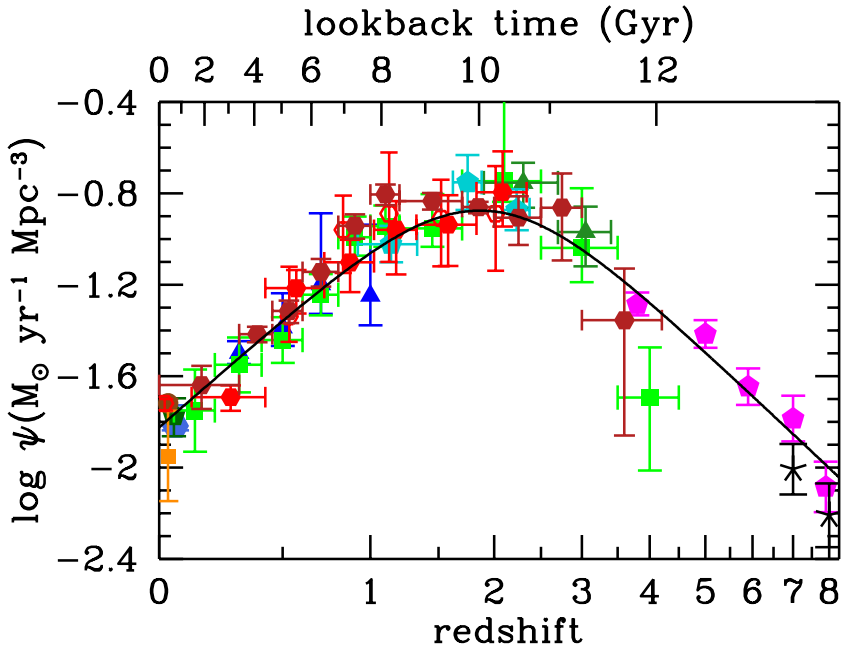

Figure 1.3: The history of cosmic star formation from far-ultraviolet (FUV) and infrared (IR) rest-frame measurements (Madau & Dickinson, 2014). The solid curve shows the best-fit star formation rate density (SFRD).

luminosity or blue in colour with low luminosity. The local galaxy population as seen in surveys such as SDSS can therefore be described by a bimodal distribution. The two peaks of this distribution correspond to a large difference in the stellar mass of these two populations of galaxies. Red galaxies have higher mass-to-light ratios than blue galaxies because they do not contain massive luminous stars which have short lifetimes.

The absence of young, massive bluer stars in ellipticals suggests that these galaxies are not actively forming new stars. It seems that star formation has been quenched in these galaxies (Schneider, 2015).

1.1 The Quenching of star formation in galaxies

The star formation rate density (SFRD) tells us the amount of star formation occurring in the Universe at any given point in time per unit volume. The first step in measuring the SFRD is to count the number of galaxies in a given volume as a function of their luminosity. If this luminosity function (LF) is measured at a particular wavelength that traces star formation in galaxies (e.g. the ultraviolet or infrared), it can tell us how much star formation is occurring in a given volume. Figure 1.3 shows the SFRD measured over a large portion of the Universe's history. The decline in the SFRD of the Universe, or "quenching" seems to have begun around $z \sim 2$.

The reasoning for why the quenching of star formation occurs remains one of the largest open questions in our understanding of galaxy evolution. We have still not been able to determine which

physical mechanism is responsible for driving it. Recent observations have shown that the dark matter haloes of quenched galaxies – usually referred to as "quiescent" or "passive" galaxies in the literature – contain enough gas such that star formation can continue (Tumlinson et al., 2013). However, something is preventing this gas from cooling and forming stars. So far, observations have determined that quenching mechanisms fall into two broad categories: "mass-quenching" and "environmental quenching" (e.g. Peng et al. 2010b). Mass-quenching involves processes internal to galaxies that cause the shutdown of star formation (such as Active Galactic Nuclei (AGN), supernova and stellar feedback). Environmental quenching concerns processes external to a galaxy which quench its star formation (e.g. ram-pressure stripping, tidal stripping or starvation). This thesis focuses on environmental quenching.

1.1.1 Environmental quenching

For a while now, it has been known that satellite galaxies are more quenched than central galaxies of a similar mass (Peng et al., 2010b; Muzzin et al., 2012). Satellite galaxies in clusters are redder in colour, less actively star-forming and more bulge-dominated than their counterparts in the low-density field environment (Abell 1965; Oemler 1974; Dressler 1980; Postman & Geller 1984; Balogh et al. 1997; Poggianti et al. 1999; Lewis et al. 2002; Gomez et al. 2003; Postman et al. 2005).

Peng et al. (2010b) studied the stellar masses of low-redshift ($0.02 < z < 0.085$) galaxies as a function of SFR and environment in SDSS. In this study the mean SFR was found to be *independent* of environment at fixed stellar mass (left panel of Figure 1.4). This indicates that SFRs are not suppressed in high-density environments such as clusters. This trend is hard to reconcile with the results of the aforementioned studies that show the fraction of red galaxies is higher in high-density regions such as clusters. To explain these observations, SFRs in cluster galaxies should be lower than SFRs of galaxies in low-density environments. Such a trend does not seem to be present in the SFRs of galaxies, instead, there is a difference in the fraction of red galaxies. As can be seen in the right panel of Figure 1.4, the fraction of red galaxies increases with stellar mass *and* environmental density. As well as suggesting two channels for quenching, this result showed that environment does have an affect on star formation. However, there is no measured change in the average SFR with environment. The same trends seen by Peng et al. (2010b) at low redshifts were seen by Muzzin et al. (2012) at high redshift ($z \sim 1$). The fact that these trends exist at high redshift means that the environmental quenching mechanisms responsible for driving these trends were in place at even higher redshifts. However, the way in which these quenching mechanisms affect

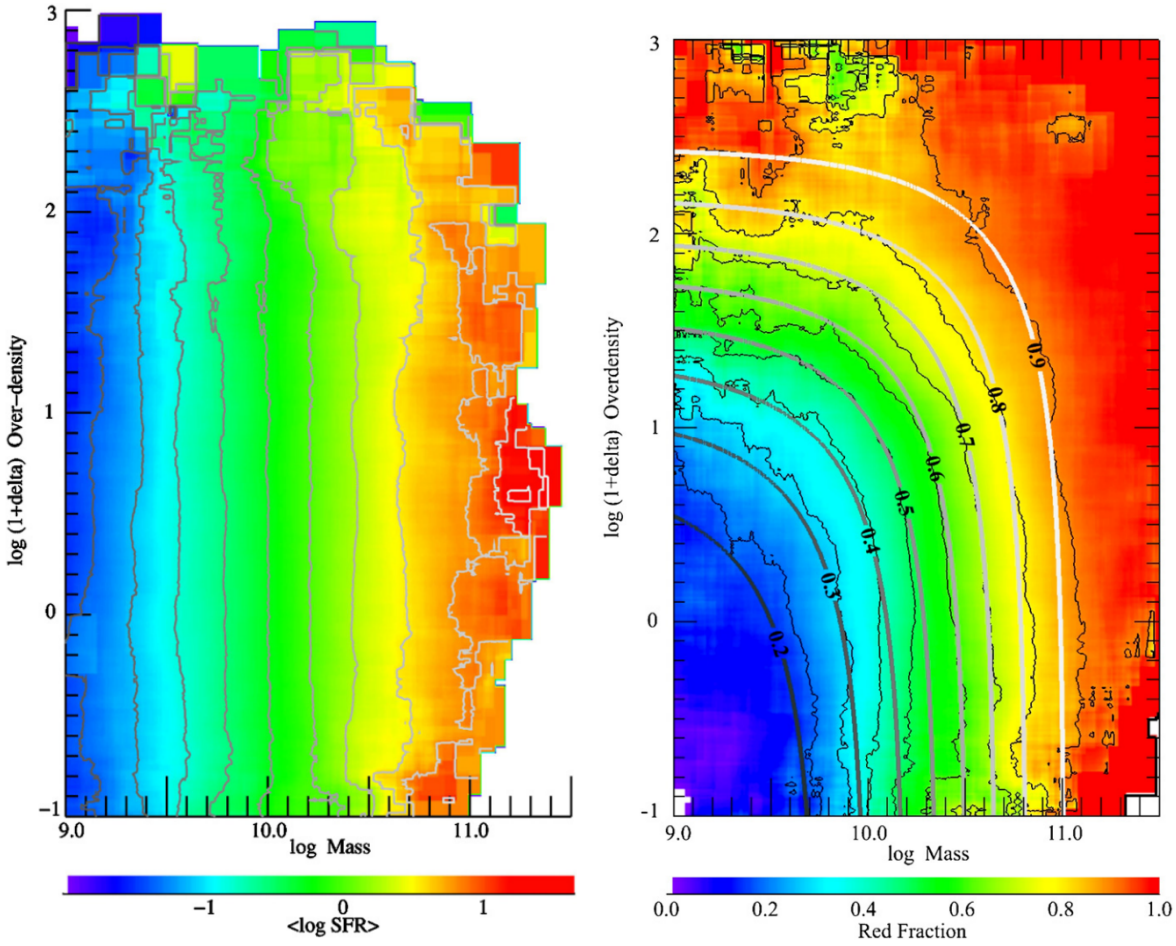

Figure 1.4: Left: Mean Log(SFR) as a function of stellar mass and environment for star-forming galaxies in SDSS. The mean SFR is *independent* of environment at fixed stellar mass. Right: Fraction of red galaxies in SDSS as a function of stellar mass and environment. Red fraction is *dependent* on both stellar mass *and* environment (Peng et al., 2010b).

galaxies physically may evolve with time. This is because between $0 < z < 1$, the structures of galaxies and their SFRs change. We can see an example of this in Figure 1.3, where the SFRD continues to fall from $z \sim 2$ to $z = 0$, rather than remaining constant.

A revolution in the study of environmental quenching came about with our ability to quantify *quenching timescales* using high-quality observational data with detailed modelling (De Lucia et al., 2012; Wetzel et al., 2012, 2013; Mok et al., 2013; Muzzin et al., 2014; Schawinski et al., 2014; Haines et al., 2015; Balogh et al., 2016; Foltz et al., 2018; Paccagnella et al., 2017, 2019). Quenching timescales can be calculated in a number of ways. For example, in Muzzin et al. (2014) two methods were used. Firstly, using the spectroscopic redshifts of cluster galaxies, a velocity versus clustercentric radius phase space analysis was conducted. Under the assumption of a particular quenching model, an attempt was made to reproduce the positions of the recently quenched cluster galaxies in this phase space with simulations. This allowed for the derivation of a quenching timescale. The second method used was the fitting of galaxy spectra with stellar population models. The spectra of recently quenched galaxies

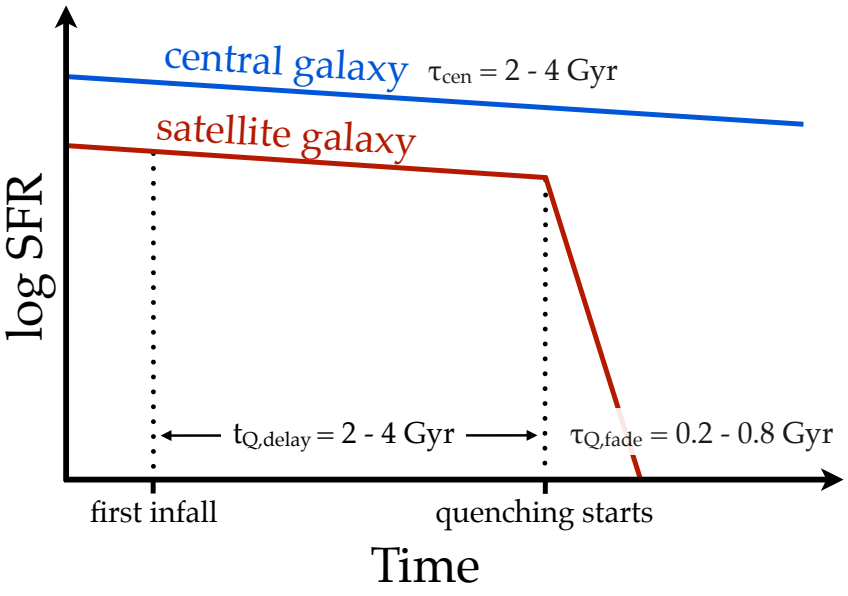

Figure 1.5: The delayed-then-rapid quenching model for satellite SFR evolution. Values for timescales come from modelling the fraction of quenched galaxies in SDSS at low redshift (Wetzel et al., 2013).

were fit with stellar population models to obtain the best-fit star formation history for the galaxies. From this star formation history, the age at which the galaxy began quenching and the age of the galaxy when it was fully quenched can be derived, providing us with a quenching timescale. One way to explain the aforementioned observations is if environmental quenching operates in a "delayed-then-rapid" manner (Wetzel et al., 2013). Satellite galaxies continue forming stars once they are accreted on to a dark matter halo of another galaxy, but they do not have different SFRs to central galaxies of the same mass. The first point suggests that quenching does not immediately begin once a galaxy becomes a satellite - hence the "delay". The second suggests the quenching is "rapid" because there is no measured gradual change in the average SFR. A schematic representation of this quenching model, based on modelling the fraction of quenched galaxies at low redshift in SDSS, can be seen in Figure 1.5.

Recent studies within this framework of environmental quenching have found that both the delay and quenching times reduce towards higher redshifts. At $z \sim 1$, delay times of $0.5 - 1.0$ Gyr and quenching times of $\sim$ 0.25 Gyr are found (Muzzin et al., 2014; Balogh et al., 2016; Foltz et al., 2018). Foltz et al. (2018) compiled a number of environmental quenching timescales in the literature. These can be seen in Figure 1.6. It can be seen that most of the points follow the shaded green region, which represents the dynamical timescale evolving as $(1 + z)^{-1.5}$. Since the points closely follow this timescale, it suggests quenching processes related to the dynamics of the host halo are responsible for environmental quenching. Such processes are connected to the motion of satellite galaxies relative to their cluster or group environment.

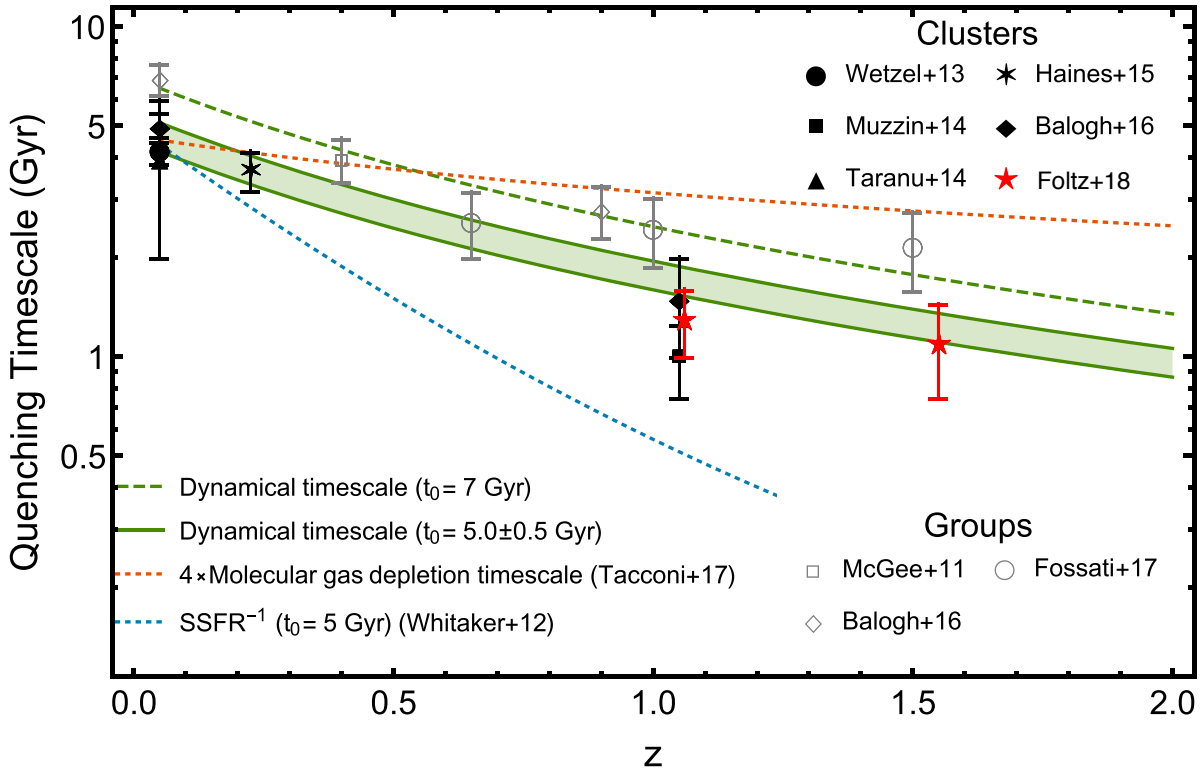

Figure 1.6: Environmental quenching timescales measured using a variety of statistical modelling techniques from Foltz et al. (2018) for galaxies with stellar masses, $\mathcal{M}_* \geqslant 10^{10.5}\mathrm{M}_\odot$. Solid points show measurements from clusters, open points show measurements from groups. The shaded green region is the dynamical timescale normalised to 5.0 ± 0.5 Gyr and spans the range of quenching times in SDSS clusters as reported in Wetzel et al. (2013) and Balogh et al. (2016). The dashed green line is the dynamical timescale normalised to 7 Gyr at $z = 0.05$. The orange dotted line represents an approximation of the total gas (atomic+molecular) depletion timescale, adapted from Tacconi et al. (2018). The dotted blue line shows the approximate evolution of an outflow gas depletion time, normalised to 5 Gyr at low redshift (Whitaker et al., 2012a). See Foltz et al. (2018) for more details.

1.1.1.1 Outside-in quenching

Studies based on statistical modelling of galaxy populations such as Foltz et al. (2018) discussed in the previous section provide important clues for the physical processes responsible for environmental quenching. However, it is difficult to constrain the detailed physics of the environmental quenching process that is in action. The biggest question that needs to be answered is *how* do environmental quenching processes physically affect galaxies? Answering this question requires spatial information on individual galaxies.

An early example of using spatial information to study environmental quenching was presented in Koopmann & Kenney (2004). These authors used imaging in narrow wavelength bands to trace star formation operating on different timescales in local cluster and field galaxies. A common tracer used for star formation on very short timescales (~ 10 Myr) is emission in Hα. Stars form within dense gas clouds. Young stars of spectral types O and B are very hot and therefore emit ultraviolet radiation. This high-energy radiation can ionise most of the hydrogen atoms within some distance from the star,

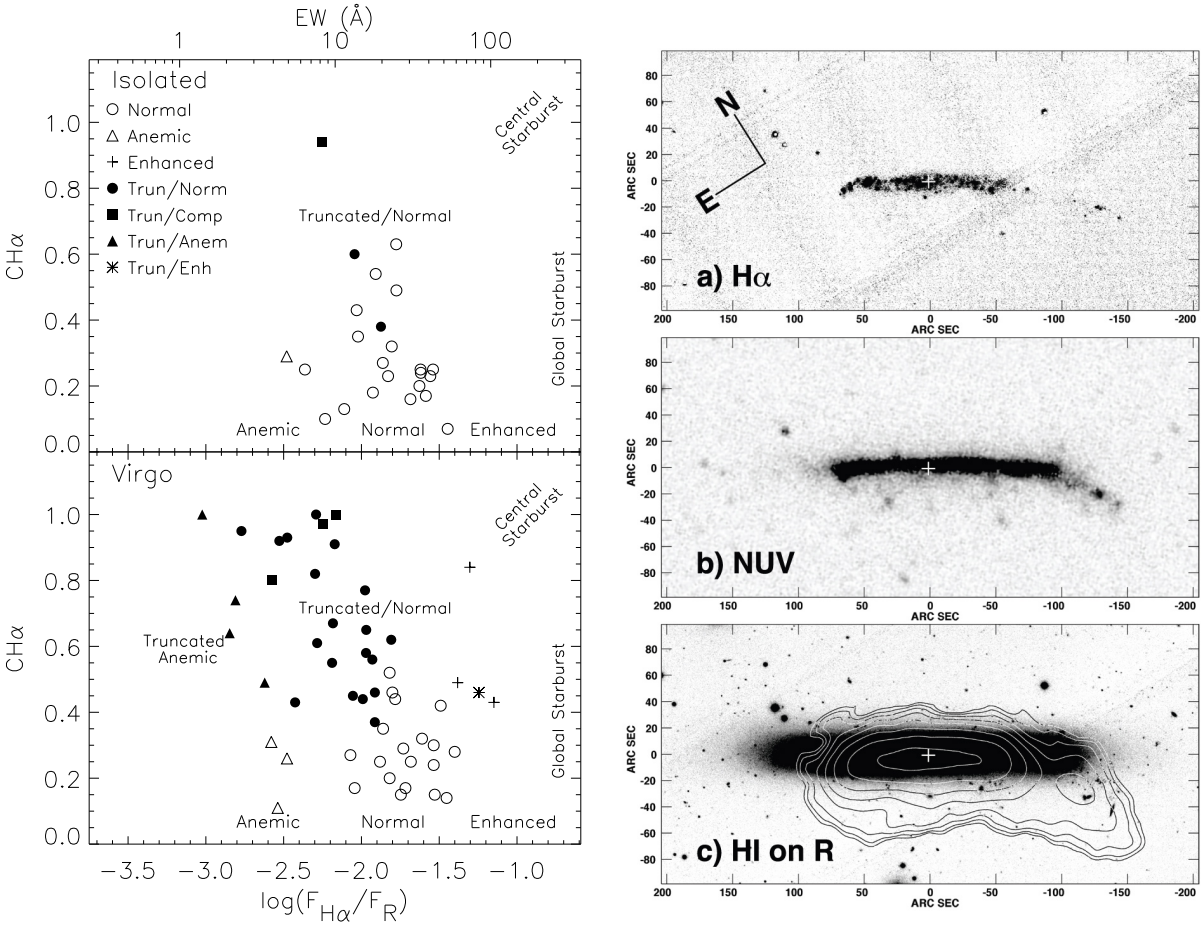

Figure 1.7: Left-panel: The concentration of Hα flux (the inverse ratio of the Hα flux within the 24 mag arcsec^{-2} isophote, r_{24}, and the $0.3r_{24}$ isophote) in field (top panel) and cluster (bottom panel) spiral galaxies in the local Universe as a function of the Hα flux to R-band flux ratio (see top axis for approximate Hα equivalent width). Filled points show spiral galaxies with truncated star formation in their discs. 52% of spiral galaxies in the Virgo cluster have truncated discs, as opposed to only 12% in the field (Koopmann & Kenney, 2004). Right-panel: Hα (top), UV (middle) and R-band emission with HI contours overlaid (bottom) of the Virgo cluster galaxy NGC 4330 from Abramson et al. (2011). The Hα disc is severely truncated with respect to the stellar continuum (R-band) disc, indicative of outside-in quenching.

beyond which the gas remains neutral. The volume within which hydrogen is ionised is called the Strömgen sphere. After a hydrogen atom is ionised, the electron and proton recombine to form a new hydrogen atom. The electron will then cascade down to the ground-state energy level of the hydrogen atom. During this cascade, it may cascade from the third- to second-lowest energy level. When this happens, the hydrogen atom will emit a Hα photon of 6563Å. Therefore, some of the Hα emission in a galaxy is cospatial with the young stars contained within it (Binney & Merrifield, 1998; Kennicutt, 1998).

By comparing the concentration of light emitted in Hα to light emitted in the R-band (which traces emission from mostly old stellar populations since they are red in colour), Koopmann & Kenney (2004) found that 52% of spiral galaxies in the Virgo cluster had truncated Hα discs i.e, the R-band emission was more spatially extended than the Hα emission in more than half of Virgo

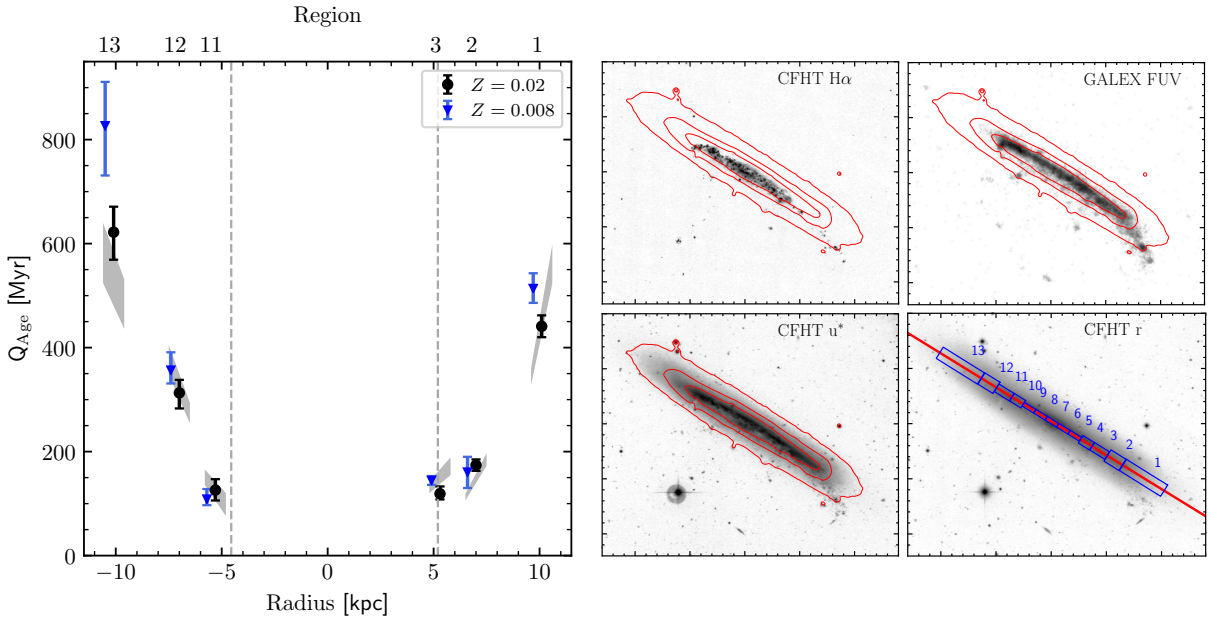

Figure 1.8: Right panels: Multiwavelength imaging of NGC 4330 in the Virgo cluster from Fossati et al. (2018). Red contours are drawn from the r-band image. The size of the galaxy reduces as we view it in u^*, FUV and then Hα. Aperture photometry was conducted in the blue regions marked on the r-band image. The solid red line shows the position of the long-slit spectroscopy with VLT/FORS2. Left panel: The time since quenching in NGC 4330 as a function of galactocentric radius. The regions marked correspond to those marked on the r-band image in the right panel. Black points are from stellar libraries at solar metallicity, blue points are from stellar libraries at subsolar metallicity. For more details, see Fossati et al. (2018).

cluster spiral galaxies. In the field environment at the same redshift, however, only 12% of spiral galaxies have truncated Hα discs. The results of this study can be seen in the left panel of Figure 1.7. These results demonstrated that quenching in high-density environments operates in an "outside-in" fashion, whereby star formation is progressively confined to smaller galactocentric radii over time. A visual representation of this effect is shown in the right-panel of Figure 1.7.

The right panel of Figure 1.7 shows narrow Hα, UV and R-band imaging of the Virgo cluster galaxy NGC 4330 taken from Abramson et al. (2011). NGC 4330 is being quenched by ram-pressure stripping. When a galaxy falls into a cluster and becomes a satellite, the intra-cluster medium (ICM) can act like a 'wind', stripping atomic gas from a galaxy (Gunn & Gott, 1972). Some of the molecular gas can survive ram-pressure stripping because it is more densely concentrated and thus more strongly bound to the galactic disc (e.g. Vollmer et al. 2005; Boselli et al. 2014). However, removing the more loosely bound atomic gas which resides at larger galactocentric radii removes the fuel for star formation from the outside-in. Early results have shown that Virgo spirals which have a deficiency in atomic gas (HI deficiency, measured as the CO flux / HI flux) of a factor $\sim$ 10 have SFRs that are lower by a factor of $2 - 3$. When comparing the radial distribution of HI and H_2 in Virgo spirals, it was found that the total gas deficiency is driven largely by a lack of HI in the outskirts of the disc (Kenney & Young, 1989).

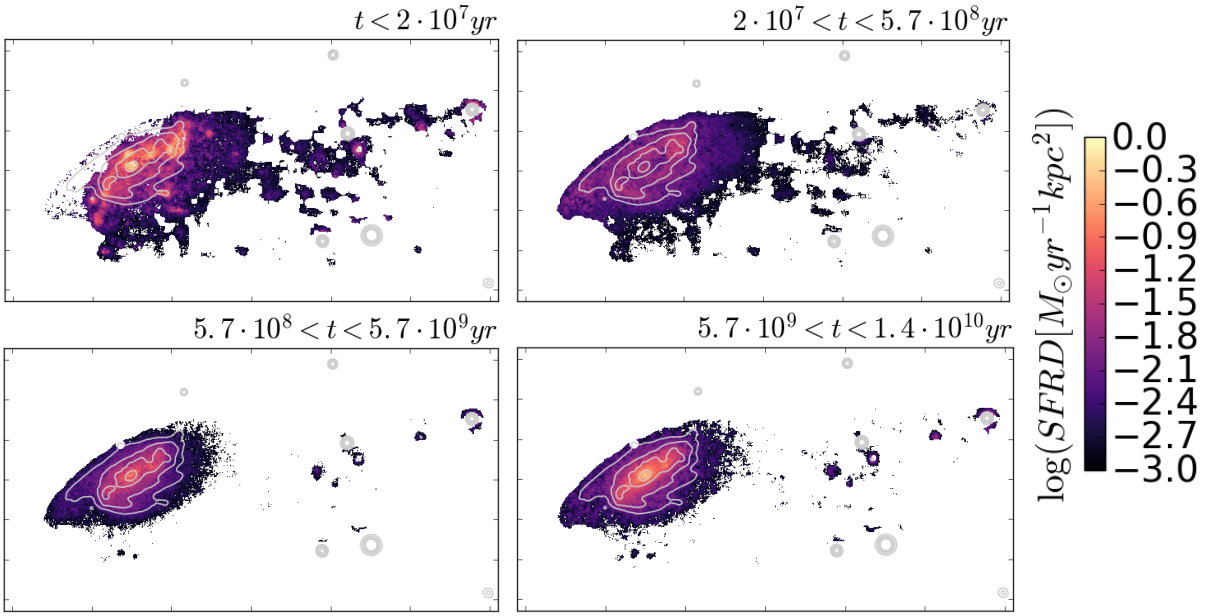

Figure 1.9: Stellar maps of different ages using the average star formation rate per kpc^2 for jellyfish galaxy J0206 (Poggianti et al., 2017). The white contours show the stellar continuum isophotes. Recent star formation is shown in the top left panel, with the oldest star formation shown in the bottom right panel.

Today, by combining narrow-band imaging with spectroscopy, we are able to track quenching timescales as a function of galactocentric radius. Figure 1.8 shows an example of such work for the same galaxy, NGC 4330, shown in the right-panel of Figure 1.7, but conducted very recently as part of the VESTIGE survey (Fossati et al., 2018). In the left panel of Figure 1.8, we can see that the time since quenching reduces as we move towards the centre of the galaxy, showing that the outskirts were quenched first. Similar work can be accomplished with integral field spectroscopy. The GASP survey makes use of MUSE on the VLT to study the details of ram-pressure stripping at low-redshift. The levels of star formation over time can be tracked on a pixel-by-pixel basis, as shown in Figure 1.9, adapted from Poggianti et al. (2017). Such observations allow us to track the detailed physics of environmental quenching.

As is evident, excellent progress has been made in our understanding of the physics behind environmental quenching at low redshift. If we are to understand why the environmental quenching timescales reduce towards higher redshift (Section 1.1.1, Figure 1.6) we need to obtain spatial information at high-redshift just like low-redshift studies. This thesis attempts to fill this space in the literature, with an attempt to measure environmental quenching using spatially resolved Hα maps of cluster and field galaxies at $z \sim 1$ (see Chapter 4).

1.2 The build-up of quiescent galaxies

Despite having very different routes to quiescence, quiescent galaxies exist in all environments. As the rate of cosmic star formation continues to decline (Section 1.1, Figure 1.3), the production of quiescent galaxies increases.

In a Lambda Cold Dark Matter (ΛCDM) Universe such as ours, structure forms hierarchically (first suggested by White & Rees 1978). Low mass structures such as galaxy-mass dark matter halos form first. Larger dark matter halos then subsequently form via merging. The hierarchical model of structure formation implies large, high-mass galaxies form from the mergers of small, low-mass galaxies. Whilst there is ample evidence for the validity of this model (e.g. massive galaxy clusters being abundant only at $z \lesssim 1$), there are some significant peculiarities. The most massive galaxies in the local Universe have the *oldest* stellar populations, whereas the low-mass galaxies are sites of on-going star formation (Schneider, 2015). At high redshift, near infrared surveys continue to find that massive galaxies with old stellar populations were already in place (e.g. Schreiber et al. 2004; Daddi et al. 2005; Ilbert et al. 2010; Caputi et al. 2011; Tomczak et al. 2015; Davidzon et al. 2017; Hill et al. 2017). The most massive galaxies therefore must have assembled most of their mass early in the Universe's history. This phenomenon of massive galaxies forming their stars earlier than low-mass galaxies is sometimes referred to as "cosmic downsizing", and is more dramatically seen in the characteristic mass at which galaxies are quenched of their star formation. As discussed earlier, galaxies follow a bimodal distribution, where most are either star-forming or quiescent. The characteristic stellar mass separating these two populations decreases by a factor of ~ 5 from $z = 1.4$ to $z = 0.4$ (e.g. Bundy et al. 2006). Therefore as the Universe ages, star formation is restricted to progressively lower mass galaxies, leading to a build-up of quiescent galaxies.

With the arrival of the *Hubble Space Telescope* (HST) came the ability to measure the *sizes* of these massive high-redshift galaxies for the first time. As well as already being quiescent, they were also compact, with sizes of ~ 1 kpc (e.g. van Dokkum et al. 2008; van der Wel et al. 2008). The question therefore arises, since these compact quiescent galaxies have already assembled most of their stellar mass early-on, how do they evolve into the *large* elliptical galaxies of today?

1.2.1 The size growth of quiescent galaxies

The most straightforward way to track galaxy growth is to measure the stellar masses and sizes of galaxies at many epochs, and measure the evolution in the stellar mass–size relation. An example of a comprehensive study using this technique with HST imaging is presented in van der Wel et al. (2014), of which the stellar mass–size relation out to $z \sim 3$ is shown in the left-hand panel of

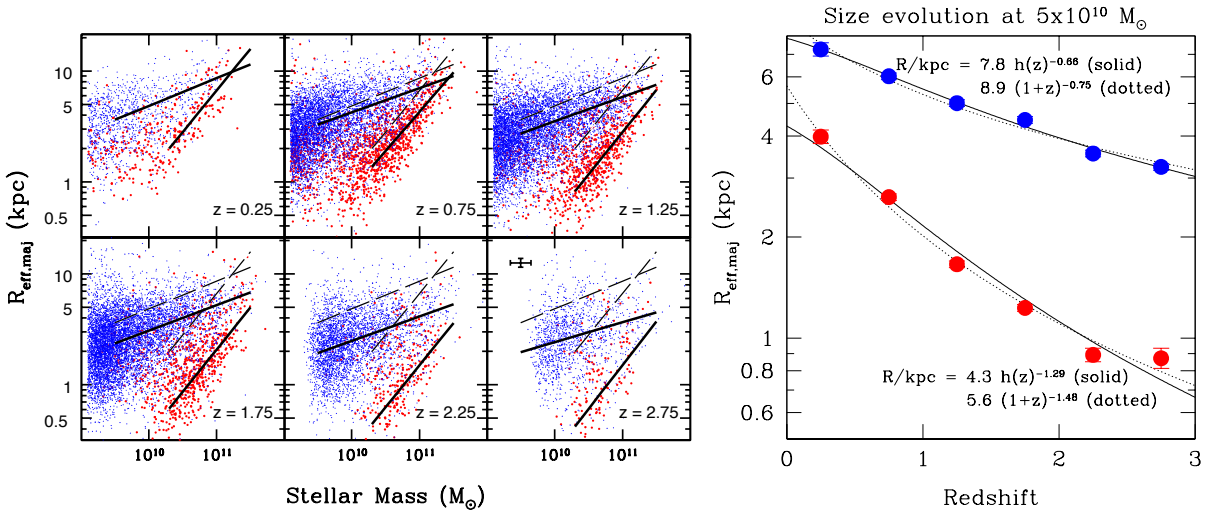

Figure 1.10: Left-panel: The stellar mass–size relation of star-forming (blue points) and quiescent (red points) galaxies in 3D-HST+CANDELS out to $z \sim 3$ (van der Wel et al., 2014). Solid lines in each panel show the mass–size relation at fixed redshift. The dashed line shows the $z = 0.25$ mass–size relations for comparison. Right-panel: The evolution of the mass–size relation intercept at a fixed stellar mass of $5 \times 10^{10} M_{\odot}$ for star-forming (blue points) and quiescent (red points) galaxies in in 3D-HST+CANDELS since $z \sim 3$ with various parameterisations shown as solid and dotted black lines (see van der Wel et al. 2014 for more details). $R_{\mathrm{eff,\,maj}}$ is the half-light radius in kpc measured along the major axis.

Figure 1.10. The build-up of quiescent galaxies is evident in the increased number density of red points for $z \lesssim 2$, until $z = 0.25$ is reached where the HST imaging has limited volume. More importantly however, we see a clear evolutionary trend of the quiescent stellar mass–size relation. Shown as the solid black line running through the red points, we see that it seems to maintain its gradient, but shifts to larger sizes at fixed stellar mass with decreasing redshift. The evolution of the mass–size relation intercept is more closely followed at fixed stellar mass in the right-hand panel of Figure 1.10. Immediately recognisable is the rapid size growth of quiescent galaxies (red points) compared to star-forming galaxies (blue points) since $z \sim 3$. How do quiescent galaxies grow disproportionately more in size than stellar mass?

1.2.1.1 The minor mergers hypothesis of size growth

One of the most advocated explanations for this disproportionately large increase in size compared to stellar mass is the minor mergers hypothesis of size growth. Minor mergers are mergers between two galaxies with very different stellar masses, usually with mass ratios of $1:3$ or smaller (Schneider, 2015). The smaller galaxy tends to be a satellite of the larger one. Due to dynamical friction, the satellite loses orbital energy and angular momentum. This causes the satellite to migrate closter to the centre, allowing it to experience stronger tidal forces (Schneider, 2015). Eventually, the stars are stripped from the smaller satellite and deposited preferentially on the outskirts of the more massive galaxy (Bezanson et al., 2009; Naab et al., 2009; Hopkins et al., 2009b, 2010; Hilz et al., 2012, 2013).

In the particular case of minor mergers between quiescent galaxies at later times, the size growth relative to the stellar mass growth can be larger, due to the low levels of gas. In such 'dry' minor mergers, there is very little gas from which new stars can form and therefore add to the stellar mass budget (Hopkins et al., 2009b). Under the assumption of the virial theorem, an initial stellar system has a total energy, E_i equal to

$$\begin{aligned} E_i &= K_i + W_i = -K_i = \frac{1}{2}W_i \\ &= -\frac{1}{2}\mathcal{M}_i \left\langle v_i^2 \right\rangle = -\frac{1}{2}\frac{G\mathcal{M}_i^2}{r_{g,i}} \end{aligned} \tag{1.1}$$

where K_i is the kinetic energy, $\mathcal{M}_i$ is the stellar mass, W_i is the potential energy, $r_{g,i}$ is the gravitational radius and $\left\langle v_i^2 \right\rangle$ is the mean square speed of the stars. We then assume this initial system will accrete systems with energies totalling E_a, stellar masses totalling $\mathcal{M}_a$, mean square speeds averaging $\left\langle v_a^2 \right\rangle$ and will have gravitational radii $r_{g,a}$. We define the fractional increase in stellar mass due to the accreted systems as $\eta = \mathcal{M}_a/\mathcal{M}_i$ and the ratio of mean square velocities of the acrreted systems to the mean square velocity of the initial system as $\gamma = \left\langle v_a^2 \right\rangle / \left\langle v_i^2 \right\rangle$. Under the assumption of energy conservation, the total energy of the final system, E_f, is

$$\begin{aligned} E_f = E_i + E_a &= -\frac{1}{2}\mathcal{M}_i \left\langle v_i^2 \right\rangle - \frac{1}{2}\mathcal{M}_a \left\langle v_a^2 \right\rangle \\ &= -\frac{1}{2}\mathcal{M}_i \left\langle v_i^2 \right\rangle - \frac{1}{2}\eta\mathcal{M}_i\gamma \left\langle v_i^2 \right\rangle \\ &= -\frac{1}{2}\mathcal{M}_i \left\langle v_i^2 \right\rangle (1 + \gamma\eta) \\ &= -\frac{1}{2}\mathcal{M}_f \left\langle v_f^2 \right\rangle \end{aligned} \tag{1.2}$$

The stellar mass of the final system $\mathcal{M}_f = \mathcal{M}_i + \mathcal{M}_a = (1 + \eta)\mathcal{M}_i$. Hence, the ratio of the final to initial mean square speeds is

$$\frac{\left\langle v_f^2 \right\rangle}{\left\langle v_i^2 \right\rangle} = \frac{(1 + \eta\gamma)}{(1 + \eta)} \tag{1.3}$$

and the ratio of the final to initial gravitational radius is

$$\frac{r_{g,f}}{r_{g,i}} = \frac{(1 + \eta)^2}{(1 + \eta\gamma)} \tag{1.4}$$

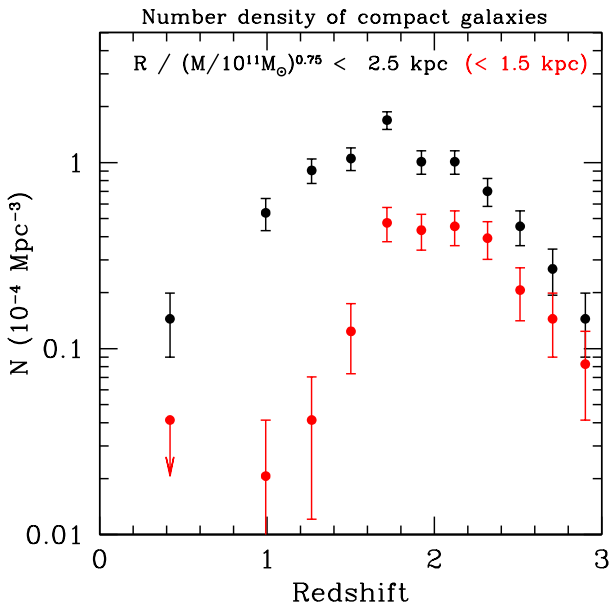

Figure 1.11: The evolution in the number density of compact early-type galaxies with $\mathcal{M}_* > 5 \times 10^{10} \mathrm{M}_\odot$ and $R_{eff}(\mathrm{kpc}) < (\mathcal{M}_*/5 \times 10^{10} \mathrm{M}_\odot)^{0.7}$ since $z \sim 3$ in 3D-HST+CANDELS (van der Wel et al., 2014). For $\mathcal{M}_* = 5 \times 10^{10} \mathrm{M}_\odot$, the size limit is 1 kpc. For $\mathcal{M}_* = 10^{11} \mathrm{M}_\odot$, the size limis is 1.6 kpc. The number density strongly decreases from $z \sim 2$ to the present day.

In a major merger, $\mathcal{M}_i = \mathcal{M}_a$ and therefore $\eta = 1$. Similarly, $\langle v_i^2 \rangle = \langle v_a^2 \rangle$ so $\gamma = 1$. Therefore the final system has the same mean square velocity as the initial system (equation 1.3) and the final system has a size that is a factor of 2 larger than the initial system (equation 1.4).

In a minor merger, $\langle v_a^2 \rangle \ll \langle v_i^2 \rangle$ and therefore $\gamma \ll 1$. To achieve the same stellar mass growth as in the major merger case – a factor of 2 increase and $\eta = 1$ – with successive minor mergers, the mean square velocity of the final system reduces by a factor of 2 (equation 1.3) and the size of the final system increases by a factor 4 (equation 1.4) compared with the initial system, since $\eta\gamma \xrightarrow[\gamma \to 0]{} 0$ (Naab et al., 2009). Therefore, in the case of major mergers, the size of a galaxy, measured by its half-light radius, R_{eff}, increases as $R_{eff} \propto \mathcal{M}_*$. But in the case of dry minor mergers, size growth goes as $R_{eff} \propto \mathcal{M}_*^2$ (Naab et al., 2009; Bezanson et al., 2009; Hopkins et al., 2010; Hilz et al., 2012, 2013).

Support for this scenario of size growth was also evident in van der Wel et al. (2014), where an apparent reduction in the number density of *compact* quiescent galaxies was seen in the field environment since $z \sim 2$ (see Figure 1.11). It was suggested that a possible reason for why the number density of compact quiescent galaxies falls between $z \sim 2$ and $z \sim 0$ is because they grow in size significantly via mergers during this period and are therefore no longer classified as compact, since minor mergers also lead to a large drop in density.

1.2.1.2 Recently quenched galaxies & Progenitor bias

The size growth of quiescent galaxies from minor mergers is not the only process by which the average size of quiescent galaxies can rise with decreasing redshift. As the Universe ages, more and more galaxies are quenched of their star formation and join the quiescent population of galaxies. This means we need to be careful when comparing populations of quiescent galaxies at low and high redshifts. Some of the present day quiescent galaxies were actually star-forming at high-redshift, meaning they were not part of the quiescent sample at high-redshift. The high-redshift sample of quiescent galaxies is therefore biased towards the oldest progenitors of today's quiescent galaxies (Van Dokkum & Franx, 1996; van Dokkum & Franx, 2001). This progenitor bias has implications on the measured size evolution of quiescent galaxies with redshift. When studying the evolution of the quiescent stellar mass–size relation with decreasing redshift, we need to appreciate that during the same period, star-forming galaxies are being quenched and are continually being added to the quiescent population of galaxies. Star-forming galaxies follow a mass–size relation that lies above the quiescent mass–size relation on the mass–size plane (see left-panel of Figure 1.10). Therefore on average, star-forming galaxies have larger sizes at fixed stellar mass compared to quiescent galaxies. When these star-forming galaxies quench, they will join the quiescent population of galaxies at the large size end of its distribution at fixed stellar mass. We can also see from Figure 1.10 that star-forming galaxies also grow in size at fixed stellar mass with decreasing redshift. Therefore with decreasing redshift, the continuous addition of recently quenched galaxies to the existing quiescent population will induce a rise in the average size of quiescent galaxies.

The argument that progenitor bias leads to size evolution in the quiescent galaxy population was first suggested by van der Wel et al. (2009). Though both minor mergers and progenitor bias are thought to play a role in the rapid size evolution of quiescent galaxies, there is debate over which is the dominant growth mechanism. Carollo et al. (2013) presented convincing evidence for recently quenched galaxies driving the observed size evolution by studying quiescent galaxies in the COSMOS field between $0.2 < z < 1$. Contrary to the findings of van der Wel et al. (2014), Carollo et al. (2013) found that the number density of compact quiescent galaxies does not significantly change over this redshift interval, particularly for galaxies with $10^{10.5} < M_*/\mathrm{M}_\odot < 10^{11}$. However, the number density of large quiescent galaxies increases significantly (see Figure 1.12).

1.3 The aims of this thesis

In Sections 1.1 and 1.2, two of the largest unanswered problems in galaxy evolution are presented:

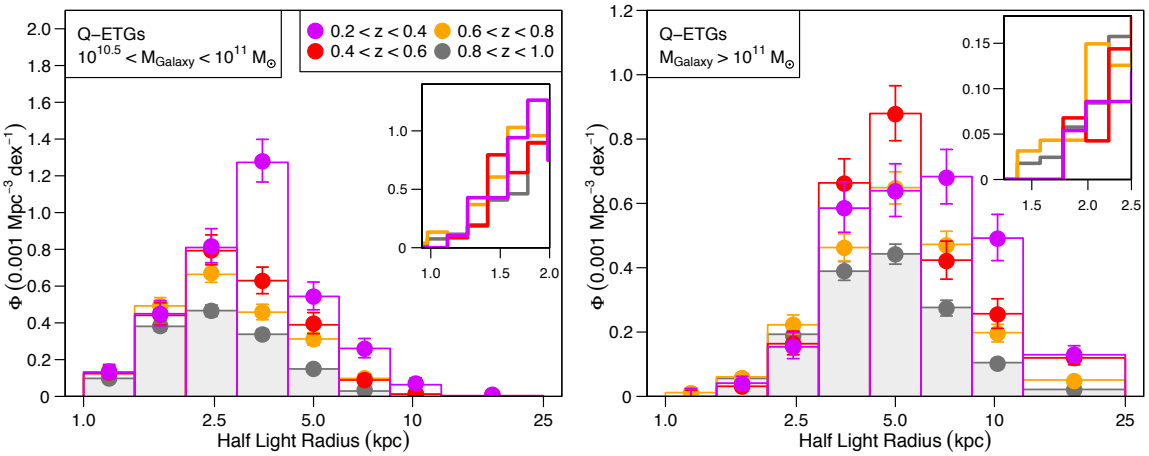

Figure 1.12: Size distributions for quiescent early-type galaxies between $0.2 < z < 1$ in the COSMOS field (Carollo et al., 2013). Left panel shows the distributions for galaxies with $10^{10.5} < \mathcal{M}_*/\mathrm{M}_\odot < 10^{11}$ and the right panel shows the distributions for galaxies with $\mathcal{M}_*/\mathrm{M}_\odot > 10^{11}$. Particularly for the lower stellar mass bin, it can be seen from the inset figure that there is no significant observed change in the number density of compact quiescent galaxies. For the high stellar mass bin, a reduction in the number density of compact quiescent galaxies is observed (see inset figure), but it seems to be more stronger for the smallest of sizes. More clearly however, we see that for both stellar mass bins, there is a larger rise in the number density of large quiescent galaxies with decreasing redshift.

1. What are the physical processes responsible for driving the quenching of star formation in the Universe?

2. What is the physical process responsible for driving the rapid size growth of quiescent galaxies?

This thesis attempts to answer the first question by trying to capture direct evidence of quenching in action at $z \sim 1$. This is an epoch in the Universe's history where the SFRD was higher than the present day, but still in decline (see Figure 1.3). Therefore, there is a higher probability of catching galaxies *in the process* of quenching during this epoch. Consequently, such observations should make it easier to pin-down the physical process responsible for quenching. Due to the clear association of quenching to galaxy clusters (Section 1.1.1), this thesis focuses on pinning-down the dominant environmental quenching mechanism at $z \sim 1$. This is done in Chapter 4 of this thesis by measuring the spatial extent of Hα emission in star-forming cluster galaxies and comparing it to the spatial extent of their stellar continuum emission. This study allows us to gain an understanding of where stars form in cluster galaxies and where they do not. An insight can therefore be gained on how quenching operates in cluster galaxies: is it "outside-in", "inside-out" or radially independent? Consequently, this can provide the missing piece of information that statistical studies of quenching timescales (Section 1.1.1) are unable to provide.

The approach to answering the second question in this thesis is to use environment as a tool. The probability of mergers occurring between satellite galaxies in high-density environments such as clusters is low, since they have high peculiar velocities (Merritt, 1985; Delahaye et al., 2017). Cluster

galaxies therefore provide us with a control sample of galaxies that have not significantly grown in size via minor mergers. The minor mergers hypothesis (see Section 1.2.1.1) can therefore be readily tested by measuring the stellar mass–size relation of cluster galaxies and comparing it to the stellar mass–size relation of field galaxies. If minor mergers do drive the rapid size growth observed for quiescent galaxies (see Section 1.2.1), we would expect to see that quiescent *cluster* galaxies are *smaller* in size at fixed stellar mass than quiescent *field* galaxies. This simple experiment is conducted in Chapter 2 and the implications of the results are explored in detail.

As was mentioned earlier, observations show quenching is clearly associated with clusters. This makes them excellent places in the Universe to look for recently quenched galaxies. Using a sample of spectroscopically identified recently quenched cluster galaxies in Chapter 3, we test whether or not recently quenched galaxies contribute to increasing the average size of quiescent galaxies at fixed stellar mass with decreasing redshift (see Section 1.2.1.2). This is done by studying their location on the cluster mass–size relation and comparing it to those of the star-forming and quiescent cluster members. We then attempt to use our findings in this study to constrain the quenching mechanism that may have been responsible for creating the recently quenched cluster population.

Throughout this thesis, all magnitudes quoted are in the AB system and we assume a ΛCDM cosmology with $\Omega_m = 0.307$, $\Omega_\Lambda = 0.693$ and $H_0 = 67.7\,\mathrm{kms}^{-1}\,\mathrm{Mpc}^{-1}$ (Planck Collaboration XIII, 2016).

The evolution of the world can be compared to a display of fireworks that has just ended: some few red wisps, ashes and smoke. Standing on a well-chilled cinder, we see the slow fading of the suns, and we try to recall the vanished brilliance.

Georges Lemaître

2

The size growth of quiescent galaxies from minor mergers

Observations of massive galaxies across a range of redshifts have now established that as the Universe ages, massive galaxies grow in size more than they do in stellar mass (see Section 1.2 and Daddi et al. 2005; Trujillo et al. 2006; van Dokkum et al. 2008; Buitrago et al. 2008; van der Wel et al. 2008; Damjanov et al. 2011; Raichoor et al. 2012; Cimatti et al. 2012; Mei et al. 2012; Huertas-Company et al. 2013a; van der Wel et al. 2014). This disproportionately larger growth in size has been the topic of many recent studies attempting to pin-down the physical process responsible for driving it. Thus far, the majority of these studies argue that minor mergers (mergers between two galaxies that have a mass ratio of $> 10:1$ or in some cases $> 3:1$) can provide a plausible explanation to these observations (see Section 1.2.1.1 and Bezanson et al. 2009; Hopkins et al. 2009a; Naab et al. 2009; Trujillo et al. 2011; Hilz et al. 2012; Oser et al. 2012; Bluck et al. 2012; Ferreras et al. 2014). Despite these findings, there is debate on whether minor mergers can fully account for this size growth. It has been suggested that much of the size growth in the quiescent population of galaxies can also be explained by the appearance of newly quenched star-forming galaxies (which have larger sizes than quiescent galaxies) that formed at later epochs (see Section 1.2.1.2 and Carollo et al. 2013). Major mergers (equal-mass mergers) can also increase the size of galaxies, but they lead to a proportionate increase in stellar mass (see Section 1.2.1.1).

If major mergers were the dominant route for galaxy size growth, there would be more high-mass galaxies than currently observed at low redshifts (Bezanson et al., 2009; López-Sanjuan et al., 2009). Major mergers are therefore unlikely to be the main drivers of galaxy size growth. Feedback from active galactic nuclei (AGN) and stellar winds can also lead to the expansion of a galaxy (Fan et al., 2008). However, the amount of mass removed in this process would have to be fine-tuned to reach the levels of galaxy size growth observed (Bezanson et al., 2009).

One aspect that can alter this picture of galaxy size growth over time is the influence of environment. Galaxies residing in high-density environments such as clusters have higher peculiar velocities than galaxies residing in the low-density field environment. The high velocity dispersions associated with clusters make mergers between satellite galaxies a rare occurrence (Merritt, 1985; Delahaye et al., 2017). It is therefore possible to use the cluster environment as a laboratory to test the currently favoured suggestion that minor mergers dominate the size growth of massive galaxies. Since minor mergers are expected to increase galaxy size more than they do stellar mass, the most direct way to test this is to measure the stellar mass–size relations in both environments at fixed redshift and compare them to see if there is a significant offset in size. This simple approach does not take into account other sub-dominant cluster-specific processes that may also alter the sizes and size distribution of cluster galaxies such as accelerated quenching, galaxy harassment (nearby high-speed encounters between satellite galaxies in clusters e.g. Moore et al. 1996, 1998) and mergers with the Brightest Cluster Galaxy (BCG) that would remove galaxies from the sample. In this simple scenario, if the predictions of minor mergers driving galaxy size growth are true, cluster galaxies should find themselves inhibited from size growth and will therefore be significantly smaller than field galaxies at fixed redshift.

Previous works that have attempted to do this find a range of results, making physical interpretation difficult. At low redshifts ($z < 0.2$), Weinmann et al. (2009), Maltby et al. (2010), Fernández Lorenzo et al. (2013) and Cappellari (2013) find the stellar mass–size relation of early-type galaxies to differ by $\leqslant$ 20% with environment, explicitly stating their results are not significant. Huertas-Company et al. (2013a,b) find that this difference has to be $< 30 - 40\%$, in-line with the errors on their size measurements. All these works state their measurements are consistent with no size difference being present for early-type galaxies with environment. Similarly, Poggianti et al. (2013) found that old compact early-type galaxies are approximately $\leqslant$ 33% smaller in clusters compared to the field. Cebrián & Trujillo (2014) find a much smaller difference of early-type cluster galaxies being $\sim$3.5% smaller than their field counterparts, but at high statistical significance ($> 4\sigma$).

Late-type galaxies are more often found to be smaller in clusters. Weinmann et al. (2009), Maltby et al. (2010) and Fernández Lorenzo et al. (2013) find them to be smaller in clusters by $\geqslant$ 15%, with the latter two studies claiming statistically significant results. Cebrián & Trujillo (2014) also find late-type galaxies to be smaller in clusters at high statistical significance, but by a much smaller amount ($\sim$7.5%). At intermediate to high redshifts ($z \geqslant 0.2$), Cooper et al. (2012), Papovich et al. (2012), Bassett et al. (2013), Lani et al. (2013), Delaye et al. (2014a), Chan et al. (2018) and Andreon (2018) find early-type galaxies to be larger in clusters by $\geqslant$ 24%. Rettura et al. (2010), Newman et al. (2014), Sweet et al. (2017) and Morishita et al. (2017) however find early-type galaxies to differ in size by $<$ 20% between environments, consistent with no size difference. On the other hand, Valentinuzzi et al. (2010a,b) find cluster galaxies to be smaller than field galaxies by $\sim$25%. A summary of cluster versus field mass–size relation measurements (since 2009) for quiescent galaxies can be found in Appendix A.

The biggest challenge that comparative studies of the stellar mass–size relation with environment face is the task of minimising systematics between measurements made from different samples. It is often the case that field and cluster datasets were taken with different instruments, using different filters and analysed using different techniques. It is imperative to compare galaxy sizes at the same rest-frame wavelength, since aspects such as colour gradients across galaxies can vary differently in different rest-frames, altering size measurements. High redshift studies face the added difficulty of obtaining statistically significant sample sizes with high enough signal-to-noise ratio and resolution to measure galaxy sizes reliably.

In this chapter, we attempt to test the hypothesis that minor mergers drive the majority of galaxy size growth by comparing the stellar mass–size relations in the cluster and field environments at $z \sim 1$. We aim to overcome shortcomings and challenges faced by previous studies in a number of ways. Firstly, we use the largest spectroscopically-confirmed sample of star-forming and quiescent cluster galaxies at $z \sim 1$ to date. Secondly, we purposefully conduct observations and data reduction in an analogous fashion to the 3D-HST/CANDELS survey, which forms our comparative field sample. Finally, we use data with high enough signal-to-noise ratio and resolution obtained using the *Wide Field Camera 3* (WFC3) on the *Hubble Space Telescope* (HST) to measure galaxy sizes reliably.

This chapter is organised as follows. In Section 2.1 we describe our cluster and field samples, our size determination method and the calculation of our stellar masses. We then go on to explain how our final sample for this comparative study is selected. In Section 2.2, we present our findings on the precision and accuracy of grism-derived redshifts in helping to boost our cluster sample size. We then

Table 2.1: The ten GCLASS clusters used in this chapter. For full names of the clusters, we refer to Muzzin et al. (2012). R_{200} is the radius at which the mean interior density is 200 times the critical density of the Universe. $\mathcal{M}_{200}$ is the mass enclosed within this radius. σ_v is the line-of-sight velocity dispersion (see Biviano et al. 2016). Note: The numbers listed in the last three columns indicate total numbers *before* / *after* quality checks relevant to this chapter are applied.

Name	z_{spec}	$\mathcal{M}_{200}$ ($10^{14}\mathrm{M}_{\odot}$)	R_{200} (kpc)	σ_v (km s^{-1})	Spec-z Members in *HST* FOV	Grism-z Members	Total Members in *HST* FOV
SpARCS-0034	0.867	2.0 ± 0.8	888 ± 110	609^{+75}_{-66}	37/33	17/16	54/49
SpARCS-0035	1.335	5 ± 2	977 ± 154	941^{+159}_{-137}	22/22	26/18	48/40
SpARCS-0036	0.869	5 ± 2	1230 ± 129	911^{+99}_{-90}	43/41	31/30	74/71
SpARCS-0215	1.004	3 ± 1	953 ± 103	758^{+85}_{-77}	42/40	32/28	74/68
SpARCS-1047	0.956	3 ± 1	926 ± 138	680^{+98}_{-86}	22/19	15/14	37/33
SpARCS-1051	1.035	1.2 ± 0.5	705 ± 102	530^{+73}_{-65}	34/32	11/10	45/42
SpARCS-1613	0.871	13 ± 3	1663 ± 130	1232^{+100}_{-93}	73/65	41/25	114/90
SpARCS-1616	1.156	3 ± 1	854 ± 107	701^{+81}_{-73}	38/35	19/17	57/52
SpARCS-1634	1.177	4 ± 2	1008 ± 131	835^{+91}_{-82}	38/34	15/15	53/49
SpARCS-1638	1.196	1.9 ± 0.9	769 ± 117	585^{+73}_{-65}	26/23	13/9	39/32

present the cluster mass–size relation at $z \sim 1$ and investigate its offset with the field relation in Section 2.3. In Section 2.4 we explore whether differences in morphological composition drive the differences in the stellar mass–size relation between the two environments. In Section 2.5, we investigate how the distinct location of a BCG at the bottom of the cluster potential well can help constrain the dominant physical process driving galaxy evolution in clusters. Finally, we summarise our findings in Section 2.6.

2.1 Methodology

2.1.1 Data

2.1.1.1 Cluster sample

Our cluster sample consists of 10 massive clusters in the redshift range $0.86 < z < 1.34$ (see Table 2.1). These were selected from the 42 square degree *Spitzer* Adaptation of the Red-sequence Cluster Survey (SpARCS, see Muzzin et al. 2009; Wilson et al. 2009; Demarco et al. 2010) for spectroscopic follow-up, as part of the Gemini Cluster Astrophysics Spectroscopic Survey (GCLASS, see Muzzin et al. 2012 and van der Burg et al. 2013). Clusters in the SpARCS survey were selected with the red-sequence method (Gladders & Yee, 2000) using the $z' - 3.6\mu$m colour to sample the 4000Å break (see Muzzin et al. 2008). The 10 clusters selected as part of GCLASS have extensive optical spectroscopy, obtained using the Gemini Multi-Object Spectrographs (GMOS) on both Gemini-South and -North. Out of 1282 galaxies that obtained a spectroscopic redshift, 457 were identified as cluster members. All 10 clusters also have 11-band photometry (*ugrizJK*$_s$, 3.6μm, 4.5μm, 5.8μm, 8.0μm), details of which can be found in Appendix A of van der Burg et al. (2013). An additional band of photometry in F140W is

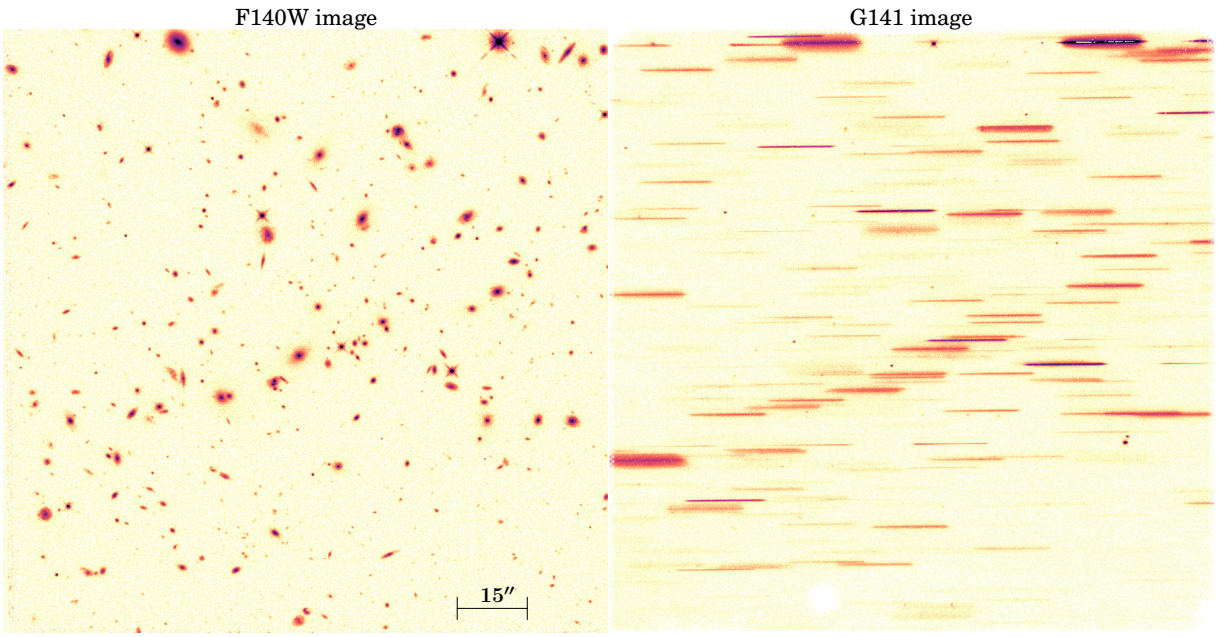

Figure 2.1: HST WFC3 data for SpARCS-1047 (see Table 2.1). Left: F140W image. Right: G141 grism spectra. Spatial scale of the F140W image is shown with a black bar in the bottom right-hand corner of the left panel. The colourmap is logarithmic. The grism provides a spatially resolved spectrum for every object in the field of view. For this particular cluster, 30% of grism-selected cluster members were too contaminated to use (see Section 2.1.1.4 for contamination criteria).

now also available as part of the *HST* data the study in this chapter is based on.

2.1.1.2 *HST* OBSERVATIONS

We obtained *HST* WFC3 F140W imaging and G141 grism follow-up in a Cycle 22 program (GO-13845; PI Muzzin), dedicated to obtaining spatially resolved Hα maps of the star-forming cluster members. The F140W filter spans the wide *JH* wavelength range ($12003 < \lambda\,/\,\text{Å} < 15843$). The G141 grism covers a wavelength range of $10750 < \lambda\,/\,\text{Å} < 17000$, and therefore contains the Hα emission line between $0.7 < z < 1.5$. It provides a spatially resolved ($0.130 \leqslant \text{FWHM}\,/\,\text{arcsec} \leqslant 0.156$ for $11000 \leqslant \lambda\,/\,\text{Å} \leqslant 17000$) spectrum for every object in the field of view, with a resolving power of $R \sim 130$.

Data for 9 of the 10 clusters are taken with a 1×2 or 2×1 mosaic of WFC3 pointings with a random orientation. For the 10th cluster, SpARCS-1047 (see Table 2.1), data is taken with a single pointing at the centre of the cluster. All clusters are observed to a 2-orbit depth, with ∼90% of this time spent on grism spectroscopy and ∼10% on direct imaging with the F140W filter. The exposure time in F140W for 9 of the 10 clusters is ∼800 seconds, with a 5σ F140W limiting magnitude for galaxies of ∼26.6. The exception to this is SpARCS-0035, which has varying depth, ranging from

$\sim$800 to $\sim$7460 seconds*. All mosaics are centered on the cluster core and cover $\sim$ 8 arcmin^2 for each cluster. This coincides with approximately a quarter of the GMOS observing area, which covered 35 arcmin^2 per cluster. For all of the GCLASS clusters, the *HST* imaging covers most if not all of the area within R_{500}. Four of the GCLASS clusters (SpARCS-0035, SpARCS-1616, SpARCS-1634 and SpARCS-1638; See Table 2.1) have imaging going out to $\sim R_{200}$. Nevertheless, the spectroscopic density is highest in the core, leading to a far greater overlap with spectroscopically confirmed cluster members. 392 of the 457 spectroscopically confirmed cluster members from GCLASS are in the *HST* fields-of-view (see Table 2.1). Figure 2.1 shows the F140W and G141 images for one of the GCLASS clusters for illustration.

2.1.1.3 Data reduction

The F140W imaging consists of 20 SPARS50† readouts per cluster with a native pixel scale of 0.12″ per orbit. These are reduced using the same data reduction process as for 3D-HST (Brammer et al., 2012; Momcheva et al., 2016), which forms our field sample (see Section 2.1.1.5). In summary, the standard calibrated data products from the HST archive are used with reduction pipelines to flag bad pixels, subtract bias structure, dark current and apply flat-field corrections. The `MultiDrizzle` software is then used to identify cosmic rays and hot pixels missed by these pipelines. The PyRAF routine `tweakshifts` is used to adjust the mosaics for dither offsets and the World Coordinate System (WCS) coordinates are subsequently refined to match the locations of objects on the mosaics. To subtract the sky background, a second-order polynomial fit is subtracted from each exposure after masking objects detected in the `MultiDrizzle` mosaics, and mapped back to the original frame using the PyRAF routine `blot`. This entire process is explained in detail in Brammer et al. (2012), and leads to undistorted, sky-subtracted F140W mosaics with a pixel scale of 0.06″. The `MultiDrizzle` process also outputs weight maps for each mosaic. These provide values for the inverse variance at each pixel, making them integral to the noise estimation process when determining the sizes of cluster galaxies (see Section 2.1.3.2).

*This cluster is being used for The Supernova Cosmology Project "See Change" program, details of which can be found in Rubin et al. (2018). As a result, this cluster's observations were deeper, with pointings of different orientations overlapping each other.

†The SPARS (short for "sparse") sequences use evenly spaces time intervals between reads. SPARS50 readouts have a sampling interval of 50 seconds.

2.1.1.4 Grism spectra contamination

One of the major concerns regarding grism data for high-density fields such as clusters is the contamination rate. Our primary criterion for evaluating contamination is anything that inhibits the ability to obtain an accurately measured redshift from the grism spectrum. Therefore, a grism spectrum is considered unusable if one or more of the following criteria are true:

1. Less than half of the grism spectrum is available in a region where prominent emission/absorption lines are absent.

2. The grism spectrum of a brighter close-by object overlaps with the grism spectrum of interest to such an extent that the data reduction process could not successfully remove the contamination.

3. The grism spectrum has a very low signal-to-noise ratio such that no prominent emission/absorption lines can be detected. This is often the case for galaxies with F140W magnitude > 25.

We checked all the grism spectra by eye for galaxies without a spectroscopic redshift from GMOS, but with a grism redshift measurement placing them in the cluster. Approximately 35% of grism-selected cluster members (see Section 2.2) were too contaminated to use. 2% of these contaminated grism spectra were unusable due to the galaxy being too close to the edge of the field-of-view, leaving less than half a grism spectrum available.

2.1.1.5 Field sample

The HST observations for GCLASS are purposely conducted in an analagous fashion to the 3D-HST survey to allow for the most straightforward comparison between galaxies in field and cluster environments. The 3D-HST survey is a 248-orbit near-infrared spectroscopic treasury program, covering three quarters of the CANDELS treasury survey area with 2 orbits of WFC3 and G141 grism coverage (Brammer et al., 2012). It obtained rest-frame optical spectra for galaxies between $0.7 < z < 3.5$ (Brammer et al., 2012; Momcheva et al., 2016). 3D-HST has obtained $\sim$100, 000 galaxy redshift measurements of which $\sim$10, 000 reside in a redshift range relevant to our work (Momcheva et al., 2016). In this chapter, we use the structural parameters for all galaxies measured by the 3D-HST team within the same redshift range as the GCLASS clusters ($0.86 < z < 1.34$), derived from the CANDELS (Grogin et al., 2011; Koekemoer et al., 2011) F160W images for the COSMOS, UDS, GOODS-S, GOODS-N and AEGIS fields in van der Wel et al. (2012).

Furthermore, we apply our size determination method for the GCLASS clusters to the CANDELS-COSMOS F160W mosaic[‡]. This is done to ensure comparable sizes are achieved with those in van der Wel et al. (2012), confirming the reliability of our method (see Appendix B for further discussion).

2.1.2 Redshifts & stellar masses

Part of obtaining a robust measurement of the stellar mass–size relation depends heavily upon reliably estimated stellar masses from fitting multi-wavelength Spectral Energy Distributions (SEDs) to the photometry. Once again, to minimise systematics between measurements from the cluster and field samples, we use the same method for the clusters as used for 3D-HST.

Photometric redshifts for all galaxies in the GCLASS mosaics are estimated using the EAZY code (Brammer et al., 2008). These are primarily used as a comparison to our spectroscopic and grism-derived redshifts (see Section 2.2). They are not used for any quantitative measurements regarding the cluster mass–size relation in this chapter. The spectroscopic redshifts in this chapter were obtained with GMOS as part of the GCLASS survey (see Section 2.1.1.1). The grism redshifts are derived from fitting the SEDs with the grism spectra obtained with the G141 grism on the HST WFC3. The P(z) obtained from the EAZY run for each galaxy is used as a prior to obtaining the grism redshift measurement.

Stellar masses are estimated using the FAST code (Kriek et al., 2009). Once the final selection of cluster members are made for the study in this chapter using grism redshifts (see Section 2.1.4), stellar masses for the cluster members are estimated with their redshifts fixed to the spectroscopic redshift of their respective cluster. We use the exponentially declining star formation history parameterisation, SFR $\propto e^{-t/\tau}$, where τ can range between 10 Myr and 10 Gyr and $0 < A_V < 4$. A Chabrier (2003) Initial Mass Function (IMF) is assumed, as well as solar metallicity and the Calzetti et al. (2000) dust law.

Stellar masses for 3D-HST were estimated in exactly the same way as for GCLASS (with redshifts fixed to their spectroscopic redshifts or photometric redshifts when spectroscopic redshifts were not available), except that the allowed minimum value for τ was set to 40 Myr as opposed to 10 Myr (Skelton et al., 2014).

[‡]The CANDELS-COSMOS F160W mosaic (as well as the other CANDELS F160W images) is deeper than the GCLASS F140W mosaics. Therefore, there is a possibility that sizes measured from the CANDELS-COSMOS F160W mosaic are systematically larger due to a higher signal-to-noise ratio than the GCLASS F140W mosaics. We ran our size determination method on the 3D-HST COSMOS F140W mosaic which has the same depth as the GCLASS F140W mosaics. We compared our F160W and F140W sizes for the same set of galaxies in COSMOS, finding in fact a systematic towards larger sizes in the 3D-HST COSMOS F140W mosaic (see Appendix C for more details).

The final stellar masses for both 3D-HST and GCLASS are corrected for the difference between the total flux as measured from the photometric catalogue and the total flux as measured by GALFIT. Since the size measurements are determined by GALFIT, the stellar masses need to be corrected such that they correspond to the flux that is measured by GALFIT.

2.1.3 Size determination

In this section we describe our methodology for measuring sizes and how we treat systematics at each stage. Our size determination method very closely follows the method used by van der Wel et al. (2012) for 3D-HST. Our size determination process is first tested on the CANDELS-COSMOS F160W mosaic[‡] from the field sample. Our results are then compared to published results from van der Wel et al. (2012) in order to verify the reliability of our method (see Appendix B). Using the same size determination method for both cluster and field is plausible given our data. This is because there is negligible crowding of sources in the cluster mosaics compared to the field mosaics and the surface brightness of the intra-cluster light (ICL) is very low for the clusters.

2.1.3.1 Source detection

SExtractor v2.19.5 (Bertin & Arnouts, 1996) is used to identify objects in the GCLASS F140W and CANDELS-COSMOS F160W mosaics. The SExtractor set-up for GCLASS is standard, details of which can be found in Appendix D. For COSMOS we use the method described in Appendix A of Galametz et al. (2013). In summary, this method runs SExtractor in a "hot" and "cold" mode separately, optimised for detecting faint and bright sources respectively. The two separate catalogues are then combined, ensuring no repeat detections. This method minimises the chances that a galaxy is split into multiple objects as well as ensuring neighbouring galaxies are deblended adequately.

2.1.3.2 Noise estimation

We construct noise maps for the GCLASS images and CANDELS-COSMOS mosaic in the same way noise maps were constructed in van der Wel et al. (2012). These consist of a background noise estimate plus the Poisson noise from the sources themselves. The SExtractor segmentation maps are used in conjunction with the drizzled weight images from the data reduction process (see Section 2.1.1.3) to select all the pixels that are not occupied by sources or detector defects. The root-mean-square value of the background pixels for each image is our estimate for the background noise per pixel in electrons s^{-1}. The Poisson noise from the sources is calculated using the exposure

time maps and science images. The units of the science image pixels are converted to electrons before the Poisson noise is calculated. We then convert this back to electrons s^{-1} and add this to our background noise map. The exception to this method of noise estimation is SpARCS-0035. Due to this cluster's non-trivial mosaic* – leading to heterogeneous noise properties – the noise estimation is calculated using the weight image, where the noise, $\sigma = 1/\sqrt{weight}$ at each pixel in electrons s^{-1}. This noise estimation is usually an underestimation, since it does not include the Poisson term from the sources. In practice, this only becomes a problem for the brightest sources which are in a minority. Furthermore, ICL levels for the GCLASS clusters are very low. Consequently, they do not have a large affect on background measurements made by GALFIT.

2.1.3.3 Structural parameters with GALFIT

Rather than opting to use the GALAPAGOS package (Barden et al., 2012) to measure the sizes of our cluster and field galaxies, we built our own GALFIT wrapper to have better control over the size determination process. This allowed us to test systematics between the cluster and field data and deal with them individually. This custom built wrapper is run on both the GCLASS and CANDELS-COSMOS mosaics. It is run and tested on the CANDELS-COSMOS mosaic first, to ensure comparable half-light radii to those in van der Wel et al. (2012) are measured. GALFIT is a fitting algorithm that fits two-dimensional analytic functions to light profiles in an image (Peng et al., 2002, 2010a). As was done in van der Wel et al. (2012), we fit all galaxies with a single-component Sérsic profile, defined as:

$$I(r) = I(r_e) \exp\left[-\varkappa\left(\left(\frac{r}{r_e}\right)^{\frac{1}{n}} - 1\right)\right] \tag{2.1}$$

where r_e is the half-light radius. This is the radius within which half of the galaxy's total flux is emitted§. n is the Sérsic index and $I(r_e)$ is the intensity at the half-light radius. $\varkappa$ is an n-dependent parameter that is fixed for a given n by defining r_e to be the half-light radius.

Along with the mosaics and noise maps, GALFIT requires a point-spread function (PSF) as an input. The PSF accounts for the smearing of images due to the resolution limit of WFC3. The PSFs used in this work are stars pre-selected from the GCLASS and CANDELS-COSMOS mosaics under the following criteria: the star must have SExtractor $15 < \texttt{MAG\_AUTO} < 19$ and no other sources present near it within a 70×70 pixel cutout. The presence of other sources is also checked 5 pixels beyond the cutout boundary, to ensure their light does not contribute to the PSF cutout. The reason for this

§Throughout this thesis, the half-light radii measurements are *not* circularised.

magnitude range is based on preliminary fitting tests, where we found using a star with a magnitude fainter than 19 resulted in poor residuals after subtracting the best-fit model. The cutout dimensions are chosen to encompass the diffraction wings of the star and an adequate amount of sky background. For each galaxy fit, the PSF used from this pre-selected list is the star closest to the galaxy in question in terms of its pixel coordinates on the mosaic. This is done to minimise systematics arising from variations in the PSF across the mosaic.

The GALFIT wrapper will then find all the sources in each cutout and their SExtractor catalogued information. SExtractor values for pixel coordinates, magnitude, r_e, axis ratio and position angle are used as initial guesses for every source in the cutout field of view. The initial guess for the Sérsic index is set at 2.5 for every source. Every fitting run fits all the sources present in the cutout field-of-view simultaneously. The target galaxy is always the source positioned at the centre of the cutout. We run GALFIT twice for each galaxy fit. The first run keeps all parameters free, with a square fitting region that has a side-length equal to 10[¶] times the SExtractor half-light radius (`FLUX_RADIUS`) of the galaxy in pixels. The purpose of this run is to obtain refined values for the galaxy shape parameters (pixel coordinates, axis ratio and position angle). The second run uses these refined values, but keeps them fixed in the fit, with a square fitting region that has a side-length equal to 15 times the SExtractor half-light radius (`FLUX_RADIUS`) of the galaxy in pixels[‖]. The parameters left free are magnitude, r_e and n. Although this increases the computational time spent per fit, it vastly improves our size agreement on COSMOS with van der Wel et al. (2012). This is likely due to the tendency of GALFIT to find the local solution to the parameter estimation. The GALFIT initial values for the shape parameters will be closer to the global solution than the SExtractor values. Hence this two-GALFIT-run approach forces the final fit parameter values closer to the global solution. The level of agreement on COSMOS between the half-light radii measured in this work and van der Wel et al. (2012) is discussed in Appendix B. In general, we find that there were no systematics present between the two sets of measurements, with a mean offset of 0.28%. Our sizes are smaller by this amount. For both GALFIT runs, we keep the sky a free parameter to be fit. We fit every source in the CANDELS-COSMOS and GCLASS mosaics with this procedure, and later filter for the samples required for the mass–size relation study in this chapter (see Section 2.1.4).

Approximately 8, 000 galaxies are fit with minimal residuals in the cluster fields-of-view. We show

[¶]This cutout size was chosen to ensure that no more than 110 objects were present in a single cutout, since GALFIT can only fit a maximum of 110 objects in one go (van der Wel et al., 2012).

[‖]We understand that this cutout size may be too small for the largest of galaxies in the cluster sample, such as the BCGs. We therefore re-fit the BCGs with larger cutouts ($\sim$100 $\times$ 100 kpc), finding that the resulting sizes did not change the results presented in this chapter.

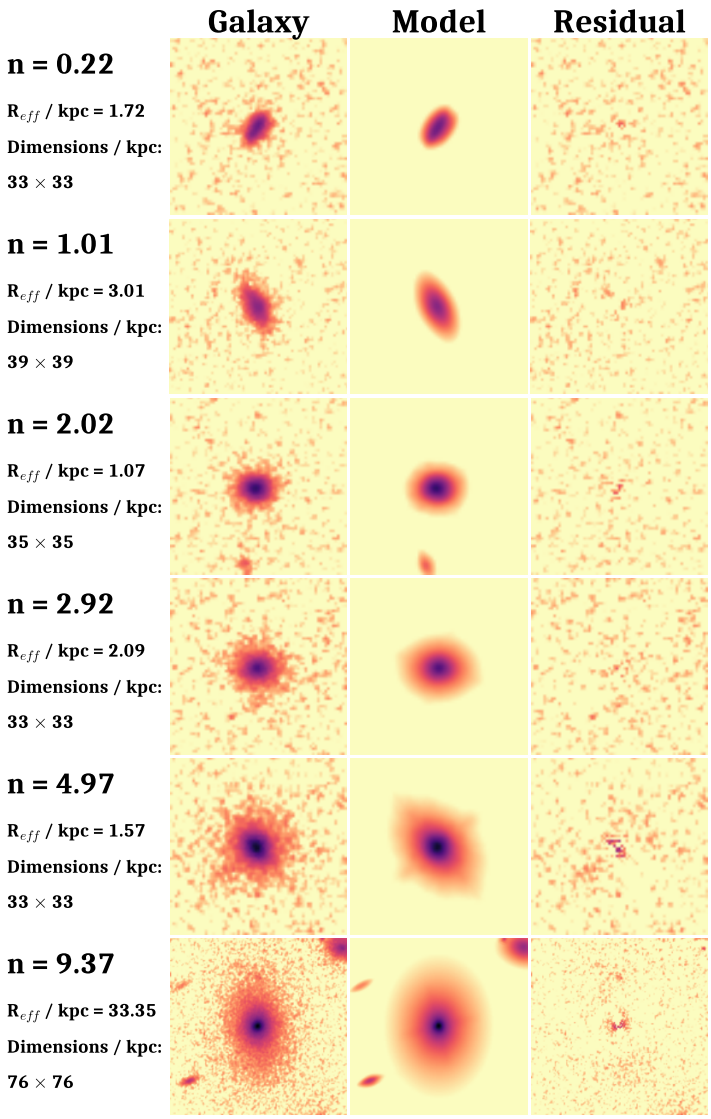

Figure 2.2: Example Sérsic profile fits with our GALFIT wrapper for a selection of cluster member galaxies spanning the entire range in Sérsic index for the cluster sample. First column lists the Sérsic index and half-light radius measurements for the galaxy, along with the dimensions of the thumbnails. Second, third and fourth columns show the galaxy, model and residual thumbnails for each fit. The colourmap used is logarithmic in scale.

a subset of fits for cluster members in Figure 2.2, demonstrating the wide range of shape profiles our GALFIT wrapper can cope with.

2.1.3.4 Quality check criteria for GALFIT results

Since the reduced chi-squared results of each GALFIT fit are not necessarily informative on the goodness of fit, we decide to quality check every fit by eye. A GALFIT fit was deemed unusable if one or more of the following criteria are true:

1. The GALFIT Sérsic model is more extended than the galaxy, leading to over-subtraction.
2. The position angle of the GALFIT Sérsic model does not match the position angle of the galaxy.

3. The axis ratio of the GALFIT Sérsic model does not match the axis ratio of the galaxy.
4. GALFIT fails to create a Sérsic model.

Any one of these criteria leads to poor residuals and therefore a rejection of fits from the final sample.

2.1.4 Sample selection

When selecting samples of galaxies from both high and low density environments, we need to make sure that they are at comparable redshifts and that the galaxies we are selecting from the clusters are indeed cluster members. In this section, we explain in detail how we selected galaxies from both environments so that measurements based on both samples could be compared directly.

As explained throughout Section 2.1.3, our entire size determination method was first tested on the F160W CANDELS-COSMOS mosaic to ensure it produced comparable sizes to those in van der Wel et al. (2012). Once this was achieved, we could be confident that our size determination method would produce comparable sizes for the rest of the galaxies in the F160W CANDELS fields. This testing run of our size determination method also allowed us to determine its limits. We find that galaxies in a relevant redshift range to our study ($0.86 < z < 1.34$) with a half-light radius measurement from GALFIT of $R_{eff} > 50$ kpc or F160W magnitude > 25 exhibit the largest disagreements in size with van der Wel et al. (2012). This divergence in disagreement is driven by increasingly lower signal-to-noise ratio beyond these size and magnitude limits (see Appendix B). As a result, when we select galaxies from the entirety of the 3D-HST survey, we select those galaxies that are below these size and magnitude thresholds based on measurements made by van der Wel et al. (2012). We also only choose those measurements that have a flag value of 0 (signifies reliable GALFIT results) according to the van der Wel et al. (2012) catalogue. This gives a sample of 12, 501 field galaxies. We then apply the GCLASS mass completeness limits (see Section 2.1.4.1) to this sample, reducing it to 3, 205 galaxies.

The same magnitude and size limits for reliable size measurements that were found when testing the size determination method on the F160W CANDELS-COSMOS mosaic are used for the GCLASS measurements as well. Then within these limits for GCLASS, all the spectroscopically confirmed cluster members with GMOS that have good quality spectra and GALFIT residuals are selected as part of the cluster sample. This amounts to 344 galaxies. This number is smaller than the total amount of spectroscopically confirmed cluster members with GMOS (457) because the HST fields-of-view are smaller than those of GMOS. The HST fields-of-view cover ∼86% of the spectroscopically confirmed cluster members (see Section 2.1.1.2). Additionally, not all spectroscopically confirmed cluster members obtained reliable size measurements (see Table 2.1) due

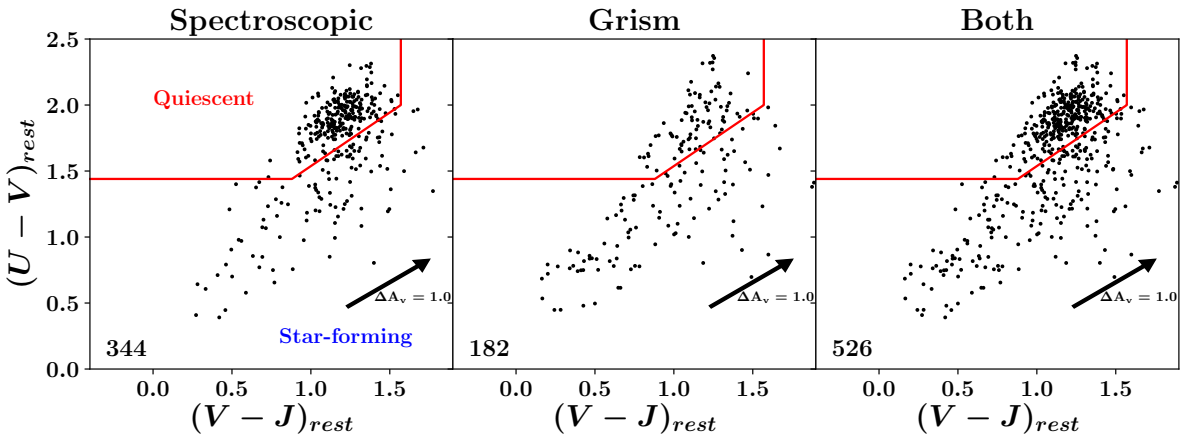

Figure 2.3: Left: Rest frame $U - V$ versus $V - J$ colour-colour diagram for the spectroscopically confirmed cluster sample. Middle: Rest frame $U - V$ versus $V - J$ colour-colour diagram for the grism-selected cluster sample. Right: Rest frame $U - V$ versus $V - J$ colour-colour diagram for the final cluster sample. Numbers in the bottom left-hand corner of each panel indicate the sample size. The red line shows the dividing line, modified from Williams et al. (2009), to define the quiescent and star-forming populations. The dust-reddening vector is shown as the black arrow in each panel. Note: Grism sample includes the 5 cluster members with poor quality GMOS spectra, but good quality grism spectra (see Section 2.1.4).

to poor Sérsic profile fits with GALFIT. The G141 grism data is used in conjunction with all the galaxies that obtained a spectroscopic redshift with GMOS, to determine a selection threshold on grism redshifts, z_{grism} by which additional cluster members can be identified from the grism sample (for more details on this, see Section 2.2). The entire grism sample is first quality-checked by eye. This procedure adds 177 cluster members to the 344 spectroscopically confirmed cluster members. Finally, cluster members that were flagged as "low confidence" due to poor quality spectroscopic redshifts are checked for good quality grism redshifts consistent with their respective cluster redshifts. This adds 5 more cluster members to the sample. The grism data therefore leads to an addition of 182 cluster members to the 344 spectroscopically confirmed cluster member sample. In total, the final cluster sample amounts to 526 galaxies. A cluster-by-cluster breakdown of the spectroscopic and grism samples can be seen in Table 2.1. A summary of this sample selection can be seen in Figure 2.3. Finally, the cluster sample is reduced to 474 galaxies after the GCLASS mass completeness limits are applied to the sample.

2.1.4.1 Mass completeness limits

The GCLASS mass completeness limits are set to match the grism spectroscopic completeness limits of the final cluster member sample. Every galaxy in the final cluster member sample (reliable grism spectra, F140W magnitude < 25 and $R_{eff} < 50$ kpc) has a good quality grism spectrum from which reliable grism redshifts are calculated, confirming their cluster membership (see Section 2.2 for more details). The GCLASS mass completeness limits are calculated for the star-forming and quiescent

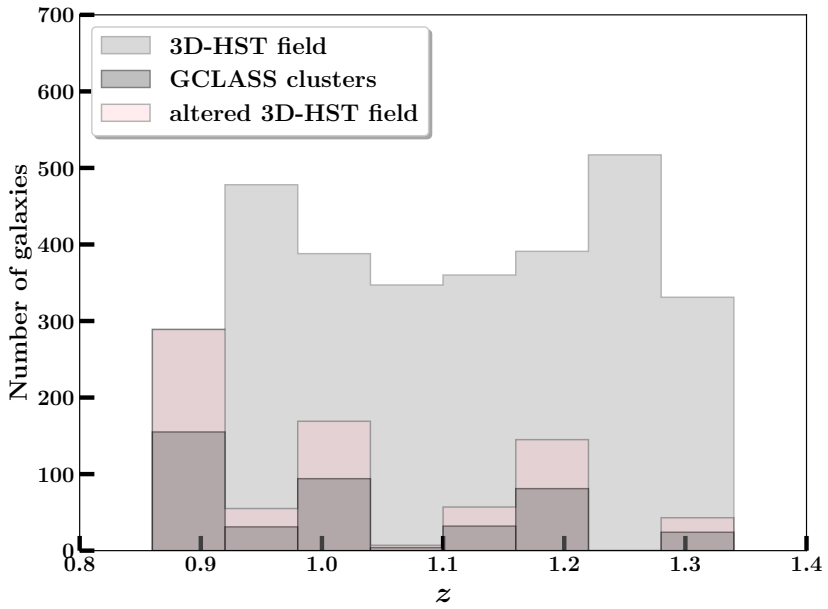

Figure 2.4: Alteration of the field redshift distribution, such that it follows the shape of the cluster redshift distribution. The original field sample (light grey histogram) contains more galaxies in every redshift bin compared to the cluster sample (dark grey histogram). The bin with the largest number of galaxies in the cluster sample (first bin) is used to work out its height ratio with the corresponding bin in the field. The heights of all the other cluster bins are scaled up using this ratio, leading to the distribution shown in pink.

cluster galaxies in the final cluster member sample separately, using the following method: the luminosity distances and absolute magnitudes of all cluster galaxies are calculated. Stellar mass-to-light ratios for all cluster galaxies are then calculated. The cluster galaxy with the highest mass-to-light ratio is found. This galaxy is the spectroscopically confirmed (either spectroscopic or grism) cluster galaxy for which the most stellar mass is measured for the least amount of flux. Then, the faintest galaxy with a spectroscopic or grism redshift in the sample is found. We then calculate what stellar mass this cluster galaxy would have, if it had a mass-to-light ratio corresponding to the highest value measured in the sample. This provides us with the lowest stellar mass for which a reliable grism spectrum can be obtained. We find mass completeness limits of $\log(\mathcal{M}_*/\mathrm{M}_\odot) = 9.96$ and $\log(\mathrm{M}_*/\mathcal{M}_\odot) = 9.60$ for quiescent and star-forming cluster galaxies, respectively. These mass completeness limits are comparable to those calculated by van der Burg et al. (2013) for the GCLASS clusters using ground-based *K*-band data. The limits used in our study are deeper due to the increased depth of the F140W imaging in comparison to the ground-based *K*-band data.

2.1.4.2 Redshift distribution matching

After the mass completeness limits have been applied to the field sample, we draw 1000 random field samples in a bootstrap-like method that follow the same redshift distribution as the cluster sample.

This is done in the following way: histograms of the cluster and field sample redshifts are plotted with the same redshift bins. Since there are more galaxies in the field sample, each bin in the field sample contains more galaxies than the same bin in the cluster sample. We take the bin with the largest number of galaxies in the cluster sample and calculate its normalisation with the corresponding field sample bin. This provides us with a factor with which we can multiply the height of all the cluster sample bins, and this establishes how many field galaxies should populate each bin. As a result, a distribution of field galaxy redshifts is obtained that matches the shape of the cluster distribution exactly. Figure 2.4 more clearly illustrates this process. Field galaxies are then randomly selected 1000 times within each of these redshift bins. The total number of field galaxies selected per bin corresponds to the height of each pink redshift bin shown in Figure 2.4. The result is 1000 different field samples, each containing 799 galaxies with the same mean redshift as the cluster sample. This alteration in the field redshift distribution is needed because when we select 3D-HST+CANDELS galaxies in the redshift range $0.86 < z < 1.34$, the median z is 1.09, however, the median redshift of the cluster distribution is $z = 1.00$. This difference is large enough to introduce a systematic in our size offset measurements in Section 2.3 of order our uncertainties (up to 0.03 dex for quiescent galaxies and up to 0.01 dex for star-forming galaxies) (van der Wel et al., 2014). Consequently, many field samples are required to measure reliable size offsets with the cluster sample since the mass–size distributions can vary between field samples. This leads to variations in the field relations that are fit, from which size offsets are measured (see Section 2.3 for more details).

2.1.4.3 Rest-frame colours

EAZY (Brammer et al., 2008) is used to interpolate the input SED to obtain the $U - V$ and $V - J$ rest-frame colours for each galaxy (van der Burg et al., 2013). This UVJ colour separation for star-forming and quiescent populations has been shown to be a powerful technique in separating the two populations, even if the former is reddened by dust extinction (Wuyts et al., 2007; Williams et al., 2009; Patel et al., 2012). This method is also used on the field sample. The dividing line used for the field sample is an interpolation of the lines defined in Williams et al. (2009) for $0.5 < z < 1.0$ and $1.0 < z < 2.0$. Quiescent field galaxies are defined as

$$(U - V)_{rest} > 1.3, \quad (V - J)_{rest} < 1.6 \tag{2.2}$$

and

$$(U - V)_{rest} > 0.88\,(V - J)_{rest} + 0.54 \tag{2.3}$$

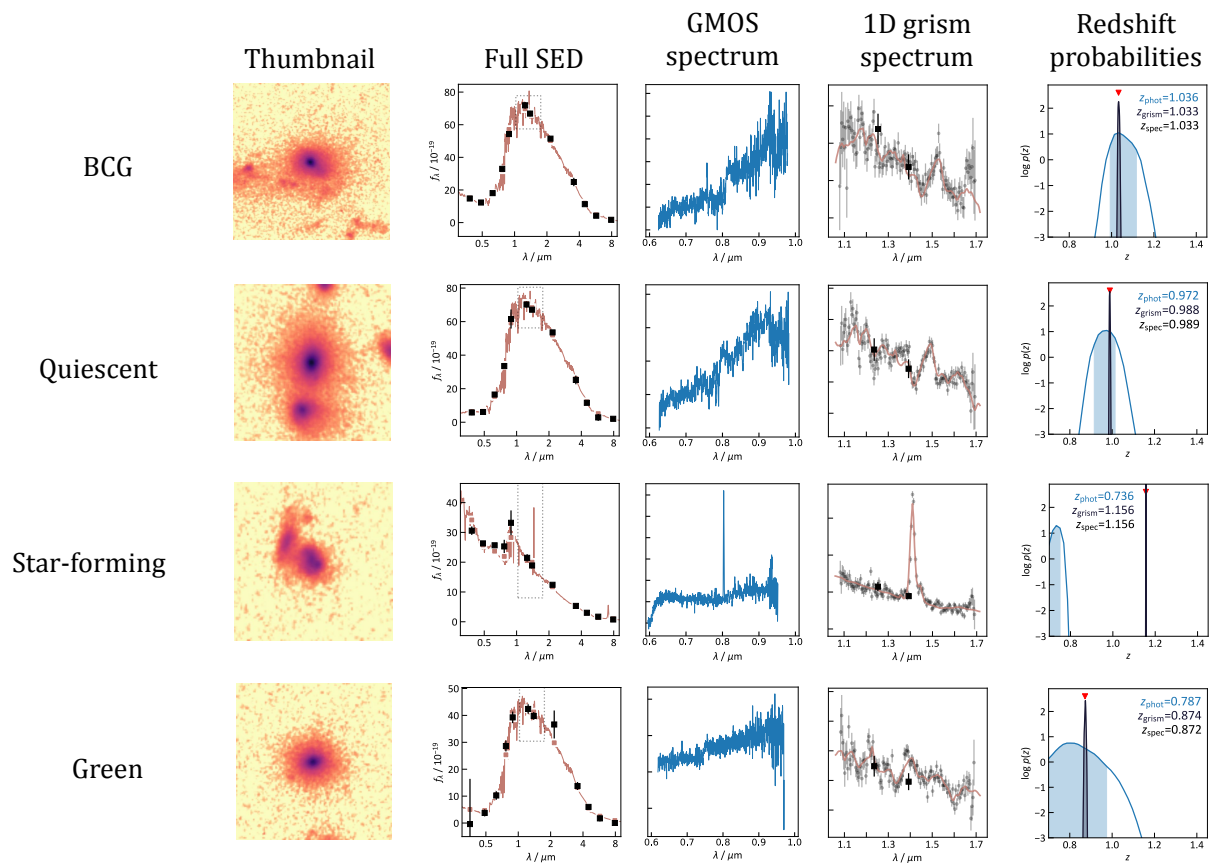

Figure 2.5: First column: cutouts from the GCLASS HST F140W mosaics of an example BCG, quiescent, star-forming and green cluster galaxy that have been spectroscopically confirmed. Colourmap is logarithmic. Second column: Full SED fits by EAZY on the 12-band photometry and grism spectra of the galaxies. The dotted grey rectangle highlights the region in which the grism spectrum lies. Third column: GMOS spectrum. Fourth column: A zoom-in of the regions highlighted with dotted grey rectangles in the second column. Data points from the raw-one dimensional grism spectra are also shown in grey. Black data points in both the second and third columns are from the 12-band photometry. Fifth column: redshift probability distributions. Photometric redshift distributions are shown in blue, with the shaded region representing the 2σ range. Grism redshift distributions are shown in black and red triangles show the location of the spectroscopic redshift.

We modify this dividing line for GCLASS to fit our rest-frame colour distribution. This is the red line shown in Figure 2.3, with quiescent cluster galaxies defined as

$$(U-V)_{rest} > 1.44, \quad (V-J)_{rest} < 1.57 \tag{2.4}$$

and

$$(U-V)_{rest} > 0.81\,(V-J)_{rest} + 0.73 \tag{2.5}$$

An example quiescent, star-forming, green (close to where Equation 2.5 becomes an equality) and Brightest Cluster Galaxy (BCG) from the GCLASS spectroscopic sample are shown in Figure 2.5 with their accompanying GMOS spectra, grism data and measurements. The second column shows the full SEDs from the 12-band photometry. The grey dotted rectangles in these plots show the location of the grism spectra with respect to the SEDs. A zoom-in of these regions is seen in the

fourth column, with data points from the raw one-dimensional grism spectra. The third column shows the GMOS spectra obtained as part of the GCLASS survey. The final column shows the redshift probability distributions based on fitting the two-dimensional grism spectra (see Figure 2.1) and the 12-band photometry simultaneously (see Section 2.1.1.1 for more details). This is done using a modified version of the EAZY code (Brammer et al., 2008). The extensive photometric coverage for GCLASS produces improved fits to the SEDs and grism spectra. The level of improvement is best seen in the almost one-to-one agreement with the spectroscopic and grism redshifts in the redshift probability distributions. What is perhaps more striking is the improvement in redshift estimates between the photometrically derived redshifts, z_{phot} and the grism redshifts, z_{grism}. In Section 2.2, we will demonstrate how this improved level of accuracy on redshift estimates is utilised to increase our cluster membership sample.

2.2 The precision and accuracy of grism redshifts

We take all the galaxies in the GCLASS HST fields-of-view that have reliable spectroscopic and grism redshifts and compare their redshift measurements from photometry (z_{phot}), spectroscopy (z_{spec}) and grism spectroscopy (z_{grism}) to their respective cluster redshifts, $z_{cluster}$. We do this to determine a selection threshold by which cluster members can be identified from the sample of galaxies that did not obtain a spectroscopic redshift with GMOS, but did obtain a grism redshift. To do this, we use the following terminology that was first introduced in van der Burg et al. (2013). A "false positive" is a galaxy that is not part of the cluster by virtue of its z_{spec}, but has a z_{phot} or z_{grism} consistent with the cluster redshift. A "false negative" is a galaxy that belongs to the cluster due to its z_{spec} measurement, but has a z_{phot} or z_{grism} placing it outside the cluster. "secure cluster" galaxies are those which are classified as being part of the cluster by virtue of both their z_{spec} and z_{phot} or z_{grism}. "secure field" galaxies are consistent with being outside the cluster due to their z_{spec} and z_{phot} or z_{grism} measurements. A clearer representation of this can be seen in Figure 2.6. The top row shows the comparison between z_{phot} and z_{grism} measurements for quiescent galaxies with good quality z_{spec} measurements. The bottom row shows the same, but for star-forming galaxies. The quiescent and star-forming separation is done using the *UVJ* selection criteria discussed in Section 2.1.4.3. What is immediately striking is the tight clustering of green crosses in the central regions of the z_{grism} vs. z_{spec} comparison plots. These are all grism-redshift selected cluster members with a spectroscopic redshift to support the reliability of their cluster membership. Another noticeable feature is all the star-forming galaxies that lie on an almost one-to-one correspondence line in the z_{grism} vs. z_{spec} comparison. This is another

representation of the excellent level of agreement between z_{spec} and z_{grism} measurements, attributed both to the Hα emission line that is prevalent in star-forming galaxy grism spectra (see Figure 2.5) and the 12-band GCLASS photometry.

The black horizontal dotted lines represent the cluster membership selection threshold used in van der Burg et al. (2013) based on a z_{phot} and z_{spec} comparison. When comparing the plots in the first and second columns, it is clear that there is no obvious selection threshold in the z_{phot} measurements by which cluster members can be reliably selected. The van der Burg et al. (2013) selection threshold of $-0.05 < \Delta z < 0.05$ was selected due to its convenience in producing a similar number of false positives and false negatives. The higher precision of the grism redshift measurements allow us to choose a selection threshold that is much narrower, lying at $-0.02 < \Delta z < 0.02$ (black dot-dashed line). This increases the number of cluster members per cluster by an average of 53% of the spectroscopic sample, due to galaxies without a z_{spec} measurement, but with a reliable z_{grism} measurement placing them inside their respective cluster (see Table 2.1). Our selection threshold has more than a factor of 2 improvement over the one used in the photometric cluster membership selection in van der Burg et al. (2013). We have also listed the average difference between the z_{phot} and z_{grism} measurements with the z_{spec} measurements for each sample in Figure 2.6. The precision of photometric and grism redshifts compared to spectroscopic redshifts in kms^{-1} is 8400 and 2000 kms^{-1} respectively: a factor of 4 improvement of grism redshifts over photometric redshifts. A factor of 3 and 7 improvement is seen for quiescent and star-forming galaxies respectively. The fraction of false negatives and false positives to secure cluster members falls from 28% and 23% to 8% and 10%, a factor of $\sim$3 improvement in contamination. Due to these low contamination rates, we do not perform corrections on our grism-selected cluster membership sample like those that were done on the photometric-selected cluster membership sample in van der Burg et al. (2013).

It must be stressed that this impressive improvement in precision and accuracy is due to the 12-band photometry GCLASS possesses. Both photometric and grism redshift measurements rely on the SEDs since they are used in both fitting processes. Therefore greater SED quality results in increased measurement precision and accuracy for both z_{phot} and z_{grism} measurements. A larger number of photometric bands — especially in the optical and near infra-red — for a given wavelength range improve the quality of the resulting SEDs from which photometric redshifts, grism redshifts and stellar masses are derived. Bezanson et al. (2016) studied the accuracy of grism redshifts with respect to photometric redshifts for the 3D-HST survey. They found similar values for the scatter in z_{phot} vs. z_{spec} and z_{phot} vs. z_{grism} (0.0159 ± 0.0005 and 0.0154 ± 0.0005), highlighting that

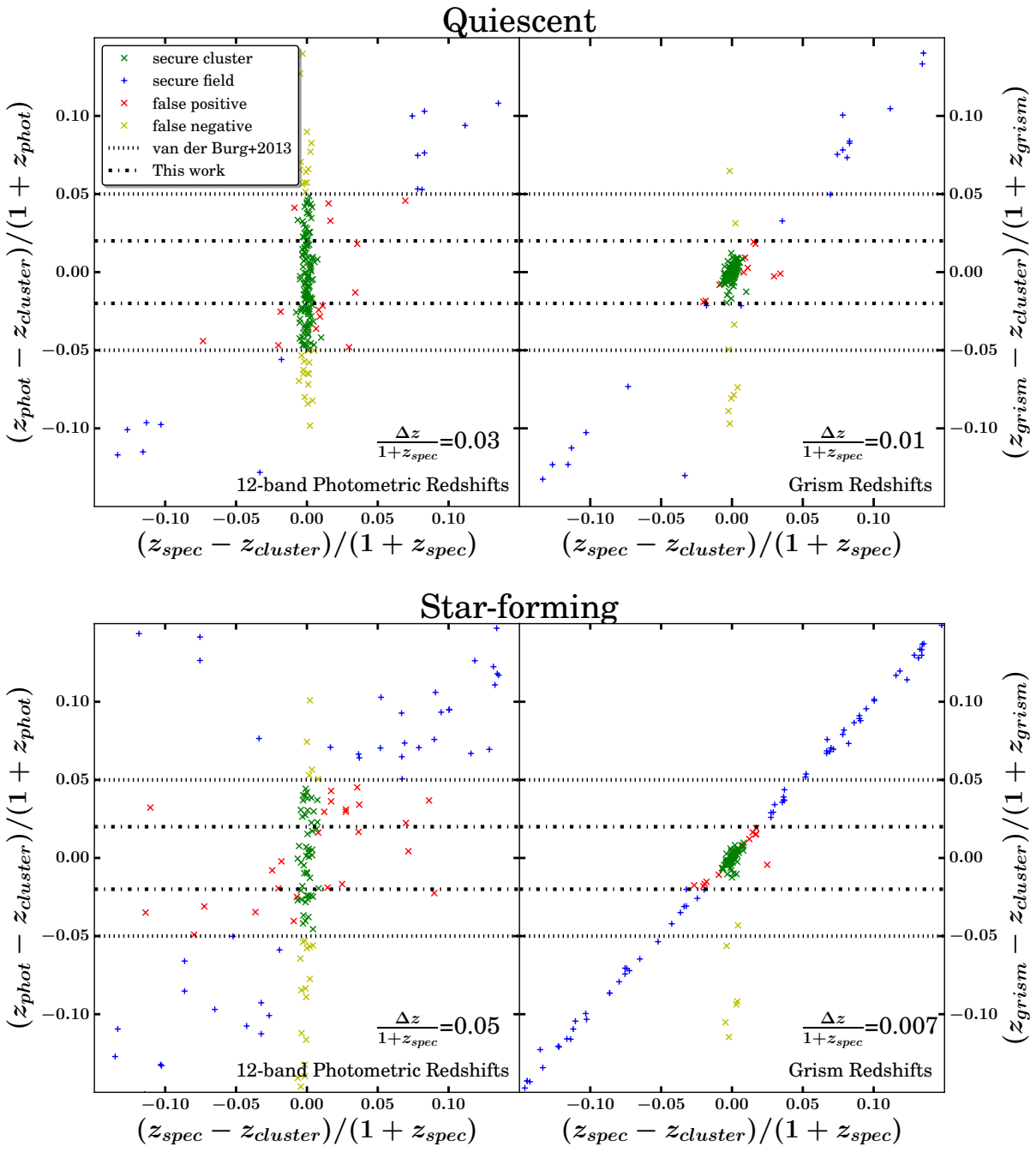

Figure 2.6: Top row: comparison of spectroscopic redshift measurements (z_{spec}) with photometric (left) and grism (right) redshift measurements (z_{phot} and z_{grism}) for quiescent galaxies in the HST fields of view with reliable z_{spec} and z_{grism} measurements. Bottom row: Same as the first row, but for star-forming galaxies. All comparisons are done relative to the spectroscopic redshift of the cluster centre (in most cases the BCG), $z_{cluster}$. Dotted black lines show the photometric redshift selection threshold from van der Burg et al. (2013) used to select cluster members. The dot-dashed black lines show the grism redshift selection threshold chosen for this work after comparing z_{spec} and z_{grism} measurements for this sample (second column). $\Delta z = |z_{phot} - z_{spec}|$ for the first column and $|z_{grism} - z_{spec}|$ for the second column. Values for $\frac{\Delta z}{1+z_{spec}}$ shown are the averages for the entire sample in that respective panel.

grism and spectroscopic redshifts are of equal quality relative to photometric redshifts. We also find similar values (0.06 ± 0.06 and 0.07 ± 0.07) with overall values $\sim$4 times higher than those of 3D-HST. Given that our methods for deriving photometric redshifts and stellar masses are near-to identical (see Section 2.1.2) and that our photometry spans the same wavelength range as for 3D-HST, the one thing we do not have is a comparable number of photometric bands and signal-to-noise ratio. The five 3D-HST fields (see Section 2.1.1.5) have photometry spanning between 18 (UDS) and 44 (COSMOS) bands, going deeper by $1-3$ magnitudes when comparing common photometric bands between GCLASS (Appendix A of van der Burg et al. 2013) and 3D-HST (Skelton et al., 2014). 3D-HST's superior photometry allowed for better photometric and grism redshift measurements compared to those for GCLASS.

Nevertheless, the GCLASS *HST* data has demonstrated that grism redshift measurements derived from good quality SEDs can be used to select samples of galaxies for cluster membership that are $\sim$90% pure. Space-based grism slitless spectroscopy – used in conjunction with photometry spanning multiple bands – therefore provides a unique alternative to conventional spectroscopic surveys, especially when large samples are required. JWST, WFIRST and *Euclid* will all have grism capability, with part of their science goals dedicated to studying high-redshift galaxies (Gardner et al. 2006; Laureijs et al. 2011; Green et al. 2012). This technical result demonstrates that grisms on future space-based telescopes will be able to provide large samples of cluster galaxies with high reliability.

2.3 The cluster versus field stellar mass–size relation at $z \sim 1$

The high quality grism redshift measurements for GCLASS provide us with the largest spectroscopically-confirmed sample of star-forming and quiescent cluster galaxies at $z \sim 1$ for which the stellar mass–size relation can be measured. By first testing the reliability of our size determination method using published results for the CANDELS-COSMOS F160W mosaic (see Appendix B), we have ensured our measurements for the cluster sample will be robust. Figure 2.7 shows the mass–size relation for the 10 GCLASS clusters in the left panel, with the BCGs** circled in grey. The solid black field lines were calculated using the 1000 field samples (see Section 2.1.4.2) in the following way: The stellar mass (corrected for the difference in flux measurements, see Section 2.1.2) and half-light radii measurements with uncertainties from van der Wel et al. (2012) for the star-forming and quiescent field galaxies in our 1000 field samples are used to fit for straight lines in log space using the Bayesian method from Kelly (2007). The star-forming and quiescent field relations are fit separately for slope,

**The BCGs were identified as the brightest cluster member in the observer-frame K_s band (Lidman et al., 2012).

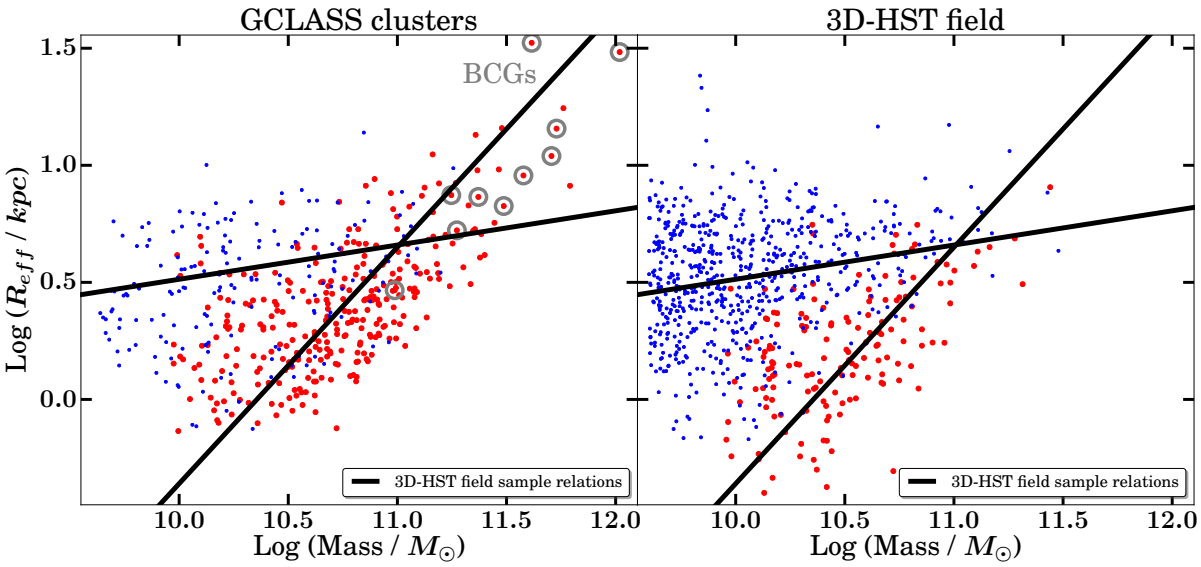

Figure 2.7: Stellar mass–size relation for the GCLASS clusters (left panel) and for one of the 3D-HST field samples (right). Smaller blue (larger red) circles show star-forming (quiescent) galaxies within the mass completeness limits of GCLASS. R_{eff} is the half-light radius in kpc. GCLASS Brightest Cluster Galaxies (BCGs) are circled in grey. Solid black lines show the field relations at $z \sim 1$ calculated using results from van der Wel et al. (2012) (see text).

intercept and intrinsic scatter for each of the 1000 samples. The mean slope and intercept value from these 1000 fits are used to calculate the final field relations, shown in Figure 2.7. We choose this method of line-fitting because we find that using simple orthogonal distance regression does not produce field relations that pass through the mean of the mass–size measurements used to fit the relations. It is therefore apparent that a fitting method which also fits for the intrinsic scatter is essential to producing realistic field relations. When fitting, we only use star-forming and quiescent field galaxies that meet the GCLASS mass completeness limits and are within the stellar mass thresholds used in the fitting process described in van der Wel et al. (2014) (star-forming galaxies with $\mathcal{M}_* > 3 \times 10^9\ \mathcal{M}_\odot$ and quiescent galaxies with $\mathcal{M}_* > 2 \times 10^{10}\ \mathcal{M}_\odot$). In an attempt to follow the fitting method in van der Wel et al. (2014) as closely as possible, we add an uncertainty of 0.15 dex in the Log (Stellar Mass / $\mathcal{M}_\odot$) measurements. For comparison, in the right panel of Figure 2.7, we plot the stellar mass–size relation for one of the 1000 field samples for which the resulting field relation fits were close to the final field relations.

We then compare the stellar mass–size measurements for both the field and cluster samples more rigorously. We measure the size offsets in log space along the y-axis from each of the 1000 field relations for each of the mass–size measurements in each of the 1000 field samples. We also measure the size offsets of the cluster sample from each of the 1000 field relations. We then take the mean of each size offset distribution. The difference between the field and cluster mean size offsets is calculated for each of the 1000 field samples. The distribution of these differences in the mean size

offsets in log space for quiescent and star-forming galaxies is shown in Figure 2.8. The reason we do not select one field sample and measure size offsets from a single field relation is because the field mass–size distribution varies between the 1000 field samples. As a result, the calculated field relations vary. This is particularly important for calculating the quiescent field relations. There are fewer quiescent galaxies compared to star-forming galaxies in the field samples (evident in Figure 2.7). As a result, fewer galaxies are used to fit for the quiescent field relations than for the star-forming field relations. This leads to wider variations in the slope and intercept values for the 1000 quiescent field relations compared to the variations found for the 1000 star-forming field relations. When we take the mean of all individual average size offset differences measured between cluster and field, we find that quiescent and star-forming cluster galaxies are smaller than their field counterparts by (0.08 ± 0.04) dex and (0.07 ± 0.01) dex respectively. The result for quiescent cluster galaxies does not change significantly if we remove the BCGs from the cluster sample. The magnitude of these size offsets, particularly in the case of quiescent galaxies, is exactly what we would expect from the minor-mergers hypothesis of size growth advocated by van der Wel et al. (2014) and many others (e.g. Bezanson et al. 2009; Hopkins et al. 2009b; van Dokkum et al. 2010).

In the minor-mergers hypothesis of size growth, galaxies are able to grow disproportionately more in size compared to stellar mass with decreasing redshift. This is because minor mergers cause mass to be preferentially deposited at larger radii. Such growth would be able to increase the intercept of the mass–size relation without significantly affecting the slope. This is seen in the field for 3D-HST between $0 < z < 3$ in van der Wel et al. (2014). In order to test whether it is indeed minor mergers driving the evolution in the intercept, we need a population of galaxies that we know are virtually unable to grow via minor mergers, and compare their stellar mass–size relation to 3D-HST at fixed redshift. This population is represented by our cluster galaxies. The high velocity dispersions in clusters suppress mergers from occurring, consequently suppressing size growth via minor mergers. If minor mergers are truly responsible for the majority of the disproportionate size growth observed in the field, we should find that the sizes of cluster galaxies are offset to smaller sizes at fixed redshift. The magnitude of this offset needs to be equivalent to the expected evolution in the intercept of the field mass–size relation between the redshift at which the current cluster galaxies fell into their clusters and $z \sim 1$. If the magnitude of the size offset is significantly smaller than this value, we cannot be sure that minor mergers are responsible for the majority of the size growth observed in the field.

A cluster with the average mass of a GCLASS cluster (4.2×10^{14} $M_{\odot}$; see Table 2.1) at $z \sim 1$ is

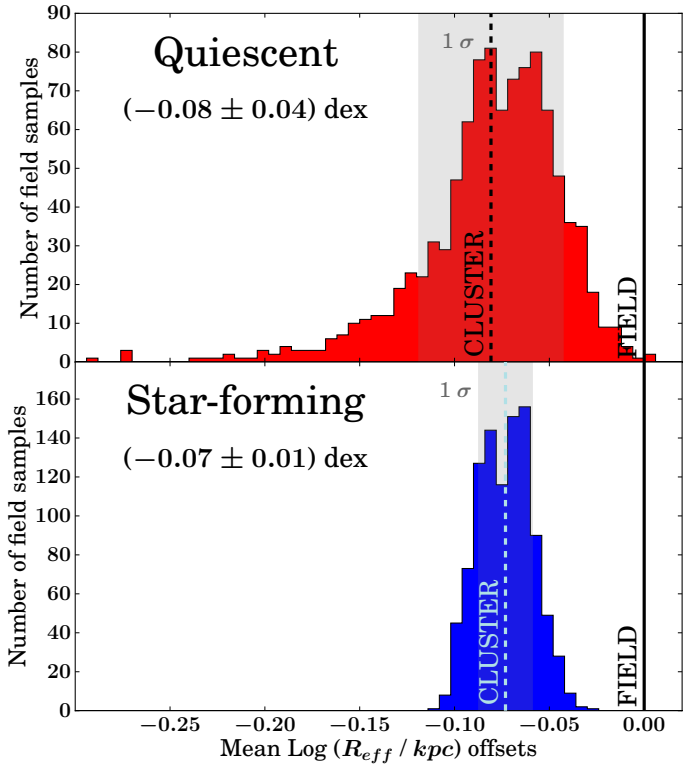

Figure 2.8: Histograms of the differences between the mean size offsets of cluster and field galaxies in log space (mean cluster size offset - mean field size offset). Cluster and field size offsets are measured relative to the 1000 possible field mass–size relations for the 1000 different field samples. This is done for quiescent and star-forming galaxies separately. Solid black vertical lines show the location of no difference in average size between field and cluster galaxies at fixed stellar mass. Dashed vertical lines show the mean of all the differences measured in the mean size offsets of cluster and field galaxies. Grey shaded regions show one standard deviation in the mean size offset differences. On average, quiescent and star-forming cluster galaxies are smaller than their field counterparts by (0.08 ± 0.04) dex and (0.07 ± 0.01) dex respectively.

expected to accrete most of its mass by approximately $1.2 \leqslant z \leqslant 1.5$ (Fakhouri et al., 2010; van der Burg et al., 2015)[††]. Under the assumption that most of the current GCLASS cluster members fell into their clusters from the field at these redshifts – and had their size growth suppressed since then – they should exhibit sizes that follow the field stellar mass–size relations at these redshifts. We use the preferred parameterisations for the evolution in the intercept of the field mass–size relation found in van der Wel et al. (2014) (R_{eff} / kpc = 4.3 $h(z)^{-1.29}$ for quiescent galaxies and R_{eff} / kpc = 7.8 $h(z)^{-0.66}$ for star-forming galaxies) to check the expected size offset in the field between $z \sim 1$ and $1.2 \leqslant z \leqslant 1.5$. We find size offset ranges of $0.06 - 0.2$ dex and $0.03 - 0.08$ dex for quiescent and star-forming galaxies respectively. Our results of (0.08 ± 0.04) dex and (0.07 ± 0.01) dex for quiescent and star-forming galaxies are therefore consistent with these allowed ranges, supporting the possibility that minor mergers are the dominant route for galaxy size growth.

Previous work on measuring the difference between the field and cluster stellar mass–size relations

[††]This is found by looking at the halo mass a cluster with the average M_{200} of a GCLASS cluster at $z \sim 1$ would reach by $z \sim 0$ in the Millenium Simulations. The redshift at which approximately > 50% of the mass is assembled is read-off from the top panel of Figure 6 in Fakhouri et al. (2010).

at fixed redshift has consisted of a diverse range of results. At low redshifts ($z < 0.2$), Cebrián & Trujillo (2014) is the only study which finds smaller sizes in both early-type and late-type galaxies in the cluster environment. They find that early-type and late-type cluster galaxies are ∼3.5% and ∼7.5% smaller than their field counterparts respectively. These percentages are approximately what is expected at these redshifts if we use the same parameterisations from van der Wel et al. (2014) and assume that most of the current cluster members in the clusters used in Cebrián & Trujillo (2014) fell into their clusters at a redshift that corresponds to $\sim$ 1 Gyr prior to observation. However, Weinmann et al. (2009) and Maltby et al. (2010) find no difference in early-type galaxies with environment. At a similar redshift to our work, Delaye et al. (2014a) studied the mass–size relation for massive early-type galaxies in 9 clusters compared to a field sample selected from a variety of datasets. They found no difference in the median sizes with environment, but a skew towards larger sizes in clusters by $30 - 40\%$. This is a significantly different result to ours, where we find early-type galaxies are $\sim$ 20% *smaller* in clusters compared to the field, at fixed stellar mass. At a slightly higher redshift of z∼1.3, Raichoor et al. (2012) found early-type galaxies to be $30 - 50\%$ smaller in clusters. This result is also consistent with what is expected at this redshift using the intercept evolution parameterisation for quiescent galaxies from van der Wel et al. (2014) and assuming the current cluster members fell into their clusters at a redshift corresponding to $\sim$ 1 Gyr prior to observation. We postulate that these conflicting results in the literature might be due to a combination of small sample sizes at high redshifts and the difficulty in minimising systematics between field and cluster samples.

We have shown that when a careful treatment of systematics between datasets is carried out, there is a difference between the field and cluster stellar mass–size relations at $z \sim 1$. The magnitude of this difference is consistent with the expected size growth from minor mergers in the field for the likely duration the current cluster galaxies at $z \sim 1$ have been in their clusters.

It should be mentioned that size growth in the quiescent field population is also thought to be due to newly-quenched field galaxies joining the quiescent field population at later times (Carollo et al., 2013). Galaxies that quench later are larger than galaxies that quenched earlier. Therefore, if a large fraction of the quiescent field population consists of newly-quenched galaxies, quiescent field galaxies would be on average larger than quiescent cluster galaxies at fixed redshift and stellar mass. Nevertheless, while this does play a role in the average size growth of the quiescent field population, it is not thought to be the only explanation, with merging thought to be the other important contribution (e.g. van der Wel et al. 2009).

Our suggestion that the lack of minor mergers in the cluster environment inhibits size growth would consequently lead to a significant difference between the cluster and field environment at low redshifts. In Section 2.5 we will discuss the implications of this in more detail.

In the next section, we will investigate whether the differences in the cluster and field mass–size relations are due to morphological differences.

2.4 Morphology and the cluster versus field stellar mass–size relation at $z \sim 1$

We use the Sérsic index measurements from the structural parameter estimation with GALFIT for GCLASS (see Section 2.1.3.3) and 3D-HST (van der Wel et al., 2012) as a proxy to track morphology across the mass–size plane. Figure 2.9 shows the mass–size relation for both cluster and field samples in three bins of Sérsic index. Disc-like and bulge-like morphologies tend to correlate with Sérsic index (e.g. Ravindranath et al. 2004). We therefore use the Sérsic index measurements as proxies, classing galaxies as "disc-like" if they have $n \leqslant 1$ and "bulge-like" if they have $n \geqslant 2.5$. We then categorise the rest of the galaxies as intermediate-types in a Sérsic index bin between these two. To illustrate this comparison between the two environments, we truncate both samples to the mass completeness limits of GCLASS. The field sample used is one of the 1000 field samples that led to a cluster size offset close to the values found in Section 2.3. These values are also stated in Figure 2.8.

Firstly, when comparing the location of galaxies on the mass–size plane based on their morphologies in both environments, it can be established that disc-like (bulge-like) galaxies lie closer to the star-forming (quiescent) field relation at $z \sim 1$. Alternatively, it shows that Sérsic index is well-correlated with quiescence, as has been seen in other samples (e.g. Franx et al. 2008; Bell et al. 2012). Therefore, these field relations can be used as markers to track morphological changes across the mass–size plane. The mass–size relations for each morphological type are broadly the same in both environments.

There is however a larger fraction of quiescent intermediates and quiescent bulge-like galaxies in the clusters compared to the field, whereas the disc-like population in both environments is dominated by star-forming galaxies. This is more clearly seen in Figure 2.10. This excess population of quiescent intermediate-type galaxies points towards a cluster-specific process that quenches them more efficiently than if they resided in the field. A number of studies have identified an abundant population of "passive spirals" or "red discs" in clusters compared to the field (van den Bergh, 1976; Goto et al., 2003; Moran et al., 2007; Gallazzi et al., 2009). The most recent study of which is a study of the mass–size relation in the $z = 0.44$ cluster MACS J1206.2 − 0847 (Kuchner et al., 2017). Here, they attribute its existence to cluster-specific quenching processes that lead to a fading of the stellar

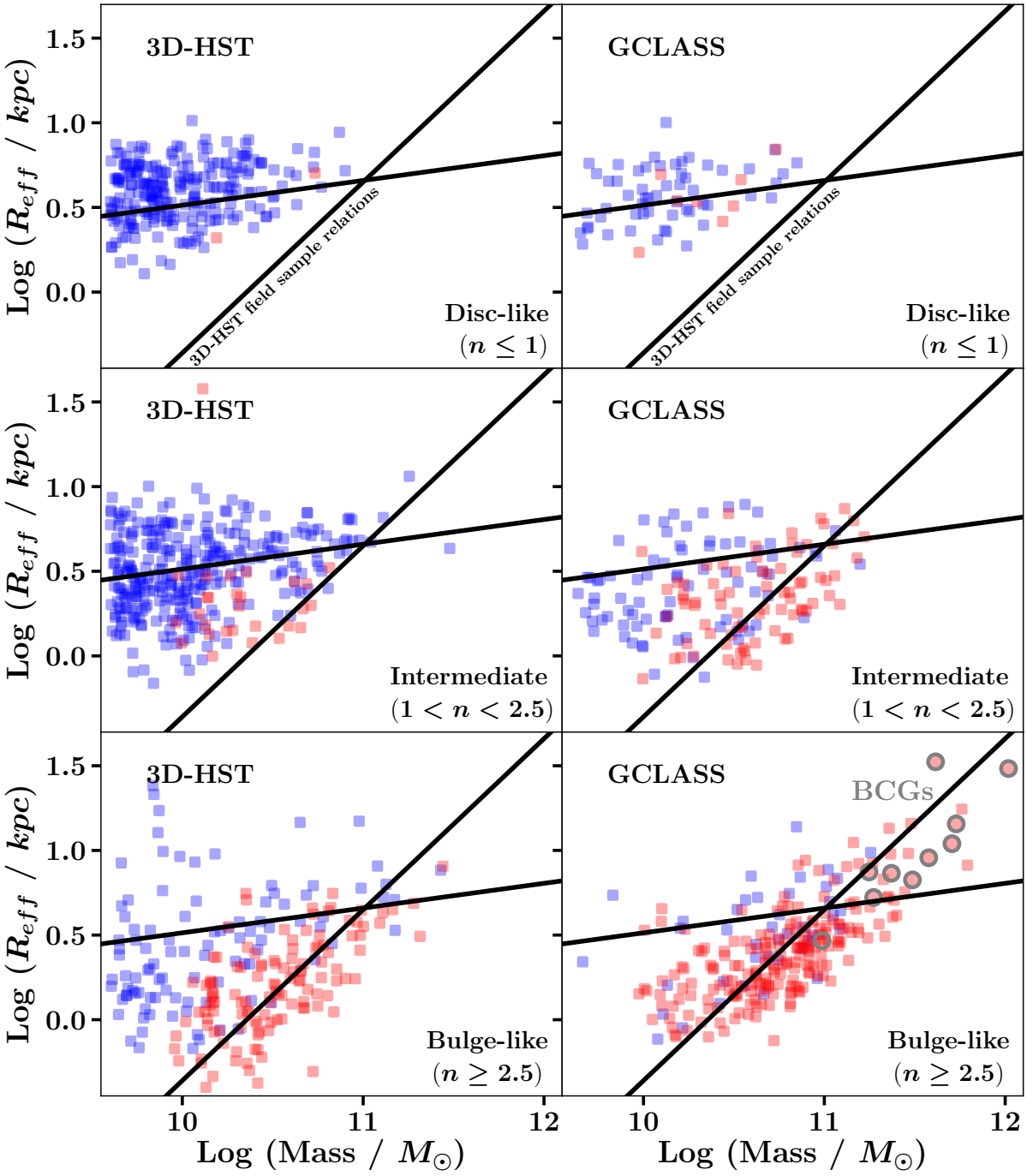

Figure 2.9: The stellar mass–size relation at $z \sim 1$ in both the field (left column) and cluster (right column) environment, split into three bins of Sérsic index (top, middle and bottom rows) to track morphology. Blue squares indicate star-forming galaxies, red squares quiescent galaxies. Solid black lines indicate the field mass–size relations for $z \sim 1$ derived using results from van der Wel et al. (2012, 2014). Grey circles indicate the GCLASS BCGs.

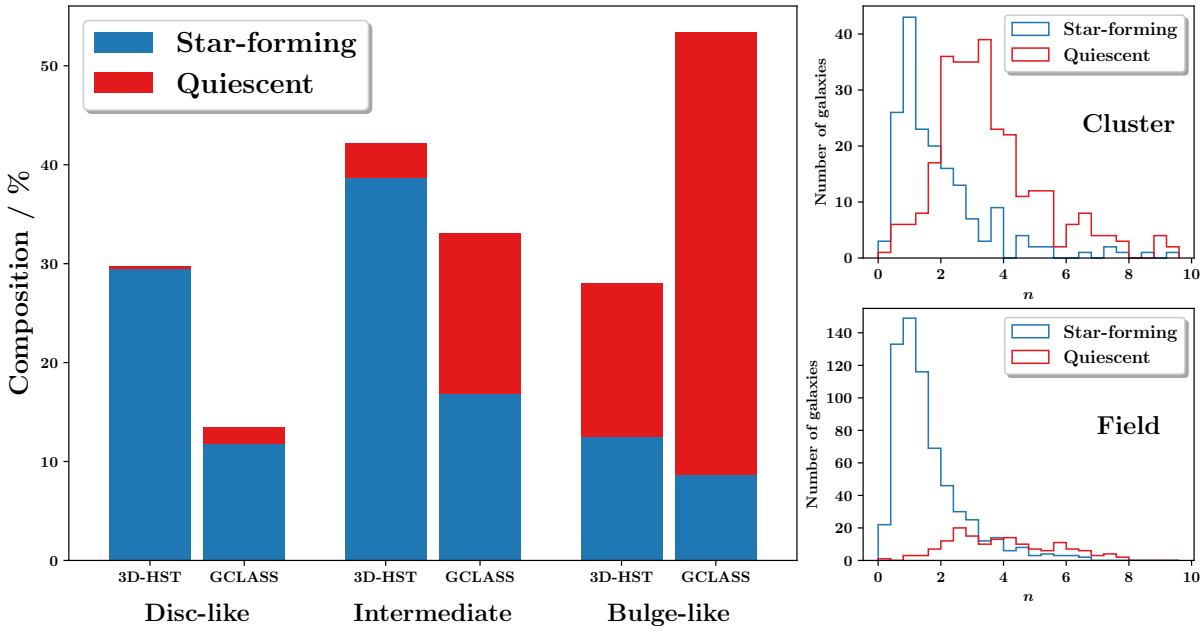

Figure 2.10: The morphological composition of both the field and cluster environments at fixed stellar mass. Quiescent intermediate-type and bulge-like galaxies are more popular in the cluster environment.

disc with respect to the inner bulge region. This would make the galaxy look smaller than a disc-like galaxy, which is probably why many of the quiescent intermediates lie in the region between the two field relations.

Furthermore, Kuchner et al. (2017) also found that this population was more prevalent in the regime $R_{500} < R < R_{200}$, which is where in-falling galaxies first feel the effects of the cluster's tidal field and start to be subjected to "starvation" (Moran et al., 2007). This can occur after gas from a galaxy's halo is stripped by the intracluster medium (ICM). As a result, the star formation declines in a galaxy since the cold gas is not replenished (Larson et al., 1980). The stripping can distort the distribution of gas. This was seen by Vogt et al. (2004), who found that a larger population of asymmetric, stripped and quenched spirals are predominant in the hottest and richest of clusters based on H I properties. With the galaxy's gas supply removed, star formation is unable to continue in the galaxy. Eventually, the disc will fade further to the point where the bulge region of the galaxy will look brighter than the disc. The galaxy will then look bulge-like. Hence, this increased efficiency in quenching intermediate-types may be directly responsible for the larger fraction of quiescent bulges in the clusters. This result suggests that there is a direct morphological consequence of environmentally-driven quenching. This morphological transformation in the light profiles of cluster galaxies may be the driver of the well-known morphology-density relation (Dressler, 1980). Dressler (1980) however argued that gas stripping was unlikely to drive the larger populations of S0s

in high-density environments, and therefore unlikely to drive the morphology-density relation.

2.5 Evolution of the cluster mass–size relation with redshift

In Section 2.3, we presented results that may support the hypothesis that minor mergers drive the size growth of galaxies in the field environment. However, the fact still remains that at low redshifts, small or negligible differences exist between the cluster and field stellar mass–size relations (Weinmann et al., 2009; Maltby et al., 2010; Cebrián & Trujillo, 2014). Since the intercept of the field mass–size relation increases with decreasing redshift (van der Wel et al., 2014), the same must therefore happen to the cluster mass–size relation for there to be such small differences between the cluster and field mass–size relations at low redshifts. This poses a problem for cluster galaxies. Whilst the observed decline in the number density of compact quiescent field galaxies with decreasing redshift (e.g van der Wel et al. 2014) could be explained by size growth via minor mergers, it cannot explain the increasing intercept of the cluster quiescent mass–size relation with decreasing redshift. This is because cluster galaxies are unlikely to grow in size via minor mergers. The size offsets towards smaller sizes measured in the GCLASS clusters support this hypothesis. Based on this hypothesis, as a galaxy cluster evolves, it will continually accrete new field galaxies, subsequently "freezing" their size growth once they enter the cluster. Over time, larger field galaxies will be accreted, but the older, smaller field galaxies that were accreted at earlier times will still be present in the cluster. A build-up of compact cluster galaxies is created that will suppress increases in the intercept of the mass–size relation with decreasing redshift. To allow for the intercept of the cluster mass–size relation to significantly increase with decreasing redshift, there is only one option left. Since the compact cluster galaxies are unlikely to grow in size via minor mergers in the clusters, they need to be destroyed by some mechanism that is most likely cluster-specific.

2.5.1 Toy model

The two ways satellite galaxies in clusters can be destroyed are by either merging with their BCGs or being tidally disrupted into the ICL. We therefore construct a toy model to investigate whether the most compact cluster galaxies that exist in the GCLASS clusters at $z \sim 1$ can be destroyed by merging with their BCGs or being tidally disrupted into the ICL, such that the small differences observed between the cluster and field stellar mass–size relations at $z \sim 0$ can be achieved. The plausibility of this scenario depends upon several constraints.

2.5.1.1 Constraints

Recent studies have shown that BCGs increase their stellar mass by a factor of $\sim$2 between $z \sim 1$ and $z \sim 0$ (Lidman et al., 2012, 2013; Lin et al., 2013; Bellstedt et al., 2016). Therefore, the final stellar masses of the GCLASS BCGs at $z \sim 0$ cannot be more than approximately double their current stellar masses at $z \sim 1$ in the toy model. The remaining compact cluster galaxies left after this maximum stellar mass has been reached by the GCLASS BCGs would need to be tidally destroyed and contribute to the stellar mass of the ICL. However, there are also constraints on the stellar mass of the ICL at $z \sim 0$. Recent work at $z \sim 0.3 - 0.5$ has shown that the ICL stellar mass budget is $6 - 23\%$ of the entire cluster stellar mass contained within $\sim R_{500}$ (Presotto et al., 2014; Montes & Trujillo, 2014; Giallongo et al., 2014). Hence if we assume the ICL stellar mass is negligible at $z \sim 1$, the total stellar mass of those compact cluster galaxies in the GCLASS clusters that need to be tidally destroyed can be no more than $6 - 23\%$ of their cluster's total stellar mass within $\sim R_{500}$ at $z \sim 0$.

2.5.1.2 Assumptions & Sample selection

We make the overall assumption that the majority of minor mergers a BCG will have between $z \sim 1$ and $z \sim 0$ will be with compact cluster galaxies that are already in place at $z \sim 1$. Simulations have also found that the majority of stars which end up in the BCG and ICL components fell into clusters before $z \sim 1$ (Puchwein et al., 2010). Galaxies which fell in later do not have enough time to sink towards the centre of the cluster and subsequently merge with the BCG. This is also a natural consequence of dynamical friction.

As mentioned earlier, low redshift work has shown that if there are any differences between the stellar mass–size relations in high and low density environments, they are very small. Therefore, we can assume that the stellar mass and size distribution of galaxies in both environments at low redshift are similar. Hence we can use the low redshift field mass–size relation to identify a region which is required to be relatively absent of compact galaxies at $z \sim 0$. This region can then be used as our selection area for compact cluster galaxies in GCLASS that should be destroyed by $z \sim 0$. We show the low redshift field stellar mass–size relation from 3D-HST in the left-hand panel of Figure 2.11 accompanied with the low redshift quiescent field relation shown as the black dashed line[‡‡]. We also show the $z \sim 1$ quiescent field relation as the solid black line for comparison. The low redshift quiescent field relation was calculated using the same Bayesian technique used to calculate the $z \sim 1$

[‡‡]These measurements are selected in the same way as the field sample in this study, except a low redshift *UVJ* colour sample selection is used to distinguish star-forming and quiescent galaxies.

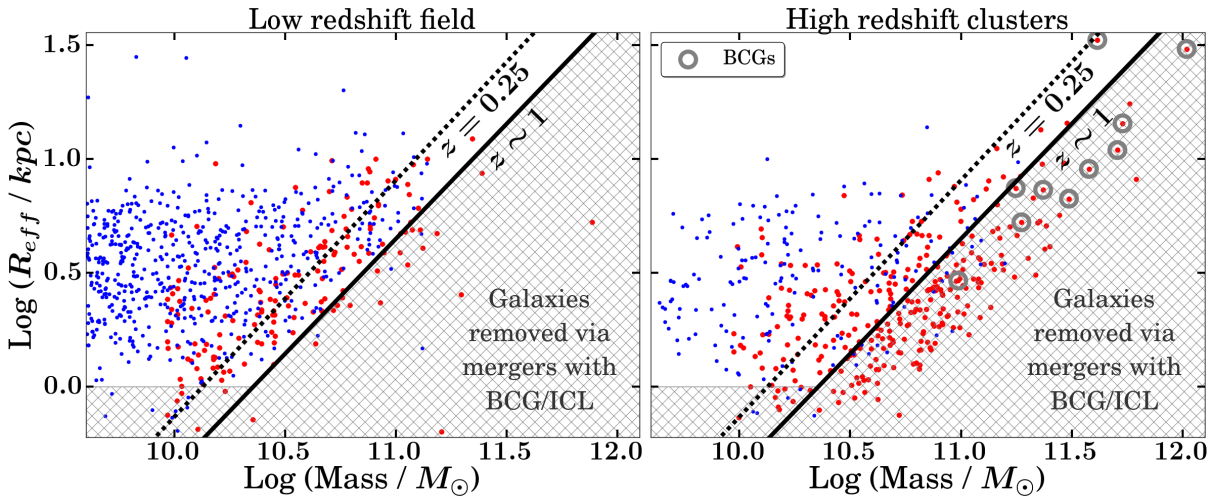

Figure 2.11: Left panel: $0 < z < 0.5$ field stellar mass–size relation from 3D-HST within the mass completeness limits of GCLASS. The black dashed line is the corresponding quiescent field relation calculated using results from van der Wel et al. (2012) (see text). The solid black line shows the $z \sim 1$ quiescent field relation calculated in this study using 3D-HST measurements. Right panel: $z \sim 1$ cluster stellar mass–size relation from GCLASS within mass completeness limits. Lines are the same as in the left panel. Hatched region in both panels shows our toy model selection area for compact galaxies in GCLASS that should merge with their BCGs or become part of the ICL by low redshifts.

field relations in Section 2.3. Due to the small sample of low redshift quiescent galaxies in 3D-HST with reliable size measurements (flag value 0 in the van der Wel et al. (2012) F160W catalogue, GALFIT measured $R_{eff} < 50$ kpc and F160W magnitude < 25), we ran the fitting process 1000 times on the sample to capture the range of possible intercept and gradient values. The average line of all these fits is then used as the final quiescent field relation. Plotted points also include GALFIT fits that had a flag value of 1 in the van der Wel et al. (2012) F160W catalogue. The region marked with hatches signifies the region of the mass–size plane that is relatively absent of compact galaxies at $z \sim 0$.

In the right panel of Figure 2.11, we show this selection area and the low redshift field relation with respect to the GCLASS mass–size measurements. It can be seen that our chosen selection area is more populated in the $z \sim 1$ GCLASS clusters compared to the $z \sim 0$ field. For our toy model, we will select compact cluster galaxies from GCLASS that are within this region. We only apply our toy model to the sample of GCLASS galaxies that meet the mass completeness limits.

2.5.1.3 Toy model results

We use the analytic model for growth via minor mergers from Bezanson et al. (2009), which dictates a growth in size of $R_{eff} \propto M_*^2$ after every minor merger. To simplify our toy model, we do not use different growth prescriptions for minor mergers with star-forming/quiescent compact cluster galaxies to account for differing amounts of dissipation during the merger. Instead, we use a model appropriate

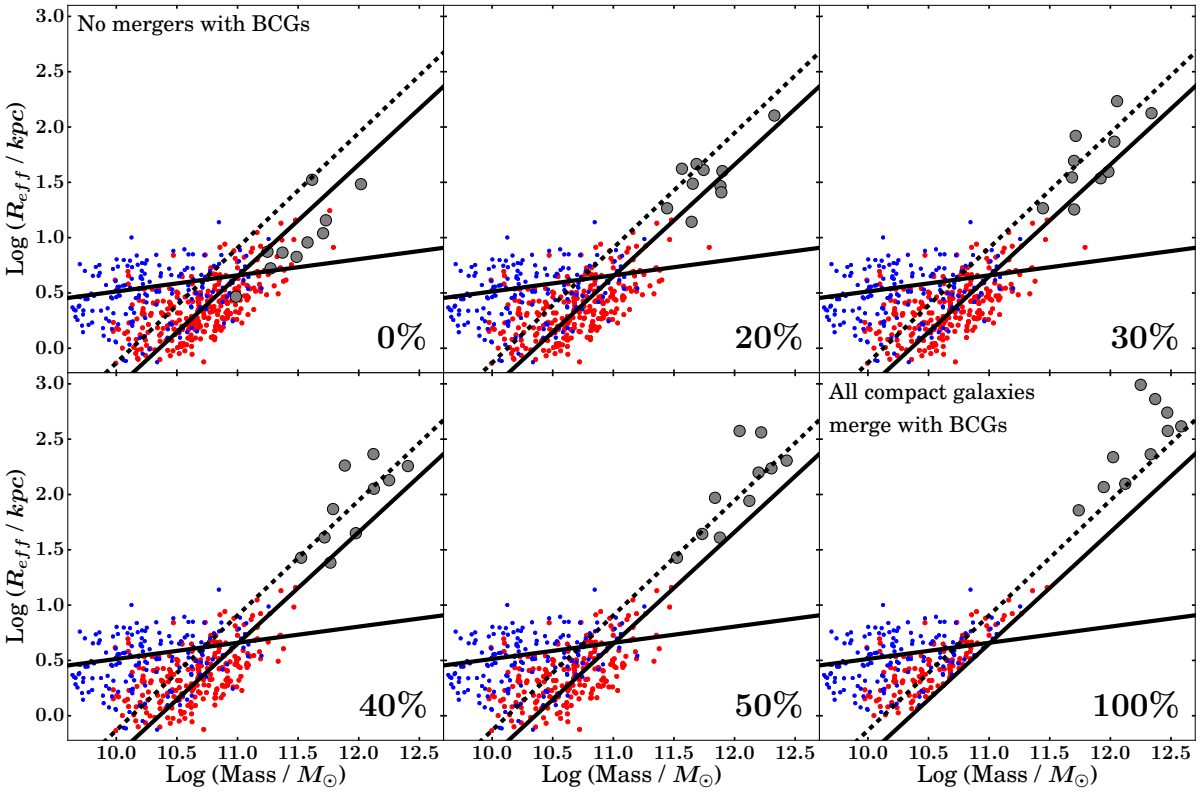

Figure 2.12: GCLASS BCG growth to low redshifts using the analytic model for growth via minor mergers from Bezanson et al. (2009). The first (top left) panel shows the original GCLASS stellar mass–size relation with the BCGs as large grey filled points. The last (bottom right) panel shows the position of the GCLASS BCGs in the extreme case where all compact cluster galaxies merge with their respective BCGs. In between, we show the best fit results for increasing percentage selections of compact cluster galaxies. Solid black lines are the $z \sim 1$ field relations calculated in this study and the black dashed line is the low redshift quiescent field relation calculated using results from van der Wel et al. (2012) (see text).

for minor mergers between quiescent galaxies, since the majority of galaxies in the selection area are quiescent.

In Figure 2.12, we show the results for this growth prescription as well as the extreme case where all compact cluster galaxies merge with their respective BCGs. Compact galaxies that merge with their BCGs are randomly selected for each cluster from the hatched selection area (see right-hand panel of Figure 2.11) for each percentage selection of compact galaxies shown in Figure 2.12. The same random seed is used for each percentage, such that compact galaxies selected in smaller percentage prescriptions are part of the selection in higher percentage prescriptions plus additionally selected compact galaxies. This allows for a direct comparison between the different percentage prescriptions. It is clear that if all the compact cluster galaxies did merge with their respective BCGs (100% panel in Figure 2.12), the sizes and stellar masses of the BCGs would be far too large compared to what has been observed for BCGs in the local universe.

We check what percentage of compact galaxies are required to merge with their BCG for each GCLASS cluster such that the BCG grows its stellar mass by a factor of $\sim$2. This is the amount of

stellar mass growth observed for BCGs between $z \sim 1$ and $z \sim 0$ for BCGs in clusters similar to those in GCLASS (see Section 2.5.1.1). Once again, we randomly select compact galaxies from the hatched selection area shown in Figure 2.11 for each cluster to do this. Despite finding percentages ranging from 0% (for SpARCS-1634) to 65% (for SpARCS-1638), the average for the entire GCLASS sample is 40%. This suggests that no more than 40% of compact galaxies on average in each GCLASS cluster can merge with their BCGs in our model. This fits nicely with the results of our toy model in Figure 2.12, which suggests that most BCGs will follow the low redshift field quiescent stellar mass–size relation if 40% of compact galaxies in each GCLASS cluster merge with their BCGs. Under our assumption that 100% of compact cluster galaxies must be removed from the sample by $z \sim 0$, this implies the remaining 60% of compact cluster galaxies are destroyed, most likely by tidal disruption into the ICL.

The HST imaging for all the clusters covers most, if not all of R_{500} (see Section 2.1.1.2). The total stellar mass of a GCLASS cluster is on average $\log(M_*/M_\odot)\sim$12.47 assuming negligible ICL at $z \sim 1$. This is calculated by adding the stellar mass of all galaxies in each cluster above the mass-completeness limits and then finding the average of these 10 values. Based on the total stellar mass of the compact galaxies that did not merge with their BCGs in the 40% prescription of our model, this destruction mechanism would lead to the build-up of an ICL by $z \sim 0$ with a stellar mass of $\log(M_*/M_\odot)\sim$11.96. The average M_{200} of the GCLASS sample is $\sim 4.2 \times 10^{14}\ M_\odot$ (see Table 2.1). A cluster of this mass at $z \sim 1$ is expected to grow by a factor of $\sim$4 by $z \sim 0$ (see Figure 1 of van der Burg et al. 2015). If we assume the stellar mass contained within $\sim R_{500}$ of the cluster increases by the same factor, this would lead to a total cluster stellar mass of $\log(M_*/M_\odot)\sim$13.07 at $z \sim 0$. The ICL stellar mass fraction at $z \sim 0$ will therefore be $\sim$8% for a typical GCLASS cluster in our toy model. This agrees well with the $6 - 23$% found in more thorough studies of the ICL stellar mass fraction at low redshifts.

2.5.1.4 Caveats

Due to the simplicity of our toy model, there are other processes we have not considered that can alter the ICL stellar mass fraction. The first is that we only consider the possibility where compact cluster galaxies get completely destroyed into the ICL or completely merge with their BCGs. In a more realistic scenario, many compact cluster galaxies would be partially stripped into the ICL and partially merge with their BCGs. This partial stripping and partial merging can alter stellar mass fractions of the cluster and ICL. There is also the possibility that a small number of compact cluster galaxies survive between $z \sim 1$ and $z \sim 0$, thereby reducing the ICL stellar mass fraction. Low redshift analogs of

these compact cluster galaxies have been found in other works, suggesting that some do survive (e.g. Jiang et al. 2012). It is also likely that some of the most massive quiescent cluster galaxies at $z \sim 1$ contribute stars to the ICL via tidal stripping of their outer regions as well (DeMaio et al., 2018). This is an additional process that was not considered in our toy model which is capable of altering the ICL and total cluster stellar mass fractions. Our toy model is only applicable to cluster galaxies beyond the GCLASS mass completeness limits. Realistically, low mass galaxies below the mass completeness limits would also contribute stellar mass to the BCG/ICL components, but this contribution is likely to be sub-dominant. This is because most of the stellar mass in the GCLASS clusters is contained within galaxies that have a stellar mass of $\log(\mathcal{M}_*/\mathcal{M}_\odot)\sim11$ (see Figure 2 in van der Burg et al. 2014).

We understand that realistically, BCGs will experience mergers with all types of galaxies - not just compact galaxies. We have therefore tested whether sampling from the entire cluster population rather than just the hatched region violates observational constraints of BCG stellar masses and the ICL stellar mass fraction at $z \sim 0$. This is done by re-running the toy model without confining the BCG/ICL selection area to the hatched region shown in Figure 2.11. We find that a smaller percentage (20%) of cluster galaxies are required to merge with their BCGs such that the BCGs grow their stellar mass by a factor of $\sim$2, leading to a larger ICL stellar mass fraction of 18% at $z \sim 0$. This ICL stellar mass fraction is still within the constraints found in low redshift studies (see Section 2.5.1.1). The reason the hatched region was chosen was because the purpose of the toy model is to test whether there is a stellar mass budget available to account for the most compact galaxies that would place a drag on any increases in the intercept of the mass–size relation.

2.5.1.5 Toy model conclusions

The results of our toy model show that it is possible to achieve plausible ICL stellar mass fractions, BCG masses and BCG sizes by accounting for compact cluster galaxies in this way. This can consequently allow for the intercept of the cluster mass–size relation to increase with decreasing redshift, as has been observed. Recent work on the build-up of the ICL in clusters has shown that at $z < 0.9$, the dominant route for ICL formation is the tidal stripping of galaxies with $\mathrm{Log}\,(\mathcal{M}_*/\mathrm{M}_\odot) > 10.0$. At least 75% of the ICL luminosity in massive clusters is consistent in colour with originating from galaxies with $\mathrm{Log}\,(\mathcal{M}_*/\mathrm{M}_\odot) > 10.4$ (DeMaio et al., 2018). It is therefore not surprising that we find the majority of compact galaxies – which are all mostly quiescent – in the GCLASS clusters with $\mathrm{Log}\,(\mathcal{M}_*/\mathrm{M}_\odot) > 10.0$ are required to contribute to the ICL to match low redshift observations of the stellar mass–size relation in our toy model. Cluster galaxies below these

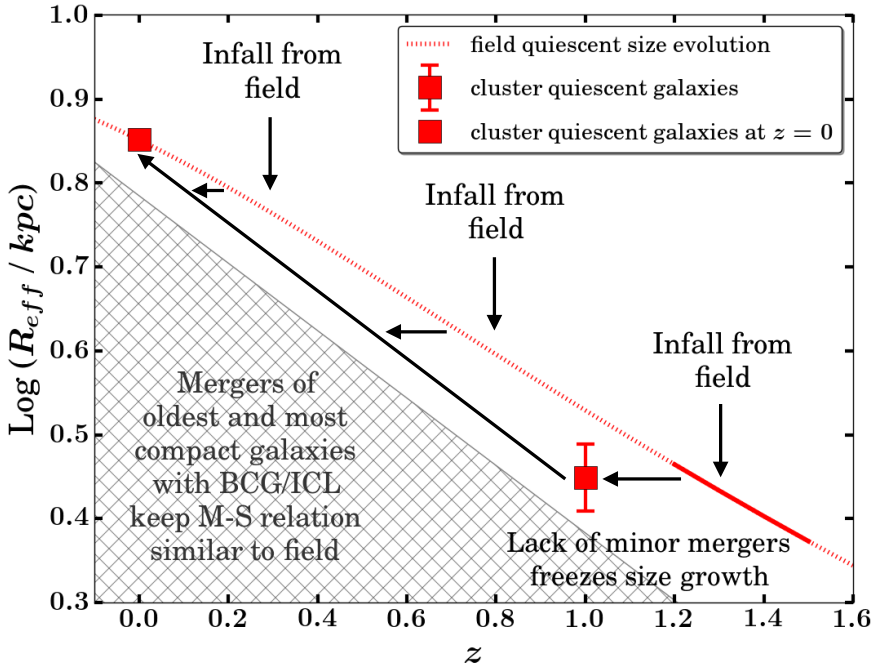

Figure 2.13: The physical processes occurring to reconcile the cluster quiescent stellar mass–size relation with the field quiescent stellar mass–size relation by $z \sim 0$. The field quiescent size evolution follows R_{eff} / kpc = $4.3\,h(z)^{-1.29}$ (see Section 2.3). This is the evolution in the intercept of the field quiescent mass–size relation. No evolution in the slope of the quiescent mass–size relation is seen in the field over these redshifts (see Figure 6 of van der Wel et al. 2014)

mass limits do not contribute as significantly to the BCG and ICL components, since most of the stellar mass in the GCLASS clusters is contained within galaxies that have a stellar mass of Log ($\mathcal{M}_*/\mathrm{M}_\odot$)$\sim$11 (see Figure 2 in van der Burg et al. 2014).

2.5.2 Final remarks

Figure 2.13 summarises the physical processes thought to be occurring to reconcile the cluster quiescent stellar mass–size relation with the field quiescent stellar mass–size relation by low redshifts based on results found in this study. The preferred parameterisation for the evolution in the intercept of the quiescent mass–size relation with redshift for the 3D-HST fields is shown as the dotted red line (see Section 2.3). The square point with the error bar shows the average size of a GCLASS quiescent cluster galaxy at $z \sim 1$. The current quiescent cluster galaxies we observe in the GCLASS clusters today likely fell into their clusters around $1.2 \leqslant z \leqslant 1.5$ (see Section 2.3). At this time, they had average sizes that sit somewhere on the solid red line. Once these galaxies entered the cluster environment, they had their size growth suppressed due to the lack of minor mergers (based on the minor-mergers hypothesis). However, between the time of infall and observation of these galaxies, their field counterparts continued to grow via minor mergers in the field. Consequently, when the size offset between field and cluster is measured at $z \sim 1$, quiescent cluster galaxies are

found to be smaller on average. At low redshifts however, negligible differences between cluster and field are seen. Between $z \sim 1$ and $z \sim 0$, most of the compact quiescent cluster galaxies are removed from the cluster sample via mergers with their BCGs or tidal destruction into the ICL. The sizes of these compact quiescent cluster galaxies would lie approximately in the hatched region shown in Figure 2.13, with some that are even smaller than Log (R_{eff}/kpc) = 0.3. The removal of these small galaxies, and the continual addition of larger galaxies from the field, leads to smaller and smaller average size offsets between cluster and field quiescent galaxies with decreasing redshift. Furthermore, the minor mergers between the compact quiescent cluster galaxies and their BCGs allows the BCGs to grow disproportionately more in size, such that their sizes follow the low-redshift field quiescent mass–size relation by $z \sim 0$. The combination of these physical processes lead to better agreement between the field and cluster quiescent stellar mass–size relations at low redshifts.

These results show that the observed increase in the intercept of the cluster mass–size relation can be explained by cluster-specific processes that we know to be occurring as a cluster evolves with time. Our results highlight the need for a careful comparison of the cluster mass–size relation over a broad redshift range, such that the physical mechanisms responsible for the evolution in the cluster mass–size relation can be directly observed, and therefore confirmed.

2.6 Conclusions

Using the cluster environment as a laboratory, we tested whether minor mergers can explain the majority of the size growth observed in quiescent field galaxies.

To do this, we performed a comparison study of the stellar mass–size relation at $z \sim 1$ between cluster and field environments using the largest spectroscopically-confirmed sample of cluster galaxies at this redshift to date.

In a bid to reduce systematics as much as possible, observations, data reduction and stellar mass measurements were made in an almost identical fashion to those for our field sample from 3D-HST. A custom built GALFIT wrapper was developed in order to control for systematics between size and structural measurements for the comparative samples. The entire size determination method was first tested on a subset of the field sample and compared to existing published results to verify its reliability. Our method of size determination was proven to be highly reliable, with a systematic offset of 0.28% (see Appendix B).

Our main conclusions are as follows:

1. Grism-derived redshifts for GCLASS have a precision of 2000 kms^{-1}, which is more than a

factor of 4 improvement over the photometric redshift precision. This allowed us to select a cluster membership sample from our grism data that was ∼90% pure. Overall, this increased our cluster membership sample by 51% of our spectroscopically confirmed sample with GMOS. This provided us with the largest sample of cluster galaxies at $z \sim 1$ for which stellar mass–size relation studies have been conducted.

2. Cluster galaxies are smaller than their field counterparts at fixed stellar mass. Average size offsets of (-0.08 ± 0.04) dex and (-0.07 ± 0.01) dex for quiescent and star-forming cluster galaxies are found respectively. The magnitude of these offsets are consistent with what is expected if minor mergers were the main drivers of galaxy size growth in the field.

3. There is a larger population of quiescent intermediate-type galaxies in the clusters compared to the field. These are likely to be galaxies undergoing environmental quenching – most likely via "starvation" – such that their disc fades relative to their bulge over time. This is subsequently thought to be responsible for the larger population of quiescent bulge-like galaxies in the clusters compared to the field, suggesting a direct morphological consequence of environmental quenching.

4. Using a toy model, we test whether the observed evolution in the intercept of the cluster mass–size relation with decreasing redshift can be explained by cluster-specific processes. We find that the small differences observed between the cluster and field stellar mass–size relations at low redshift can be achieved if ∼40% of the compact cluster galaxies in GCLASS merge with their BCGs and the remaining ∼60% become tidally disrupted into the ICL by $z \sim 0$. This leads to an ICL stellar mass fraction averaging ∼8% at $z \sim 0$ for the GCLASS clusters. These results are consistent with the expected stellar mass growth of BCGs between $0 \leqslant z \leqslant 1$ and the expected stellar mass fraction of the ICL at $z \sim 0$.

There's plenty of sense in nonsense sometimes, if you wish to look for it.

Cassandra Clare, Clockwork Angel

3

Size growth induced by recently quenched galaxies

The two leading explanations for the disproportionately large size growth at fixed stellar mass for quiescent galaxies are the minor mergers hypothesis of size growth and the addition of recently quenched galaxies to the quiescent population (see Section 1.2.1).

In Chapter 2, we used the cluster environment as a laboratory to test whether minor mergers can explain the majority of the size growth of quiescent galaxies in the *field* environment. Galaxies in high density environments such as clusters have higher peculiar velocities compared to galaxies residing in low density environments. Consequently, satellite galaxies in clusters rarely collide with one another and merge (Merritt, 1985; Delahaye et al., 2017). This merger suppression makes growth via minor mergers in clusters a rarity. By measuring the average difference in size between cluster and field galaxies at $z \sim 1$ in this chapter, it was found that cluster galaxies are on average smaller than field galaxies at fixed stellar mass. The magnitude of the size difference was found to be consistent with the size growth cluster galaxies would have undergone if they had remained in the field rather than accreted on to their clusters at the time most of the mass in their clusters was assembled. This result suggested that minor mergers could indeed be responsible for the dramatic size growth observed in the quiescent field population of galaxies. However, what is now required is evidence for whether or not recently

quenched galaxies contribute to this observed size growth.

As a direct consequence of progenitor bias (quiescent galaxies at high redshift represent a subset of the quiescent population at low redshift, since this high redshift sample does not take into account star-forming galaxies – which on average have larger sizes than quiescent galaxies at fixed stellar mass and redshift – that will become quiescent by low redshifts), galaxies that quench in later epochs are larger than galaxies that quenched at higher redshifts. When these younger galaxies quench, they join the quiescent population of galaxies at the large size end of the distribution. The addition of recently quenched galaxies to the quiescent population (van der Wel et al., 2009; Carollo et al., 2013) therefore predicts that age gradients as a function of size should exist for quiescent galaxies, where larger quiescent galaxies are younger than smaller quiescent galaxies at fixed stellar mass. Several studies have found evidence both for (e.g. Fagioli et al. 2016; Williams et al. 2017) and against (e.g. Whitaker et al. 2012a; Keating et al. 2014; Yano et al. 2016) this age gradient existing.

In this chapter, we investigate whether recently quenched cluster galaxies – sometimes referred to as "poststarburst" (PSB) galaxies in the literature – can lead to an increase in the average size of quiescent cluster galaxies with decreasing redshift. We do this by comparing the position of 23 spectroscopically confirmed recently quenched cluster galaxies on the stellar mass–size relation to the position of the star-forming and quiescent cluster members. Our size measurements for the cluster sample come from *Hubble Space Telescope* (HST), *Wide Field Camera 3* (WFC3) F140W imaging of ten clusters at $z \sim 1$ drawn from the GCLASS survey. This sample represents the largest sample of spectroscopically confirmed cluster galaxies at $z \sim 1$ to-date and is the same data used to conduct the study presented in Chapter 2.

This chapter is organised as follows. In Section 3.1 we describe our data and the sample of recently quenched cluster galaxies. Section 3.2 discusses the F140W direct images of the recently quenched galaxies and what clues this provides for the quenching mechanism(s) responsible. The position of the recently quenched cluster galaxies on the stellar mass–size relation is presented and studied in Section 3.3. A more thorough analysis of their morphology with respect to other cluster members is then studied in Section 3.4. In Section 3.5, we investigate if the distinct properties of the recently quenched galaxies in GCLASS can aid in explaining their evolutionary path on the mass–size plane. We discuss the implications of our findings in Section 3.6 and summarise in Section 3.7.

3.1 Data

3.1.1 Cluster sample

The cluster sample used in this Chapter is the same cluster sample that was used in Chapter 2, details of which can be found in Section 2.1.1.1.

3.1.2 HST data

The HST observations used in this Chapter are the same observations used in Chapter 2, details of which can be found in Section 4.1.2.

The stellar mass–size relation study presented in Chapter 2 allowed for the structural analysis of the GCLASS cluster galaxies for the first time: and with it, the PSBs – the results of which we will present in this Chapter.

3.1.3 PSB sample

The PSBs form part of the sample of cluster galaxies that were spectroscopically confirmed as part of the GCLASS survey (see Section 3.1.1). As part of a study into the effects of environment and stellar mass on galaxy properties, the PSBs were identified as recently quenched star-forming galaxies based on features in their GMOS spectra. These were identified from 9 of the 10 clusters, since the rest-frame wavelength coverage of the spectra for the 10th cluster were limited to $\lambda_{\rm rest} < 4050$Å due to its high redshift. The spectra were taken with the R150 grating, giving a spectral resolution of $R = 450$. In the rest-frame, this corresponds to a spectral resolution of $\sim$ 8Å, and is sufficient for identifying absorption lines. The wavelength coverage of the spectra are $6300 < \lambda/\text{Å} < 9200$, corresponding to $3000 \lesssim \lambda/\text{Å} \lesssim 4500$ in the rest-frame. For full details on the GMOS spectra, we refer the reader to Muzzin et al. (2012).

The criteria for the poststarburst classification was chosen to select galaxies similar to K+A galaxies which are identified from rest-frame optical spectra in the literature (Dressler et al., 1999; Poggianti et al., 1999; Balogh et al., 1999; Poggianti et al., 2009; Yan et al., 2009). Despite there being no strict definition for these galaxies, they are usually defined by their spectral properties, as having an absence of emission lines, but strong Balmer line absorption (EW(Hδ)$\geqslant$ 5Å). The Hδ absorption feature that is required in the K+A classification has weak equivalent widths of $2 - 7$Å. The signal-to-noise ratio of most galaxies in GCLASS at $z \sim 1$ make it difficult to detect reliably. This line is also further weakened by the contamination of many sky lines. Consequently for GCLASS, $D(4000)$ was used

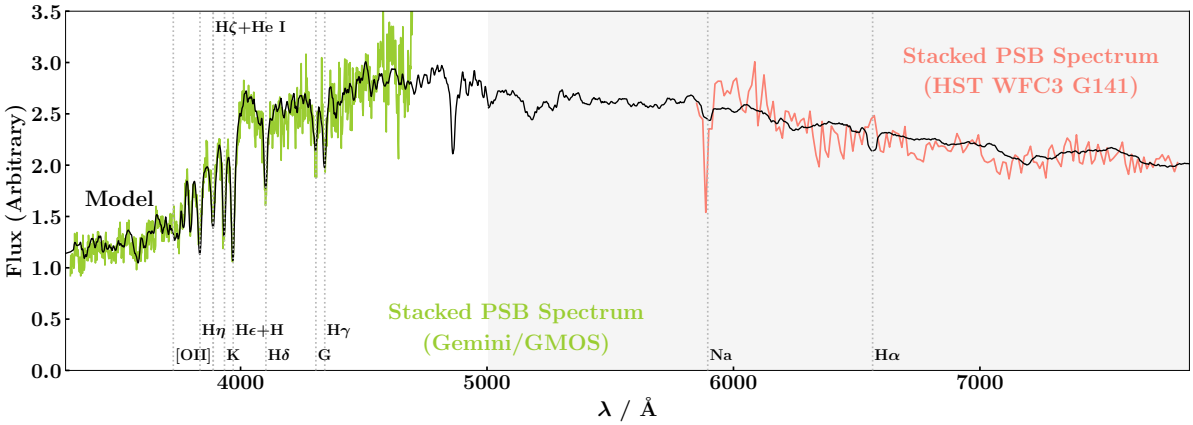

Figure 3.1: Normalised mean stacked spectra for the GCLASS PSBs from Gemini/GMOS in the optical (shown in green) and from the HST WFC3 G141 grism in the infrared (shown in red). Stacked spectrum in the optical is calculated from 28 PSBs. Stacked spectrum in the infrared is calculated from 13 PSBs (13 of the 23 in the HST fields-of-view had good quality grism spectra). Overlaid black spectrum shows the best-fit Bruzual & Charlot (2003) spectrum (Muzzin et al., 2014). This model has been smoothed with a uniform filter such that it has the approximate resolution of GMOS ($R = 450$) up to $\sim$5000Å, after which it has the approximate resolution of the G141 grism ($R = 130$). The part of the plot in which the model has been smoothed to the resolution of the G141 grism has been shaded with a light grey background. Prominent emission/absorption lines have been labeled with dotted grey vertical lines. [OII] is *not* detected, but its position is labeled for reference.

since it is correlated with EW(Hδ) (Balogh et al., 1999). $D(4000)$ is defined as the strength of the 4000Å break in spectra. For the GMOS PSB spectra, it is measured by taking the ratio of the flux in the red continuum at $4000 - 4100$Å to that in the blue continuum at $3850 - 3950$Å (Balogh et al., 1999; Muzzin et al., 2012). The GCLASS PSBs were therefore defined as those galaxies with an absence of [OII] emission and $1.0 < D(4000) < 1.45$ in their GMOS spectra. A stacked spectrum of the cluster galaxies that met this criteria revealed a spectrum very similar to that of a K+A galaxy, suggesting that the average galaxy selected by this criteria is a K+A galaxy. For more details on the PSB classification process, we refer the reader to Muzzin et al. (2012).

The stacked spectrum from GMOS, along with the stacked spectrum obtained from the G141 grism for the PSBs is shown in Figure 3.1. The grism spectra were taken with the WFC3 G141 grism on-board the HST. These spectra have a resolution of $R = 130$ and a wavelength coverage of $10750 < \lambda/\text{Å} < 17000$. This corresponds to a rest-frame coverage of $5300 \lesssim \lambda/\text{Å} \lesssim 8500$. Raw grism spectra are two-dimensional, providing a spatially-resolved spectrum of each object in the field-of-view (see Figure 2.1 of Chapter 2 for example). One-dimensional spectra can be obtained from these and stacked. 13 of the 23 PSBs presented in this chapter had grism spectra with good enough quality (no contamination from neighbouring objects and more than half the grism spectrum available) such that they could be stacked. 28 PSBs were used for the stacked spectrum in the optical, of which 5 are not in the HST fields-of-view and therefore not part of the study presented in this chapter. It is clear from Figure 3.1 that the optical spectra (shown in green) follow

the model (shown in black) well. Despite the much lower signal-to-noise ratio of the grism spectra (shown in red), they remain consistent with the optical template. There is also evidence for very weak Hα emission. Nevertheless, the weak – and in most cases absent – Hα emission for most of the PSBs confirms that these galaxies have strongly suppressed star formation.

Since the classification of the GCLASS PSBs was made using a spectroscopic criteria that was designed to apply to $z \sim 0$ galaxies (Dressler & Gunn, 1983), a clarification is required as to what galaxies this selection criteria leads to at $z \sim 1$, the redshift of GCLASS. In general, galaxies in the nearby universe have much lower star formation rates (SFRs) than those at higher redshifts. To explain a PSB spectrum at low redshifts, the galaxy in question must have experienced a starburst before it quenched. i.e, it must have had high levels of star formation, which are uncommon for $z = 0$ star-forming galaxies. A galaxy undergoing a starburst usually lies systematically above the star-forming main sequence at fixed redshift, with SFRs $\gtrsim 4$ at $z = 0$ for example (e.g. Noeske et al. 2007; Rodighiero et al. 2011; Elbaz et al. 2018). Towards higher redshifts, the intercept of the star-forming main sequence (SFR–stellar mass relation for star-forming galaxies) increases (Noeske et al., 2007; Whitaker et al., 2012b). Therefore, a galaxy that is considered a starburst galaxy at $z = 0$ will be considered a *normal* star-forming galaxy at higher redshifts. The GCLASS PSBs reside at $z \sim 1$, where SFRs were ~ 6 times higher* than at $z \sim 0$ (Whitaker et al., 2012b, 2014). Employing the term "poststarburst" is somewhat misleading in connection with this sample of galaxies because these are normal star-forming galaxies at $z \sim 1$ that have had their regular levels of star formation suddenly terminated, rather than true PSB galaxies akin to those found locally. There is no requirement to invoke a starburst as the explanation for their spectral properties. At this redshift, they can therefore be considered as "post star-forming" galaxies. Despite the term "poststarburst" being misleading for this sample of galaxies, we choose to continue using it to maintain consistency with previous analyses on this sample (Muzzin et al., 2012, 2014) and with the K+A notation used throughout the literature.

3.2 Direct imaging of the PSBs

In Figure 3.2 we show the F140W direct images of the PSBs in square cutouts. The dimensions of each cutout in kiloparsecs is shown in the top right-hand corner of each cutout. The spectroscopic redshift of each galaxy is shown in the bottom left-hand corner of each cutout. The images are ordered by increasing stellar mass. Cutouts with solid line (dashed line) borders are those PSBs with reliable (low-

*At a fixed stellar mass of $\mathrm{Log}(\mathcal{M}_*/\mathrm{M}_\odot) \sim 10$.

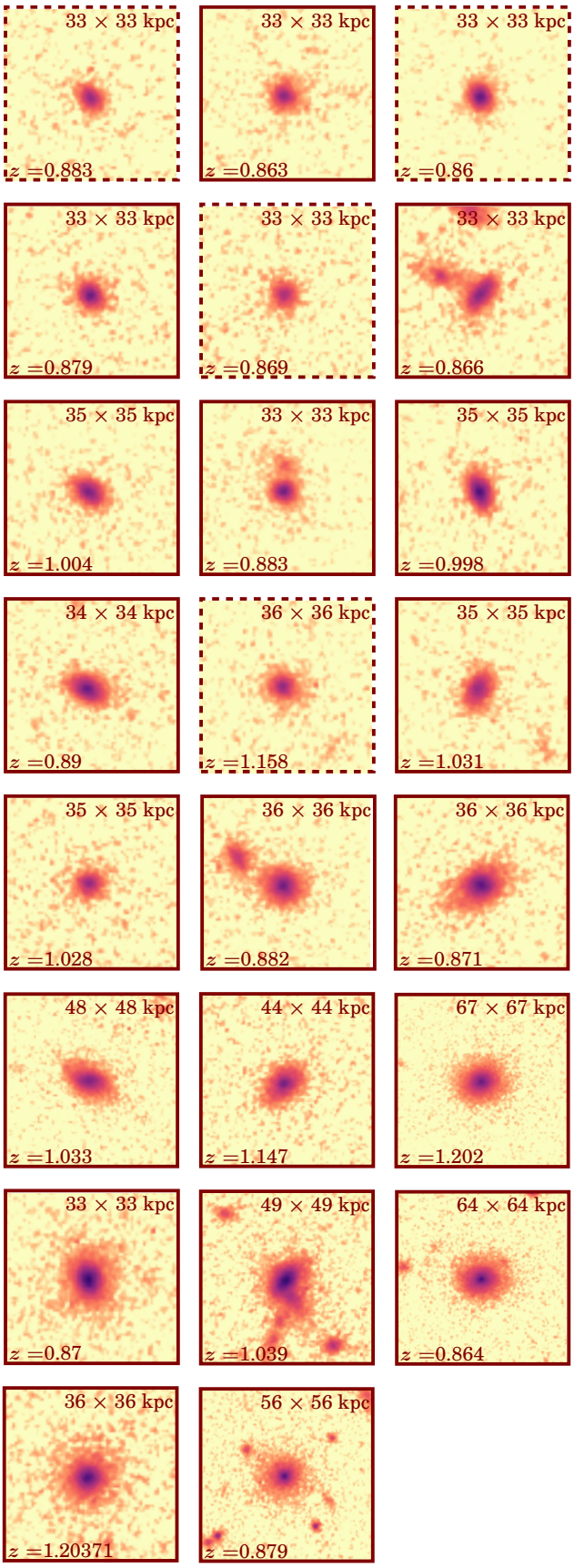

Figure 3.2: HST WFC3 F140W cutouts of the GCLASS PSBs in order of increasing stellar mass. PSBs with reliable (low-confidence) spectroscopic redshifts are shown with solid (dashed) line borders. The dimensions of each cutout in kiloparsecs and the spectroscopic redshift of each PSB is shown in the top right- and bottom left-hand corners of each cutout respectively. The colourmap is logarithmic.

confidence) spectroscopic redshifts.

The majority of the PSBs show no signs of disturbances or interactions and are symmetric in shape. This is somewhat puzzling, since the abrupt end in these galaxies' star formation suggests that a severe violent process (e.g. a merger or a high-speed close-proximity flyby, both of which would likely leave tidal signatures or some sort of asymmetry) would likely be responsible. The fact that most of the PSBs are symmetric and undisturbed effectively rules out violent quenching mechanisms that are capable of altering the stellar distribution of galaxies. These include harassment, mergers and tidal-stripping.

These quenching mechanisms were already ruled out in more detailed previous work done on the PSBs. A detailed study using the large sample of spectroscopically confirmed cluster galaxies in GCLASS unveiled that the PSBs reside in a distinct location of clustercentric velocity versus position phase space (Muzzin et al., 2014). Using several zoom-in dark-matter-only simulations, the coherent "ring" traced by the PSBs in this phase space could be reproduced by quenching galaxies rapidly (within $0.1 - 0.5$ Gyr) after they made their first passage of $R \sim 0.5R_{200}$. Similarly in this work, it was found that the GMOS spectra of the PSBs could only be fit well with high resolution Bruzual & Charlot (2003) stellar population models if a rapid quenching timescale of $0.4^{+0.3}_{-0.4}$ Gyr is assumed. The rapidity of the quenching, suggested *both* by the phase space analysis and the Spectral Energy Distribution (SED) fitting of the PSBs, ruled out quenching mechanisms that operate on long timescales such as mergers, harassment and tidal-stripping. The short quenching timescale is consistent with gas stripping processes such as ram-pressure stripping (Gunn & Gott, 1972). It is also consistent with strangulation (Larson et al., 1980), since typical gas fractions at $z \sim 1$ (Carilli & Walter, 2013) along with specific star formation rate (sSFR) measurements made for GCLASS (Muzzin et al., 2012) imply the PSBs would consume their cold gas supply in ~ 0.5 Gyr (Muzzin et al., 2014).

Some of the PSBs however do show evidence of processes involving the possible stripping of stars or mergers. The most striking example is the second PSB on the penultimate row, which seems to have a tail of stripped stars as well as asymmetry in the overall galaxy. The last PSB on the second row shows evidence of a bridge between itself and a close companion. A close companion is also seen near the second PSB on the fifth row, which may be tidally interacting with the PSB. Whilst some of the PSBs have clear neighbouring galaxies, none have identifiable tidal features. Additionally, it is reasonable to expect close companions in projection when observing high density environments such as clusters. Furthermore, the PSBs quenched ~ 0.5 Gyr prior to observation (Muzzin et al., 2014). If a merger, harassment or tidal interaction was responsible for triggering the PSB phase, 0.5 Gyr is not

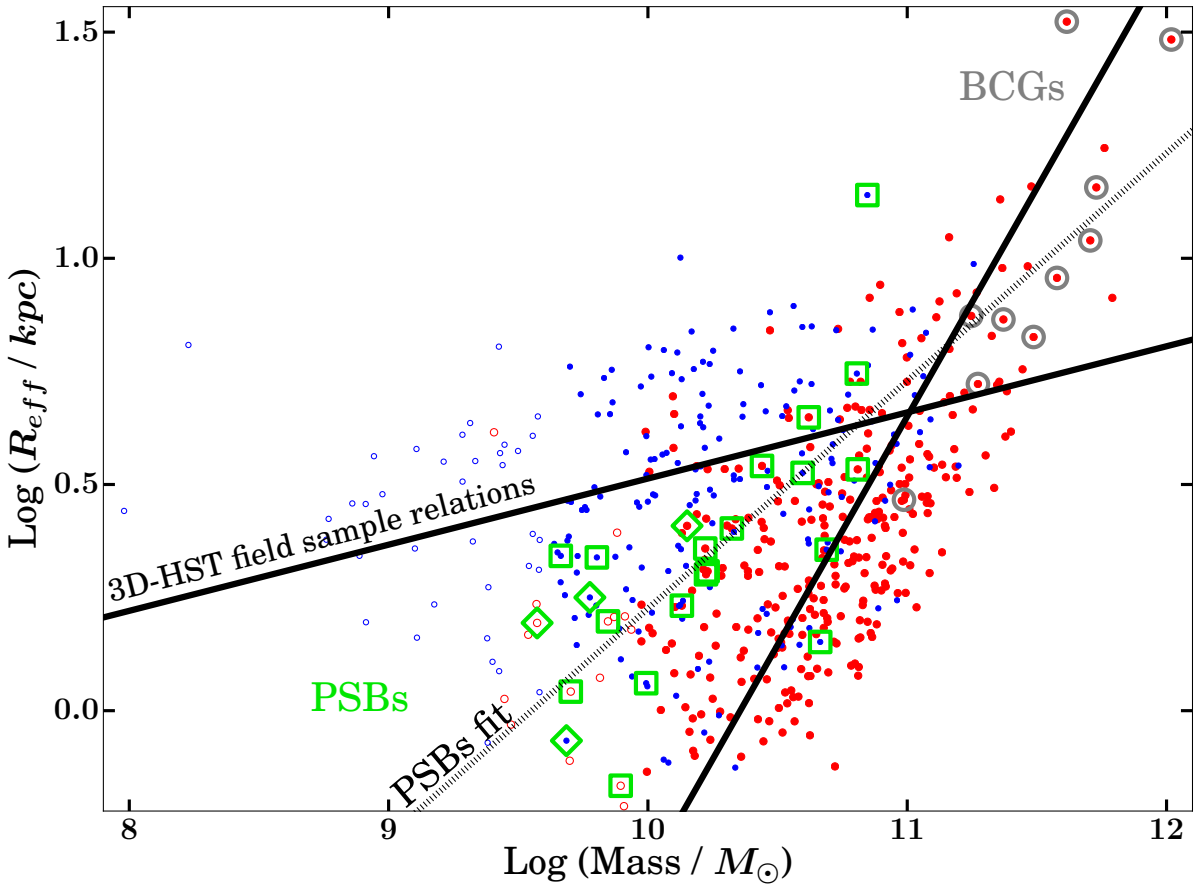

Figure 3.3: Stellar mass–size relation for the GCLASS clusters. Blue (red) filled circles show star-forming (quiescent) galaxies within the mass completeness limits. R_{eff} is the half-light radius in kpc. Brightest Cluster Galaxies (BCGs) are circled in grey. Poststarburst (PSBs) galaxies with reliable spectroscopic redshifts are marked with green squares. PSBs with low-confidence spectroscopic redshifts are marked with green diamonds. Solid black lines show the field relations at $z \sim 1$ calculated using results from van der Wel et al. (2012, 2014). Open blue (red) circles show measurements for star-forming (quiescent) galaxies beyond the mass completeness limits.

enough time for the stars to settle into a symmetric, undisturbed disc. Therefore, it seems unlikely that mergers or tidal stripping are the dominant processes responsible for the emergence of the GCLASS PSBs.

3.3 PSBs on the cluster stellar mass–size relation

Figure 3.3 shows the cluster stellar mass–size relation for all 10 of the GCLASS clusters with the PSBs highlighted in green. The PSBs that are highlighted with green squares have reliable spectroscopic redshifts, and were therefore included in the cluster mass–size relation study for GCLASS in Chapter 2. The PSBs highlighted by green diamonds have low-confidence spectroscopic redshifts which resulted in them being excluded from the analysis in Chapter 2. Nevertheless, we include them on this plot for reference, since they have properties consistent with the PSBs that have higher quality spectra. Open blue (red) circles indicate star-forming (quiescent) cluster galaxies below the mass

completeness limits of GCLASS. The mass completeness limits of GCLASS are $\log(\mathcal{M}_*/\mathrm{M}_\odot) = 9.96$ and $\log(\mathcal{M}_*/\mathrm{M}_\odot) = 9.60$ for quiescent and star-forming cluster galaxies respectively. For details on how these were calculated, we refer the reader to Chapter 2, Section 2.1.4.1. Galaxies were classified as star-forming or quiescent based on their rest-frame *UVJ* colours (see Chapter 2, Section 2.1.4.3). The solid black lines show the field relations at $z \sim 1$ calculated using stellar mass and size measurements from 3D-HST (see Chapter 2, Section 2.3 for a detailed explanation on how these were calculated).

It can be clearly seen that the PSBs do not follow the same stellar mass–size relation as the star-forming or quiescent galaxies. They seem to lie in a distinct region, halfway between the star-forming and quiescent mass–size relations. We would like to emphasise that the PSBs were selected based solely on their spectroscopic properties and not on any visual property such as morphology. The PSB sample of galaxies in GCLASS were defined in Muzzin et al. (2012, 2014), well before the HST imaging (Section 3.1.2) was obtained. Now, after measuring their stellar masses and sizes, we have found they also lie on a distinct mass–size relation, indicative of galaxies transitioning from star-forming to quiescent-like structural properties. We therefore choose to fit a relation to the PSBs, shown as the black dotted line. This is a least-squares fit to the PSBs with reliable spectroscopic redshifts.

It is clear that the PSBs do not follow the mean mass–size relation of star-forming galaxies for their redshift. This is remarkable, because they have only *recently* quenched. These galaxies must have been on the star-forming mass–size relation a few hundred million years prior to $z \sim 1$. Since the PSBs have only recently quenched, it is not expected that they would have had enough time to alter their structural properties significantly from those of typical star-forming galaxies. Previous work on the PSBs has shown that they likely began quenching ~ 0.5 Gyr prior to observation (Muzzin et al., 2014). This was determined by fitting the GMOS spectra of the PSBs with high resolution Bruzual & Charlot (2003) stellar population models with solar metallicity, a Calzetti et al. (2000) dust law and a Chabrier (2003) Initial Mass Function (IMF) (please see Section 5 of Muzzin et al. 2014 for more details). Most of the PSBs have symmetric, undisturbed morphologies in the stellar continuum (see Section 3.2). They also have transitional stellar mass–size properties between those reminiscent of star-forming and quiescent galaxies. Together, these results seem to suggest that the quenching mechanism responsible affects solely the gas content of galaxies, and not the stars. However, it is somehow capable of altering the light profile of a galaxy in a very specific way.

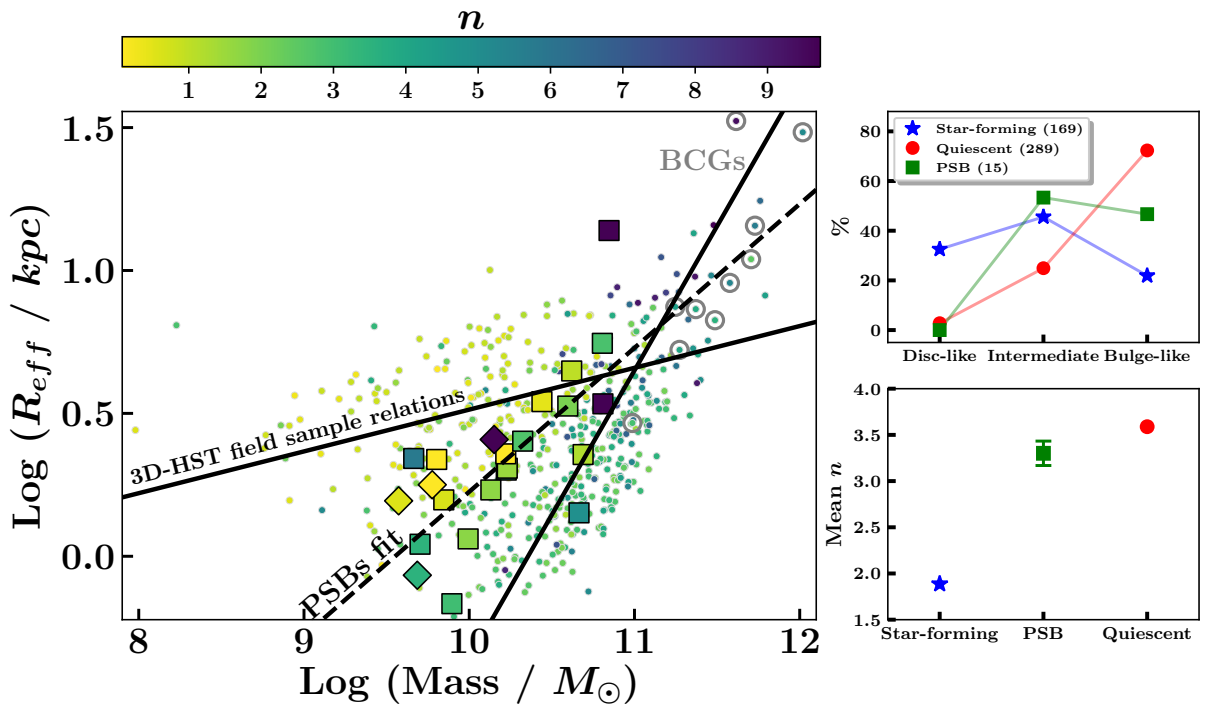

Figure 3.4: Main panel: GCLASS stellar mass–size relation with points colour-coded by Sérsic index. PSBs with reliable spectroscopic redshifts are shown as large squares. PSBs with low-confidence spectroscopic redshifts are shown as large diamonds. All other cluster galaxies are shown as small circular points in the background. Lines are the same as in Figure 3.3 and the BCGs are circled in grey. Top right panel: The percentage of each morphological type – disc-like ($n \leqslant 1$), intermediate ($1 < n < 2.5$) and bulge-like ($n \geqslant 2.5$) – within the quiescent, star-forming and PSB classifications. These calculations only take into account galaxies within the mass completeness limits, of which the sample sizes are stated in the legend within brackets. Bottom right panel: The average Sérsic index of the star-forming, PSB and quiescent populations for galaxies within the mass completeness limits. Error bars show the standard error in the mean.

3.4 Morphology of the PSBs

Figure 3.4 shows the cluster stellar mass–size relation in the largest panel, but now with the points colour-coded by their Sérsic index, n. In general, lower Sérsic indices are a proxy for more disc-like morphologies and vice versa. PSBs with reliable (low-confidence) spectroscopic redshifts are shown as large squares (diamonds). The smaller circular points in the background show the rest of the cluster galaxies. BCGs are circled in grey. The lines are the same as in Figure 3.3. The top right panel shows the percentage of each morphological type – disc-like ($n \leqslant 1$), intermediate ($1 < n < 2.5$) and bulge-like ($n \geqslant 2.5$) – within the star-forming, quiescent and PSB populations within the mass completeness limits. The quiescent mass completeness limit is used for the PSBs. The bottom right panel shows the mean Sérsic index for each of the three populations within the mass completeness limits. The errors bars show the standard error in the mean.

Since Sérsic index has been found to be well-correlated with quiescence (e.g. Franx et al. 2008; Bell et al. 2012), it is not surprising that we find the quiescent (star-forming) population with the highest

percentage of bulge-like (disc-like) galaxies. The smooth change in Sérsic index across the mass–size plane can also be seen in the main panel. Somewhat surpisingly, 22% of the star-forming cluster galaxies are bulge-like. Upon closer inspection, all the star-forming cluster galaxies that are bulge-like have $\log(\mathcal{M}_*/\mathrm{M}_\odot) > 9.80$ and are clustered close to the intersection point of the two mass–size relations. Also evident from the top right panel is that the PSBs have the highest percentage ($\sim 50\%$) of intermediate-type galaxies out of the three populations[†]. They also have a percentage of bulge-like galaxies that falls almost exactly between the percentages of bulge-like galaxies found for the star-forming and quiescent populations. Interestingly, they have the lowest percentage of disc-like galaxies among the three populations. Since the PSB population is dominated by intermediate-types and bulge-like galaxies, it is therefore not surprising that the PSBs have a mean Sérsic index that is closer to the mean Sérsic index of the quiescent population, yet still intermediary between the mean Sérsic indices of the star-forming and quiescent populations (bottom right-hand panel).

Since the PSBs have only recently quenched, we would have expected them to have a similar percentage of disc-like galaxies to the star-forming population and therefore a mean Sérsic index much closer to that of the star-forming population. Instead, these results suggest that the PSBs are galaxies which morphologically transformed both recently and rapidly.

The PSBs do not exhibit disturbed morphologies in the stellar continuum (see Section 3.2), but do have Sérsic indices more reminiscent of bulge-like morphologies. Since the PSBs are recently quenched galaxies, it is surprising how quickly their morphology has become bulge-dominated. One hypothesis is that before these galaxies quenched, they had both a disc and bulge component, but the disc is likely to have been brighter than the bulge. The rapid quenching could have caused a rapid fading of the disc, such that the bulge became relatively brighter than the disc. Quenching processes that are capable of causing a rapid fading of galactic discs without affecting the stellar distribution are processes which solely affect the gas content of galaxies. Candidate processes for this are ram-pressure stripping (Gunn & Gott, 1972) and strangulation/starvation (Larson et al., 1980). The gas – which is required for star formation – is more loosely bound in galactic discs. Therefore, these processes remove gas more efficiently from the discs of galaxies rather than their bulges (Abadi et al., 1999).

In the next Section, we investigate whether a simple disc-fading model of galaxy quenching can explain the formation of most of the GCLASS PSB population.

[†]Poisson errors for the PSB morphology fractions are large ($\sim \pm 20\%$). Therefore to maintain clarity, we have chosen not to show any errors in the top right panel of Figure 3.4, but have stated the sample sizes with which calculations are made in the legend.

3.5 Are PSBs faded discs?

As mentioned at the end of the previous section, the quenching processes that are likely to be responsible for the emergence of the PSBs can cause the fading of galactic discs. To build a better understanding of how disc-fading affects the structural properties of typical star-forming galaxies at $z \sim 1$, we will be presenting a variety of disc-fading toy models in this Section. For each model, we will track how typical star-forming galaxies move across the mass–size plane as their discs fade, and how their morphology (as dictated by the Sérsic index) changes.

The star-forming, PSB and quiescent cluster galaxies in GCLASS have very well defined stellar populations as dictated by their spectral properties (e.g. see Section 3.1.3 for a discussion on the spectral properties of the PSBs). Therefore, there are tight constraints on the allowed amount of disc-fading in each model, such that the final galaxy exhibits stellar populations reminiscent of the average PSB.

The aim of this Section is therefore twofold: we will be exploring whether disc-fading can simultaneously create a population of galaxies with similar stellar populations to the PSBs *and* similar structural properties to the PSBs, as dictated by their distinct mass–size relation.

3.5.1 Disc-fading toy model (bulge and disc)

The first model we explore is one in which galaxies are modelled as having both a bulge and disc component. In typical star-forming galaxies, galactic bulges tend to host the oldest stars in the galaxy. Therefore, in our model, we ensure that the bulge models have a brightness that reflects older stellar populations than the disc models.

Since the stellar populations of the GCLASS cluster galaxies are well defined (Section 3.5), there are strict constraints on the brightness of the bulge and disc components in this model. Similarly, there are tight constraints on how much the disc can fade such that the resulting galaxy has stellar populations reminiscent of the average PSB.

The first step in applying these constraints requires an understanding of how the brightness of a stellar population varies with age at fixed stellar mass. To do this, we determine the F140W stellar mass-to-light ratios as they would be observed at $z \sim 1$ for a set of stellar population models with solar metallicity using the Bruzual & Charlot (2003) libraries. A Chabrier (2003) initial mass function is used. We then see how these mass-to-light ratios vary with $D(4000)$, which is a good indicator for age (see Section 3.1.3). The Balogh et al. (1999) definition of $D(4000)$ is used, which is the ratio of the flux density at $4000 - 4100$Å to the flux density at $3850 - 3950$Å.

Table 3.1: Summary of parameters for model galaxies in the disc-fading toy model presented in Section 3.5.1. n is Sérsic index, b/a is axis ratio and P.A. is position angle.

Galaxy	Component	$D(4000)$	Combined $D(4000)$	Contribution to total brightness (%)	Magnitude	n	b/a	P.A. (degrees counter-clockwise)
Starting	Bulge	1.7	1.2	17	23.75	4	0.76	90
	Disc	1.09		83	22.00	1	0.62	90
Faded	Bulge	1.7	1.4	33	23.75	4	0.76	90
	Disc	1.25		67	22.75	1	0.62	90

3.5.1.1 Relative brightnesses of the bulge and disc

In the GCLASS spectroscopic sample (see Section 3.1.1), disc-dominated ($n \leqslant 1$) star-forming cluster galaxies have an average $D(4000) = 1.2$, the PSBs have an average $D(4000) = 1.4$ and bulge-dominated ($n \geqslant 2.5$) quiescent cluster galaxies have an average $D(4000) = 1.7$. In our disc-fading model, we require our starting galaxies to resemble star-forming disc-dominated galaxies and our faded galaxies to resemble the PSBs. Therefore, we use the average $D(4000)$ values for these two populations in GCLASS to determine the $D(4000)$ values of the disc components for the starting and disc-faded galaxies in our model. For simplicity, we create model galaxies *only* for the case where the stellar mass of the bulge equals the stellar mass of the disc. For the bulge components, we use $D(4000) = 1.7$, the average $D(4000)$ of bulge-dominated quiescent cluster galaxies in GCLASS. We then find the corresponding F140W mass-to-light ratio for $D(4000) = 1.7$ from the relation between $D(4000)$ and the F140W stellar mass-to-light ratios in our stellar population models. The $D(4000)$ value for the disc component that ensures the *overall* $D(4000) = 1.2$ for the starting galaxy is then found, which is 1.09. Similarly, the $D(4000)$ value for the disc component that ensures the overall $D(4000) = 1.4$ for the faded galaxy is found, which is 1.25. These are found by calculating the weighted mean (based on the relative brightness of the disc and bulge from their F140W mass-to-light ratios) of the $D(4000)$ values for the bulge and disc components in each case. These parameters are summarised in Table 3.1. For the starting galaxy models, the disc is 5 times brighter than the bulge. For the faded galaxy models, the disc is 2 times brighter than the bulge. Therefore, the disc is faded by a factor of ~ 2 in our disc-fading model.

3.5.1.2 Sérsic profiles of model galaxies

Model Sérsic profiles for the discs and bulges are created using GALFIT (Peng et al., 2002, 2010a). These have the same properties as the GCLASS F140W images (e.g. resolution and magnitude zeropoint). Since the PSBs began quenching ~ 0.4 Gyr ago (Muzzin et al., 2014), the input discs in the disc-fading toy model must follow the mass–size relation for disc-dominated star-forming

galaxies at this epoch, which corresponds to $z \sim 1.1$. We calculate this mass–size relation using a large sample of disc-dominated star-forming galaxies in the field at $z \sim 1.1$, taken from 3D-HST (van der Wel et al., 2012). These are calculated with the same method[‡] used to calculate the $z \sim 1$ field relations (Section 3.3). We assume that the PSBs will eventually evolve into quiescent galaxies that are similar to the quiescent bulge-dominated population in GCLASS. Quiescent bulge-dominated galaxies in 3D-HST at $z \sim 1$ have a mass–size relation that is consistent with the $z \sim 1$ field mass–size relation for the entire quiescent population (see for example Figure 2.9 in Chapter 2). Therefore, our bulge models have stellar masses and sizes that follow the $z \sim 1$ quiescent field mass–size relation. We create disc and bulge models spanning the stellar mass range of the GCLASS PSBs ($9.32 < \mathrm{Log}(\mathcal{M}_*/\mathrm{M}_\odot) < 11$).

We assign axis ratios to the disc and bulge models that are typical of star-forming and quiescent field galaxies at $z \sim 1$ (see Figure 4 of Hill et al. 2019). Disc and Bulge models are assigned Sérsic indices typical of disc-dominated star-forming and bulge-dominated quiescent galaxies, respectively (see Figure 2.9 in Chapter 2). All disc models have a Sérsic index $n = 1$ and an axis ratio $b/a = 0.62$[§]. All bulge models have $n = 4$ and $b/a = 0.76$[¶].

The magnitudes of all the discs are set to F140W magnitude= 22, which is the average magnitude of the star-forming disc-dominated cluster galaxies in GCLASS. The bulges are 5 times fainter than the discs for the starting galaxies (F140W magnitude= 23.75) and the discs are 2 times brighter (F140W magnitude= 22.75) than the bulges for the faded galaxies.

A summary of all the important parameters for the disc and bulge models is shown in Table 3.1.

Model galaxies are then created by adding the corresponding disc and bulge model Sérsic profiles. Examples of galaxy models for three stellar masses within the mass completeness limits of GCLASS (Section 3.3) are shown in Figure 3.5. Alongside the disc-faded galaxy models, we show select PSBs that have a similar stellar mass to the disc-faded model galaxies.

3.5.1.3 The stellar mass–size relation of faded discs

The Sérsic models have their sizes and Sérsic indices determined using the same two-GALFIT-run approach described in Chapter 2, Section 2.1.3.3. The same point-spread function (PSF) is used for all the models. This is just one of the pre-selected stars (see Chapter 2, Section 2.1.3.3) in the WFC3

[‡]Except that in this case there is one sample. We run the fitting method 1000 times on this sample to capture the range of possible intercept and gradient values. The average value for the intercept and gradient are used for the final relation.

[§]This is the axis ratio of *UVJ*-selected star-forming galaxies at $z \sim 1$ with $\mathcal{M}_* = 10^{11}\mathrm{M}_\odot$ in 3D-HST+CANDELS, interpolated from values calculated for $0.5 < z < 1.0$ and $1.0 < z < 1.5$ shown in Figure 4 of Hill et al. 2019.

[¶]This is the axis ratio of *UVJ*-selected quiescent galaxies at $z \sim 1$ with $\mathcal{M}_* = 10^{11}\mathrm{M}_\odot$ in 3D-HST+CANDELS, interpolated from values calculated for $0.5 < z < 1.0$ and $1.0 < z < 1.5$ shown in Figure 4 of Hill et al. 2019.

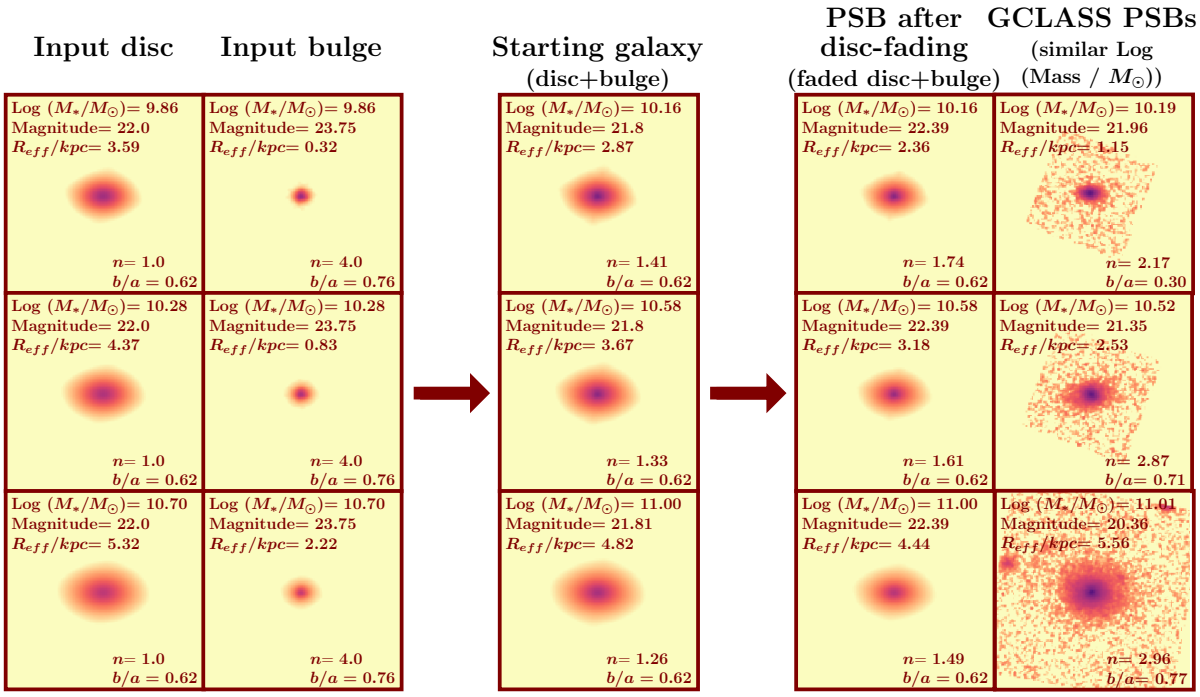

Figure 3.5: Examples of models created with GALFIT for the disc-fading toy model (Section 3.5.1). Model galaxies for three stellar masses (Log($\mathcal{M}_*/\mathrm{M}_\odot$) = 10.16, 10.58 and 11.00) are shown (third and fourth column). First and second columns show the disc and bulge models, respectively. The discs follow the $z \sim 1.1$ star-forming disc mass–size relation in the field. The bulges follow the $z \sim 1$ quiescent field mass–size relation (see Section 3.5.1.2). All disc models have Magnitude= 22.0, Sérsic index, n = 1.0 and axis ratio, b/a = 0.62. All bulge models have a magnitude that is 5 times fainter than the disc models (see Section 3.5.1.1). All bulge models are set to have n = 4.0 and b/a = 0.76. Bulge and disc models have the same stellar masses. The disc and bulge models are then combined to create starting galaxies shown in the third column. The disc model is then faded by a factor of 2 and combined with the input bulge model to create faded disc galaxies, shown in the penultimate column. Final column shows PSBs from GCLASS with similar stellar masses to the galaxy models. Parameters listed in all cutouts show the measured values from GALFIT. For the models, sizes are converted into kpc assuming the models are at z = 1. The dimensions of all cutouts are the same, as well as the position angle (measured counter-clockwise) of all models and the PSBs, set to 90 degrees. The colourmap is logarithmic.

F140W images of one of the GCLASS clusters. A noise map is not used since our models are noiseless (apart from the noise introduced by convolving the models with the PSF such that they match the resolution limit of WFC3) and no sky estimation is carried out since there is no sky background in our models.

The resulting median size measurements for multiple stellar mass bins (9.32 < Log($\mathcal{M}_*/\mathrm{M}_\odot$) < 11 for discs, 9.80 < Log($\mathcal{M}_*/\mathrm{M}_\odot$) < 11 for bulges and 9.62 < Log($\mathcal{M}_*/\mathrm{M}_\odot$) < 11 for galaxies) are shown as large points on the mass–size relation in the largest panel of Figure 3.6. The disc and bulge input model measurements are shown as small blue and large red circles respectively. The resolution limit of the F140W images is equivalent to 0.5 kiloparsecs at z = 1. Therefore, the sizes measured for the bulge models that fall below this threshold are unresolved and therefore unreliable. This regime of unresolved sizes is shown as the shaded grey region. The median size measurements of the starting star-forming galaxies are shown as open green squares. The median size measurements of the faded

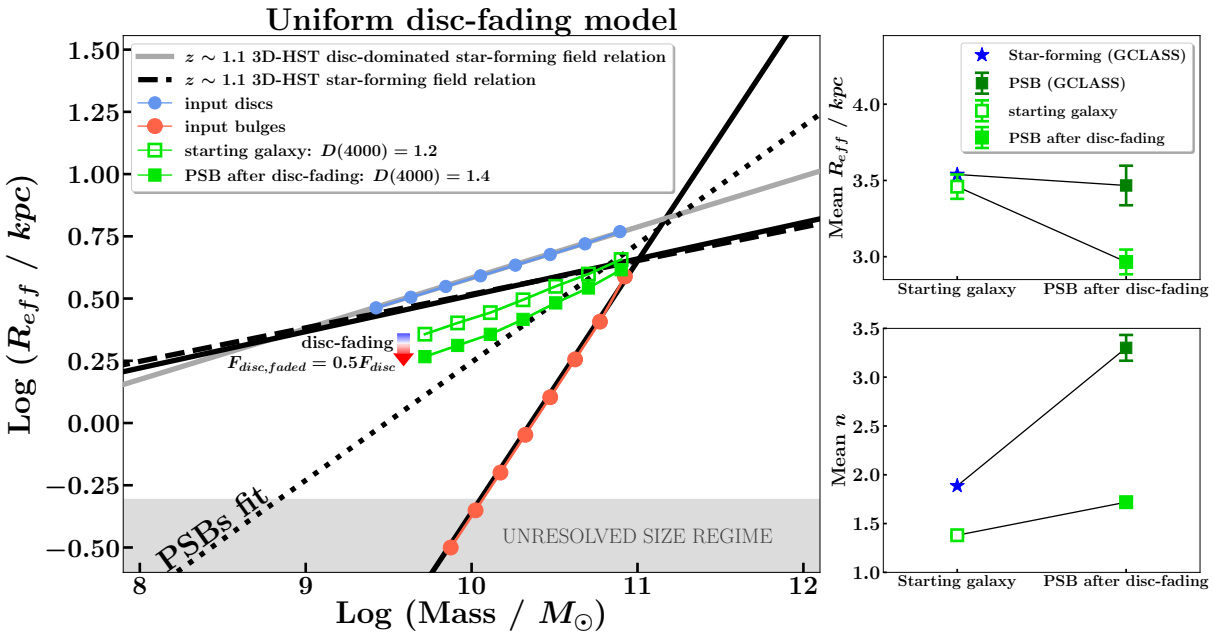

Figure 3.6: Disc-fading toy model. Main panel: median size measurements for 8 stellar mass bins of the disc (small blue circles) and bulge (large red circles) input Sérsic models that were created to follow the $z \sim 1.1$ disc-dominated star-forming field mass–size relation and the $z \sim 1$ quiescent field mass–size relation, respectively. For reference, we show the $z \sim 1.1$ star-forming field mass–size relation as the dashed black line. The $z \sim 1$ field mass–size relations are the solid black lines (the same solid black lines as in Figures 3.3 and 3.4). Bulges are five times fainter than the discs at fixed stellar mass (see text for reasoning). The starting galaxy is composed of the disc+bulge input models, median size measurements of which in seven stellar mass bins are shown as open green squares. Corresponding median size measurements of the disc-faded galaxies are shown as filled green squares. Since $\mathcal{M}_{*,bulge} = \mathcal{M}_{*,disc}$, the stellar masses of the starting and disc-faded galaxies are $2\mathcal{M}_{*,bulge}$ (or $2\mathcal{M}_{*,disc}$). The disc is faded by a factor of 2 (see text for reasoning). The region in which size measurements fall below the resolution limit of the GCLASS F140W images is shaded in grey. Top and bottom right panels: average half-light radius and Sérsic index values for the starting and disc-faded galaxy models along with the values for the GCLASS star-forming and PSB cluster galaxies within mass completeness limits (see text for more details). Error bars on GCLASS measurements are standard errors in the mean. Error bars on the model results are standard deviations from monte carlo sampling (see text for details).

disc galaxies are shown as filled green squares. The dashed black line shows the $z \sim 1.1$ star-forming field relation[‖], which is expected to approximately follow the mass–size relation of the starting galaxies. The solid grey line is the $z \sim 1.1$ mass–size relation for disc-dominated star-forming galaxies in the field (see Section 3.5.1.2). The solid black lines show the $z \sim 1$ field relations (which are the same solid black lines in Figures 3.3 and 3.4) for reference.

It is evident that disc-fading leads to a reduction in the overall size of a galaxy at fixed stellar mass. However, given the tight constraints on the allowed amount of fading from the measured $D(4000)$ values, the magnitude of this reduction is not enough to explain the stellar mass–size relation of the PSBs. The reason the starting galaxies do not lie on the $z \sim 1.1$ star-forming field mass–size relation is because their discs are not bright enough. If the discs were brighter than they currently are, the bulge components would become even more subdominant in brightness, leading to an increase in

[‖]This is calculated in exactly the same way as the $z \sim 1.1$ mass–size relation for disc-dominated star-forming galaxies in the field (Section 3.5.1.2 and the solid grey line in Figure 3.6), except all star-forming field galaxies at $z \sim 1.1$ are used.

the overall half-light radius of the starting galaxy model. Consequently, the position of the starting galaxy models on the mass–size plane would be in better agreement with the $z \sim 1.1$ star-forming field mass–size relation. There are two ways in which this can be improved. The first is to increase the disc stellar mass (and therefore by definition the size due to the mass–size relation) for each starting galaxy. However, a more disc-dominated starting galaxy will lead to a smaller size reduction as a result of disc-fading. The second option is to reduce the stellar age of the disc, thereby increasing its brightness. This would increase the difference in stellar age between the starting and faded galaxies, thereby increasing the size reduction due to disc-fading. However, reducing the average age of the stellar populations in the disc violates our $D(4000)$ constraints from the observations. Therefore, the results shown in Figure 3.6 show the optimal performance of our disc-fading model under our tight constraints. The magnitude of the size drop, shown by the length of the blue-to-red coloured arrow, is not able to bring the faded disc galaxies inline with the PSB mass–size relation. Quantitatively, at the median stellar mass of the PSBs that fall within the quiescent mass completeness limit ($\mathrm{Log}(\mathcal{M}_*/\mathrm{M}_\odot) = 10.44$), the half-light radius shrinks by 15% as a result of disc-fading.

In the top right-hand panel of Figure 3.6, we show the average sizes of the starting and faded galaxies within the GCLASS mass completeness limits, as well as the average sizes of the star-forming and PSB galaxies in GCLASS. For GCLASS, these averages are calculated by taking all the star-forming and PSB galaxies within the star-forming and quiescent mass completeness limits, and then calculating the mean size. For the models, the mean sizes are for model galaxies that have exactly the same stellar masses as the PSBs beyond the quiescent mass completeness limit. The errors on the model means are standard deviations in the mean size measurements from monte carlo sampling. We run the disc-fading model 10 times for model galaxies with exactly the same stellar masses as the GCLASS PSBs beyond the quiescent mass completeness limit. Each time, we add a 10% random uncertainty to the size, drawn from a normal distribution. We then calculate the mean size in each run and the standard deviation in the mean sizes calculated from the 10 runs are the error bars shown. For GCLASS measurements, the errors are standard errors in the mean.

It is clear from the top right-hand panel of Figure 3.6 that disc-fading does lead to a drop in the average size of a galaxy, which in this case, is a larger drop in average size than observed between the average sizes of the star-forming and PSB galaxies in GCLASS.

3.5.1.4 The average Sérsic index of faded discs

In the bottom right-hand panel of Figure 3.6, we compare the average Sérsic indices of our starting and disc-faded galaxies in the toy model to the average Sérsic indices of the GCLASS star-forming cluster members and PSBs. For GCLASS, these averages are calculated by taking all the star-forming and PSB galaxies within the star-forming and quiescent mass completeness limits, and then calculating the mean Sérsic index. For the models, the mean Sérsic indices are for model galaxies that have exactly the same stellar masses as the PSBs beyond the quiescent mass completeness limit. The errors are calculated from the same monte carlo sampling described in Section 3.5.1.3. For GCLASS measurements, the errors are standard errors in the mean.

It is expected that in the event of disc-fading, the bulge will become more prominent. This is also reflected in Table 3.1, where the bulge contributes to the total brightness of the galaxy by a larger amount in the disc-faded case. Since bulge-dominated galaxies have on average higher Sérsic indices than disc-dominated galaxies, it is not surprising that we see a rise in the average Sérsic index as a result of disc-fading in the toy model. However, the most striking aspect of these results is that the difference between the average Sérsic index of the faded disc galaxies and the starting galaxies is very small compared to the difference seen in the observations. The large difference in the average Sérsic index of the PSBs relative to the star-forming galaxies in GCLASS suggests that disc fading alone is not responsible for the structural properties of the PSBs. Another process is required that is capable of enhancing the brightness of the bulge.

3.5.2 Disc-fading toy model (outside-in fading)

3.5.2.1 Properties of the starting and faded galaxies

In Section 3.5.1, we presented a disc-fading model whereby the galaxy was modelled as having a bulge and disc component. The disc was uniformly faded such that the resulting disc plus bulge model resembled the stellar populations of the GCLASS PSBs. While this uniform fading of the disc did make galaxies smaller overall, the magnitude of this size reduction did not lead to galaxies that resembled the structural properties of the PSBs.

Observations of ram-pressure stripping at low redshift have shown that environmental quenching happens in an "outside-in" fashion (e.g. Koopmann & Kenney 2004; Abramson et al. 2011). Star formation in environmentally-quenched galaxies is truncated from the outside-in, such that over time, it is confined further and further towards the centre of the galaxy. This leads to truncated Hα

discs in cluster galaxies. Recently, more detailed observations of ram-pressure stripping have led to the quantification of quenching timescales and ages as a function of galactocentric radius (Fritz et al., 2014; Bellhouse et al., 2017; Gullieuszik et al., 2017; Jaffé et al., 2018; Vulcani et al., 2018; Fossati et al., 2018; Cramer et al., 2019). Since the outskirts of the disc is quenched first, there is a gradient in the stellar populations of a galaxy undergoing ram-pressure stripping, such that the outskirts hold older stellar populations than the central region. Therefore, the uniform fading of the disc in the disc-fading model presented in Section 3.5.1 is not a realistic representation of how disc-fading as a result of ram-pressure stripping operates.

In a bid to model disc-fading as a result of ram-pressure stripping more realistically, we present an alternative disc-fading model in this Section, where the disc is faded differentially, such that the outskirts are faded more than the central regions. As was the case in the previous model, the amount of fading is constrained by the $D(4000)$ measurements of the star-forming and PSB galaxies in GCLASS.

For this disc-fading model, we do not model the galaxy with bulge and disc components. We model the starting galaxies with a single disc component, since a typical star-forming galaxy is disc-dominated (see Figure 3.4 for example). The brightness of the starting galaxy models is dictated by the stellar populations of a typical disc-dominated ($n \leqslant 1$) star-forming cluster galaxy in GCLASS. At fixed stellar mass, the average disc-dominated star-forming cluster galaxy in GCLASS has $D(4000) = 1.2$. After disc-fading, our galaxy models must have a brightness similar to that of the average PSB in GCLASS. The average PSB has $D(4000) = 1.4$. As was done in the previous disc-fading model, we refer to our stellar populations models to find out the difference in brightness of a stellar population with $D(4000) = 1.2$ and $D(4000) = 1.4$ at fixed stellar mass in the F140W filter. As a reminder, we do this by determining the F140W stellar mass-to-light ratios as they would be observed at $z \sim 1$ for a set of stellar population models with solar metallicity using the Bruzual & Charlot (2003) libraries. A Chabrier (2003) initial mass function is used. We then see how these mass-to-light ratios vary with $D(4000)$, which is a good indicator for age (see Section 3.1.3). The Balogh et al. (1999) definition of $D(4000)$ is used, which is the ratio of the flux density at $4000 - 4100$Å to the flux density at $3850 - 3950$Å.

3.5.2.2 Outside-in fading

The difference in brightness between a stellar population with $D(4000) = 1.2$ and $D(4000) = 1.4$ tells us the approximate difference in brightness between a typical disc-dominated star-forming galaxy and PSB in GCLASS. In our outside-in fading model, this difference in brightness will correspond to how

Table 3.2: Summary of parameters for model galaxies in the outside-in disc-fading toy model. n is Sérsic index, b/a is axis ratio and P.A. is position angle. Dashes correspond to parameters that were not fixed to a single value, and left free in the GALFIT fitting process.

Galaxy	$D(4000)$	Magnitude	n	b/a	P.A. (degrees counter-clockwise)
Starting	1.2	22.00	1	0.62	90
Faded	1.4	-	-	-	-

much the central regions of our starting galaxy models will be faded by. It is particularly important that the central regions of the faded galaxies reflect the stellar populations of a typical PSB. This is because the spectra from which the PSB properties are measured depend mostly upon light from this region of the galaxy. The central regions of a galaxy are the brightest, and therefore contribute most to the measured spectrum. A stellar population of solar metallicity with $D(4000) = 1.4$ (typical PSB) is a factor 1.5 fainter than a stellar population of solar metallicity with $D(4000) = 1.2$ (typical disc-dominated star-forming cluster galaxy). Therefore, the central regions of the starting galaxy models will be faded by a factor of 1.5.

For a guide on the required levels of fading for the outskirts of the galaxy models, we use the results presented in Fossati et al. (2018) for NGC 4330. NGC 4330 is a galaxy in the Virgo cluster that is undergoing ram-pressure stripping. Using multiwavelength imaging, Fossati et al. (2018) were able to confirm "outside-in" quenching as well as quantify quenching times as a function of galactocentric radius for this galaxy. They find that "outside-in" quenching started at approximately 10 kpc from the centre of the galaxy, 625 Myr ago. We therefore find out the $D(4000)$ of a stellar population that is 625 Myr older than the stellar populations of the average PSB. We find this value to be $D(4000) = 1.55$. Next, we check what the difference in brightness is between this stellar population and that of a typical disc-dominated star-forming cluster galaxy ($D(4000) = 1.2$). We find that a stellar population of solar metallicity with $D(4000) = 1.55$ is a factor of 2 fainter than a stellar population of solar metallicity with $D(4000) = 1.2$. Therefore, the outskirts of the starting galaxy models will be faded by a factor of 2 in our outside-in disc-fading toy model.

3.5.2.3 Sérsic profiles of the model galaxies

Starting galaxies are modelled as single component Sérsic profiles using GALFIT, with structural parameters fixed to those values stated in Table 3.2. The F140W magnitude for the starting galaxy models is set to the average magnitude of disc-dominated star-forming cluster galaxies in GCLASS. $n = 1$ is the typical Sérsic index of a disc-dominated star-forming cluster galaxy (e.g. Figure 3.4) and

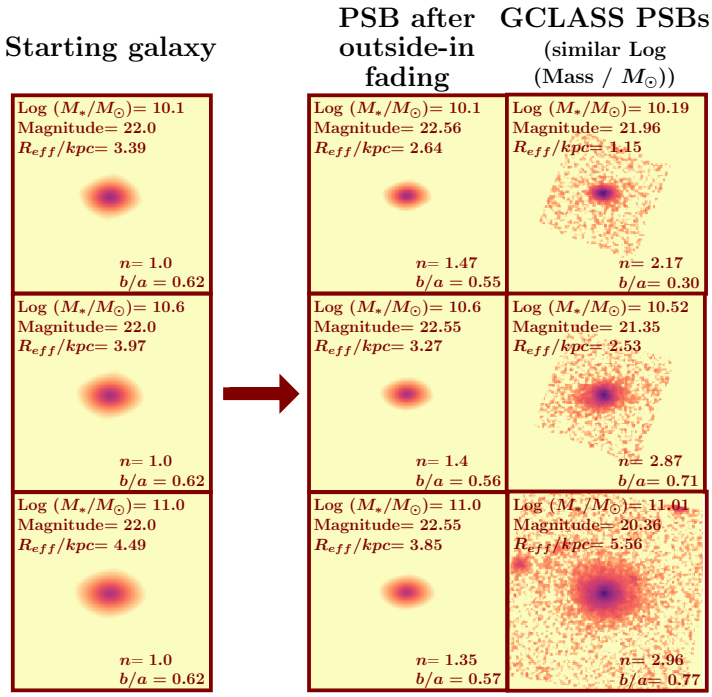

Figure 3.7: Examples of models created with GALFIT for the outside-in disc-fading toy model. Model galaxies for three stellar masses ($\mathrm{Log}(\mathcal{M}_*/\mathrm{M}_\odot) = 10.1, 10.6$ and 11.0) are shown (first and second column). The starting galaxy models follow the $z \sim 1.1$ star-forming mass–size relation in the field. All starting galaxy models have Magnitude= 22.0, Sérsic index, $n = 1.0$ and axis ratio, $b/a = 0.62$. The starting galaxy model is then faded from the outside-in to replicate the stellar populations of the GCLASS PSBs (see text for details). The resulting faded galaxy models are shown in the second column. Final column shows PSBs from GCLASS with similar stellar masses to the galaxy models. Parameters listed in all cutouts show the measured values from GALFIT. For the models, sizes are converted into kpc assuming the models are at $z = 1$. The dimensions of all cutouts are the same, as well as the position angle (measured counter-clockwise) of all models and the PSBs, set to 90 degrees. The colourmap is logarithmic.

the axis ratio is set to the typical axis ratio of a star-forming galaxy at $z \sim 1$ (Hill et al., 2019). The PSBs began quenching $\sim$ 0.4 Gyr ago (Muzzin et al., 2014) and were therefore star-forming galaxies $\sim$ 0.4 Gyr ago. $\sim$ 0.4 Gyr prior to $z \sim 1$ corresponds to $z \sim 1.1$. Therefore, the starting galaxy models have sizes as dictated by the $z \sim 1.1$ star-forming field mass–size relation. These models are then convolved with a PSF from the GCLASS F140W images. This is to account for the smearing of images due to the resolution limit of WFC3. This PSF is the same pre-selected star (see Chapter 2, Section 2.1.3.3) from the WFC3 F140W images of the GCLASS clusters used in the disc and bulge disc-fading toy model. A noise map is not used, since our models are noiseless (apart from the noise introduced by convolving with the PSF) and no sky estimation is carried out since there is no sky background in our models. The same two-GALFIT-run approach described in Chapter 2, Section 2.1.3.3 is used to determine the sizes and Sérsic indices of the starting galaxy models.

We also create starting galaxy models that are not convolved with the PSF. These are used to create the faded galaxy models. The benefit of the unconvolved starting galaxy models is that their pixel values are symmetric about the x and y axes running through the central pixel. This allows us to

implement an outside-in fading gradient evenly across the model. As mentioned in Section 3.5.2.2, we will be using NGC 4330 as a guide for how outside-in fading operates on a galaxy undergoing ram-pressure stripping. This galaxy has a stellar mass of $\mathrm{Log}(\mathcal{M}_*/\mathrm{M}_\odot) = 9.8$, and the onset of outside-in quenching begins at $\sim$ 10 kpc from the centre of the galaxy. We check what size NGC 4330 has as dictated by the low-redshift star-forming mass–size relation**. We find that NGC 4330 would have $R_{eff} = 3.2$ kpc in F140W if it followed the low redshift star-forming mass–size relation. Comparing this size to the size at which outside-in quenching begins for this galaxy (10 kpc), we can say that outside-in quenching begins at $\sim 3R_{eff}$ for NGC 4330. We use this radial boundary as the boundary at which outside-in fading begins for our model galaxies. Therefore at $3R_{eff}$ from the centre of each unconvolved galaxy model, the pixel values are divided by 2, and the central pixel of each model is divided by 1.5 (see Section 3.5.2.2 for reasoning). For all pixel values in between, linear interpolation is performed to find the relevant fading factors. The same interpolation grid is extended to beyond $3R_{eff}$ all the way to the edges of each model cutout, such that there is no discontinuity in the fading. These unconvolved faded galaxy models are then convolved with the PSF to create the final faded galaxy models. Again, no noise map is used and no sky background estimation is performed. The same two-GALFIT-run approach described in Chapter 2, Section 2.1.3.3 is used to determine the sizes and Sérsic indices of these faded galaxy models. Examples of galaxy models for three stellar masses within the mass completeness limits of GCLASS (Section 3.3) are shown in Figure 3.7. Alongside the faded galaxy models, we show select PSBs that have a similar stellar mass to the faded model galaxies.

3.5.2.4 The stellar mass–size relation of outside-in faded galaxies

In the largest panel of Figure 3.8, we show the resulting median size measurements for the starting and faded galaxy models for multiple stellar mass bins within the GCLASS star-forming mass completeness limit ($\mathrm{Log}(\mathcal{M}_*/\mathrm{M}_\odot) > 9.60$). We find that there is a fall in the size of a galaxy at fixed stellar mass due to outside-in fading. Whilst this fall in size is larger than that seen in the disc and bulge disc-fading model (20% at the median stellar mass of the PSBs compared to 15% in the disc and bulge disc-fading model), it is not enough to explain the stellar mass–size relation of the PSBs.

In the top right-hand panel of Figure 3.8, we show the average sizes of starting and faded galaxies

**This relation is calculated in the same way the $z \sim 1$ field relations were calculated in Chapter 2, Section 2.3, except we use all the star-forming galaxies in 3D-HST at $0 < z < 0.5$, under the fitting criteria. There is also only one sample, so the fitting method is run 1000 times on this sample to capture the range of possible intercept and gradient values. The average value for the intercept and gradient are used for the final relation.

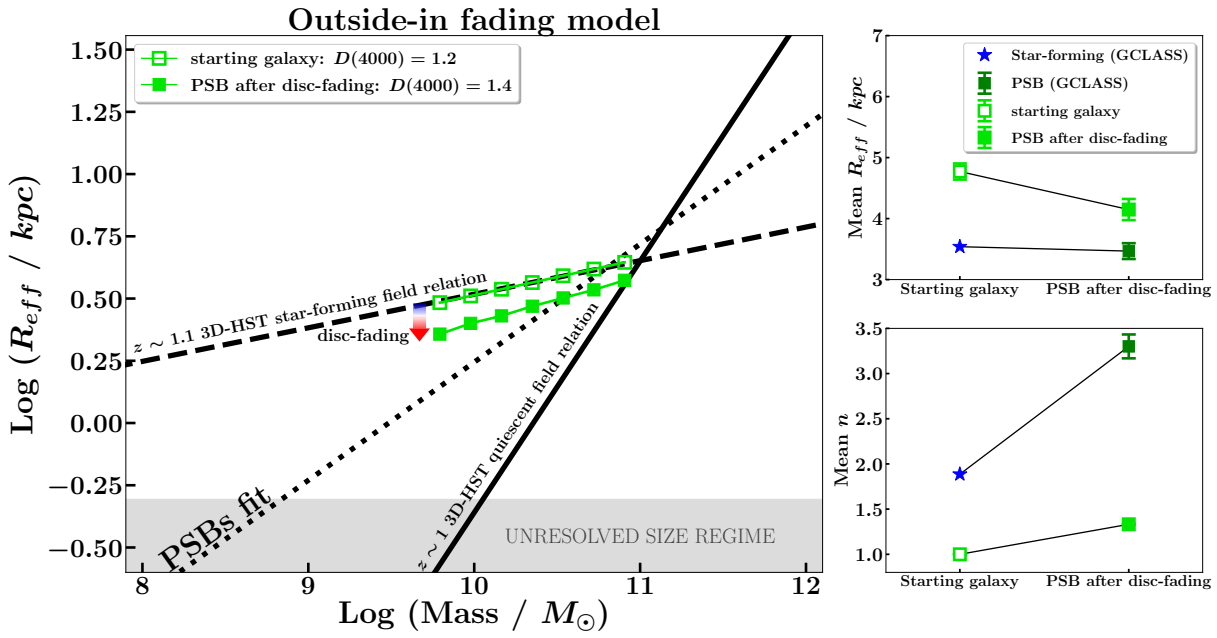

Figure 3.8: Outside-in disc-fading toy model. Main panel: median size measurements for seven stellar mass bins of the starting (open green squares) and faded (filled green squares) galaxy models. Starting galaxy models were created to follow the $z \sim 1.1$ star-forming field mass–size relation (see text for reasoning). Starting galaxy models are faded from the outside-in to replicate the stellar populations of the GCLASS PSBs (see text for details). The region in which size measurements fall below the resolution limit of the GCLASS F140W images is shaded in grey. Top and bottom right panels: average half-light radius and Sérsic index values for the starting and faded galaxy models along with the values for the GCLASS star-forming and PSB cluster galaxies within mass completeness limits (see text for more details). Error bars on GCLASS measurements are standard errors in the mean. Error bars on the model results are standard deviations from monte carlo sampling (see text for details).

which have identical stellar masses to the PSBs beyond the quiescent mass completeness limit[††]. We also show the average sizes of the star-forming and PSB galaxies in GCLASS within the star-forming and quiescent mass completeness limits, respectively, for comparison. It is evident that just as there is a drop in average size between the star-forming and PSB cluster galaxies, there is also a drop in average size as a result of outside-in fading in the models. The magnitude of this drop is much larger than that observed in the disc and bulge disc-fading model.

3.5.2.5 The average Sérsic index of outside-in faded galaxies

In the bottom right-hand panel of Figure 3.8, we compare the average Sérsic indices of the starting and faded galaxy models[‡‡] to the average Sérsic indices of the GCLASS star-forming cluster members and the PSBs[§§].

We can straight away see that outside-in fading has led to a more bulgier morphology on average for the faded galaxy models. However similar to the bulge + disc-fading model, the difference in the

[††]The errors on these measurements come from monte carlo sampling, which is described in Section 3.5.1.3.

[‡‡]These averages are calculated from model galaxies that have identical stellar masses to the GCLASS PSBs beyond the quiescent mass completeness limit.

[§§]within the star-forming and quiescent mass completeness limits, respectively.

average Sérsic index is much smaller than the difference observed in the observations.

3.5.3 Disc-fading toy model (bulge and outside-in faded disc)

In Section 3.5.2, we presented a more realistic model of disc-fading, based on recent observations of how ram-pressure stripping operates in low redshift cluster galaxies. However, we did not model our galaxies with a bulge and disc component, as was done in the uniform disc-fading model presented in Section 3.5.1. The natural question therefore arises, whether modelling a galaxy with a bulge and disc component, *and* fading the disc with the more realistic outside-in fading, can produce galaxies with structural and stellar population properties similar to the PSBs.

In this Section, we therefore present a disc-fading model that attempts to combine realistic modelling of a galaxy's structure and the fading process. The bulge and disc models are constructed in exactly the same way as those in the bulge and disc disc-fading model (Section 3.5.1). The difference between the model presented in this Section and the previous two models is how the fading is implemented. The allowed amount of fading in this model remains constrained by the $D(4000)$ measurements of the star-forming, PSB and quiescent cluster galaxies in GCLASS.

3.5.3.1 Outside-in disc fading in the bulge+disc case

As was highlighted in Section 3.5.1.1, there are strict boundaries set on how much the disc can be faded in a bulge+disc model. These boundaries are dictated by the spectroscopic properties of the cluster galaxies. In the case of uniform disc-fading, the disc was faded by a factor of 2 such that the resulting composite bulge+disc model would represent a galaxy that had similar stellar populations to the PSBs. In the model presented in this Section, we want to fade the disc "outside-in", yet still produce a galaxy with similar stellar populations to the PSBs. To do this, we need to ensure that the outside-in fading we implement on the disc components results in the same total brightness as when we fade the same discs uniformly by a factor of 2.

The outside-in fading is implemented using the same method described in Section 3.5.2.3 with a few modifications. For each model disc, we first check what the total brightness of the disc is when it is uniformly faded by a factor of 2. We do not fade the central pixel of the disc model. We check how much the disc model needs to be faded at $\sim 3R_{eff}$ (see Section 3.5.2.2 for reasoning) from the centre, such that the entire model has the same brightness as when it is uniformly faded by a factor of 2. We then adjust the slope of our linearly interpolated fading accordingly. Examples of galaxy models for three stellar masses within the mass completeness limits of GCLASS are shown in Figure 3.9.

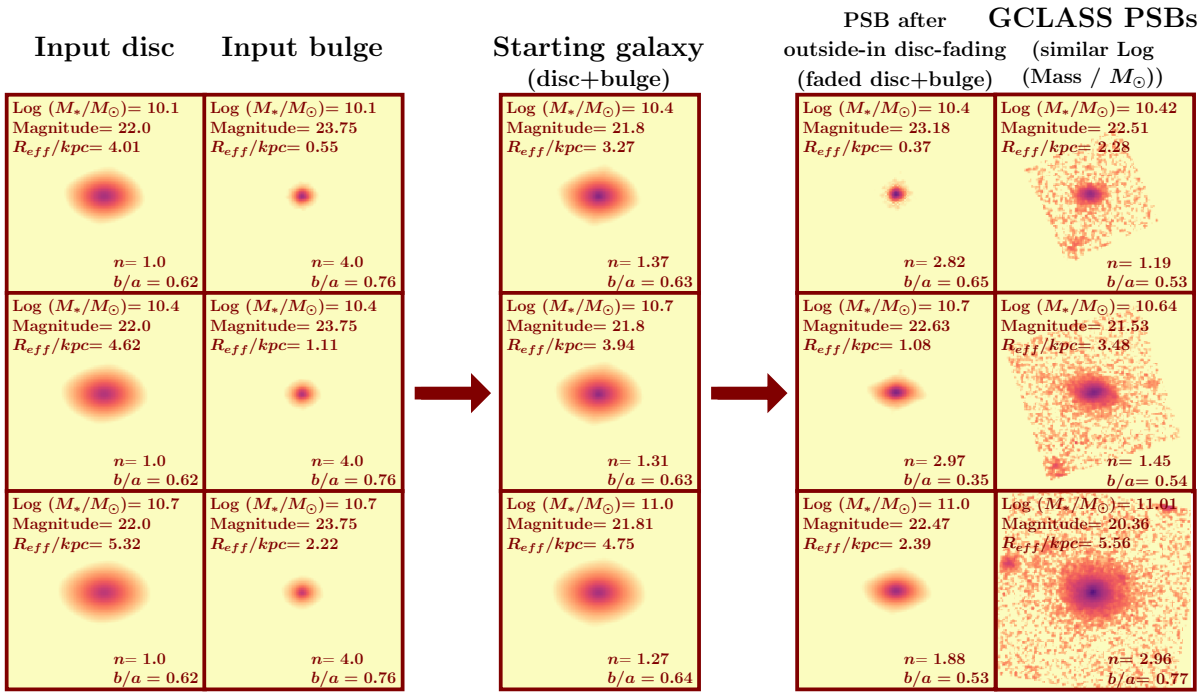

Figure 3.9: Examples of models created with GALFIT for the bulge + outside-in disc-fading toy model. Model galaxies for three stellar masses ($\mathrm{Log}(\mathcal{M}_*/\mathrm{M}_\odot) = 10.4, 10.7$ and 11.0) are shown (third and fourth column). First and second columns show the disc and bulge models, respectively. The discs follow the $z \sim 1.1$ star-forming disc mass–size relation in the field. The bulges follow the $z \sim 1$ quiescent field mass–size relation (see Section 3.5.1.2). All disc models have Magnitude= 22.0, Sérsic index, $n = 1.0$ and axis ratio, $b/a = 0.62$. All bulge models have a magnitude that is 5 times fainter than the disc models (see Section 3.5.1.1). All bulge models are set to have $n = 4.0$ and $b/a = 0.76$. Bulge and disc models have the same stellar masses. The disc and bulge models are then combined to create starting galaxies shown in the third column. The disc model is then faded from the outside-in, as per the details discussed in Section 3.5.3.1, and combined with the original bulge models. The resulting faded galaxies are shown in the penultimate column. Final column shows PSBs from GCLASS with similar stellar masses to the galaxy models. Parameters listed in all cutouts show the measured values from GALFIT. For the models, sizes are converted into kpc assuming the models are at $z = 1$. The dimensions of all cutouts are the same, as well as the position angle (measured counter-clockwise) of all models and the PSBs, set to 90 degrees. The colourmap is logarithmic.

Alongside the faded galaxy models, we show select PSBs that have similar stellar masses to the model galaxies.

3.5.3.2 The stellar mass–size relation of bulges + outside-in faded discs

In the largest panel of Figure 3.10, we show the median size measurements for the starting (open green squares) and faded (filled green squares) galaxy models for multiple stellar mass bins, as well as the disc (small blue circles) and bulge (large red circles) components. The lines are the same as in Figure 3.6. The most striking aspect of these measurements is that this model of disc-fading leads to a dramatic drop in the size of galaxies. So much so, that the half-light radii are smaller than those of the bulge models. At the median stellar mass of the PSBs within the quiescent mass completeness limit ($\mathrm{Log}(\mathcal{M}_*/\mathrm{M}_\odot) = 10.44$), the half-light radius shrinks by 85%. This large size reduction is likely due to the fact that the central pixels of the disc models have not been faded. As a result, the outside-in

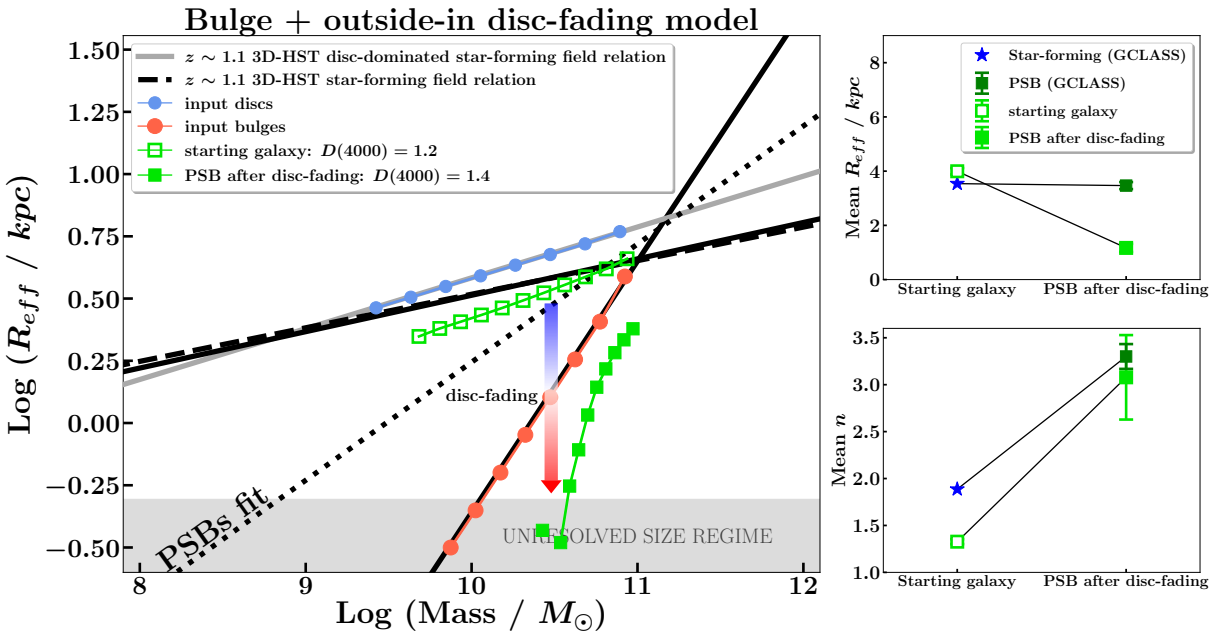

Figure 3.10: Bulge + outside-in disc-fading toy model. Main panel: median size measurements for 8 stellar mass bins of the disc (small blue circles) and bulge (large red circles) input Sérsic models that were created to follow the $z \sim 1.1$ disc-dominated star-forming field mass–size relation and the $z \sim 1$ quiescent field mass–size relation, respectively. For reference, we show the $z \sim 1.1$ and $z \sim 1$ star-forming field mass–size relations as dashed and solid black lines respectively. Bulges are five times fainter than the discs at fixed stellar mass (see text for reasoning). The starting galaxy is composed of the disc+bulge input models, median size measurements of which in eleven stellar mass bins are shown as open green squares. Corresponding median size measurements of the disc-faded galaxies are shown as filled green squares. Since $\mathcal{M}_{*,bulge} = \mathcal{M}_{*,disc}$, the stellar masses of the starting and disc-faded galaxies are $2\mathcal{M}_{*,bulge}$ (or $2\mathcal{M}_{*,disc}$). The disc is faded outside-in such that the stellar populations of the faded galaxy match the stellar populations of the PSBs (see Section 3.5.3.1). The region in which size measurements fall below the resolution limit of the GCLASS F140W images is shaded in grey. Top and bottom right panels: average half-light radius and Sérsic index values for the starting and disc-faded galaxy models along with the values for the GCLASS star-forming and PSB cluster galaxies within mass completeness limits (see text for more details). Error bars on GCLASS measurements are standard errors in the mean. Error bars on the model results are standard deviations from monte carlo sampling (see text for details).

fading implemented has a particularly steep gradient. Consequently, there is far more light in the central regions of the faded galaxies compared to the corresponding bulge model. This is also evident in the first row of Figure 3.9. This leads to a galaxy with a particularly steep light profile, and therefore a smaller half-light radius.

In the top right-hand panel of Figure 3.10, we show the average sizes of the starting and faded galaxy models for models that have stellar masses identical to the PSBs beyond the quiescent mass completeness limit. We also show the average sizes of the star-forming and PSB cluster galaxies in GCLASS within the star-forming and quiescent mass completeness limits, respectively. Errors are calculated in the same way as for the previous disc-fading models[¶¶]. The dramatic reduction in the average size of a galaxy is evident in this model, with the faded models reaching an average size that is almost half that of the average PSB.

[¶¶]If error bars are not visible, it is because the error bar is smaller than the size of the marker.

3.5.3.3 The average Sérsic index of bulges + outside-in faded discs

In the bottom right-hand panel of Figure 3.10, we compare the average Sérsic indices of the starting and faded galaxy models to the average Sérsic indices of the star-forming and PSB cluster galaxies[***]. It is immediately noticeable that this disc-fading model – unlike the previous two models – can reproduce the dramatic rise in Sérsic index that is seen in the observations.

3.5.4 Caveats

It should be emphasised that while considerable effort has been made to model disc-fading realistically, the three toy models presented in Sections 3.5.1, 3.5.2 and 3.5.3 are still very simplistic. For the models that consider bulge and disc components, only the case where the two components have the same stellar mass has been considered. In all three of the models presented, we only consider models with specific Sérsic indices, axis ratios, F140W magnitudes and position angles. Realistically, galaxies will have a range of disc-to-bulge stellar mass ratios, Sérsic indices, axis ratios, F140W magnitudes and position angles. The fading of galactic discs would also occur in varying amounts and the stellar populations would vary. These variances would cause a scattering in the positions of the starting and faded galaxies on the mass–size plane.

Furthermore, our understanding of outside-in fading, and its implementation in Sections 3.5.2 and 3.5.3, is based on a single – albeit well-studied – example of a cluster galaxy undergoing ram-pressure stripping at low redshift (see Section 3.5.2.2). Ram-pressure stripping may operate very differently at high redshift, where gas fractions are higher than at low redshift. There may also be a stellar mass dependency on how ram-pressure stripping operates, which we will discuss in more detail in Section 3.6.

Particularly in the last disc-fading model (Section 3.5.3), the outside-in fading seems to be too aggressive. The way in which the fading is implemented leads to a large contraction in the half-light radius of a galaxy. Certainly, if the gradient of the outside-in fading was shallower, the magnitude of this contraction could be reduced (as is evident in Figure 3.8 for example), and faded galaxies that approximately follow the PSB mass–size relation could be achieved.

Nevertheless, it is clear that the combination of modelling a galaxy with a bulge and disc component, as well as implementing outside-in disc-fading (Section 3.5.3) could lead to the required contraction in size *and* the required increase in bulge-dominance that is observed between the star-forming and PSB cluster galaxies.

[***]These, as well as their errors are calculated in the same way as in the first two disc-fading toy models.

3.6 Discussion

3.6.1 Evidence for the PSBs being transition galaxies

The PSBs are cluster galaxies that were selected as being recently quenched – and therefore intermediary to star-forming and quiescent galaxies – based solely on their spectroscopic properties in the optical (Section 3.1.3). In Sections 3.3 and 3.4, we presented two pieces of evidence that suggest the PSBs also have structural properties intermediary to those exhibited by typical star-forming and quiescent cluster galaxies: 1) The PSBs lie on a distinct stellar mass–size relation that almost perfectly bisects the region between the star-forming and quiescent mass–size relations, and 2) Morphologically, out of the three populations (Star-forming, PSB and Quiescent), the PSB population contains the largest fraction of intermediate-type galaxies. The fraction of bulge-like galaxies in the PSB population is also intermediary to the fraction of bulge-like galaxies found in the star-forming and quiescent populations. The fact that the PSBs all lie on the same mass–size relation suggests that most, if not all of them formed via the same physical process. After inspecting the HST WFC3 F140W imaging of the PSBs (Section 3.2), we find most of them have symmetrical, undisturbed morphologies in the stellar continuum. This observation rules out physical quenching mechanisms such as mergers, harassment (Moore et al., 1996, 1998) or tidal stripping which lead to the redistribution of stars. Instead, it supports a scenario where the PSBs are formed via a quenching process that only effects the gas reservoir of the galaxy.

Quenching mechanisms prevalent in the cluster environment which solely affect the gas content of a galaxy include ram-pressure stripping (Gunn & Gott, 1972) and strangulation (Larson et al., 1980). Spectacular examples of on-going ram-pressure stripping quenching galaxies rapidly have been observed in low redshift clusters (e.g. Abramson et al. 2011; Ebeling et al. 2014; Bellhouse et al. 2017; Gullieuszik et al. 2017; Sheen et al. 2017; Fossati et al. 2018; Cramer et al. 2019). Both the rapidity of this process and its potential to indirectly reduce the half-light radius of a galaxy support the short quenching timescales found for the PSBs from our previous work (Muzzin et al., 2014) and the location of the PSB mass–size relation relative to the star-forming one in this chapter.

It must be noted that there is no definitive way to identify galaxies that are transitioning from star-forming to quiescent. Therefore, results on galaxies that are similarly selected to the GCLASS PSBs tend to vary, making comparison with the literature challenging. In general, PSBs have strong Balmer absorption and no emission lines which are induced by star formation. However, by altering the exact spectroscopic selection criteria, very different samples of transition galaxies can be selected which

exhibit a range of physical properties (e.g. Lemaux et al. 2017; Wilkinson et al. 2017). Some of these selection criteria can lead to significant contamination by dusty star-forming galaxies (Wu et al., 2014). Particularly strong Balmer absorption can be indicative of a starburst occurring in the galaxy prior to quenching (Section 3.1.3). Such starbursts are likely to be the result of violent interactions such as galaxy-galaxy mergers or harassment, not gas-related processes such as ram-pressure stripping or starvation (e.g. Wild et al. 2009).

Nevertheless, many other similar works to ours have also concluded that PSB galaxies in clusters are most likely the product of ram-pressure stripping (Poggianti et al., 2009; Rodríguez Del Pino et al., 2013; Fritz et al., 2014; Paccagnella et al., 2019). In most cases, this is usually associated with the higher occurence of PSBs in clusters compared to other environments such as the field and groups (Ma et al., 2008; Poggianti et al., 2009; Vergani et al., 2010; Muzzin et al., 2012; Wu et al., 2014; Galametz et al., 2018; Paccagnella et al., 2019), suggesting cluster-specific quenching mechanisms are more efficient in transforming star-forming galaxies into PSBs. More detailed studies on the spatial distribution of PSBs in clusters have uncovered more convincing evidence for ram-pressure stripping being responsible for their emergence. Ma et al. (2008) found that their E+A cluster galaxies were evenly distributed within the projected ram-pressure stripping radius of the cluster MACS J0717.5 + 3745. Going a step further, Fritz et al. (2014) found that their PSBs were radially distributed in a shell-like structure, congregating in between where most of the star-forming and quiescent cluster galaxies were found. This seemed to suggest a transition region in clusters, where there is a change in the physical properties, perhaps in the density of the intracluster medium, triggering efficient ram-pressure stripping. Similarly, Muzzin et al. (2014) found that most of the GCLASS PSBs with spectroscopic redshifts from GMOS followed a coherent "ring" in clustercentric velocity versus position phase space. Most of the GCLASS PSBs are situated at small clustercentric radii ($< 0.5R_{200}$) with high clustercentric velocities. Such conditions were found to be consistent with the radii at which ram-pressure stripping and starvation are most effective in clusters (Treu et al., 2003; Moran et al., 2007; Bahé et al., 2013).

Since ram-pressure stripping is capable of removing the cold gas reservoir of a galaxy, it can remove the fuel for star formation. With no younger stars actively forming, the average age of the stellar populations in the galaxy increases, eventually leading to a fall in the brightness of the galaxy. Ram-pressure stripping is more effective at removing gas from galactic discs (Abadi et al., 1999). With a strong body of evidence suggesting the GCLASS PSBs are a product of ram-pressure stripping, we decided to test whether the fading of a star-forming galaxy's disc could lead to a population of galaxies that would lie along the PSB mass–size relation.

3.6.2 Outside-in disc-fading qualitatively explains the structural properties of the PSBs

Initially, we modelled star-forming galaxies as having both a disc and bulge component of equal stellar mass. The disc would then uniformly fade such that the galaxy's stellar populations matched those of the PSBs (Section 3.5.1). In this scenario, we found that the fading did not produce model galaxies with similar sizes and Sérsic indices to the average PSB (Figure 3.6). Far more fading was required to explain the small sizes and high Sérsic indices of the PSBs. This is perhaps unsurprising, since observational evidence suggests quenching in clusters does not operate in this way.

Given that numerous previous results suggest that outside-in quenching occurs in low redshift clusters, we therefore proceeded to model outside-in fading on the mass–size plane (Section 3.5.2), finding that it also fails to produce model galaxies with similar structural properties to the PSBs. Furthermore, this model fails to reproduce the steep slope of the PSB stellar mass–size relation. A possible reason for this could be due to a difference in the fading rate for low- and high-mass galaxies. Outside-in fading may operate at a faster rate for low-mass galaxies, but much slower for high-mass galaxies. This may also allow for the average Sérsic index to rise, since at fixed stellar mass, all the galaxies with $\mathrm{Log}(\mathcal{M}_*/\mathrm{M}_\odot) \lesssim 10.9$ –which are in the majority – will have smaller sizes at fixed stellar mass, more similar to quiescent galaxies.

Nevertheless, we decided to combine our first and second attempts at modelling disc-fading into a third model (Section 3.5.3). From the first model (Section 3.5.1), we took the more realistic modelling of galactic structure, modelling our galaxies with a disc and bulge component. From the second model (Section 3.5.2), we took the more realistic modelling of "outside-in" fading. The result is a model that can explain the high Sérsic indices of the PSBs and has the potential to produce disc-faded galaxies that approximately follow the PSB mass–size relation. The results of these three disc-fading toy models have shown that the PSBs are plausibly the product of star-forming galaxies which have experienced disc-fading. This disc-fading is likely to have been brought on by quenching processes such as ram-pressure stripping. To better reproduce the structural properties of the PSBs with disc-fading, various fading gradients with more sophisticated modelling need to be explored. The gradient of outside-in fading could very much rely upon the stellar mass of the galaxy, which in turn dictates the slope of the relation the faded galaxies lie on.

Many recent works have found that disc fading could explain the formation of transition galaxies in clusters. Using a bulge and disc decomposition of quiescent galaxies in the Coma cluster, Head et al. (2014) find that S0 (intermediate-type) galaxies have systematically bluer bulges and discs

further away from the cluster centre. This observation favoured environmentally-induced disc fading as the dominant route for S0 formation. Going further, Bedregal et al. (2011) were able to show that most S0 galaxies in the Fornax cluster have quenched "outside-in", with the latest star formation in the central regions being capable of enhancing the brightness of the bulge. Similarly, Jaffé et al. (2011) find that kinematically-disturbed emission-line cluster galaxies out to $z \sim 1$ have truncated gas discs and that their star formation is more centrally concentrated than analogous galaxies in low density environments. They suggest that gas is either more efficiently removed from the outskirts of galaxies and/or is driven towards the centre. Driving gas towards the centre of the galaxy would further fuel the centrally-concentrated star formation and contribute to the build-up of a significant bulge. Perhaps this may be an attribute of gas-stripping processes which was not considered in our toy models. If ram-pressure stripping could also contribute to enhancing the stellar mass build-up of the bulge, a scenario could emerge where there is bulge *brightening* as well as disc fading. This could most certainly explain the more bulgier morphologies of the PSBs compared to the faded galaxies in our fading models. Enhanced star formation in the core of a ram-pressure stripped galaxy in the Coma cluster was seen in Cramer et al. (2019) for example. Furthermore, Fraser-McKelvie et al. (2018) found that the bulges of low mass ($\mathcal{M}_* < 10^{10}\mathrm{M}_\odot$) S0 galaxies in the MaNGA survey hosted younger stellar populations than their discs, supporting an outside-in fading scenario where the bulge may end up brighter than the disc.

Nonetheless, other works have stated that outside-in quenching may not be the only explanation for how cluster galaxies quench. Using a bulge-disc decomposition of late- and early-type galaxies in six low redshift clusters, Christlein & Zabludoff (2004) found that the bright end of the disc luminosity function does not vary much with bulge fraction, but the bright end of the bulge luminosity function increases with bulge fraction. Quenching in clusters seems to favour the bulge becoming brighter rather than the disc fading as a galaxy moves from spiral to elliptical morphology. This seems to suggest that environmental quenching processes are not enough to explain the structural properties of recently quenched cluster galaxies. For example, to explain how low mass ($\mathrm{Log}(\mathcal{M}_*/\mathrm{M}_\odot) < 10.5$) PSBs evolved from compact star-forming galaxies in $z < 1$ clusters, Socolovsky et al. (2019) found that a combination of gas stripping and strong outflows from stellar or AGN feedback were needed to explain their structural properties.

3.6.3 Recently quenched galaxies & evolution in the quiescent mass–size relation with redshift

The distinct location of the PSBs on the mass–size plane has important implications for the growth in the average size of quiescent cluster galaxies with decreasing redshift. The majority of the PSBs lie on the large size end of the quiescent distribution at fixed stellar mass (see Figure 3.3). Their location in Figure 3.3 provides direct evidence showing that galaxies which quench later are on average larger in size than galaxies that quenched earlier. Therefore, the addition of recently quenched galaxies to the quiescent population can induce an increase in the average size of quiescent galaxies with decreasing redshift.

In Chapter 2, we found that minor mergers could explain the size growth observed in quiescent field galaxies with decreasing redshift at fixed stellar mass. Now, with the study presented in this chapter, we confirm that the addition of recently quenched galaxies to the quiescent population will also induce a rise in the average size of quiescent galaxies with decreasing redshift. The relative importance of these two size growth mechanisms however still needs to be determined. For example, a higher occurence of PSBs in clusters have been found by a number of other studies (Poggianti et al., 2009; Vergani et al., 2010; Muzzin et al., 2012; Wu et al., 2014; Paccagnella et al., 2019). Since minor mergers are rare between satellite cluster galaxies, these findings may suggest that the addition of recently quenched galaxies to the quiescent population is more important for the size growth observed in the quiescent *cluster* population than for the size growth observed in the quiescent *field* population with decreasing redshift.

On the other hand, Carollo et al. (2013) claim that the addition of recently quenched galaxies to the quiescent population can explain the majority of the size growth observed in the median size of quiescent field galaxies between $0.2 < z < 1$. This conclusion was motivated by the fact that these authors do not observe a decrease in the number density of compact quiescent galaxies in this redshift range (which, if observed, would have suggested they have grown physically in size). Since this result, many other studies have also found that progenitor bias plays an important role in the size growth of quiescent galaxies at fixed stellar mass (Cassata et al., 2013; Krogager et al., 2014; Damjanov et al., 2015; Zahid et al., 2016; Charbonnier et al., 2017; Tacchella et al., 2017; Abramson & Morishita, 2018; Damjanov et al., 2018). In further support of this conclusion, Fagioli et al. (2016) found that large quiescent field galaxies with $10.5 < \mathrm{Log}(\mathcal{M}_*/\mathrm{M}_\odot) < 11$ at $0.2 < z < 0.8$ were composed of younger stellar populations than smaller quiescent field galaxies within the same stellar mass range. Similar results to this one have also been found by Delaye et al. (2014b), Gargiulo et al. (2017), Scott et al.

(2017), Williams et al. (2017), Zahid & Geller (2017) and Wu et al. (2018). van der Wel et al. (2014) however did observe a decrease in the number density of compact quiescent galaxies with a much larger sample of field galaxies between $0 < z < 2$, concluding that minor mergers drive the observed growth in the average size of quiescent galaxies with decreasing redshift. Many other works have also concluded that minor mergers are the main drivers of size growth at fixed stellar mass for the quiescent population (Morishita et al., 2014; Damjanov et al., 2014; van Dokkum et al., 2015; Chan et al., 2016; Zanella et al., 2016; Oldham et al., 2017; Kubo et al., 2018). Regardless, there remains disagreement in which of the two processes dominates the observed size growth (Belli et al., 2014; Rutkowski et al., 2014; Keating et al., 2014; Belli et al., 2015).

Using the results in Chapter 2 and this Chapter, we confirm that both minor mergers and recently quenched galaxies are responsible for the observed growth in the average size of quiescent galaxies at fixed stellar mass with decreasing redshift. However, better sample statistics spread over a large range in redshift and environments will be required to quantify which of the two processes dominates.

3.7 Summary

In this chapter, we have studied the structural properties of 23 spectroscopically identified recently quenched (or "poststarburst" (PSB)) cluster galaxies residing in nine clusters at $z \sim 1$, to better understand the physical process responsible for their quenching. Our main conclusions are as follows:

1. In most cases, the F140W direct images of the recently quenched galaxies show no disturbances to their stellar light profiles that could be the result of violent interactions such as mergers, harassment or tidal stripping. This suggests the quenching mechanism responsible effects solely the gas content of these galaxies.

2. By fitting the F140W direct images of the recently quenched galaxies with single component Sérsic profiles, we find that most of the recently quenched galaxies lie on a distinct mass–size relation that almost perfectly bisects the region lying in between the star-forming and quiescent field stellar mass–size relations. This suggests the quenching mechanism responsible is capable of altering the light profile of these galaxies in a very specific way, with the likelihood that most of the recently quenched galaxies underwent the same quenching process.

3. Using Sérsic index as a proxy for morphology, we compare the Sérsic profiles of the recently quenched, star-forming and quiescent cluster galaxies. The highest fraction of intermediate-type galaxies is found in the recently quenched population. Recently quenched galaxies also exhibit a higher fraction of bulge-dominated galaxies than the star-forming population, but a lower fraction compared to the quiescent population. Therefore, recently quenched galaxies have morphologies that are intermediary to those of the star-forming and quiescent populations. However, on average, their morphologies are more similar to those exhibited by the quiescent population.

4. By modelling a star-forming cluster galaxy with a bulge and disc component of equal stellar mass, we explored how star-forming galaxies move across the mass–size plane as their discs fade uniformly, resulting in galaxies with similar stellar populations to the recently quenched galaxies. Although a reduction in half-light radius and a rise in Sérsic index is found, the magnitude of these changes in physical properties are too small to explain the structural properties of the PSBs.

5. We then used a more realistic model of outside-in fading based on recent observations of quenching in clusters. We found that this model still failed to produce galaxies with similar structural properties to the PSBs. A significant drop in average size is achieved, but the high Sérsic indices of the PSBs and the steep slope of the PSB mass–size relation was not achieved. This suggests longer fading timescales with increasing stellar mass are required and/or bulge brightening also occurs as part of quenching processes like ram-pressure stripping which could drive gas towards the centre.

6. By combining the more realistic modelling of a galaxy with a disc and bulge component, and the more realistic outside-in disc-fading, we showed that disc-fading can explain the high Sérsic indices of the PSBs and has the potential to produce galaxies that follow the PSB mass–size relation. Further exploration of outside-in fading gradients combined with more sophisticated modelling is required to fully reproduce the structural properties of the PSBs.

7. The fact that the PSB mass–size relation runs through the large size end of the quiescent distribution of galaxies provides direct evidence for recently quenched galaxies contributing to the size growth of quiescent galaxies with decreasing redshift.

In tandem with the results presented in Chapter 2, we confirm both minor mergers and the addition of recently quenched galaxies to the quiescent population are responsible for the rapid size growth at fixed stellar mass observed in the quiescent population of galaxies with decreasing redshift. However, it remains unclear which of these two processes dominate. Determining this will require better sample statistics over a broad redshift range in a variety of environments.

I don't want to believe. I want to know.

Carl Sagan

4

Spatially resolved star formation in cluster galaxies

It has now been known for a long time that cluster galaxies are on average redder in colour, less actively star-forming and bulge-dominated in morphology (see Section 1.1.1) compared to galaxies in the low-density field environment. In more recent times, it has been found that even at fixed stellar mass, the fraction of galaxies with quenched star formation is higher in high density regions such as clusters, both at low ($z \sim 0$) *and* high ($z \sim 1$) redshift (see Section 1.1.1 and Peng et al. 2010b; Muzzin et al. 2012). Population studies such as these provide us with the ability to constrain global properties of galaxies residing in different environments, such as star formation rates, quenched fractions and quenching timescales. However, the statistical power of these studies do not allow for strong constraints on the physics that drives these global trends.

In the case of star formation and its quenching, the strongest probe allowing us to understand how it operates in galaxies has been spatial information. Early results on this were obtained using narrow-band imaging, where different wavelengths tracing star formation operating on different timescales are exploited. A common tracer used for instantaneous ($\sim$ 10 Myr) star formation is Hα emission. The ultraviolet radiation emitted by young, massive O and B stars leads to recombination at the boundary of their Strömgen spheres and therefore emission in Hα (Kennicutt, 1998). An early study which

exploited this tracer using narrow-band imaging is Koopmann & Kenney (2004). In Koopmann & Kenney (2004), more than half of spiral galaxies in the Virgo cluster were found to have truncated Hα discs relative to their *R*-band discs, compared to only $\sim$ 10% in the low density field environment (see Figure 1.7 and Section 1.1.1.1 for more details.). For the first time, a statement could be made on how environmental quenching operates: it seems to destroy discs from the "outside-in", making galaxies appear smaller with a more concentrated light profile.

Recently, with the emergence of integral field spectroscopy, studies on environmental quenching have become more sophisticated. We now have the ability to make statements on how the kinematics of galaxies are affected by environmental quenching processes such as ram-pressure stripping (see Figure 1.9, Section 1.1.1.1 and e.g. GASP, Poggianti et al. 2017; Bellhouse et al. 2017; Gullieuszik et al. 2017; Fritz et al. 2017; Moretti et al. 2018; Jaffé et al. 2018; Vulcani et al. 2018). Similarly, new deeper narrow-band imaging surveys have made it possible to measure quenching timescales as a function of galactocentric radius (see Figure 1.8, Section 1.1.1.1 and e.g. VESTIGE, Fossati et al. 2018). For the first time, we are able to quantify the rate at which specific environmental quenching mechanisms operate and where they start and finish acting in a galaxy.

However, this progress in our understanding of environmental quenching is confined to the low-redshift Universe. Naturally, such detailed observations are challenging to obtain at high-redshift, but are arguably more necessary. To make statements on which quenching mechanism dominates the production of the many red, dead and bulge-dominated galaxies in today's galaxy clusters, we must look to high redshifts, where galaxy clusters were still in the process of forming, cosmic star formation rates were higher (see Figure 1.3, Section 1.1 and Madau & Dickinson 2014) and galaxies can be caught directly in the process of quenching.

In a first study of its kind, Nelson et al. (2016b) used *Hubble Space Telescope* (HST) *Wide Field Camera 3* (WFC3) slitless spectroscopy to construct spatially resolved Hα maps of star-forming field galaxies at $z \sim 1$. By comparing the spatial extent of the Hα emission to the stellar continuum, they were able to conclude that star-forming field galaxies are growing in an "inside-out" fashion via star formation, since their Hα emission is more spatially extended than their stellar continuum at all stellar masses. In this chapter, we use this technique on the largest sample of spectroscopically confirmed cluster galaxies at $z \sim 1$ in an attempt to make the first measurement of environmental quenching at high-redshift.

High-redshift population studies on environmental quenching timescales suggest that quenching becomes more rapid with increasing redshift (see Figure 1.6, Section 1.1.1 and Mok et al. 2013; Muzzin

et al. 2014; Balogh et al. 2016; Paccagnella et al. 2017; Foltz et al. 2018). If, for example, ram-pressure stripping is more rapid in the high-redshift Universe, we may expect to see severely truncated Hα discs with respect to the stellar continuum compared to similar observations in low-redshift clusters. Alternatively, we may find it is difficult to catch many star-forming cluster galaxies in the quenching phase, and an "outside-in" environmental quenching signature cannot be measured.

In this chapter, we investigate whether there is a measurable environmental quenching signature in star-forming galaxies residing in 10 clusters at $z \sim 1$. We do this by measuring the spatial extent of their Hα emission and comparing it to the spatial extent of their stellar component. At low redshifts, this technique has been shown to be a powerful tool in constraining environmental quenching mechanisms and their timescales (e.g. Abramson et al. 2011; Finn et al. 2018; Fossati et al. 2018). For our study in this chapter, we use spatially resolved Hα maps of these galaxies obtained using the WFC3 G141 grism on board the HST and WFC3 F140W imaging of the same galaxies to accomplish this.

This chapter is organised as follows. In Section 4.1, we describe the data we use and relevant details regarding grism spectroscopy. A detailed explanation of our methodology, including the construction of our Hα maps, sample selection and size determination process is given in Section 4.2. We present our results in Section 4.3 and discuss their implications in Section 4.4. Finally, we summarise our results in Section 4.5.

4.1 Data

4.1.1 The GCLASS survey

The Gemini Cluster Astrophysics Spectroscopic Survey (GCLASS, see Muzzin et al. 2012 and van der Burg et al. 2013) is the spectroscopic follow-up of 10 massive clusters in the redshift range $0.86 < z < 1.34$, drawn from the 42 deg^2 Spitzer Adaptation of the Red-sequence Cluster Survey (SpARCS, see Muzzin et al. 2009, Wilson et al. 2009 and Demarco et al. 2010). Extensive optical spectroscopy was obtained with the Gemini Multi-Object Spectrographs (GMOS) on both Gemini-South and -North. In total, 1282 galaxies obtained a spectroscopic redshift, with 457 of these being confirmed as cluster members. There is also 12-band photometry available for these clusters. The details of the photometry in 11 bands (*ugrizJK*$_s$, 3.6μm, 4.5μm, 5.8μm and 8.0μm) is summarised in Appendix A of van der Burg et al. (2013). Newly acquired photometry in the F140W band (wide *JH* gap) has been obtained as part of the GCLASS HST follow-up (see Section 4.1.2). Physical properties of the 10 clusters in the GCLASS survey are summarised in Table 2.1, Chapter 2.

4.1.2 HST data

The HST follow-up to GCLASS contains WFC3 F140W imaging and G141 grism spectroscopy for all of the clusters to a 2-orbit depth. 90% of this time is spent on the grism spectroscopy (details of which are discussed in Section 4.1.2.1) and the remaining 10% on F140W imaging. The HST observations are centered on the cluster core and cover approximately ~ 8 arcmin^2 for each cluster. This corresponds to approximately a quarter of the observing area covered by GMOS in the GCLASS survey (Section 4.1.1). Despite this smaller overlap with GCLASS, spectroscopic density is highest in the cores of clusters. 86% of galaxies confirmed as cluster members in GCLASS are in the HST fields of view. For specifics on F140W coverage, exposure times, limiting magnitudes and data reduction, we refer the reader to Sections 2.1.1.2 and 2.1.1.3 of Chapter 2.

4.1.2.1 Grism spectroscopy

As mentioned in Section 4.1.2, the majority of the HST observing time was dedicated to obtaining the G141 grism spectroscopy. This was done to ensure we could obtain spatially-resolved Hα maps of the star-forming cluster galaxies with a sufficient signal-to-noise ratio, such that stacks containing $\sim 30 - 40$ galaxies could have their Hα profiles measured to $\sim 10\%$ accuracy (Nelson et al., 2013).

A grism is the combination of a diffraction grating and prism. In the context of the G141 grism, a series of ridges on the glass surface of a prism act as the diffraction grating, dispersing light from an object at an angle. The prism directs the dispersed light towards the WFC3 detector, keeping the light at some chosen central wavelength undeviated (Viana & Wiklind, 2009). The result is an image of the galaxy at different wavelengths, in 46Å increments spanning $10750 < \lambda \,/\, \text{Å} < 17000$. An emission line in this two-dimensional spectrum manifests itself as an image of the galaxy in that line on top of the underlying continuum. G141 grism spectra for the cluster SpARCS-1047 can be seen in the right-hand panel of Figure 2.1, Chapter 2. The small pixel scale of the WFC3 (0.13 arcsec per pixel) and the low spectral resolution of the G141 grism ($R \sim 130$) therefore allows for the possibility of spatially-resolved ($0.130 \leqslant \text{FWHM} \,/\, \text{arcsec} \leqslant 0.156$ for $11000 \leqslant \lambda \,/\, \text{Å} \leqslant 17000$) emission line maps (Nelson et al., 2016b).

The wavelength coverage of the G141 grism is such that Hα emission can be detected in galaxies within the redshift range $0.7 < z < 1.5$. This redshift range coincides perfectly with the redshift range of the GCLASS clusters ($0.86 < z < 1.34$). One resolution element for a galaxy at $z \sim 1$ corresponds to a velocity dispersion of approximately 1000 kms^{-1}. The majority of galaxies have line widths well below this. Therefore, structure in the emission line maps is *not* due to kinematics: it is due to

morphology (Nelson et al., 2016b).

4.2 Methodology

4.2.1 Making Hα maps

The *Grism redshift & line analysis software for space-based slitless spectroscopy* (Grizli*) is used to reduce the G141 data and make Hα maps. In the context of our HST data (Section 4.1.2), this software works by modelling what the two-dimensional spectral trace of a galaxy detected in the F140W image would look like, and then subtracting this model from the galaxy's G141 spectrum. This subtraction effectively removes the stellar continuum, exposing any emission lines present in the spectrum (see Figure 4.1).

One of the biggest problems with slitless spectroscopy obtained with HST – especially for galaxy clusters, where there is a high density of sources – is contamination. Spectra from neighbouring sources can blend into the spectra of galaxies one is interested in, adding contaminating flux. Instances of this contamination can be seen in Figure 2.1, Chapter 2. Fortunately, Grizli is able to remove this contamination in an analogous method to how the stellar continuum of a G141 spectrum is removed. The spectral trace of each neighbouring source is modelled to create a contamination model for each galaxy of interest. Along with the stellar continuum model, this contamination model can be subtracted from the G141 spectrum. A pictorial demonstration of this process is shown in Figure 4.1.

Grizli creates postage stamps of these emission line maps, with associated weight and contamination maps (see Figure 4.2). For the work presented in this chapter, Grizli was only used to create the postage stamps. The generation of the stellar continuum models, contamination models, weight maps, segmentation maps, the subtraction of the stellar continuum models from the grism spectra and the extraction of emission line maps was carried out by collaborator Gabriel Brammer (please see Declaration in preface). The weight maps provide values of the inverse variance at each pixel. During the construction of these postage stamps, the user has the ability to set the level of masking for pixels in emission line map postage stamps that are contaminated by neighbouring emission line maps in the grism spectrum. If the flux of a contaminating emission line is greater than ten times the flux of the emission line of interest in a given pixel, the pixel is masked. In the context of the Hα maps, this masking is particularly important for neighbouring S[II] λλ6718 + 6732 emission. These masked pixels are also incorporated in the associated weight maps for each postage

*https://grizli.readthedocs.io/en/master/

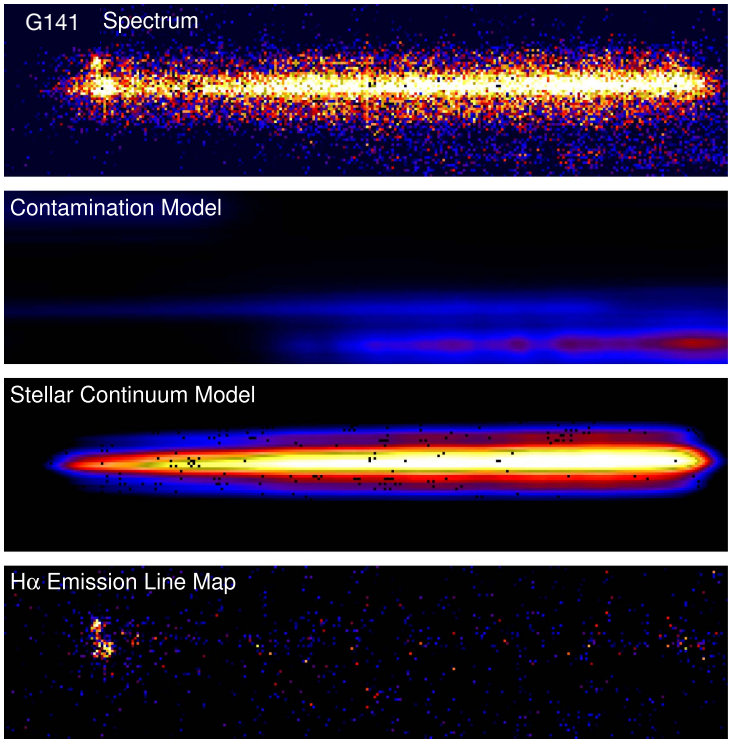

Figure 4.1: An example G141 spectrum of a galaxy at $z \sim 1$ obtained with the HST WFC3 G141 grism (first row), and its associated contamination and stellar continuum models (second and third rows, respectively). Once these models are subtracted from the original G141 spectrum, any emission line maps present become exposed (bottom row). This figure has been adapted from Nelson et al. (2016b).

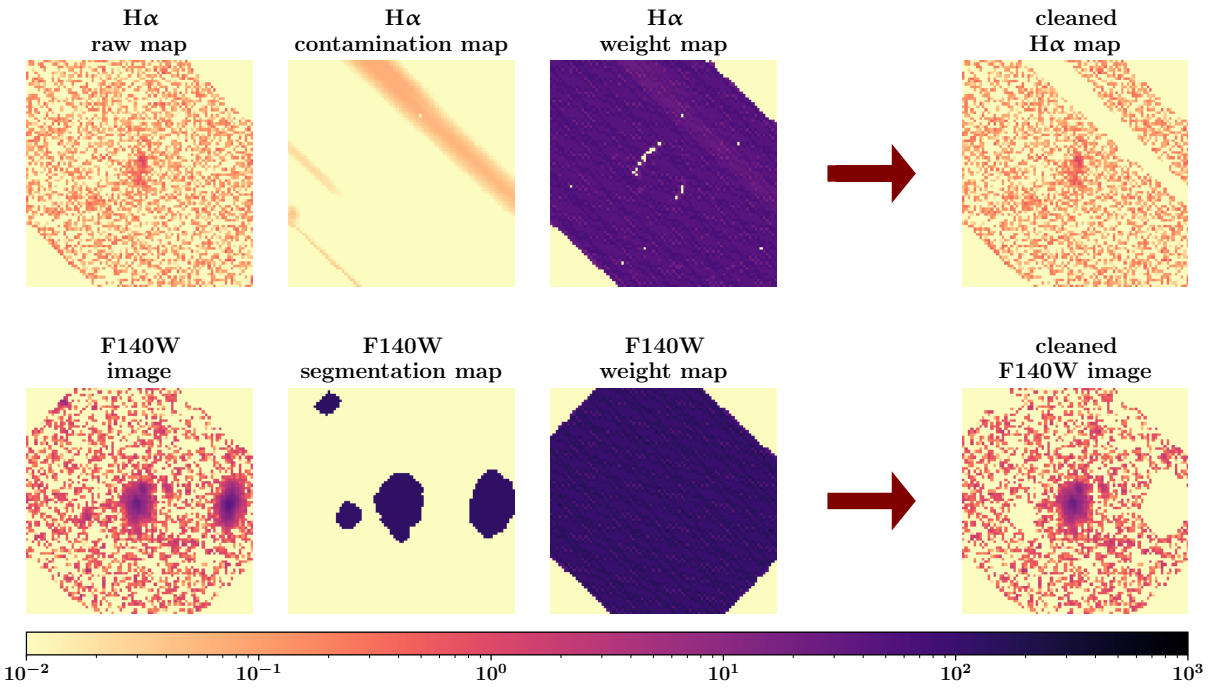

Figure 4.2: An example of F140W and Hα postage stamps generated by Grizli for a GCLASS cluster galaxy. For the Hα/F140W raw maps/images, the Hα/F140W cleaned maps/images and the Hα contamination map, the units of the colourbar are 10^{-17} ergs s^{-1} cm^{-2}. For the Hα and F140W weight maps, the units of the colourbar are inverse variance, $1/\sigma^2$ (where σ is the noise). Values in the F140W segmentation map correspond to the object ID's of the sources.

stamp (see Figure 4.2, top row).

Along with the postage stamps of the emission line maps, Grizli also creates postage stamps of the galaxy in F140W and its segmentation map (see Figure 4.2). The segmentation map is generated by SExtractor. It marks which pixels are occupied by flux from the galaxy, and which are not. The pixels that are occupied by flux from the galaxy are used to create the stellar continuum model for the grism spectrum of the galaxy (Figure 4.1).

Accompanying point spread function (PSF) postage stamps in F140W for each galaxy are generated using the WFC3/IR empirical PSF library from Anderson (2016). The PSFs for the data used in this chapter were generated by collaborator Gabriel Brammer (please see Declaration in preface). PSFs exist for various positions across the detector sampled on a 3×3 grid. At each of these grid points, four sub-pixel centre positions are available. For each galaxy, the relevant empirical PSF is placed at the exact location of the galaxy in the detector frame of each individual exposure within which the galaxy is detected. These PSF models are then drizzled to the same pixel grid as the emission line maps (Mowla et al., 2018). The resulting PSFs are therefore superior to those used in Chapter 2 (discussed in Section 2.1.3.3). Since these are inserted at the *exact* location of the galaxy, rather than being close to the position of the galaxy on the mosaic, systematics which arise from variations in the PSF across the mosaic, instrument orientation, pixel resampling and image weighting are further reduced (Mowla et al., 2018). However, during the testing phase of the two-GALFIT-run approach discussed in Section 2.1.3.3, Chapter 2 – which will also be used in this Chapter – using different PSFs based on their proximity to the galaxy on the mosaic versus using a single PSF for all galaxies on the mosaic did not change any of the results presented in Chapter 2. Therefore, PSF variations do not significantly impact our measurements made with GALFIT.

By default, Grizli outputs all its postage stamps to a pixel scale of 0.1 arcsec per pixel. We decide not to alter the output pixel scale, since all postage stamps are optimised to work with GALFIT, which will be used in the size determination process (Section 4.2.4). All postage stamps are 80×80 pixels in dimension.

4.2.2 Sample selection

4.2.2.1 Cluster sample

We run Grizli on the star-forming sample of cluster galaxies determined in Chapter 2. These are spectroscopically (GMOS and/or grism) confirmed cluster members with stellar masses $\mathrm{Log}(M_*/M_\odot) \geqslant 9.60$, half-light radii $R_{eff} < 50$ kpc, F140W magnitudes < 25 and rest-frame *UVJ*

colours which fall into the star-forming classification criteria for GCLASS, defined in Equation 4.1 (The quiescent classification criteria for GCLASS are defined in equations 2.4 and 2.5). This sample amounts to 177 galaxies.

$$\text{Star-forming} = \begin{cases} (U-V)_{rest} < 1.44 & (V-J)_{rest} < 0.88 \\ (U-V)_{rest} < 0.81\,(V-J)_{rest} + 0.73 & 0.88 < (V-J)_{rest} < 1.57 \\ (V-J)_{rest} > 1.57 & \text{otherwise} \end{cases} \tag{4.1}$$

58 galaxies without an Hα detection are removed, leaving 119 galaxies. An additional 4 galaxies are removed from this sample due to Grizli failing to extract Hα maps. For the remaining 115 galaxies, the F140W postage stamps obtained through Grizli are checked against the F140W cutouts of the same galaxies obtained through the GALFIT size determination process in Chapter 2 (details described in Section 2.1.3.3) to check for object mismatches between the Grizli and original catalogues. The remaining galaxies have their Hα maps cleaned and quality checked by eye (details of this procedure are given in Section 4.2.3). 29 galaxies are removed during this process (reasoning discussed in Section 4.2.3), leaving a final sample of 86. These 86 galaxies, relative to the original full sample of star-forming cluster galaxies that were studied in Chapter 2, can be seen in the context of the *UVJ* diagram in the left-hand panel of Figure 4.3. Since the sample size has considerably reduced from the original sample of star-forming cluster galaxies that was studied in Chapter 2, we perform additional checks to ensure the sample of star-forming cluster galaxies studied in this chapter are representative of the sample studied in Chapter 2. Figure 4.4 shows the redshift and stellar mass distributions of the two aforementioned samples. The mean redshift and stellar mass of the Hα sample are almost identical to those of the full sample of star-forming cluster galaxies studied in Chapter 2. This suggests that the Hα detected sample studied in this chapter is representative of the original sample of star-forming cluster galaxies studied in Chapter 2.

4.2.2.2 Field sample

The field sample of galaxies used in this chapter is extracted from the GCLASS survey (Section 4.1.1) and its HST data (Section 4.1.2). By not using galaxies from the 3D-HST/CANDELS survey as in Chapter 2, we are able to provide a consistency check on results from a similar study conducted by the 3D-HST team in Nelson et al. (2016b) to the one presented in this chapter.

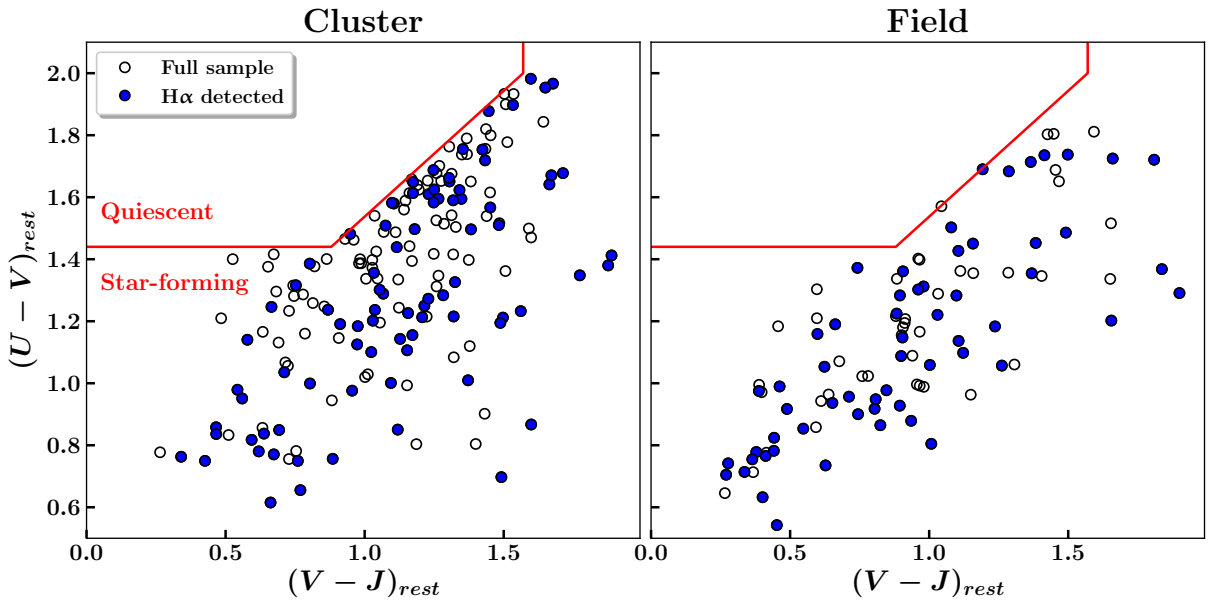

Figure 4.3: *UVJ* diagrams showing the sample of galaxies used for the study presented in this chapter. Left panel: The star-forming cluster galaxies that were studied in Chapter 2 (open + blue filled points) in comparison to the star-forming cluster galaxies studied in this chapter (blue filled points). Right panel: The star-forming field galaxies with (filled blue points) and without (open points) Hα detections as part of the Grizli data reduction process. Both cluster and field samples are selected based on the same F140W magnitude, size, stellar mass and rest-frame colour criteria (see Sections 4.2.2.1 and 4.2.2.2 for more details). The red line is the dividing line used to define quiescent and star-forming galaxies of which the star-forming region is defined in Equation 4.1 and the quiescent region by equations 2.4 and 2.5. The red line is the same line shown in Figure 2.3.

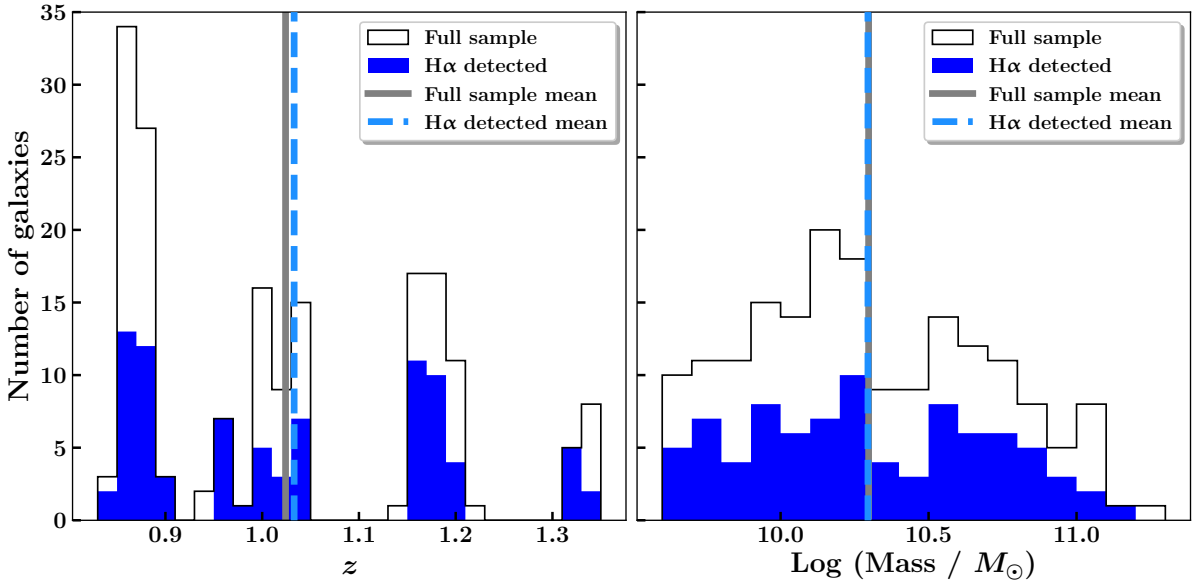

Figure 4.4: Comparison of Hα detected sample to the original sample of star-forming cluster galaxies studied in Chapter 2. Left panel: redshift distribution. Right panel: stellar mass distribution. The Hα detected sample has an almost identical mean redshift and stellar mass to the original sample of star-forming cluster galaxies studied in Chapter 2.

Firstly, those galaxies in GCLASS for which a good quality spectroscopic redshift with GMOS was obtained, lie at $z > z_{clust} + 0.1$ or $z < z_{clust} - 0.1$ (where z_{clust} is the redshift of the cluster, in most cases the redshift of the Brightest Cluster Galaxy (BCG)), but are still within $0.86 < z < 1.34$, are the first galaxies to be selected for the field sample.

Then, all those galaxies with poor-quality spectroscopic redshifts obtained with GMOS are cross-matched with the grism redshift catalogue to check for good-quality grism redshifts that lie within $z > z_{clust} + 0.1$ or $z < z_{clust} - 0.1$ and $0.86 < z < 1.34$. The grism spectra were quality-checked by eye, based on the criteria outlined in Section 2.1.1.4 of Chapter 2. The grism redshifts are derived from fitting the 12-band photometry and grism spectra simultaneously (described in Figure 2.5 and associated text in Section 2.1.4.3).

Out of the two sample selections described above, only star-forming galaxies (based on the *UVJ* star-forming selection criteria for GCLASS *cluster* galaxies, defined in Equation 4.1) with stellar masses $\mathrm{Log}(M_*/M_\odot) \geqslant 9.60$, half-light radii, $R_{eff} < 50$ kpc, F140W magnitudes < 25 (see Section 4.2.2.1 for reasoning) and Hα detected are selected. For the resulting 78 galaxies, the F140W postage stamps obtained through Grizli are checked against the F140W cutouts of the same galaxies obtained during the GALFIT size determination process in Chapter 2 (described in Section 2.1.3) to check for mismatches between the Grizli and original catalogues. The GALFIT fits for these galaxies are also quality-checked, based on the criteria outlined in Section 2.1.3.4. The remaining galaxies have their Hα maps cleaned and quality checked by eye (details of this procedure are given in Section 4.2.3). Seventeen galaxies are removed from the sample during this process, leaving a final sample of 61 galaxies. The sample of 61 field galaxies can be seen relative to the full sample of field galaxies in the right-hand panel of Figure 4.3. The full sample of field galaxies (open and filled points in the right-hand panel of Figure 4.3) includes those galaxies which did not obtain a Hα detection and/or a Hα map as part of the Grizli data reduction process, but met all other criteria as part of the field sample selection.

4.2.3 Stacking

The contamination maps that are output as part of the Grizli data reduction process (Section 4.2.1 and Figure 4.1) provide information on how much contaminating flux there is in each Hα map per pixel. One can therefore select a contamination threshold dictating which of these pixels are to be completely masked in the Hα map. During the determination of this threshold, a balance needs to be struck between strict masking (most of the Hα emission itself becomes masked) and relaxed

masking (resulting stacks become very noisy). We therefore choose this threshold based on how clean the resulting stacks look by eye. Any pixel in the contamination map which had Hα flux $> 3 \times 10^{-19}$ ergs s^{-1} cm^{-2} is masked in the Hα map. Following this procedure, when the Hα maps are quality checked during sample selection (Section 4.2.2), if $\gtrsim$ 30% of the Hα emission's spatial coverage is masked, the galaxy is removed from the sample.

Stacking is done in four bins of stellar mass for each sample: $9.6 < \mathrm{Log}(\mathcal{M}_*/\mathrm{M}_\odot) \leqslant 10.0$, $10.0 < \mathrm{Log}(\mathcal{M}_*/\mathrm{M}_\odot) \leqslant 10.5$, $10.5 < \mathrm{Log}(\mathcal{M}_*/\mathrm{M}_\odot) \leqslant 11.0$ and $11.0 < \mathrm{Log}(\mathcal{M}_*/\mathrm{M}_\odot) \leqslant 11.5$. Once sorted into these three stellar mass bins, each F140W and Hα map is normalised and weighted by its F140W flux from the photometric catalogue. Explicitly, each map is multiplied by the mean F140W flux of the stack it belongs to, and divided by the total F140W flux for that particular galaxy. All F140W total fluxes are taken from the GCLASS photometric catalogues. The F140W and Hα maps are then summed within each stellar mass bin.

To create exposure-corrected F140W stacks, we sum all the segmentation maps for each galaxy within each stellar mass bin, and divide the final F140W stack by this summed segmentation map. For the exposure-corrected Hα stacks, we first combine the segmentation maps and contamination maps for each galaxy. This creates a map of all the unmasked and masked pixels in each Hα map. We then sum these maps for each stack, and divide the final Hα stack by this summed map. Next, we rescale the Hα emission in the Hα stacks to account for contaminating [N II] emission. Since the G141 grism has low spectral resolution (see Section 4.1.2.1), Hα λ6563 and [N II] $\lambda\lambda$6548 + 6583 are blended. To obtain the normalisation factor for this rescaling, we first use Equation 8 of Sobral et al. (2015) shown below in Equation 4.2, to obtain values for the flux ratio between the [N II] and Hα emission, $f([\mathrm{N\,II}]/\mathrm{H}\alpha)$, in each stack[†]. For the equivalent width of the Hα+[N II] emission, $\mathrm{EW}_{\mathrm{H}\alpha+[\mathrm{N\,II}]}$, we use the H$\alpha$ equivalent widths output by Grizli for each galaxy, and take the median value for each stack.

$$f([\mathrm{N\,II}]/\mathrm{H}\alpha) = -0.296 \times \mathrm{Log}_{10}(\mathrm{EW}_{\mathrm{H}\alpha+[\mathrm{N\,II}]}) + 0.8 \tag{4.2}$$

The Hα flux in each stack is scaled down by the normalisation factor $1 + f([\mathrm{N\,II}]/\mathrm{H}\alpha)$, where the rescaled H$\alpha$ flux, $\mathrm{H}\alpha_{\mathrm{rescaled}}$, is defined in Equation 4.3 below.

$$\mathrm{H}\alpha_{\mathrm{rescaled}} = \frac{\mathrm{H}\alpha_{\mathrm{measured}}}{1 + f([\mathrm{N\,II}]/\mathrm{H}\alpha)} \tag{4.3}$$

[†]This relation was derived from the observed relationship between $f([\mathrm{N\,II}]/\mathrm{H}\alpha)$ and rest-frame $\mathrm{EW}_{\mathrm{H}\alpha+[\mathrm{N\,II}]}$ for a large sample of $z = 0.8$ emission-line galaxies using FMOS and MOSFIRE spectra (see Section 4.1 of Sobral et al. 2015).

4.2.4 Size determination

The initial size determination process for measuring the spatial extent of the F140W and Hα emission in each stack (see Section 4.2.4) is conducted using SExtractor (Bertin & Arnouts, 1996) and GALFIT (Peng et al., 2002, 2010a). SExtractor requires weight images for each stack, and GALFIT requires PSFs and sigma images for each stack. The construction of these maps is explained in detail in this Section.

4.2.4.1 Source detection

SExtractor v2.19.5 (Bertin & Arnouts, 1996) is used to obtain preliminary measurements on the shape parameters (position (x, y), axis ratio, half-light radius and position angle) and photometry (F140W or Hα magnitude) for each F140W and Hα stack. The SExtractor set-up is standard, details of which can be found in Appendix D. Our SExtractor set-up requires a weight image for each stack, which provides values for the inverse variance per pixel such that variable noise across the image is taken into account during source detection. These weight images are output by Grizli for each individual F140W and Hα map. To create one for each stack, the individual weight maps are first summed over each pixel. A mask is created for each individual weight map, indicating which pixels contain a value (marked with a value of 1), and which pixels do not (marked with a value of 0). These masks are then also summed over each pixel. The summed weight map is then divided by this mask to create a weight map for the stack.

4.2.4.2 Noise estimation

We use the weight maps for the stacks described in Section 4.2.4.1 to calculate the background noise per pixel. The background noise per pixel, σ, is equal to $1/\sqrt{\text{weight}}$, since the weight map provides the inverse variance per pixel.

4.2.4.3 Structural parameters with GALFIT

We use our custom-built GALFIT wrapper described in Section 2.1.3.3 of Chapter 2 to measure the half-light radii of the F140W and Hα emission in our stacks. GALFIT is software which fits two-dimensional analytic functions to light profiles in an image (Peng et al., 2002, 2010a). We fit our stacks with a single-component Sérsic profile, which is defined in Equation 2.1, Chapter 2.

As well as noise maps (Section 4.2.4.2), GALFIT requires a PSF to account for image smearing due to the resolution limit of WFC3. We create PSFs for each stack by stacking the F140W PSFs for

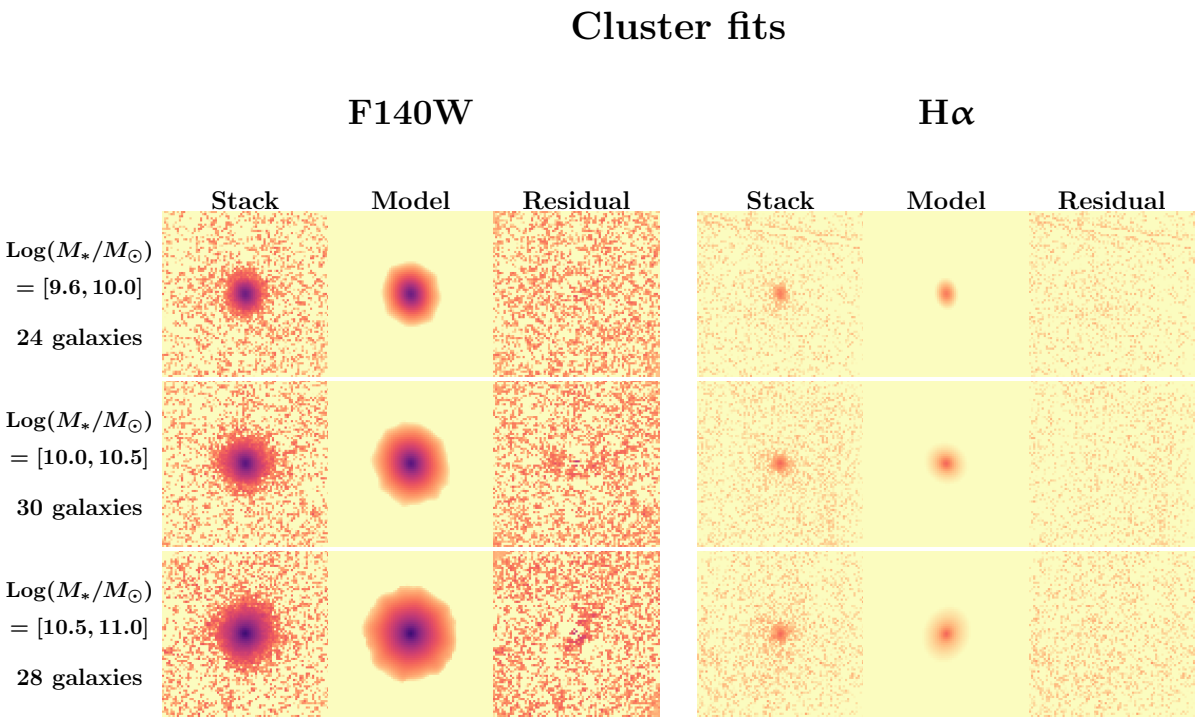

Figure 4.5: F140W and Hα stacks for the cluster sample and their associated two-dimensional model fits from GALFIT. The colourmap is logarithmic.

individual galaxies obtained from the Grizli data reduction process (Section 4.2.1). We stack these in the same way the weight maps are stacked (Section 4.2.4.1). The PSFs for each stack are summed, then divided by a mask indicating how many individual PSFs in the stack contained flux per pixel[‡].

We use the two-GALFIT-run approach described in Section 2.1.3.3 of Chapter 2 to measure the half-light radii of the F140W and Hα stacks. This approach runs GALFIT twice on each stack in succession. For the first run, our GALFIT wrapper uses the values for position (x, y pixel coordinates), F140W magnitude, half-light radius, axis ratio and position angle from the SExtractor catalogues for each stack as initial estimates. The initial value for Sérsic index is set at 2.5. All parameters are left free in the fit. This GALFIT run provides refined values for the galaxy stack shape parameters (position, axis ratio and position angle). The second GALFIT run takes these refined values and keeps them fixed in the fit. The parameters left free are F140W magnitude (initial estimate from SExtractor), half-light radius (initial estimate from SExtractor) and Sérsic index (initial value set at 2.5). This two-GALFIT-run approach was shown to be effective in the size determination process for the study presented in Chapter 2 (see Section 2.1.3.3 and Appendix B).

During the two-GALFIT-run approach, we found that the half-light radius and Sérsic index are particularly unstable for some Hα stacks. Upon closer inspection of the Hα stacks, it was found that

‡

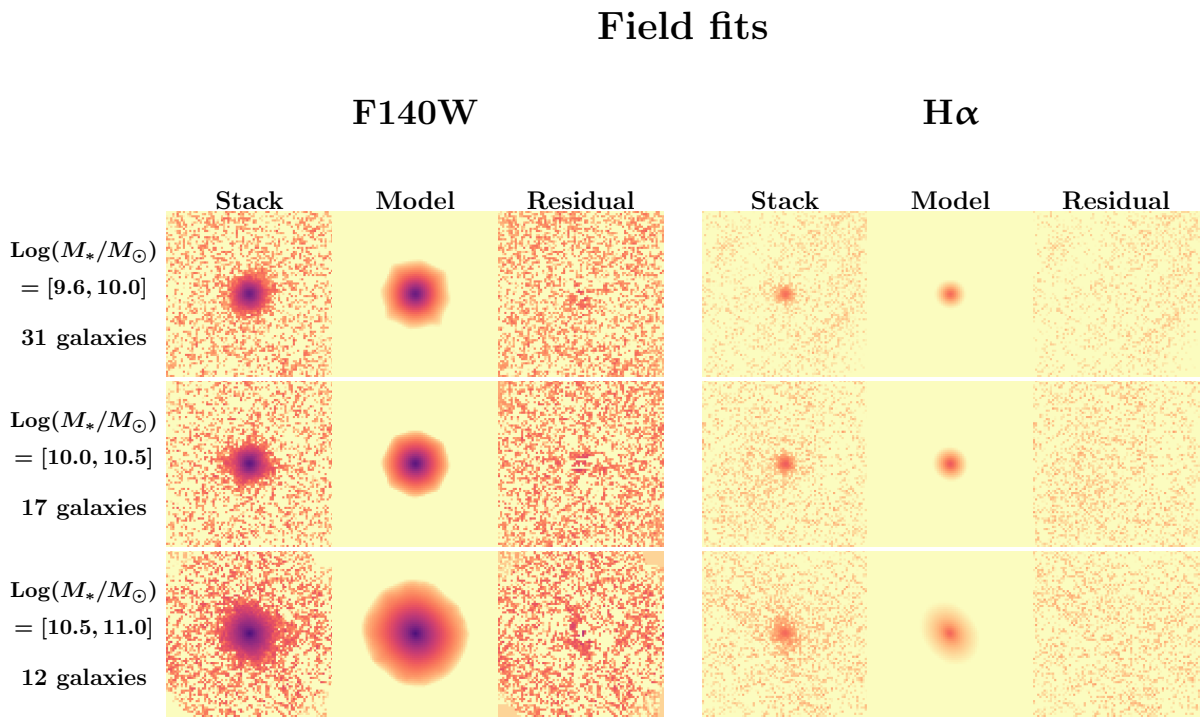

Figure 4.6: F140W and Hα stacks for the field sample and their associated two-dimensional model fits from GALFIT. The colourmap is logarithmic.

poor contamination and continuum subtraction had led to non-trivial residual background which could not be described by a constant or linear gradient. GALFIT is unable to fit for such a background. Furthermore, there is also low signal-to-noise ratio in Hα. Together, these challenges make it difficult for GALFIT to fit Sérsic profiles which have reasonable structural parameters to the stacks. Similarly, we found that a single component Sérsic profile was an insufficient model when fitting the F140W stacks for the third stellar mass bin in both the cluster and field samples. Due to the high concentration of light in the central regions of these stacks, a single component Sérsic profile was often skewed towards abnormally large Sérsic indices, leading to large low surface brightness wings in the model. In this scenario, the combination of a point source model and Sérsic model mitigated this problem. The point source model accounts for the high concentration of light in the centre, such that the resulting Sérsic model is reasonable.

We show our GALFIT fits to the stacks for the cluster and field samples in Figures 4.5 and 4.6 respectively. Due to very few galaxies being in the largest stellar mass bin of $11.0 < \mathrm{Log}(\mathcal{M}_*/\mathrm{M}_\odot) \leqslant 11.5$ (4 for the cluster sample and 1 for the field sample), we removed these galaxies from our sample and did not conduct measurements for this stellar mass bin. Final measurements are therefore based on a total of 82 cluster galaxies and 60 field galaxies.

To provide more reliable size measurements of the stacks, we also measured the half-light radii of

all the stacks non-parametrically, without using GALFIT. Details of this process are explained in the next Section.

4.2.4.4 Non-parametric fitting

Before we conduct non-parametric fitting of the F140W and Hα stacks, we attempt to deal with the poor background subtraction. To correct for this, we calculate the median value of all the pixels beyond an aperture of radius 35 pixels (each postage stamp is 80 $\times$ 80 pixels) for each stack, and subtract this value from all the pixels in that stack. The size of this aperture is comparable to the size of each postage stamp, suggesting that we can be fairly confident minimal flux from the galaxy is contributing to pixels outside the aperture.

To measure the half-light radii of the F140W and Hα stacks non-parametrically, we first construct their growth curves. These are calculated by integrating the mean flux from the centre of the stack to the outskirts of the postage stamp within concentric rings spaced by one pixel scale. The mean flux within each concentric ring is weighted based on the weights for each pixel in the Grizli weight map (Section 4.2.4.1) and another weight map based on the fraction of each pixel that lies within each concentric ring. The total flux is taken to be the absolute maximum of the growth curve. At half the total flux, we linearly interpolate to find the half-light radius. The curves of growth (up to their absolute maximum), F140W and Hα background-corrected stacks are shown in Figures 4.7 and 4.8 for the cluster and field samples respectively. In the third columns of both Figures 4.7 and 4.8, we also show the F140W and Hα surface brightness profiles. These were constructed by calculating the weighted mean of the flux within concentric rings spaced by one pixel scale. The mean flux within each concentric ring is weighted based on the weights for each pixel in the Grizli weight map (Section 4.2.4.1) and another weight map based on the fraction of each pixel that lies within each concentric ring. The surface brightness profiles and curves of growth have been normalised by their maximum values, and the calculated half-light radii are marked with small vertical lines. Error bars for the surface brightness profiles are the weighted standard deviations in each concentric ring.

4.3 The stellar continuum versus Hα mass–size relation in clusters and the field at $z \sim 1$

4.3.1 GALFIT results

We take the half-light radii results output by GALFIT in pixels and convert them to kiloparsecs. To do this, we first find the mean redshift of the galaxies within each stack. We then calculate the half-light

Cluster

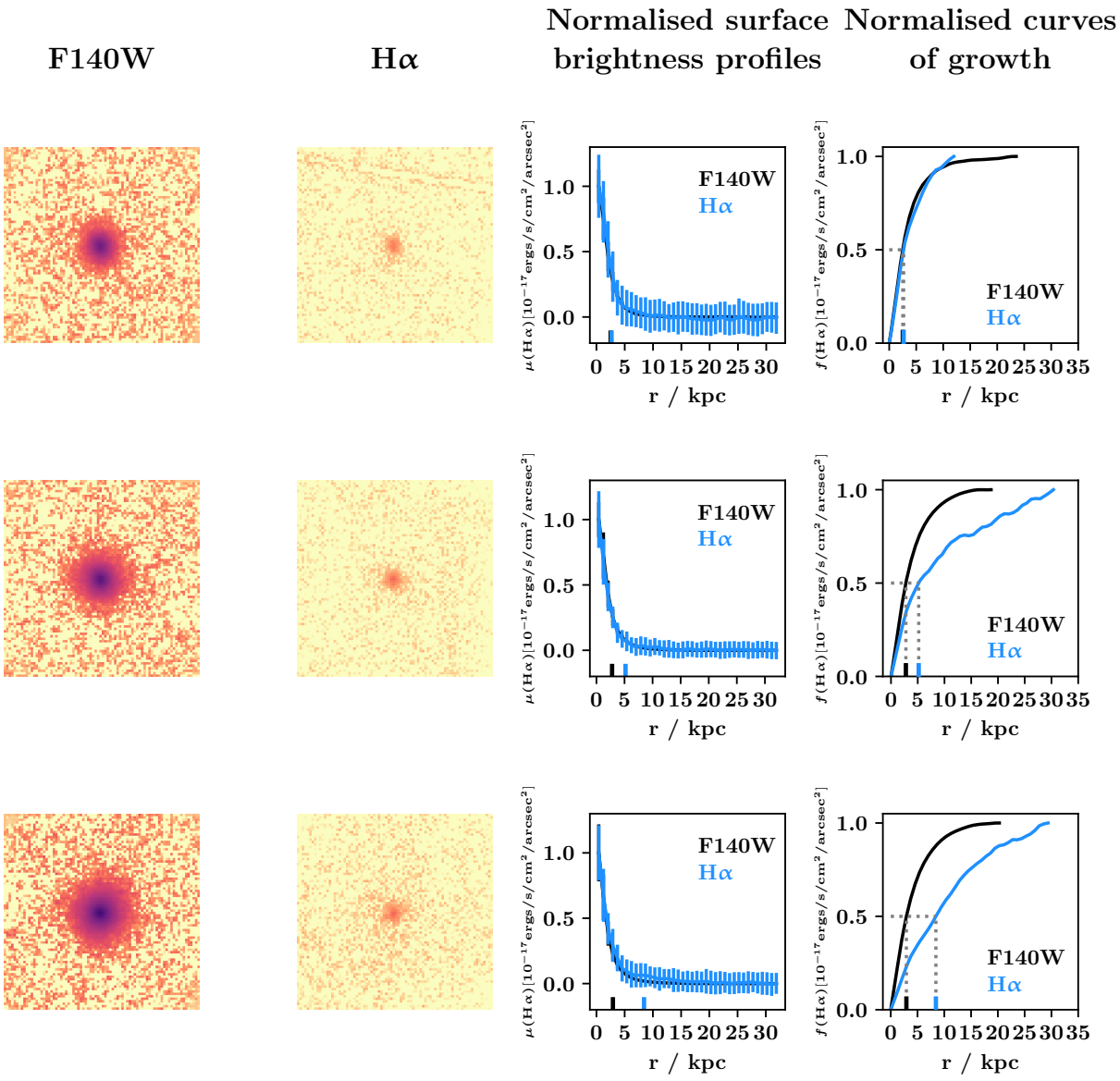

Figure 4.7: F140W and Hα stacks for the cluster sample, their normalised surface brightness profiles and their normalised curves of growth. Half-light radii from non-parametric fitting are marked with small solid vertical lines. The colourmap is logarithmic.

Field

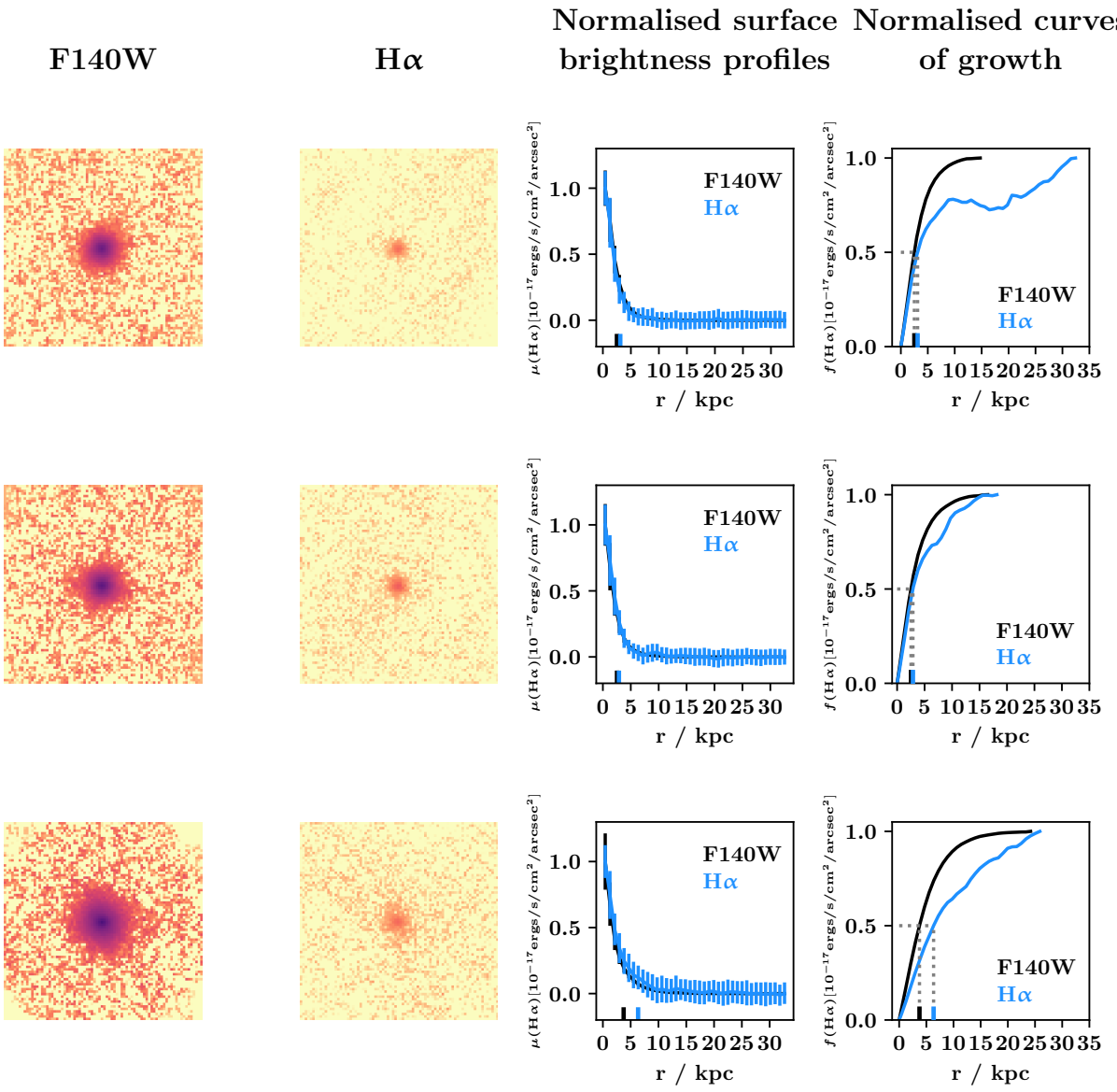

Figure 4.8: F140W and Hα stacks for the field sample, their normalised surface brightness profiles and their normalised curves of growth. Half-light radii from non-parametric fitting are marked with small solid vertical lines. The colourmap is logarithmic.

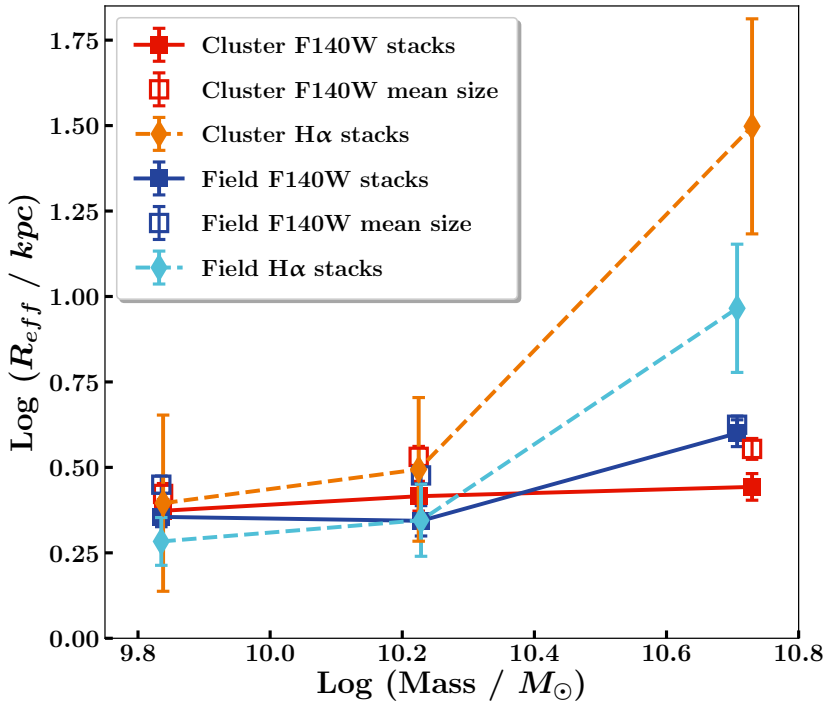

Figure 4.9: The F140W (filled square points with solid lines) and Hα (diamonds with dashed lines) stellar mass–size relations for cluster and field star-forming galaxies at $0.86 < z < 1.34$ using GALFIT measurements. Mean F140W sizes (open squares) are obtained from the individual sizes for each galaxy that go into the stack. These individual sizes were obtained from their individual GALFIT fits in F140W during the study presented in Chapter 2. For the stacks, errors are calculated using bootstrapping and represent one standard deviation. For the F140W mean sizes, the errors are the standard errors in the mean.

radius, R_{eff}, for each stack in kiloparsecs using the angular diameter distance to this redshift. Similarly, we also find the mean stellar mass[§] for the galaxies in each stack. The stellar mass–size relation for the F140W and Hα stacks can be seen in Figure 4.9.

The open square points are the F140W mean sizes of galaxies within each stack based on their individual GALFIT results, which were obtained during the study presented in Chapter 2. They provide a sanity check for the sizes obtained from the F140W stacks, since they should follow them closely.

Errors for the stacks are standard deviations from 1000 bootstrap resamples for each stack. The entire GALFIT size determination process is carried out (see Section 4.2.4) on each bootstrap resample. For the F140W mean sizes, the errors are the standard errors on the mean.

It can be seen in Figure 4.9 that there is no significant difference between the F140W and Hα sizes in the cluster and field, except perhaps for the largest stellar mass bin. In the largest stellar mass bin of the cluster and field samples, the Hα emission has a larger half-light radius than the F140W emission by ~ 3 and $\sim 2\sigma$ respectively.

[§]These stellar masses are corrected for the difference between the total F140W flux from the photometric catalogue and the total F140W flux as measured by GALFIT.

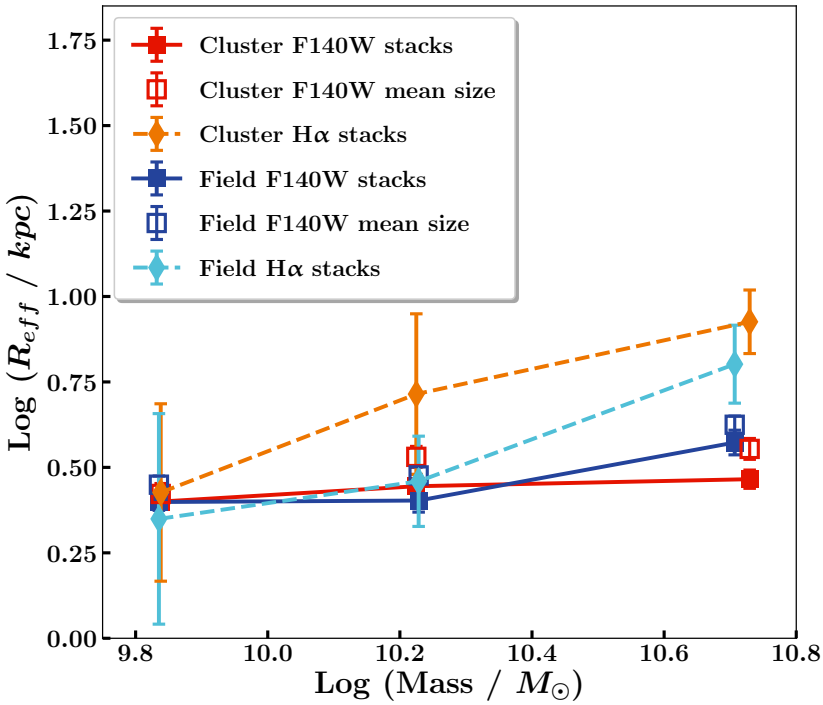

Figure 4.10: The F140W (filled square points with solid lines) and Hα (diamonds with dashed lines) stellar mass–size relations for cluster and field star-forming galaxies at $0.86 < z < 1.34$ using non-parametric size measurements. Mean F140W sizes (open squares) are obtained from the individual sizes for each galaxy that go into the stack. These individual sizes were obtained from their individual GALFIT fits in F140W during the study presented in Chapter 2. Errors show one standard deviation, and are a combination of systematic errors and random errors from bootstrapping (see Section 4.3.2 for details).

4.3.2 Non-parametric results

Figure 4.10 shows the stellar mass–size relation for the F140W and Hα stacks where the half-light radii have been measured from non-parametric fitting. Half-light radii are converted to kiloparsecs in the same way as described in Section 4.3.1. Similarly, the stellar masses for each stack are also calculated in the same way as described in Section 4.3.1.

The error bars are a combination of systematic and random uncertainties. To calculate systematic uncertainties, we vary the aperture size that is used to determine the background correction by $\pm$5 pixels (see Section 4.2.4.4). We also measure the total flux from the *first* maximum reached in the growth curve as well as from the absolute maximum. The systematic error is the standard deviation of the size measurements obtained from these variations in the size determination process. Random errors are calculated by taking 1000 bootstrap resamples of each stack and measuring the half-light radius for each using the method described in Section 4.2.4.4. The systematic and random error for each stack is then added in quadrature.

Reassuringly, we see similar trends in Figures 4.10 and 4.9. The F140W results are almost identical between the two size determination methods. Although the non-parametric F140W results (filled

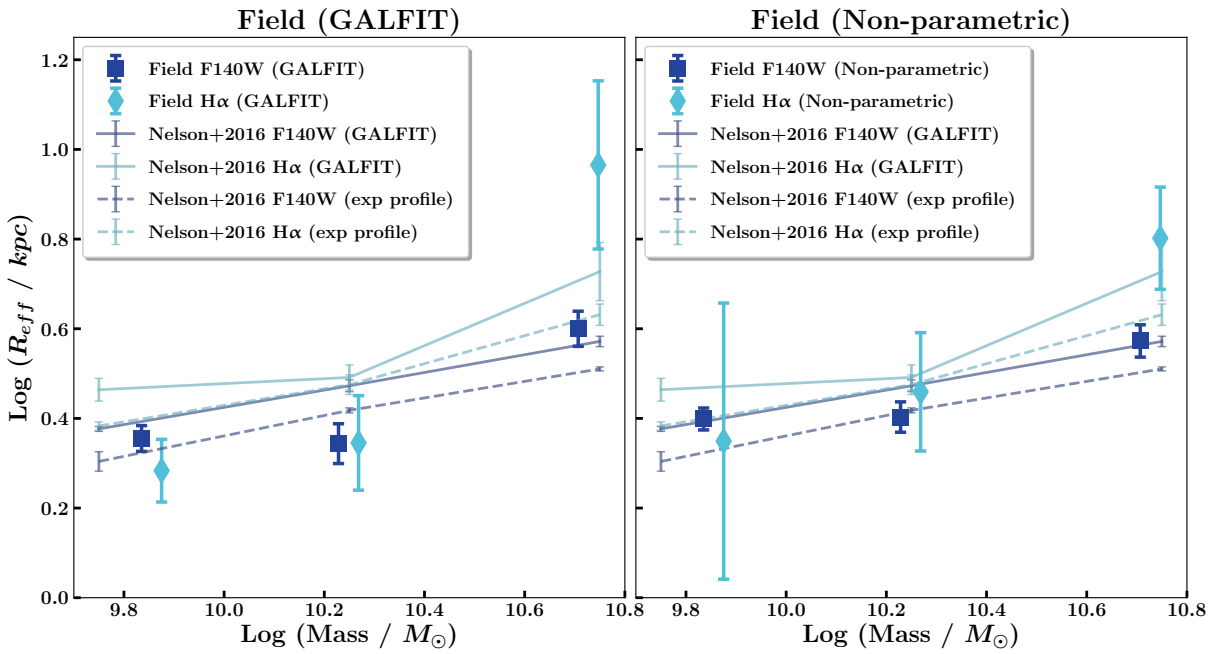

Figure 4.11: The F140W and Hα stellar mass–size relations for star-forming field galaxies at $z \sim 1$ from GCLASS and 3D-HST (Nelson et al., 2016b). GCLASS F140W and Hα measurements are shown as filled square points and diamonds, respectively. The GCLASS Hα measurements are offset from the GCLASS F140W measurements by $+0.04$ dex in stellar mass for clarity. Left-panel shows our GALFIT measurements against those of Nelson et al. (2016b). Right-panel shows our non-parametric size measurements against those of Nelson et al. (2016b). We show results from both methods Nelson et al. (2016b) used to measure the half-light radii of each stack: GALFIT (solid lines with error bars) and fitting exponential profiles to the one-dimensional surface brightness profiles (dashed lines with error bars). For the non-parametric fits, errors are a combination of systematic errors and random errors from bootstrapping (see Section 4.3.2 for details). For all other measurements, errors are calculated from bootstrapping. All errors show one standard deviation.

squares and solid lines in Figure 4.10) are closer to the F140W mean sizes (open square points) at fixed stellar mass compared to the GALFIT F140W results for each environment.

There are more differences between the Hα size measurements between the two size determination methods. However, the general trends of increasing Hα size with stellar mass, and larger Hα sizes with respect to F140W sizes in the largest stellar mass bin are present in both sets of results. There also seems to be a clearer trend of increasing Hα size with respect to F140W size at fixed stellar mass for the cluster sample in the non-parametric fits (see orange diamonds and filled red squares in Figure 4.10).

4.4 Discussion

4.4.1 Comparison of field results with previous work

As mentioned in Section 4.2.2.2, we conducted measurements on a sample of field galaxies drawn from GCLASS to serve as a consistency check to the field results presented in Nelson et al. (2016b) at a similar redshift. Our field results in comparison to the field results presented in Nelson et al. (2016b) are shown in Figure 4.11. Our GALFIT results are shown against the results of Nelson et al.

(2016b) in the left-panel and our non-parametric results are shown in the right-panel against the results of Nelson et al. (2016b). GCLASS results are shown as filled square and diamond points. GCLASS Hα results are offset in stellar mass by +0.04 dex from the GCLASS F140W results for clarity. Two methods were used to measure the spatial extent of the Hα emission in Nelson et al. (2016b). Single-component Sérsic profiles were fit to the stacks using GALFIT and exponential profiles were fit to the one-dimensional surface brightness profiles of the stacks between $0.5r_s < r < 3r_s$[¶]. We show the Nelson et al. (2016b) results from both these size determination methods in Figure 4.11. The results from Nelson et al. (2016b) are plotted at the midpoint of their mass bins for each stack.

It can be clearly seen that there is better agreement between the results in Nelson et al. (2016b) and our results from non-parametric fitting. Nevertheless, our GALFIT results are consistent with those from Nelson et al. (2016b) within $1 - 2\sigma$. The qualitative trend of greater than or equal to half-light radii in Hα compared to F140W at fixed stellar mass, as well as an increase in half-light radii with increasing stellar mass, are present in both sets of results.

Both the study presented in this chapter and the study presented in Nelson et al. (2016b) produce the stacks with the same method and measure half-light radii in the same way when using GALFIT. The difference between the method of the two studies lies in the software used to reduce the grism data – of which ours is an improved version of the software used in Nelson et al. (2016b) – and the subsequent cleaning of the Hα and F140W postage stamps. The biggest disadvantage for our measurements is the smaller sample size and therefore lower signal-to-noise ratio in Hα. Each stack in our study contains $10 - 30$ galaxies (see Figures 4.5 and 4.6) as opposed to ~ 400 for each stack in Nelson et al. (2016b).

4.4.2 The lack of an environmental quenching signature

The results in Section 4.3 suggest that there is no significant difference in the way star formation operates in cluster and field galaxies with stellar masses $\mathrm{Log}(\mathcal{M}_*/\mathrm{M}_\odot) \leqslant 10.5$, since at fixed stellar mass, the F140W and Hα half-light radii are consistent with each other within 1σ. The star formation, as dictated by the Hα emission, seems to be coincident with the underlying stellar mass distribution (traced by F140W). In the case of the cluster sample, there is even a clear trend of increasing Hα size with stellar mass, and progressively larger Hα sizes compared to F140W sizes with increasing stellar mass (Figure 4.10). This trend is more in-line with what is seen in the field environment at the same redshift in Nelson et al. (2016b), and is suggestive of inside-out growth via

[¶] r_s is the disc scale length. The half-light radius, $R_{eff} = 1.678r_s$.

star formation.

These results are at odds with observations of cluster galaxies at lower redshifts. Early results on the spatial distribution of Hα in Virgo cluster spiral galaxies versus spiral galaxies in the field found that 52% of Virgo spirals have truncated Hα discs compared to their *R*-band images as opposed to only 12% in the field (Koopmann & Kenney, 2004). It was determined that at least at low redshift, gas stripping processes such as ram-pressure stripping (Gunn & Gott, 1972) were the main quenching mechanisms responsible for shutting down star formation in cluster galaxies. Subsequent to this result, direct observations of ram-pressure stripping in the local Universe have confirmed that the process quenches galaxies from the "outside-in", leaving the overall stellar distribution intact, but forces star formation to become progressively confined towards the central regions of galaxies (Abramson et al., 2011; Ebeling et al., 2014; Bellhouse et al., 2017; Gullieuszik et al., 2017; Sheen et al., 2017; Fossati et al., 2018; Cramer et al., 2019). Therefore, at higher redshifts, evidence for ram-pressure stripping quenching cluster galaxies could be found by measuring the spatial extent of the Hα emission and comparing it to the spatial extent of its rest-frame optical emission.

We however do not see evidence for significantly truncated Hα discs in $z \sim 1$ cluster galaxies with respect to their stellar component. Despite being a surprising result, it fits well with the growing picture of environmental quenching in the literature, which suggests the rapidity of environmental quenching increases with redshift and host halo mass (see Foltz et al. 2018 and references therein). The rapidity of ram-pressure stripping at high-redshift would mean most star-forming cluster galaxies are not caught in the stripping phase, and therefore an environmental quenching signature is difficult to measure, particularly at high significance. Evidence for long-timescale (> 2 Gyr) environmental quenching at low redshift was found in Finn et al. (2018), where more centrally concentrated star formation (as traced by 24μm emission) was seen in star-forming cluster and group galaxies in contrast with star-forming field galaxies.

Furthermore, it is worth pointing out that previous studies on the GCLASS clusters which have focused on the *recently quenched* cluster galaxy population (see Section 3.1.3) have found strong evidence for environmental quenching occurring (Muzzin et al. 2012, 2014 and the study presented in Chapter 3). These studies point towards ram-pressure stripping being the likely quenching mechanism, acting within $0.4^{0.3}_{-0.4}$ Gyr after satellite cluster galaxies make their first passage of $0.5R_{200}$, leaving the stellar component of the galaxy morphologically undisturbed but truncating its measured F140W half-light radius. It seems that to find evidence of environmental quenching at high redshift, one must focus on those galaxies that have *already undergone* environmental

quenching, since the rapid decline in star formation is too fast to be observable in cluster galaxies still forming stars.

Nevertheless, ram-pressure stripping may not be the only culprit for environmentally quenching cluster galaxies at high redshift. Due to the higher star formation rates in the high-redshift Universe, galaxies will be forming stars more rapidly and could therefore exhibit higher outflow rates due to this star formation. Once such a galaxy becomes a satellite galaxy in a cluster, its supply of fresh gas from the cosmic web is cut off. The combined affect of higher outflow rates and halted cosmological accretion could quickly deplete gas in a cluster galaxy, well before ram-pressure stripping begins to act (McGee et al., 2014). There is evidence to suggest that the GCLASS cluster galaxies are more consistent with this picture of "overconsumption", with stripping processes being the sub-dominant quenching mechanism (McGee et al., 2014; Balogh et al., 2016). In lower redshift clusters, stripping processes dominate. This change in the dominant environmental quenching mechanism may explain why the environmental quenching timescales differ by a factor of $\sim$ 5 (Finn et al., 2018; Muzzin et al., 2014) in low ($z \sim 0$) and high ($z \sim 1$) redshift clusters. Consequently, it can explain why spatially truncated star formation can be seen in population studies of low redshift cluster galaxies (Koopmann & Kenney, 2004; Finn et al., 2018), but not in high redshift cluster galaxies (Section 4.3): the quenching mechanisms are fundamentally different, so the observational results are different.

There are therefore two likely scenarios to explain our results presented in Section 4.3. The first is that ram-pressure stripping is more rapid and efficient in high-redshift clusters. The second is that overconsumption is the mechanism responsible for quenching high-redshift cluster galaxies, not ram-pressure stripping. There is evidence for both these arguments in relation to the GCLASS cluster galaxies (McGee et al., 2014; Balogh et al., 2016; Foltz et al., 2018). One possible way to constrain which of these scenarios is true would be by studying the hot gas density profiles of clusters at low and high redshift as well as the physical conditions of low- and high-redshift star-forming cluster galaxies. If the gas density profiles are more centrally concentrated in high redshift clusters, with a high density gradient between the outskirts and the inner region, this could explain why ram-pressure stripping is a rapid catastrophic event for star-forming cluster galaxies, and its "outside-in" quenching signature is not observed. McDonald et al. (2017) studied the intra-cluster medium (ICM) properties of 147 galaxy clusters spanning a large range in halo mass, lying in the redshift range $0 < z < 1.9$. They found that there is no significant difference in the gas density profiles of low- and high-redshift clusters, with weak evidence of high core densities in cool-core high-redshift clusters. These results suggest that if there

is an increase in the efficiency of ram-pressure stripping towards high redshifts, it may not be due to differing ICM densities, but due to cluster galaxies having higher velocities. Contrarily, these results also suggest that overconsumption may be the more likely mechanism for quenching star formation in high-redshift cluster galaxies, and that a thorough comparison of the physical conditions in low- and high-redshift star-forming cluster galaxies is required. If most star-forming cluster galaxies quench by overconsumption well before ram-pressure stripping starts, there will be no "outside-in" quenching signature measurable in high-redshift star-forming cluster galaxies.

4.4.3 Discrepancies at high stellar masses

For star-forming galaxies with $\mathrm{Log}(\mathcal{M}_*/\mathrm{M}_\odot) > 10.5$, the relative difference in size between the Hα and F140W emission is larger in clusters (as seen in both Figure 4.9 and 4.10). Massive star-forming galaxies in clusters seem to be growing in size via inside-out star formation much more than analogous galaxies in the field. This is an unlikely scenario, since it is well-known that cluster galaxies are in general more "red and dead" compared to field galaxies. Since larger Hα sizes with respect to F140W sizes are seen *both* in the cluster and field at these stellar masses, it is likely to be an observational effect. Massive star-forming galaxies are known to contain more dust than low mass star-forming galaxies (Pannella et al., 2009; Reddy et al., 2010; Wuyts et al., 2011; Whitaker et al., 2012b; Momcheva et al., 2013; Nelson et al., 2016a; Koyama et al., 2019). Moreover, galaxies with higher SFRs tend to contain more dust than those with lower SFRs at fixed stellar mass (Reddy et al., 2010; Wuyts et al., 2011; Domínguez et al., 2013; Sobral et al., 2012; Reddy et al., 2015; Li et al., 2019). As a natural consequence of the star-formation main sequence (e.g. Whitaker et al. 2012b and many others), higher-stellar-mass galaxies have higher SFRs and are therefore more susceptible to dust attenuation. Obscuration by dust is highest at the centres of such galaxies, where column densities are at their highest (Wuyts et al., 2012; Nelson et al., 2016a). High levels of dust obscuration at the centres of these massive galaxies reduces the observed Hα flux from this region, making the Hα profiles *less* centrally concentrated (Nelson et al., 2016a). This leads to an increase in the half-light radius and could explain why we only measure more extended Hα emission relative to F140W flux for the highest mass galaxies.

Furthermore, significant dust extinction at the centres of galaxies may be obscuring on-going bulge stellar mass growth via star formation. This problem is more important for cluster galaxies undergoing outside-in quenching. Since star formation is forced to occur at smaller and smaller radii in the galaxy, outside-in quenching can potentially explain the bulgier morphologies of cluster galaxies (see also Jaffé et al. 2011; Fraser-McKelvie et al. 2018; Cramer et al. 2019 and Section 3.6.2). More bulge-dominated

morphologies lead to *smaller* half-light radii. If there is significant dust obscuration of Hα emission from the bulges of star-forming cluster galaxies, this will reduce flux from the central regions of the resulting Hα stacks, leading to a *rise* in the half-light radius. This affect has the ability to washout an outside-in quenching signal and may be a contributing factor to why such a signal is not seen in the star-forming cluster galaxies (see also Section 4.4.2).

4.4.4 Future work

The results in Section 4.3 represent the most straightforward attempt to measuring an environmental quenching signature with our data. As discussed in Sections 4.4.2 and 4.4.3, there are multiple reasons for why this signal may not be present or may be diluted. In this Section we outline some approaches we could take to refine our search for an environmental quenching signature with our data.

1. Most of the star-forming cluster galaxies in our sample are situated in the outskirts of their clusters (Muzzin et al., 2014). This means the majority of them have not been subjected to environmental effects yet. This could also explain why we even see evidence for inside-out growth via star formation in the clusters (Figure 4.10), that is consistent with what is seen in the field environment at the same redshift (Nelson et al., 2016b). Furthermore, most of the recently quenched cluster galaxies lie within $0.5R_{200}$ (Muzzin et al., 2014). It is possible that if we re-do the above analysis using only those star-forming cluster galaxies lying at $R < 0.5R_{200}$, we may see truncated Hα discs. Woo et al. (2013) found that the correlation between halo mass and quenching is strongest in low redshift groups within $0.3R_{vir}$[‖], suggesting that this radial-binning approach may be successful in exposing an environmental quenching signal. Similarly, Finn et al. (2018) found that low-redshift star-forming galaxies closer to the cores of their clusters or groups had more truncated and concentrated 24μm emission with respect to their stellar component. More recently, Owers et al. (2019) found that their low-redshift recently quenched cluster population were all situated within $R < 0.6R_{200}$, with most of them showing evidence of outside-in quenching from their Hα distributions.

2. Those star-forming cluster galaxies with the highest specific star formation rates (sSFRs) are likely to have more Hα emission. Removing star-forming galaxies from the cluster sample that have very low signal-to-noise ratios in Hα can increase the precision of our measurements shown in Figures 4.9 and 4.10. Changing the sample selection in this way may reveal an outside-in quenching signal.

3. A combination of the above two binning approaches could also further expose an environmental quenching signal.

4. During the non-parametric fitting (Section 4.2.4.4), it was discovered that the background had been poorly subtracted from the imaging. This left a non-trivial background that was difficult for GALFIT to fit Sérsic profiles to reliably. Improving the background subtraction in the imaging should lead to more reliable half-light radius measurements with GALFIT.

[‖]Where R_{vir} is the virial radius of the group.

5. Some of the Hα emission from star-forming regions gets absorbed by dust and is not observed. This leads us to systematically underestimate the levels of star formation occurring in galaxies when using Hα measurements. One way to correct for this systematic using our data is to construct spatially resolved maps of the Balmer decrement, Hα/Hβ, since dust attenuation is wavelength dependent. With our data, this can only be done for galaxies in the redshift range $1.35 < z < 1.5$. It is within this redshift window that both Hα and Hβ fall within the wavelength coverage of the G141 grism. This will therefore only be possible for galaxies in the highest redshift cluster at $z = 1.34$, SpARCS-0035 (see Table 2.1). Nevertheless, it may be able to provide some insight into the typical dust distributions in high-redshift cluster galaxies and how this affects the measurements presented in this chapter. The 3D-HST team were able to measure spatially resolved Balmer decrements for 609 galaxies at $1.35 < z < 1.5$ using their G141 data. They found that dust attenuation was highest in the central regions of galaxies with a mean stellar mass of $\mathrm{Log}(\mathcal{M}_*/\mathrm{M}_\odot) = 10.2$. This led to a factor 6 higher SFR within 1 kpc from the centre of these galaxies (Nelson et al., 2016a). As discussed in Section 4.4.3, this could lead to more centrally concentrated spatial distributions of Hα and therefore smaller half-light radii in Hα at these high masses.

4.5 Summary

In this chapter, we have measured the spatial extent of Hα and F140W emission in cluster and field galaxies at $z \sim 1$ to study whether there is evidence for environmental quenching occurring in star-forming cluster galaxies. Our results are summarised below:

1. We find no significant difference between the spatial extent of Hα and F140W emission in star-forming cluster and field galaxies with stellar masses $\mathrm{Log}(\mathcal{M}_*/\mathrm{M}_\odot) \leqslant 10.5$. However, there is a clear trend of increasing Hα size with respect to F140W size as stellar mass increases in the cluster sample (Figure 4.10). This is suggestive of inside-out growth via star formation.

2. Cluster and field galaxies with stellar masses greater than $\mathrm{Log}(\mathcal{M}_*/\mathrm{M}_\odot) = 10.5$ are found to have more extended Hα emission with respect to their F140W emission. This is likely due to significant dust attenuation which can reduce the concentration of light at the centre of the Hα stacks, inflating its half-light radius.

3. A stronger environmental signal might be observed if the analysis is repeated using *only* star-forming cluster galaxies that are situated well within their clusters and have higher signal-to-noise ratios in Hα flux.

If a child grows up to be a scientist, he finds that he is paid to play all day the most exciting game ever devised by mankind.

Murray Gell-Mann

5

Summary & future prospects

The foundations of this thesis rest upon unprecedented *Hubble Space Telescope* (HST) *Wide Field Camera 3* (WFC3) imaging and grism spectroscopy that is amongst the first of its kind for galaxy clusters outside the local Universe (see also GLASS, e.g. Vulcani et al. 2015, 2016; Hoag et al. 2016; Morishita et al. 2017; Wang et al. 2017; Schmidt et al. 2017; Abramson et al. 2018). Yet it must be emphasised that high-quality data on their own do not necessarily ensure successful scientific output. The combination of high-resolution imaging and spatially resolved spectroscopy from HST with ancillary photometry and spectroscopy from previous observational campaigns – such as the *Spitzer* Adaptation of the Red-sequence Cluster Survey (SpARCS) and the Gemini Cluster Astrophysics Spectroscopic Survey (GCLASS) – significantly enhanced the conclusions we could draw from the studies presented in Chapters 2, 3 and 4.

The statistical power of the study presented on the mass–size relation environmental comparison at $z \sim 1$ (Chapter 2) was enhanced for our cluster sample by combining the GMOS spectroscopy from GCLASS and the grism spectroscopy from HST. This synergy led to more than a factor of two improvement in precision when identifying cluster members using grism-derived as opposed to photometric redshifts, introducing 182 newly identified cluster galaxies to the original spectroscopic sample of 344. This led to the largest spectroscopically confirmed sample of cluster galaxies at this redshift.

In the study presented in Chapter 3, the combination of the GMOS spectroscopy with the F140W WFC3 HST imaging allowed for improved constraints on the likely environmental quenching mechanism responsible for creating the recently quenched cluster galaxy population. Together, the studies presented in Chapters 2 and 3 were able to show *both* minor mergers and progenitor bias – which were previously two somewhat contested theories – are responsible for the observed growth in the average size of quiescent galaxies with decreasing redshift.

The power of space-based slitless spectroscopy was demonstrated in Chapter 4, with the first spatially resolved Hα maps of cluster galaxies beyond the local Universe. Due to the large sample of cluster galaxies compiled as part of Chapter 2, a stacking analysis allowed us to boost our signal-to-noise ratio in Hα and make the first measurements of the spatial extent of Hα in comparison to the stellar component in spectroscopically confirmed cluster galaxies at $z \sim 1$. The lack of a clear environmental quenching signature in this study hints at the possible change in the physics that drives environmental quenching in the high redshift Universe and/or its efficiency. This result opens up clear opportunities for observations in this field with the next generation of space-based slitless spectrographs on-board the *James Webb Space Telescope* (JWST), *Euclid* and the *Wide-Field Infrared Survey Telescope* (WFIRST). Uniquely, JWST will allow us to push the study of galaxy growth and quenching to much earlier times in the Universe, enabling us to gain insight into the onset of these physical processes.

To summarise, the main conclusions of this thesis are:

1. At $z \sim 1$, cluster galaxies have smaller sizes at fixed stellar mass than their counterparts in the low-density field environment. Especially in the case of quiescent galaxies, this is suggestive of minor mergers being the main driver of galaxy growth in the field environment.

2. Spectroscopically identified recently quenched galaxies in $z \sim 1$ *clusters* are found to follow a mass–size relation which almost perfectly bisects the region between the star-forming and quiescent $z \sim 1$ *field* mass–size relations. This is direct evidence for the effect of progenitor bias: galaxies which quench later are on average larger in size than galaxies that quenched earlier at fixed stellar mass. At least in the clusters, the continual addition of recently quenched galaxies to the quiescent population will induce an increase in the mean size of quiescent galaxies with decreasing redshift.

3. No outside-in quenching signature is found when comparing the spatial extend of Hα and the stellar continuum in $z \sim 1$ star-forming cluster galaxies. This may suggest that ram-pressure stripping is rapid at $z \sim 1$ or not driving environmental quenching at these redshifts. Alternatively, increasing our sample and/or using only those star-forming cluster galaxies closer to the centre of their clusters may reveal an environmental quenching signal.

5.1 Future prospects

Future work will be focused on:

1. Testing models of galaxy growth in clusters using low-redshift data (Section 5.1.1).
2. Obtaining cluster and field data over a large portion of the Universe's history to sufficiently *track* galaxy growth mechanisms (Section 5.1.2).
3. Expand studies of galaxy growth and quenching to the intermediate group environment to get a better census on the balance between these processes in the Universe (Section 5.1.3).
4. Pushing detailed studies of environmental quenching in clusters to high redshift to better understand the physics driving the shorter quenching timescales (Section 5.1.4).
5. Using direct observations of molecular gas in cluster galaxies beyond the local Universe to gain a more intimate insight into how environmental quenching mechanisms affects the fuel for star formation (Section 5.1.5).

5.1.1 Constraining galaxy growth in clusters

In Section 2.5 of Chapter 2, we presented a toy model that demonstrated cluster-specific processes could plausibly explain why there is agreement between the cluster and field quiescent stellar mass–size relations at low redshifts, despite the very different physical conditions of the two environments. The toy model places constraints on the stellar masses and sizes of Brightest Cluster Galaxies (BCGs) at low redshift, as well as the stellar mass fraction of the intra-cluster light (ICL). The natural next step after the development of such a model is to test it observationally.

The galaxy clusters in the Frontier Fields (Lotz et al., 2017) and the Cluster Lensing and Supernova Survey (CLASH, Postman et al. 2012) have halo masses that correspond to the halo masses the GCLASS clusters are expected to reach by $z \sim 0$ (van der Burg et al., 2015; Merten et al., 2015). This makes these samples of galaxy clusters probable descendants of GCLASS-like clusters at $z \sim 1$.

The Frontier Fields and CLASH data are particularly well-suited for the science requirements of this proposed study. This is because each cluster was observed with parallel fields, which provide excellent sources of *field* galaxies taken under the same observational conditions as the clusters. Such data is crucial for reducing systematics in comparison studies such as the one presented in Chapter 2 of this thesis. We can therefore use the observational data from the Frontier Fields and CLASH to test the toy model presented in Section 2.5 by:

1. Verifying whether there really is a negligible difference between the field and cluster quiescent stellar mass-size relations at low redshift.

2. Measuring the stellar masses, sizes and Sérsic profiles of the BCGs to determine whether it is plausible that they have experienced a significant number of minor mergers since $z \sim 1$.

Alternatively, clusters in the Multi-Epoch Nearby Cluster Survey (MENeaCS) are also likely descendants of the GCLASS clusters and can be used for this study (see e.g. van der Burg et al. 2015).

The proposed study above could confirm whether or not cluster-specific mechanisms capable of destroying cluster galaxies occur, and whether they are responsible for the structural properties of present day cluster galaxies.

5.1.2 Quantifying the relative importance of galaxy growth mechanisms

The biggest strength of the study presented in Chapter 3 is the direct evidence for the effects of progenitor bias, where recently quenched galaxies with large sizes at fixed stellar mass are added to the existing quiescent cluster population. This will evidently lead to a rise in the average size of a quiescent galaxy at fixed stellar mass with decreasing redshift. However, so will growth via minor mergers, as demonstrated in Chapter 2. The next crucial step is to determine which of these two physical processes drives most of the observed size growth in the quiescent population of galaxies, and under which circumstances. As discussed in Section 3.6.3, the importance of each mechanism is likely to depend on environment: minor mergers seem rare between cluster galaxies (Chapter 2), but there seems to be a higher fraction of recently quenched galaxies in clusters (Poggianti et al., 2009; Rodríguez Del Pino et al., 2013; Fritz et al., 2014; Paccagnella et al., 2019). Are minor mergers driving galaxy growth in the field environment, with progenitor bias being more important for the cluster environment? Taken together, the results in Chapter 2 and 3 seem to suggest just that. An answer to this question can only be reached with better sample statistics of cluster and field galaxies spanning a wider range in redshift. The large redshift range will allow us to *track* galaxy growth via both these mechanisms over a large portion of the Universe's history, and therefore possibly quantify it for both mechanisms. Furthermore, large sample statistics could allow us to observe rare phenomena in clusters such as mergers between satellite galaxies. At high redshift, it could even allow us to catch rapid physical processes in action – a possible example of which could be ram-pressure stripping (see Chapter 4).

High quality photometry, including a range of photometric bands combined with high resolution spectroscopy will be required to: 1) measure sizes and stellar masses reliably, 2) spectroscopically identify field and cluster galaxies and 3) identify recently quenched galaxies.

However, environment is not as clear-cut as the "field" versus the "cluster". There is an entire

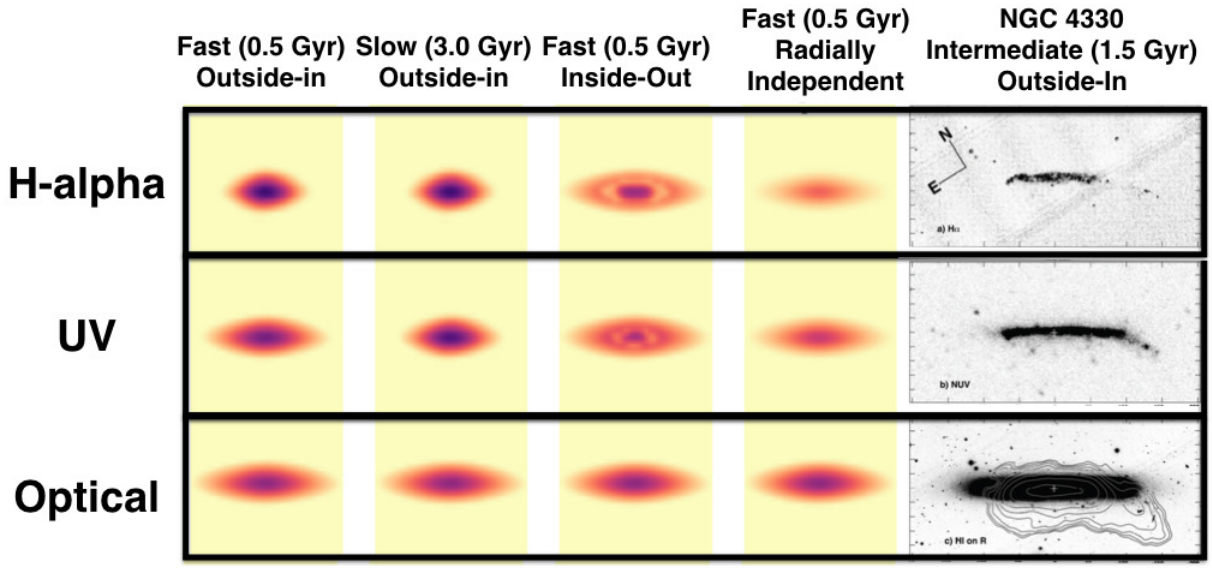

Figure 5.1: Schematic of how images of a galaxy in Hα, UV and optical wavelengths allows one to discern different quenching mechanisms and their timescales. The rightmost column shows real low redshift observations of the galaxy NGC 4330 in the corresponding wavelengths (Abramson et al., 2011). Inside-out quenching could be identified from a reduction in UV and Hα emission in a ringed region around the centre of the galaxy, leading to a characteristic donut-shaped morphology. The quenching timescale can be determined from the relative size of these rings. Radially independent quenching leads to no reduction in size as observed in the three wavelengths, but a reduction in overall brightness from optical to UV to Hα. Outside-in quenching manifests itself as a reduction in the overall size of the galaxy as we observe it in the optical, UV and then in Hα. *To be able to discern quenching timescales, all three wavelengths are required* as shown in the first two columns. The optical image provides the reference size of the galaxy. Both the fast and slow outside-in quenching have small Hα disks, but the fast case has a large UV disk and the slow case has a small UV disk.

environment that has not been studied in this thesis, which can be used to start answering the above question and much more, which we will discuss in Section 5.1.3.

5.1.3 Galaxy growth and Quenching in the group environment

The results in this thesis demonstrate an important insight: *the three physical processes of galaxy growth, star formation and quenching are inextricably linked.* The key variable which will allow us to get a better handle on the balance between these processes is *environment.* Physical conditions in the field and cluster are very different, leading to different growth and quenching mechanisms dominating in each. The fraction of recently quenched galaxies is seen to be higher in clusters (Poggianti et al., 2009; Rodríguez Del Pino et al., 2013; Fritz et al., 2014; Paccagnella et al., 2019) and minor mergers seem to dominate quiescent galaxy size growth in the field (Chapter 2).

To obtain a full view of environmental quenching over cosmic time, it is necessary to extend studies of galaxy growth and quenching to higher redshifts and a wider range of environments. This can be readily done with existing data that probes the group environment – the intermediate environment between the field and clusters – at $z \sim 1$.

The study presented in Chapter 4 can be extended and applied to the group environment to

directly infer both environmental quenching mechanisms and their timescales. Rather than using only one tracer of star formation, multiple tracers can be used to trace star formation on different timescales. An early example of this technique was demonstrated in Abramson et al. (2011), and is illustrated in the last column of Figure 5.1. Using images of the Virgo cluster galaxy NGC 4330 in the optical, ultraviolet (UV) and Hα, it was possible to observe the integrated star formation history, star formation over the past 100 Myr and star formation over the past 10 Myr in the galaxy, respectively. Immediately recognisable is the reduction in the spatial extent of the emission as we go from the optical to UV and then to Hα. Star formation is being visibly quenched from the outside-in in a clear case of ram-pressure stripping (details of which can be found in Abramson et al. 2011). Such studies have confirmed that measuring the size of the disc in these three wavelengths is a powerful tool in determining quenching mechanisms. Recently, deep narrow-band imaging of the same galaxy carried out as part of the VESTIGE survey (Fossati et al., 2018) allowed for the ability to measure the environmental quenching timescale as a function of radial distance from the centre of the galaxy. Detailed studies such as these at high redshift will be possible with the next generation of ground-based 20 $-$ 30 metre telescopes such as the *Extremely Large Telescope* (ELT), the *Giant Magellan Telescope* (GMT) and the *Thirty Metre Telescope* (TMT). Currently, it will be possible to simultaneously use the relative sizes and morphologies of galaxies in these three wavelengths to determine the quenching mechanism and timescale for $z \sim 1$ group galaxies with HST. The details of how to identify the mechanisms and timescales are given in Figure 5.1.

The data used to conduct this study are available as part of the 3D-HST/CANDELS surveys (Grogin et al., 2011; Koekemoer et al., 2011; Brammer et al., 2012; Momcheva et al., 2016). For example, there is HST Advanced Camera for Surveys (ACS) F435W, F775W and F160W imaging for the GOODS-S field (Grogin et al., 2011; Koekemoer et al., 2011), which are the ideal filters for tracing the rest-frame UV and optical at $z \sim 1$. F140W and Hα are also available for this field as part of the 3D-HST survey (Brammer et al., 2012). Spectroscopic surveys have also been conducted in this field, which could allow for the determination of galaxy groups (ESO/GOODS, Vanzella et al. 2005, 2006, 2008; Popesso et al. 2009).

The F140W/F160W imaging of GOODS-S from 3D-HST/CANDELS can also be used to conduct a mass–size relation comparison at $z \sim 1$ between groups, clusters and the field, since the cluster-versus-field comparison has been done in Chapter 2 using the same imaging. Such a study will give us an insight into the dominant galaxy growth mechanisms for quiescent galaxies in groups at this redshift. Furthermore, it would provide a complete picture on the influence of environment on galaxy

size growth at high redshift.

5.1.4 Constraining the physics of environmental quenching in clusters at high redshift

The extensive modelling of disc-fading in Section 3.5, Chapter 3 revealed important clues on how environmental quenching alters the structure of cluster galaxies as they are observed in the stellar continuum. Whilst using an outside-in fading model, it was difficult to replicate the structural properties of the poststarburst galaxies (PSBs) without the model galaxy having a significant bulge component. This ultimately raises two questions: Do all star-forming galaxies host a significant bulge component that becomes more prominent after outside-in quenching? Or does ram-pressure stripping enhance the brightness of galactic bulges?

The study presented in Chapter 4 raises an additional question however: is ram-pressure stripping even responsible for environmental quenching at $z \sim 1$? One way to gain clarity on these questions is to confirm whether or not ram-pressure stripping is acting on the PSBs or not. So far, all the physical properties of the PSBs point towards ram-pressure stripping being the likely quenching mechanism. At low redshift, we have a good understanding of the physical conditions in galaxies undergoing ram-pressure stripping thanks to the power of integral field units such as MUSE which provide insight into the kinematics of such galaxies (see GASP Survey results, e.g. Poggianti et al. 2017; Bellhouse et al. 2017; Gullieuszik et al. 2017; Fritz et al. 2017; Moretti et al. 2018; Jaffé et al. 2018; Vulcani et al. 2018). Detailed observations such as these at high redshift will be possible with the next generation of integral field spectrographs such as NIRSpec on the *James Webb Space Telescope* (JWST) and HARMONI on the ELT. Currently, the integral field spectrographs KMOS and SINFONI at the *Very Large Telescope* (VLT) and OSIRIS on the Keck II Telescope are designed to conduct IFU spectroscopy similar to that possible with MUSE at low redshift. The power of KMOS and SINFONI has already been demonstrated with the KMOS^{3D} Survey (Wisnioski et al., 2015, 2018) and the SINS/zC-SINF Survey (Förster Schreiber et al., 2018). These surveys have provided key insights into the kinematics of galaxies at high redshift. Observing the PSBs with IFU spectrographs could provide the missing piece of information required to confirm whether or not ram-pressure stripping is responsible for their observed physical properties. More importantly, these observations could provide the first look at how ram-pressure stripping operates in the high-redshift Universe, and whether or not it is rapid as many studies have suggested (including the results found in Chapter 4).

The study presented in Chapter 4 also revealed the difficulties in measuring structural properties

of Hα profiles with low sample statistics. The limitations of this study provide us with a good understanding of the sample size and depth of observations required to increase the precision of our measurements. Should an environmental quenching signature be difficult to measure after following the lines of investigation stated in Section 4.4.4, it provides a great opportunity to obtain deeper follow-up G141 grism observations with HST. Alternatively, the results in Chapter 4 showcase how expensive a measurement this is to make with HST. JWST's NIRCam grisms have smaller pixel scales and higher spectral resolution than those on HST's WFC3 (Greene et al., 2016). For future observations, it can be demonstrated that the science we conducted in Chapter 4 can be more cheaply done with JWST, albeit at $z > 1$. Therefore it will be easier to increase sample statistics with JWST, allowing us to better quantify the importance of galaxy growth and quenching processes in high-redshift galaxies (see also Section 5.1.2).

5.1.5 Molecular gas observations of cluster galaxies outside the local Universe

In Section 5.1.4, we discussed the possiblity of using IFUs to obtain kinematics of the ionised gas component in cluster galaxies. It is one thing to be able to observe its spatial distribution (as seen in Figure 2.13, Section 1.1.1.1), but being able to comment on whether the gas is rotating or being stripped in a certain direction can provide us with a deeper insight into how quenching mechanisms affect the fuel for star formation. The raw fuel for star formation however is the cold molecular gas. It has been often thought the cold molecular gas is more difficult to remove during environmental quenching processes, with there being some evidence that this is true (see Section 1.1.1.1). However, more recent observations of molecular gas in galaxies undergoing ram-pressure stripping have found evidence for molecular gas in the stripped material (Dasyra et al., 2012; Jáchym et al., 2014; Lee & Chung, 2018; Zabel et al., 2019). Using molecular gas observations of $z \sim 2$ protoclusters from ALMA, Tadaki et al. (2019) found that environmental effects on the gas were mass-dependent, where gas accretion is suppressed in more massive galaxies, but accelerated in less massive galaxies. All these results indicate that perhaps our understanding of how environmental quenching mechanisms operate is incomplete, since we have been unable to directly observe the molecular gas until recently. Such observations could prove crucial for pinning-down the quenching mechanism responsible for creating the recently quenched cluster population discussed in Chapter 3: galaxies that seem to have no emission in their spectra, suggesting that IFU observations for ionised gas may be unfruitful.

Recently, ALMA observations of a cluster in the *Spitzer* Adaptation of the Red-sequence Cluster Survey (SpARCS, see Muzzin et al. 2009; Wilson et al. 2009; Demarco et al. 2010) residing at $z \sim 1.6$

led to the detection of spatially-resolved CO(2 – 1) in eight cluster galaxies (Noble et al., 2019). Despite having rotating, but truncated CO discs with respect to the HST stellar component, these galaxies have elevated gas fractions compared to their field counterparts. These results seem to tentatively indicate signatures of molecular gas stripping, however there is no explanation for what could cause the higher gas fractions with respect to the field. To better constrain the affects of environmental quenching on molecular gas at high redshift, larger, more representative cluster and field samples are required. The SpARCS Collaboration has now obtained ALMA observations for all the cluster members in this cluster. We now hope to move forward on molecular gas studies in high redshift clusters, to better constrain how environmental quenching effects the raw fuel for star formation during an epoch where environmental quenching may be more severe and therefore important in driving the decline in the SFRD (see Section 4.4.2, Chapter 4).

A

A summary of previous results on the cluster versus field stellar mass–size relation for quiescent galaxies

In Table A.1 and Figure A.1, we summarise results from studies since 2009 of the cluster versus field stellar mass–size relation for quiescent galaxies.

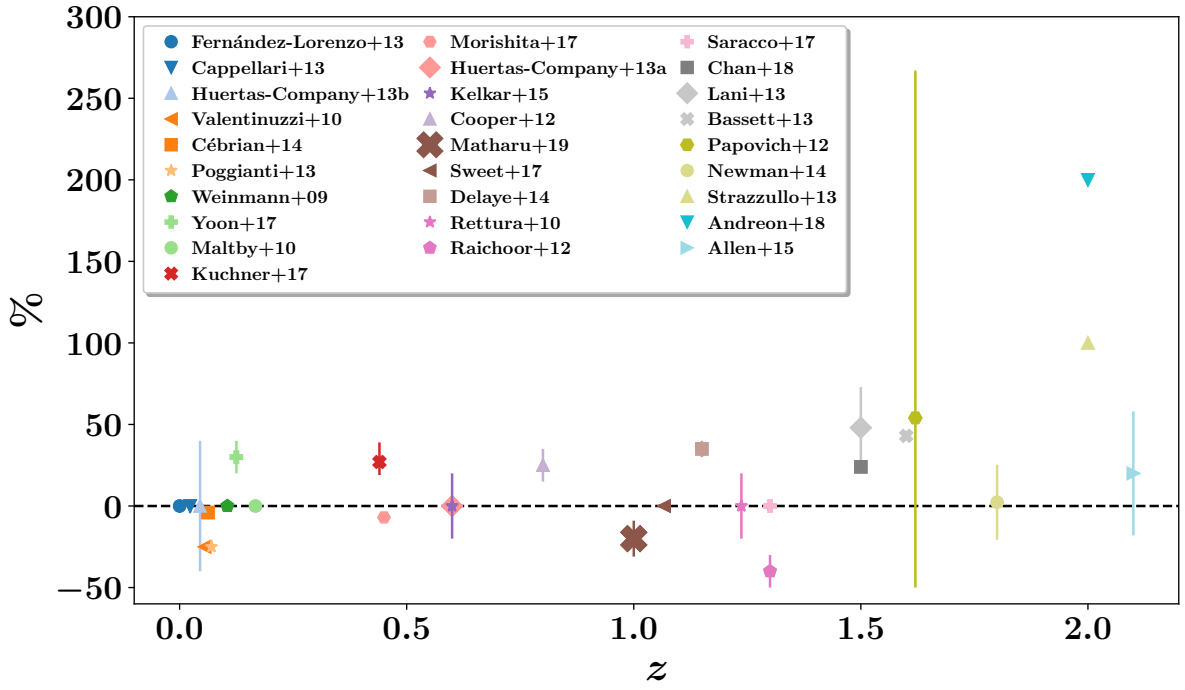

Figure A.1: A summary of results from cluster versus field stellar mass–size relation studies of quiescent galaxies since 2009. Positive percentages indicate larger sizes in clusters with respect to the field. Error bars are shown for those works which stated errors that could easily be converted into percentages. Legend labels are arranged by redshift in ascending order. See Table A.1 for more details.

Table A.1: A summary of results from cluster versus field stellar mass-size relation studies of quiescent galaxies since 2009. Studies are listed by redshift in ascending order.

Reference	Redshift	Stellar Mass $[\log(\mathcal{M}_*/\mathrm{M}_\odot)]$	Offset [w.r.t the field]	Error	Method of measurement
Fernández Lorenzo et al. (2013)	0	$9.0 \lesssim \log(\mathcal{M}_*) \lesssim 11.5$	0	-	Zeropoint
Cappellari (2013)	0.0231	$10.5 \lesssim \log(\mathcal{M}_*) \lesssim 11.3$	0	$\pm$4%	Size distributions[a]
Huertas-Company et al. (2013b)	$0 < z < 0.09$	$10.5 \lesssim \log(\mathcal{M}_*) \lesssim 11.8$	0	$30 - 40$%	Median relations
Valentinuzzi et al. (2010a)	$0.04 < z < 0.07$	$10.5 \lesssim \log(\mathcal{M}_*) \lesssim 11.6$	-0.1 dex	-	Median sizes
Cebrián & Trujillo (2014)	$0 < z < 0.12$	$9.0 \lesssim \log(\mathcal{M}_*) \lesssim 11.0$	-4.0%	$\pm$0.8%	Mean sizes
Poggianti et al. (2013)	$0.03 < z < 0.11$	$10.5 \lesssim \log(\mathcal{M}_*) \lesssim 11.7$	-1σ	-	Median relations
Weinmann et al. (2009)	$0.01 < z < 0.2$	$9.8 \lesssim \log(\mathcal{M}_*) \lesssim 12.0$	0	-	Median sizes
Yoon et al. (2017)	$0.1 < z < 0.15$	$11.2 \lesssim \log(\mathcal{M}_*) \lesssim 11.8$	$20 - 40$%	-	Median sizes
Maltby et al. (2010)	0.167	$9.0 \lesssim \log(\mathcal{M}_*) \lesssim 11.0$	0	-	Mean sizes
Kuchner et al. (2017)	0.44	$9.8 \lesssim \log(\mathcal{M}_*) \lesssim 10.8$	$2 - 5\sigma$	-	Mean sizes
Morishita et al. (2017)	$0.2 < z < 0.7$	$7.8 \lesssim \log(\mathcal{M}_*) \lesssim 12.0$	-7%	$\pm$3%	Multidimensional analysis[b]
Huertas-Company et al. (2013a)	$0.2 < z < 1$	$10.7 \lesssim \log(\mathcal{M}_*) \lesssim 11.8$	0	-	Mass-normalised radii[c]
Kelkar et al. (2015)	$0.4 < z < 0.8$	$10.2 \lesssim \log(\mathcal{M}_*) \lesssim 12.0$	0	$10 - 20$%	K-S test[d]
Cooper et al. (2012)	$0.4 < z < 1.2$	$10.0 \lesssim \log(\mathcal{M}_*) \lesssim 11.0$	0.54 kpc	$\pm$0.22 kpc	H-L estimator[e]
Chapter 2 of this thesis	$0.86 < z < 1.34$	$10.0 \lesssim \log(\mathcal{M}_*) \lesssim 12.0$	-0.08 dex	$\pm$0.04 dex	Mean sizes
Sweet et al. (2017)	1.067	$9.5 \lesssim \log(\mathcal{M}_*) \lesssim 12.0$	0	-	Fitted relations[f]
Delaye et al. (2014a)	$0.8 < z < 1.5$	$10.5 \lesssim \log(\mathcal{M}_*) \lesssim 11.5$	$30 - 40$%	-	Mass-normalised radii[g]
Rettura et al. (2010)	1.237	$10.7 \lesssim \log(\mathcal{M}_*) \lesssim 11.2$	0	< 20%	Fitted relations
Raichoor et al. (2012)	1.3	$11.0 \lesssim \log(\mathcal{M}_*) \lesssim 11.5$	$-30 - 50$%	-	Size ratio distributions[b]
Saracco et al. (2017)	1.3	$9.0 \lesssim \log(\mathcal{M}_*) \lesssim 12.0$	0	-	K-S test
Chan et al. (2018)	$1.39 < z < 1.61$	$10.5 \lesssim \log(\mathcal{M}_*) \lesssim 11.8$	24%	-	Median sizes
Lani et al. (2013)	$1 < z < 2$	$11.3 \lesssim \log(\mathcal{M}_*) \lesssim 11.8$	48%	$\pm$25	Mean sizes
Bassett et al. (2013)	1.6	$10.3 \lesssim \log(\mathcal{M}_*) \lesssim 11.3$	0.6 kpc	2σ	Median sizes
Papovich et al. (2012)	1.62	$10.5 \lesssim \log(\mathcal{M}_*) \lesssim 11.0$	0.7 kpc	$+1.7, -0.9$[i] kpc	Median sizes
Newman et al. (2014)	1.8	$10.8 \lesssim \log(\mathcal{M}_*) \lesssim 11.7$	0.01 dex	0.09 dex	Mean sizes
Strazzullo et al. (2013)	2	$10.0 \lesssim \log(\mathcal{M}_*) \lesssim 11.5$	$2\times$ larger	$\pm$0.08[j]	Mean sizes[k]
Andreon (2018)	2	$10.7 \lesssim \log(\mathcal{M}_*) \lesssim 11.5$	$3\times$ larger	-	Mass-normalised sizes[l]
Allen et al. (2015)	2.1	$10.7 \lesssim \log(\mathcal{M}_*) \lesssim 11.5$	0.36 kpc	0.69 kpc	Mass-normalised radii

[a] Difference in the mean of the size probability distributions.
[b] A relation where size is a function of multiple variables – not just stellar mass – is defined, leaving environment as the only distinguishing factor.
[c] $r_e \times (10^{11}\,\mathrm{M}_\odot/\mathcal{M}_*)$.
[d] Kolmogorov–Smirnov tests were carried out to estimate the probability, p, that the field and cluster samples were derived from the same size distribution. Environmental differences were considered significant if $p < 0.05$ ($> 2\sigma$ significance).
[e] Hodge–Lehmann estimator of the mean. This is given by the median value of the mean computed over all pairs of galaxies in the sample.
[f] Comparison of fitted mass-size relation to that of van der Wel et al. (2014) in their Figure 9.
[g] $r_e/\mathcal{M}_{11}^{0.57}$, where $\mathcal{M}_{11} = \mathcal{M}_*/10^{11}\mathrm{M}_\odot$
[h] Peak of the size ratio normalised distributions, where the size ratio is $r_e/r_{e,Valen}$. $r_{e,Valen}$ is the half-light radius as predicted by the Valentinuzzi et al. (2010a) mass-size relation.
[i] Error propagation of the interquartile ranges stated for field and cluster medians in this work.
[j] Error propagation of the mean $r_e/r_{e,Shen2003}$ errors.
[k] Difference in the average size ratio $r_e/r_{e,Shen2003}$, where $r_{e,Shen2003}$ is the average half-light radius as given by the Shen et al. (2003) mass–size relation.
[l] Comparison of the mean galaxy size at $\log(\mathcal{M}_*/\mathrm{M}_\odot) = 11$.

B

Size comparison test with van der Wel et al. (2012)

We took the F160W mosaic for CANDELS-COSMOS, and measured the half-light radii of all the galaxies in the field using our method of size determination (see Section 2.1.3). The reason we did not use the F140W mosaic – which would have made the comparison to GCLASS more direct – was because the published structural parameters for all the CANDELS fields in 3D-HST were measured using the F125W and F160W mosaics, sometimes accompanied with measurements in F098m or F105W (van der Wel et al., 2012). Both F125W and F160W span approximately half of the wavelength range covered by F140W. In Appendix C, we explore how the differing filters for field and cluster samples affect results presented in Chapter 2. In Figure B.1, we plot our half-light radii results against those from van der Wel et al. (2012) in F160W for the same set of galaxies with $0.86 < z < 1.34$, F160W magnitude < 25, GALFIT measured $R_{eff} < 50$ kpc, flag value of 0 (see Section 2.1.4 for the reasoning behind this selection) and stellar masses within the mass completeness limits of our study ($\log(\mathcal{M}_*/\mathrm{M}_\odot) > 9.96$ and $\log(\mathcal{M}_*/\mathrm{M}_\odot) > 9.60$ for quiescent and star-forming galaxies, respectively).

Despite the differing methods of size determination, there are no systematics present. The mean offset between the two sets of measurements is 0.28%. Divergence from agreement at larger half-light radii is due to poor signal-to-noise ratio (F160W magnitude ~25). In Figure B.2, we show

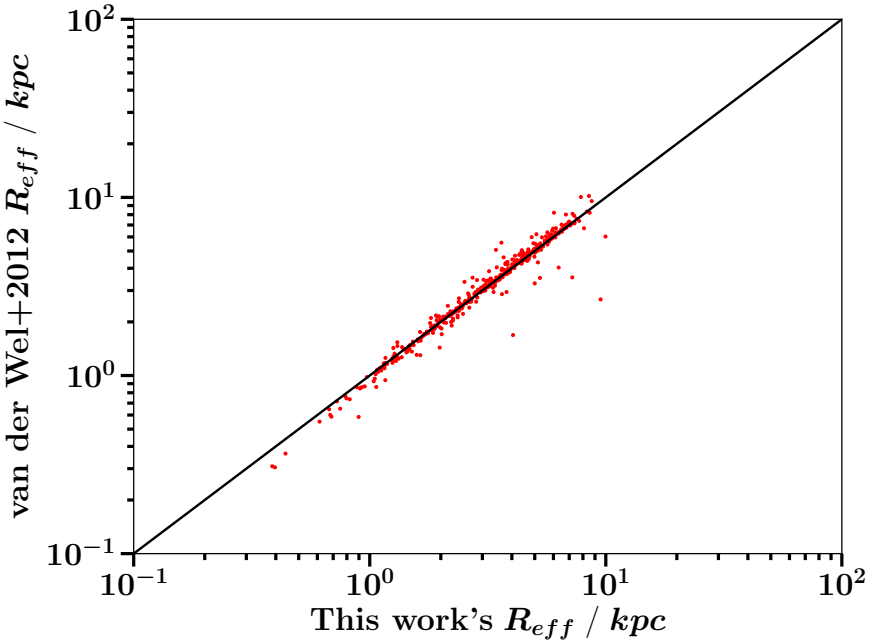

Figure B.1: Level of agreement with results from van der Wel et al. (2012) for the half-light radii measurements of the same set of galaxies with $0.86 < z < 1.34$, F160W magnitude < 25, $R_{eff} < 50$ kpc and stellar masses within the completeness limits of our study ($\log(\mathcal{M}_*/\mathrm{M}_\odot) > 9.96$ and $\log(\mathcal{M}_*/\mathrm{M}_\odot) > 9.60$ for quiescent and star-forming galaxies, respectively) from the CANDELS-COSMOS F160W mosaic. Solid line indicates the position of one-to-one agreement. The mean offset between the two measurements is 0.28%.

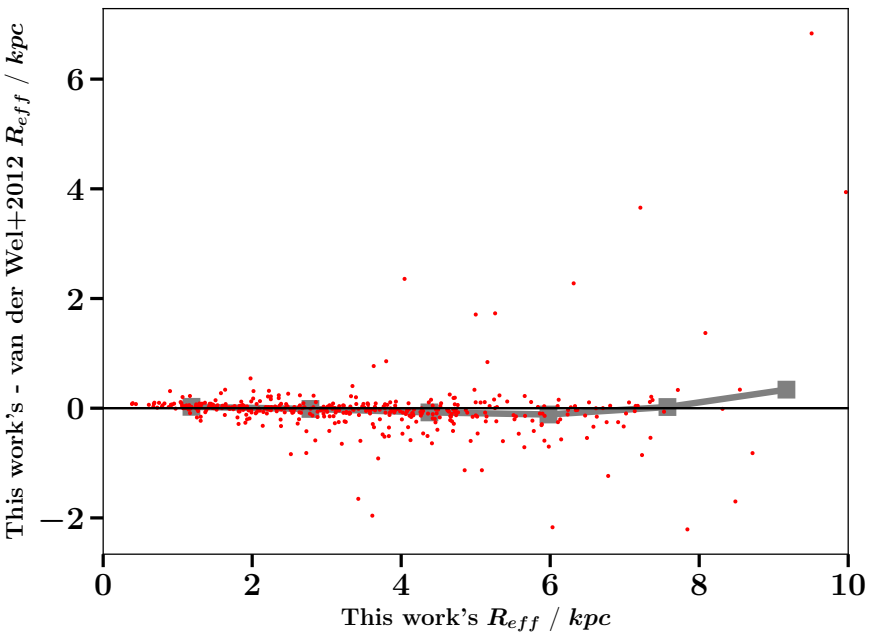

Figure B.2: How the difference in half-light radii measurements between the size determination method presented in Chapter 2 and that of van der Wel et al. (2012) varies with half-light radius for the same set of galaxies ($0.86 < z < 1.34$, F160W magnitude < 25, $R_{eff} < 50$ kpc and stellar masses within the completeness limits of the study presented in Chapter 2) in the CANDELS-COSMOS F160W mosaic. The horizontal line indicates the position of no difference between half-light radii measurements.The grey points joined with grey lines shows the median values in 6 bins.

the difference in the size measurements between the two methods against our size measurements. We can clearly see that the largest divergence from agreement between the two size determination methods happens at larger ($R_{eff} \gtrsim 5$ kpc) half-light radii. This is where the running median (solid grey line with squares) starts to deviate more from the line of agreement (horizontal black line). For galaxies that are 6 kpc (according to our size determination method), our size determination method tends to underestimate sizes by 0.1 kpc (by $\sim$ 2%) compared to the van der Wel et al. (2012) size determination method. Beyond a size of 8 kpc, our size determination method seems to start overestimating sizes, however, statistics are poor in this region. In general, at the mean size of the sample shown (3.47 kpc), the median size difference is -0.04 kpc. This is only a 1% underestimation in size, which is much smaller than the order of our uncertainties on the size offset measurements (see Section 2.3). Therefore, systematics arising from the difference in size determination methods do not significantly effect the results presented in Chapter 2.

C

The effect of differing filters on measured sizes

As mentioned in Chapter 2, colour gradients can vary for galaxies depending on which filter is used to observe them. This can lead to half-light radii measurements that differ for the same galaxy, depending on the filter used. Since the half-light radii measurements for our field sample were made using images in a different filter (F160W) to the filter used for the images of the cluster galaxies (F140W), we performed a check on how this affects conclusions drawn in Chapter 2.

In Figure C.1, we plot our half-light radii measurements made from the 3D-HST COSMOS F140W mosaic against those made by van der Wel et al. (2012) for the same set of galaxies with $0.86 < z < 1.34$, F160W and F140W magnitude < 25, $R_{eff} < 50$ kpc and stellar masses within the mass completeness limits of our study ($\log(\mathcal{M}_*/\mathrm{M}_\odot) > 9.96$ and $\log(\mathcal{M}_*/\mathrm{M}_\odot) > 9.60$ for quiescent and star-forming galaxies, respectively) from the CANDELS-COSMOS F160W mosaic. After taking into account the small systematic difference between the two size determination methods (see Appendix B), we find that galaxies are on average 12.87% larger in F140W than in F160W. Quiescent and star-forming galaxies are 12.12% and 13.04% larger in F140W than in F160W respectively. Therefore, the sizes for the field sample used in this study would be on average 12.87% larger if they were measured in F140W as opposed to F160W. This would therefore lead to a larger negative offset in the average size of cluster galaxies with respect to field galaxies, further strengthening the conclusions made in Chapter 2.

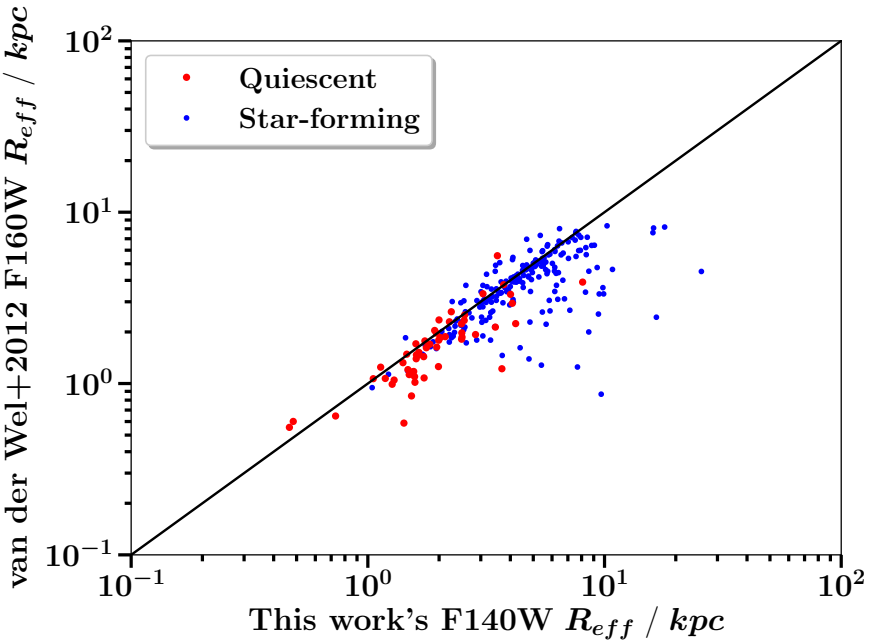

Figure C.1: Level of agreement between the half-light radius measurements made by van der Wel et al. (2012) in F160W versus those made for the same set of galaxies in F140W using our size determination method. Quiescent galaxies are shown as larger red points and star-forming galaxies are shown as smaller blue points. These galaxies have redshifts within the range $0.86 < z < 1.34$, F160W and F140W magnitude < 25, $R_{eff} < 50$ kpc and stellar masses within the completeness limits of our study ($\log(\mathcal{M}_*/\mathrm{M}_\odot) > 9.96$ and $\log(\mathcal{M}_*/\mathrm{M}_\odot) > 9.60$ for quiescent and star-forming galaxies, respectively). The solid line indicates the position of one-to-one agreement. Galaxies are on average 12.87% larger in F140W than in F160W. Quiescent and star-forming galaxies are 12.12% and 13.04% larger in F140W than in F160W respectively.

D

SExtractor settings for GCLASS F140W mosaics

Table D.1 lists the values for the parameters in the SExtractor configuration file that was run on the GCLASS F140W mosaics.

Table D.1: SExtractor configuration file parameters for the GCLASS F140W mosaics

Parameter	Value
CATALOG_TYPE	ASCII_HEAD
DETECT_TYPE	CCD
DETECT_MINAREA	5
DETECT_THRESH	2.0
ANALYSIS_THRESH	2.0
FILTER	Y
FILTER_NAME	gauss_1.5_3x3.conv
DEBLEND_NTHRESH	32
DEBLEND_MINCONT	0.005
CLEAN	Y
CLEAN_PARAM	1.0
MASK_TYPE	CORRECT
PHOT_APERTURES	5
PHOT_AUTOPARAMS	2.5, 3.5
PHOT_PETROPARAMS	2.0, 3.5
PHOT_FLUXFRAC	0.5
SATUR_LEVEL	50000.0
SATUR_KEY	SATURATE
MAG_ZEROPOINT	26.45
MAG_GAMMA	4.0
GAIN	0.0
GAIN_KEY	GAIN
PIXEL_SCALE	0.06
SEEING_FWHM	0.23
STARNNW_NAME	default.nnw
BACK_SIZE	64
BACK_FILTERSIZE	3
BACKPHOTO_TYPE	LOCAL
WEIGHT_TYPE	MAP_WEIGHT
WEIGHT_GAIN	Y
MEMORY_OBJSTACK	3000
MEMORY_PIXSTACK	300000
MEMORY_BUFSIZE	1024

References

Abadi M. G., Moore B., Bower R. G., 1999, MNRAS, 308, 947

Abell G. O., 1965, ARA&A, 3, 1

Abramson L. E., Morishita T., 2018, ApJ, 858, 40

Abramson A., Kenney J. D. P., Crowl H. H., Chung A., van Gorkom J. H., Vollmer B., Schiminovich D., 2011, AJ, 141, 164

Abramson L. E., et al., 2018, AJ, 156, 29

Allen R. J., et al., 2015, ApJ, 806, 3

Anderson J., 2016, WFC3 UVIS CTE Pixel-Based Model Evaluation, http://adsabs.harvard.edu/abs/2016hst..prop14881A

Andreon S., 2018, A&A, 617, A53

Bahé Y. M., McCarthy I. G., Balogh M. L., Font A. S., 2013, MNRAS, 430, 3017

Balogh M. L., Morris S. L., Yee H. K. C., Carlberg R. G., Ellingson E., 1997, ApJ, 488, L75

Balogh M. L., Morris S. L., Yee H. K. C., Carlberg R. G., Ellingson E., 1999, ApJ, 527, 54

Balogh M. L., et al., 2016, MNRAS, 456, 4364

Barden M., Häußler B., Peng C. Y., McIntosh D. H., Guo Y., 2012, MNRAS, 422, 449

Bassett R., et al., 2013, ApJ, 770, 58

Bedregal A. G., Cardiel N., Aragón-Salamanca A., Merrifield M. R., 2011, MNRAS, 415, 2063

Bell E. F., et al., 2012, ApJ, 753, 167

Bellhouse C., et al., 2017, ApJ, 844, 49

Belli S., Newman A. B., Ellis R. S., 2014, ApJ, 783, 117

Belli S., Newman A. B., Ellis R. S., 2015, ApJ, 799

Bellstedt S., et al., 2016, MNRAS, 460, 2862

Bertin E., Arnouts S., 1996, A&AS, 117, 393

Bezanson R., van Dokkum P. G., Tal T., Marchesini D., Kriek M., Franx M., Coppi P., 2009, ApJ, 697, 1290

Bezanson R., et al., 2016, ApJ, 822, 30

Binney J., Merrifield M., 1998, Galactic Astronomy. Princeton University Press

Biviano A., van der Burg R. F. J., Muzzin A., Sartoris B., Wilson G., Yee H. K. C., 2016, A&A, 594, A51

Bluck A. F. L., Conselice C. J., Buitrago F., Grützbauch R., Hoyos C., Mortlock A., Bauer A. E., 2012, ApJ, 747, 34

Boselli A., Cortese L., Boquien M., 2014,] 10.1051/0004-6361/201322311, 67, 1

Brammer G. B., van Dokkum P. G., Coppi P., 2008, ApJ, 686, 1503

Brammer G. B., et al., 2012, ApJS, 200, 13

Bruzual G., Charlot S., 2003, MNRAS, 344, 1000

Buitrago F., Trujillo I., Conselice C. J., Bouwens R. J., Dickinson M., Yan H., 2008, ApJ, 687, L61

Bundy K., et al., 2006, ApJ, 651, 120

Calzetti D., Armus L., Bohlin R. C., Kinney A. L., Koornneef J., Storchi-Bergmann T., 2000, ApJ, 533, 682

Cappellari M., 2013, ApJ, 778, L2

Caputi K. I., Cirasuolo M., Dunlop J. S., McLure R. J., Farrah D., Almaini O., 2011, MNRAS, 413, 162

Carilli C., Walter F., 2013, ARA&A, 51, 105

Carollo C. M., et al., 2013, ApJ, 773, 112

Cassata P., et al., 2013, ApJ, 775, 106

Cebrián M., Trujillo I., 2014, MNRAS, 444, 682

Chabrier G., 2003, PASP, 115, 763

Chan J. C. C., et al., 2016, MNRAS, 458, 3181

Chan J. C. C., et al., 2018, ApJ, 856, 8

Charbonnier A., et al., 2017, MNRAS, 469, 4523

Christlein D., Zabludoff A. I., 2004, ApJ, 616, 192

Cimatti A., Nipoti C., Cassata P., 2012, MNRAS, 422, L62

Cooper M. C., et al., 2012, MNRAS, 419, 3018

Cramer W. J., Kenney J. D. P., Sun M., Crowl H., Yagi M., Jáchym P., Roediger E., Waldron W., 2019, ApJ, 870, 63

Daddi E., et al., 2005, ApJ, 626, 680

Damjanov I., et al., 2011, ApJ, 739, L44

Damjanov I., Hwang H. S., Geller M. J., Chilingarian I., 2014, ApJ, 793, 39

Damjanov I., Geller M. J., Zahid H. J., Hwang H. S., 2015, ApJ, 806, 158

Damjanov I., Zahid H. J., Geller M. J., Utsumi Y., Sohn J., Souchereau H., 2018, ApJ, 872, 91

Dasyra K. M., Combes F., Salomé P., Braine J., 2012, A&A, 540, 1

Davidzon I., et al., 2017, A&A, 605, A70

De Lucia G., Weinmann S., Poggianti B. M., Aragón-Salamanca A., Zaritsky D., 2012, MNRAS, 423, 1277

DeMaio T., Gonzalez A. H., Zabludoff A., Zaritsky D., Connor T., Donahue M., Mulchaey J. S., 2018, MNRAS, 474, 3009

Delahaye A. G., et al., 2017, ApJ, 843, 126

Delaye L., et al., 2014a, MNRAS, 441, 203

Delaye L., et al., 2014b, MNRAS, 441, 203

Demarco R., et al., 2010, ApJ, 711, 1185

Domínguez A., et al., 2013, ApJ, 763, 145

Dressler A., 1980, ApJ, 236, 351

Dressler A., Gunn J. E., 1983, ApJ, 270, 7

Dressler A., Smail I., Poggianti B. M., Butcher H., Couch W. J., Ellis R. S., Oemler, Jr. A., 1999, ApJS, 122, 51

Ebeling H., Stephenson L. N., Edge A. C., 2014, ApJ, 781, L40

Elbaz D., et al., 2018, A&A, 616, A110

Fagioli M., Carollo C. M., Renzini A., Lilly S. J., Onodera M., Tacchella S., 2016, ApJ, 831, 173

Fakhouri O., Ma C.-P., Boylan-Kolchin M., 2010, MNRAS, 406, 2267

Fan L., Lapi A., De Zotti G., Danese L., 2008, ApJ, 689, L101

Fernández Lorenzo M., Sulentic J., Verdes-Montenegro L., Argudo-Fernández M., 2013, MNRAS, 434, 325

Ferreras I., et al., 2014, MNRAS, 444, 906

Finn R. A., et al., 2018, ApJ, 862, 149

Folkes S., et al., 1999, MNRAS, 308, 459

Foltz R., et al., 2018, ApJ, 866, 136

Förster Schreiber N. M., et al., 2018, ApJS, 238, 21

Fossati M., et al., 2018, A&A, 614, A57

Franx M., van Dokkum P. G., Schreiber N. M. F., Wuyts S., Labbé I., Toft S., 2008, ApJ, 688, 770

Fraser-McKelvie A., Aragón-Salamanca A., Merrifield M., Tabor M., Bernardi M., Drory N., Parikh T., Argudo-Fernández M., 2018, MNRAS, 481, 5580

Fritz J., et al., 2014, A&A, 566, A32

Fritz J., et al., 2017, ApJ, 848, 132

Galametz A., et al., 2013, ApJS, 206, 10

Galametz A., et al., 2018, MNRAS, 475, 4148

Gallazzi A., et al., 2009, ApJ, 690, 1883

Gardner J. P., et al., 2006, SSR, 123, 485

Gargiulo A., et al., 2017, A&A, 606, A113

Geller M. J., Huchra J. P., 1983, ApJS, 52, 61

Giallongo E., et al., 2014, ApJ, 781, 24

Gladders M. D., Yee H. K. C., 2000, AJ, 120, 2148

Gomez P. L., et al., 2003, ApJ, 584, 210

Goto T., et al., 2003, PASJ, 55, 757

Green J., et al., 2012, arXiv: 1208.4012, pp 2182–2184

Greene T. P., et al., 2016, in MacEwen H. A., Fazio G. G., Lystrup M., Batalha N., Siegler N., Tong E. C., eds, Proc. SPIE. (arXiv:1606.04161), doi:10.1117/12.2231347

Grogin N. A., et al., 2011, ApJS, 197, 35

Gullieuszik M., et al., 2017, ApJ, 846, 27

Gunn J. E., Gott J. R., 1972, ApJ, 176, 1

Haines C. P., et al., 2015, ApJ, 806, 101

Head J. T., Lucey J. R., Hudson M. J., Smith R. J., 2014, MNRAS, 440, 1690

Hill A. R., et al., 2017, ApJ, 837, 147

Hill A. R., van der Wel A., Franx M., Muzzin A., Skelton R. E., Momcheva I., van Dokkum P., Whitaker K. E., 2019, ApJ, 871, 76

Hilz M., Naab T., Ostriker J. P., Thomas J., Burkert A., Jesseit R., 2012, MNRAS, 425, 3119

Hilz M., Naab T., Ostriker J. P., 2013, MNRAS, 429, 2924

Hoag A., et al., 2016, ApJ, 831, 182

Hopkins P. F., Bundy K., Murray N., Quataert E., Lauer T. R., Ma C.-P., 2009a, MNRAS, 398, 898

Hopkins P. F., Hernquist L., Cox T. J., Keres D., Wuyts S., 2009b, ApJ, 691, 1424

Hopkins P. F., Bundy K., Hernquist L., Wuyts S., Cox T. J., 2010, MNRAS, 401, 1099

Hubble E., 1936, Realm of the Nebulae. Yale University Press

Huertas-Company M., et al., 2013a, MNRAS, 428, 1715

Huertas-Company M., Shankar F., Mei S., Bernardi M., Aguerri J. A. L., Meert A., Vikram V., 2013b, ApJ, 779, 29

Ilbert O., et al., 2010, ApJ, 709, 644

Jáchym P., Combes F., Cortese L., Sun M., Kenney J. D., 2014, ApJ, 792

Jaffé Y. L., et al., 2011, MNRAS, 417, 1996

Jaffé Y. L., et al., 2018, MNRAS, 476, 4753

Jiang F., van Dokkum P., Bezanson R., Franx M., 2012, ApJ, 749, L10

Keating S. K., Abraham R. G., Schiavon R., Graves G., Damjanov I., Yan R., Newman J., Simard L., 2014, ApJ, 798, 26

Kelkar K., Aragón-Salamanca A., Gray M. E., Maltby D., Vulcani B., De Lucia G., Poggianti B. M., Zaritsky D., 2015, MNRAS, 450, 1246

Kelly B. C., 2007, ApJ, 665, 1489

Kenney J. D. P., Young J. S., 1989, ApJ, 344, 171

Kennicutt R. C., 1998, ARA&A, 36, 189

Koekemoer A. M., et al., 2011, ApJS, 197, 36

Koopmann R. a., Kenney J. D. P., 2004, ApJ, 613, 866

Koyama Y., Shimakawa R., Yamamura I., Kodama T., Hayashi M., 2019, PASJ, 71, 1

Kriek M., van Dokkum P. G., Labbé I., Franx M., Illingworth G. D., Marchesini D., Quadri R. F., 2009, ApJ, 700, 221

Krogager J.-K., Zirm A. W., Toft S., Man A., Brammer G., 2014, ApJ, 797, 17

Kubo M., Tanaka M., Yabe K., Toft S., Stockmann M., Gómez-Guijarro C., 2018, ApJ, 867, 1

Kuchner U., Ziegler B., Verdugo M., Bamford S., Häußler B., 2017, A&A, 604, A54

Lani C., et al., 2013, MNRAS, 435, 207

Larson R. B., Tinsley B. M., Caldwell C. N., 1980, ApJ, 237, 692

Laureijs R., et al., 2011, arXiv: 1110.3193

Lee B., Chung A., 2018, ApJ, 866, L10

Lemaux B. C., Tomczak A. R., Lubin L. M., Wu P.-F., Gal R. R., Rumbaugh N., Kocevski D. D., Squires G. K., 2017, MNRAS, 472, 419

Lewis I., et al., 2002, MNRAS, 334, 673

Li H., Wuyts S., Lei H., Lin L., Lam M. I., Boquien M., Andrews B. H., Schneider D. P., 2019, ApJ, 872, 63

Lidman C., et al., 2012, MNRAS, 427, 550

Lidman C., et al., 2013, MNRAS, 433, 825

Lin Y.-T., Brodwin M., Gonzalez A. H., Bode P., Eisenhardt P. R. M., Stanford S. A., Vikhlinin A., 2013, ApJ, 771, 61

López-Sanjuan C., Balcells M., Pérez-González P. G., Barro G., García-Dabó C. E., Gallego J., Zamorano J., 2009, A&A, 501, 505

Lotz J. M., et al., 2017, ApJ, 837, 97

Ma C.-J., Ebeling H., Donovan D., Barrett E., 2008, ApJ, 684, 160

Madau P., Dickinson M., 2014, ARA&A, 52, 415

Maltby D. T., et al., 2010, MNRAS, 402, 282

Matharu J., et al., 2019, MNRAS, 484, 595

McDonald M., et al., 2017, ApJ, 843, 28

McGee S. L., Bower R. G., Balogh M. L., 2014, MNRAS, 442

Mei S., et al., 2012, ApJ, 754, 141

Merritt D., 1985, ApJ, 289, 18

Merten J., et al., 2015, ApJ, 806, 4

Mok A., et al., 2013, MNRAS, 431, 1090

Momcheva I. G., Lee J. C., Ly C., Salim S., Dale D. A., Ouchi M., Finn R., Ono Y., 2013, AJ, 145, 47

Momcheva I. G., et al., 2016, ApJS, 225, 27

Montes M., Trujillo I., 2014, ApJ, 794, 137

Moore B., Katz N., Lake G., Dressler A., Oemler A., 1996, Nature, 379, 613

Moore B., Lake G., Katz N., 1998, ApJ, 495, 139

Moran S. M., Ellis R. S., Treu T., Smith G. P., Rich R. M., Smail I., 2007, ApJ, 671, 1503

Moretti A., et al., 2018, MNRAS

Morishita T., Ichikawa T., Kajisawa M., 2014, ApJ, 785, 18

Morishita T., et al., 2017, ApJ, 835, 254

Mowla L., et al., 2018, arXiv: 1808.04379

Muzzin A., Wilson G., Lacy M., Yee H. K. C., Stanford S. A., 2008, ApJ, 686, 966

Muzzin A., et al., 2009, ApJ, 698, 1934

Muzzin A., et al., 2012, ApJ, 746, 188

Muzzin A., et al., 2014, ApJ, 796, 65

Naab T., Johansson P. H., Ostriker J. P., 2009, ApJ, 699, L178

Nelson E. J., et al., 2013, ApJL, 763, 1

Nelson E. J., et al., 2016a, ApJ, 817, L9

Nelson E. J., et al., 2016b, ApJ, 828, 27

Newman A. B., Ellis R. S., Andreon S., Treu T., Raichoor A., Trinchieri G., 2014, ApJ, 788, 51

Noble A. G., et al., 2019, ApJ, 870, 56

Noeske K. G., et al., 2007, ApJ, 660, L43

Oemler A. J., 1974, ApJ, 194, 1

Oldham L., et al., 2017, MNRAS, 465, 3185

Oser L., Naab T., Ostriker J. P., Johansson P. H., 2012, ApJ, 744, 63

Owers M. S., et al., 2019, ApJ, 873, 52

Paccagnella A., et al., 2017, ApJ, 838, 148

Paccagnella A., Vulcani B., Poggianti B. M., Moretti A., Fritz J., Gullieuszik M., Fasano G., 2019, MNRAS, 482, 881

Pannella M., et al., 2009, ApJ, 698, L116

Papovich C., et al., 2012, ApJ, 750, 93

Patel S. G., Holden B. P., Kelson D. D., Franx M., van der Wel A., Illingworth G. D., 2012, ApJ, 748, L27

Peng C. Y., Ho L. C., Impey C. D., Rix H.-W., 2002, AJ, 124, 266

Peng C. Y., Ho L. C., Impey C. D., Rix H.-W., 2010a, AJ, 139, 2097

Peng Y.-j., et al., 2010b, ApJ, 721, 193

Planck Collaboration XIII 2016, A&A, 594, A13

Poggianti B. M., Smail I., Dressler A., Couch W. J., Barger A. J., Butcher H., Ellis R. S., Oemler, Jr. A., 1999, ApJ, 518, 576

Poggianti B. M., et al., 2009, ApJ, 693, 112

Poggianti B. M., et al., 2013, ApJ, 762, 77

Poggianti B. M., et al., 2017, ApJ, 844, 48

Popesso P., et al., 2009, A&A, 494, 443

Postman M., Geller M. J., 1984, ApJ, 281, 95

Postman M., et al., 2005, ApJ, 623, 721

Postman M., et al., 2012, ApJS, 199

Presotto V., et al., 2014, A&A, 565, A126

Puchwein E., Springel V., Sijacki D., Dolag K., 2010, MNRAS, 406, 936

Raichoor A., et al., 2012, ApJ, 745, 130

Ravindranath S., et al., 2004, ApJ, 604, L9

Reddy N. A., Erb D. K., Pettini M., Steidel C. C., Shapley A. E., 2010, ApJ, 712, 1070

Reddy N. A., et al., 2015, ApJ, 806, 259

Rettura A., et al., 2010, ApJ, 709, 512

Rodighiero G., et al., 2011, ApJL, 739, 2

Rodríguez Del Pino B., Bamford S. P., Aragón-Salamanca A., Milvang-Jensen B., Merrifield M. R., Balcells M., 2013, MNRAS, 438, 1038

Rubin D., et al., 2018, ApJ, 866, 65

Rutkowski M. J., et al., 2014, ApJ, 796, 101

Saracco P., Gargiulo A., Ciocca F., Marchesini D., 2017, A&A, 597, A122

Schawinski K., et al., 2014, MNRAS, 440, 889

Schmidt K. B., et al., 2017, ApJ, 839, 17

Schneider P., 2015, Extragalactic Astronomy and Cosmology: An Introduction, second edn. Springer

Schreiber N. M. F., et al., 2004, ApJ, 616, 40

Scott N., et al., 2017, MNRAS, 472, 2833

Sheen Y.-K., et al., 2017, ApJL, 840, L7

Shen S., Mo H. J., White S. D. M., Blanton M. R., Kauffmann G., Voges W., Brinkmann J., Csabai I., 2003, MNRAS, 343, 978

Skelton R. E., et al., 2014, ApJS, 214, 24

Sobral D., Best P. N., Matsuda Y., Smail I., Geach J. E., Cirasuolo M., 2012, MNRAS, 420, 1926

Sobral D., et al., 2015, MNRAS, 451, 2303

Socolovsky M., Maltby D. T., Hatch N. A., Almaini O., Wild V., Hartley W. G., Simpson C., Rowlands K., 2019, MNRAS, 482, 1640

Strazzullo V., et al., 2013, ApJ, 772, 118

Sweet S. M., et al., 2017, MNRAS, 464, 2910

Tacchella S., Carollo C. M., Faber S. M., Cibinel A., Dekel A., Koo D. C., Renzini A., Woo J., 2017, ApJ, 844, L1

Tacconi L. J., et al., 2018, ApJ, 853, 179

Tadaki K.-i., et al., 2019, PASJ, 71, 1

Tomczak A. R., et al., 2015, ApJ, 817, 118

Treu T., Ellis R. S., Kneib J., Dressler A., Smail I., Czoske O., Oemler A., Natarajan P., 2003, ApJ, 591, 53

Trujillo I., et al., 2006, ApJ, 650, 18

Trujillo I., Ferreras I., de la Rosa I. G., 2011, MNRAS, 415, 3903

Tumlinson J., et al., 2013, ApJ, 777, 59

Valentinuzzi T., et al., 2010a, ApJ, 712, 226

Valentinuzzi T., et al., 2010b, ApJ, 721, L19

Van Dokkum P. G., Franx M., 1996, MNRAS, 281, 985

Vanzella E., et al., 2005, A&A, 434, 53

Vanzella E., et al., 2006, A&A, 454, 423

Vanzella E., et al., 2008, A&A, 478, 83

Vergani D., et al., 2010, A&A, 509, A42

Viana A., Wiklind T., 2009, NICMOS Instrument Handbook, Version 11.0

Vogt N. P., Haynes M. P., Giovanelli R., Herter T., 2004, AJ, 127, 3300

Vollmer B., Braine J., Combes F., Sofue Y., 2005, A&A, 441, 473

Vulcani B., et al., 2015, ApJ, 814, 161

Vulcani B., et al., 2016, ApJ, 833, 178

Vulcani B., et al., 2018, MNRAS

Wang X., et al., 2017, ApJ, 837, 89

Weinmann S. M., Kauffmann G., van den Bosch F. C., Pasquali A., McIntosh D. H., Mo H., Yang X., Guo Y., 2009, MNRAS, 394, 1213

Wetzel A. R., Tinker J. L., Conroy C., 2012, MNRAS, 424, 232

Wetzel A. R., Tinker J. L., Conroy C., van den Bosch F. C., 2013, MNRAS, 432, 336

Whitaker K. E., Kriek M., van Dokkum P. G., Bezanson R., Brammer G., Franx M., Labbé I., 2012a, ApJ, 745, 179

Whitaker K. E., van Dokkum P. G., Brammer G., Franx M., 2012b, ApJ, 754, L29

Whitaker K. E., et al., 2014, ApJ, 795, 104

White S. D. M., Rees M. J., 1978, MNRAS, 183, 341

Wild V., Walcher C. J., Johansson P. H., Tresse L., Charlot S., Pollo A., Le Fèvre O., De Ravel L., 2009, MNRAS, 395, 144

Wilkinson C. L., Pimbblet K. A., Stott J. P., 2017, MNRAS, 472, 1447

Williams R. J., Quadri R. F., Franx M., van Dokkum P., Labbé I., 2009, ApJ, 691, 1879

Williams C. C., et al., 2017, ApJ, 838, 94

Wilson G., et al., 2009, ApJ, 698, 1943

Wisnioski E., et al., 2015, ApJ, 799, 209

Wisnioski E., et al., 2018, ApJ, 855, 97

Woo J., et al., 2013, MNRAS, 428, 3306

Wu P.-F., Gal R. R., Lemaux B. C., Kocevski D. D., Lubin L. M., Rumbaugh N., Squires G. K., 2014, ApJ, 792, 16

Wu P.-F., et al., 2018, ApJ, 868, 37

Wuyts S., et al., 2007, ApJ, 655, 51

Wuyts S., et al., 2011, ApJ, 738, 106

Wuyts S., et al., 2012, ApJ, 753, 114

Yan R., et al., 2009, MNRAS, 398, 735

Yano M., Kriek M., van der Wel A., Whitaker K. E., 2016, ApJ, 817, L21

Yoon Y., Im M., Kim J.-W., 2017, ApJ, 834, 73

York D. G., et al., 2000, AJ, 120, 1579

Zabel N., et al., 2019, MNRAS, 483, 2251

Zahid H. J., Geller M. J., 2017, ApJ, 841, 32

Zahid H. J., Hochmuth N. B., Geller M. J., Damjanov I., Chilingarian I. V., Sohn J., Salmi F., Hwang H. S., 2016, ApJ, 831, 146

Zanella A., et al., 2016, ApJ, 824, 68

van Dokkum P. G., Franx M., 2001, ApJ, 553, 90

van Dokkum P. G., et al., 2008, ApJ, 677, L5

van Dokkum P. G., et al., 2010, ApJ, 709, 1018

van Dokkum P. G., et al., 2015, ApJ, 813, 23

van den Bergh S., 1976, ApJ, 206, 883

van der Burg R. F. J., et al., 2013, A&A, 557, A15

van der Burg R. F. J., Muzzin A., Hoekstra H., Wilson G., Lidman C., Yee H. K. C., 2014, A&A, 561, A79

van der Burg R. F. J., Hoekstra H., Muzzin A., Sifón C., Balogh M. L., McGee S. L., 2015, A&A, 577, A19

van der Wel A., Holden B. P., Zirm A. W., Franx M., Rettura A., Illingworth G. D., Ford H. C., 2008, ApJ, 688, 48

van der Wel A., Bell E. F., van den Bosch F. C., Gallazzi A., Rix H.-W., 2009, ApJ, 698, 1232

van der Wel A., et al., 2012, ApJS, 203, 24

van der Wel A., et al., 2014, ApJ, 788, 28

This thesis was typeset using LaTeX, originally developed by Leslie Lamport and based on Donald Knuth's TeX. The body text is set in 12 point Egenolff-Berner Garamond, a revival of Claude Garamont's humanist typeface. A template that can be used to format a PhD dissertation with this look & feel has been released under the permissive AGPL license, and can be found online at github.com/suchow/Dissertate or from its lead author, Jordan Suchow, at suchow@post.harvard.edu.